1506
UNIVERSITÀ
DEGLI STUDI
DI URBINO
CARLO BO

DEPARTMENT OF BIOMOLECULAR SCIENCES (DISB)

PhD program in Life Sciences, Health and Biotechnologies

Curriculum

Cell and Organism Biology

XXXIII Cycle

FLUORESCENT DYE DOPED CORE-SHELL SILICA NANOPARTICLES FOR DIAGNOSTIC AND THERAPEUTIC APPLICATIONS: PRELIMINARY STUDIES AS INNOVATIVE MULTIMODAL TOOL IN IMAGING AND THERAPY

SSD: BIO/16

Supervisor:

Prof. Stefano Papa

PhD Student:

Dr. Federica Sola

Co-supervisor:

PhD Barbara Canonico

PhD Alfredo Ventola

ACADEMIC YEAR 2019/2020

Table of contents

Abbreviations

ABC, accelerated blood clearance

AC, affinity chromatography

AcOH, acetic acid

ACNPs, antibody conjugated nanoparticles

ADCs, antibody drug conjugates

ADME, absorption, distribution, metabolism and excretion

AF4, asymmetrical flow field-flow fractionation

AUC, analytical ultracentrifugation

CNT, carbon nanotubes

CSC, cancer stem cell

CT, computed tomography

Ctrl, untreated control cells

Cy5, cyanine 5

Cy5.5, cyanine 5.5

DAR, drug to antibody ratio

DEB, diethynylbenzene

DCFH-DA, dichlorodihydrofluorescein diacetate acetyl ester

DCM, dichloromethane

ddH_2O, double distilled water

DLS, dynamic light scattering

DMSO, dimethyl sulfoxide

DOX, doxorubicin

DTT, 1,4-dithiothreitol

EDC, ethyl-3-(3-dimetilaminopropil)carbodiimide

ECM, extracellular matrix

EPR, enhanced permeability and retention

EtOH, ethanol

EVs, extracellular vesicles

FBS, fetal bovine serum

FCS, forward scatter

FITC, fluorescein isothiocyanate

FRET, fluorescence resonance energy transfer

GRAS, Generally Regarded as Safe

HA, hyaluronic acid

HPLC, High Performance Liquid Chromatography

IMM, inner mitochondria membrane

LTG, LysoTracker Green

LSPR, localized surface plasmon resonance

mAb, monoclonal antibody

MDC, monodansylcadaverine

MDV, mitochondrial-derived vesicle

MFI, mean fluorescence intensity

MPS, mononuclear phagocyte system

MRI, magnetic resonance imaging

MTG, MitoTracker Green

MTMS, methyltrimethoxysilane

NaOAc, sodium acetate

NHS, N-hydroxysuccinimide

NK, natural killer

NMs, nanomaterials

NNI, National Nanotechnology Initiative

NPs, nanoparticles

NTA, nanoparticle tracking analysis

O/N, over night

PBMC, peripheral blood mononuclear cell

PCC, Pearson's correlation coefficient

PEG, polyethylene glycols

PET, positron emission tomography

PI, propidium iodide

PS, phosphatidylserine

PSMA, prostate-specific membrane antigen

PVDF, polyvinylidene fluoride

QD, quantum dots

RES, reticuloendothelial system

RGD, arginine-glycine-aspartate

Rhod, Rhodamine

ROS, reactive oxygen species

RPE, R-phycoerythrin

RPMI, Roswell Park Memorial Institute

RT, room temperature

SEC, size exclusion chromatography

SEM, scanning electron microscopy

SiNPs, silica nanoparticles

SMCC, succinimidyl-4-(N-maleimidomethyl) cyclohexane-1-carboxylate

SPECT, single photon emission computed tomography

SSC, side scatter

TAT, trans-activator of transcription

TMB, tetramethylbenzidine

TNF- α, tumor necrosis factor α

TMRE, tetramethylrhodamine ethyl ester perchlorate

US, ultrasound

Abstract

Since most biologically active macromolecules are natural nanostructures, operating in the same scale of biomolecules gives the great advantage to enhance the interaction with cellular components, as cell membrane and proteins. Among the variety of new nanomaterials investigated and developed during last decades, nanoparticles (NPs) provide a particularly useful platform, showing unique properties with wide-ranging applications. As a result, NPs are by far the most versatile and deeply studied class of nanomaterials. NT_B700 NPs, employed for our research, are fluorescent core-shell silica nanoparticles, synthesized through a micelle-assisted method. The aim of the present study was firstly NP characterization and interaction with some biological models (U937 and peripheral blood mononuclear cells), describing the specific triggered biologic response, in order to exploit this new technology for future applications. The use of U937 cells guaranteed the possibility to collect data on a homogeneous, numerically plentiful, myeloid population, whereas peripheral blood mononuclear cells (PBMCs) allowed for the simultaneous analysis of NP effects on many and varied important immune cells like B-cells, T-cells, monocytes and natural killer cells, which is fundamental once introduced into the blood torrent. Initially, we investigated NT_B700 physicochemical properties, their size and the presence of aggregates, related to pH. For the purpose of using these nanomaterials as drug delivery and/or imaging tools, it is necessary to study their endocytosis, sub-cellular fate, localization and clearance mechanisms in target cells. To characterize how NT_B700 NPs were taken up by cells, we quantified their incorporation through flow cytometry, supported by a qualitative analysis performed by confocal microscopy. Results showed that the internalization process is time-, concentration-, energy- and cell type-dependent. Once inside the cells NPs were transported within plasma-membrane bounded vesicles along microtubules to organelles, as lysosomes and, in particular, mitochondria, but without affecting cell viability. Cells, in fact, did not go to death but we may hypothesize a slight arrest of cell growth. By flow cytometry and confocal microscopy, we also investigated the effect of NT_B700 NPs on several trafficking routes and pathways involving e.g. lysosomes, autophagosome, mitochondria and ROS production. Based on previous results, we isolated mitochondria from U937 cells treated with NPs to more in deep investigate their localization and to study the mitochondrial redox environment, which is important for mitochondrial dysfunction and cell death. Finally, both lymphoid and myeloid cells were able to release NPs and this is essential to assess their biosafety and future developments. Since NPs appeared a promising imaging platform, showing a specific subcellular localization, we

decided to conjugate one of the most commonly used anticancer drug, doxorubicin (DOX). We tested these modified NPs on breast cancer cell line MCF-7, since DOX is currently one of the most effective agents in the treatment of breast cancer. We evaluated DOX-NP cytotoxicity and effect on the expression of CD44 antigen, a molecule involved in adhesion, therefore in cell spreading in tumour invasion, both on cell surface and on extracellular vesicles (EVs) released from cells, compared to free DOX and stand-alone NPs. We did not observe an increased cytotoxic effect, as we expected, but an interesting ability to release a minor amount of CD44+ EVs in cells treated with DOX-NPs. In parallel, we also conjugated some of the most common monoclonal antibodies (mAbs) on NP surface, by exploiting the amine groups on NP shell, to investigate the targeting abilities of NT_B700 NPs. Among the various potential applications of this versatile technology, we decided to study in deep the capability of multiple dye doped NPs to be fluorescent probes. NPs resulted brilliant probes for these immune cell antigens, confirming their capability to target the desired cells. All these data allow us to consider fluorescent SiNPs a promising platform for a multifunctional device in which collimate both the imaging and therapeutic applications in a unique tool conveying to a specific target.

Introduction

1 Nanotechnology

Nanotechnology, historically, has been defined as research and technology development at the atomic or molecular scale leading to the controlled assembly and manipulation of materials, devices and systems within a nanometer range. It has achieved the status as one of the keys and most promising technologies of the 21st century (McNeil, 2005, Nagamune, 2017, Bayda et al., 2020). The prefix "nano" refers to the Greek prefix νάνος, which means "small of its kind/dwarf" and represents one thousand millionth of a meter in the measurement system (10^9 m). It is important to distinguish between nanoscience and nanotechnology. The last one is, therefore, the ability to convert the theory of nanoscience, which is mainly the study of structures and molecules in a length scale from 1 to 100 nm, in practical applications (Bayda et al., 2020).The concept of nanoscience has been introduced for the first time in 1959 from the physicist Richard Feynman, which is considered the father of modern nanotechnology, in its lecture entitled *"There's plenty of room at the bottom: An invitation to enter a new field of physics"*, in which he hypothesized that in the future it would be possible to manipulate and control things on a small scale, by acting directly on the position of individual atoms and molecules (Feynman, 1960). After fifteen years, in 1974, Norio Taniguchi introduced and defined the term "nanotechnology" as: *"the processing of separation, consolidation, and deformation of materials by one atom or one molecule"* (Taniguchi, 1974). Nowadays, the National Nanotechnology Initiative (NNI) in the United States defines nanotechnology as *"a science, engineering, and technology conducted at the nanoscale (1 to 100 nm), where unique phenomena enable novel applications in a wide range of fields, from chemistry, physics and biology, to medicine, engineering and electronics"*. In summary, the NNI definition refers to three basic concepts: it is necessary to develop special tools to work at nanometer scale because of the very small dimensions, at the nanoscale materials may behave in different and unexpected ways and researchers have to exploit these different functioning to create new technologies (Bayda et al., 2020). Therefore, nanotechnology is highly interdisciplinary and involves several disciplines such as physics, chemistry, biology, materials science and the full range of the engineering areas (Picraux, 2020).

Despite not being a newly discovered concept, nanotechnology and nanomaterials in general are, even today, fascinating research areas with multiple application potentials, especially in biomedical fields such as therapy and diagnostics. Since most biologically active

macromolecules are natural nanostructures (Fig. 1), operating in the same scale of biomolecules gives the great advantage to enhance the interaction with cellular components, as cell membrane and proteins (McNeil, 2005, Mahapatro & Singh, 2011).

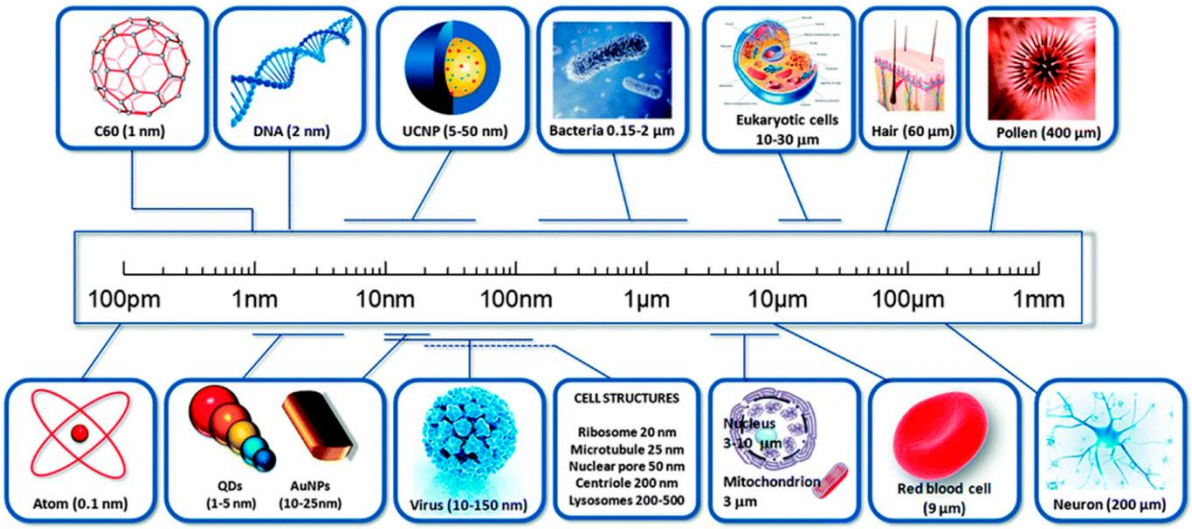

Fig. 1 A comparison of sizes of different nanomaterials and biological nanostructures and organelles (Bayda et al., 2020)

1.1 Nanotechnology applied to biological systems

The ability to control size of the resulting structures and devices is the obvious advantage of applying nanotechnology to biological systems in a wide variety of tools and applications. Nanostructured materials operate in the same size realm of biological entities which facilitates the interaction with cell membrane, proteins and organelles, without altering the behaviour or biochemical properties of those molecules (McNeil, 2005, Mahapatro & Singh, 2011). This is important in living cells for studying and providing data on the complex signaling networks and transport processes that govern the behaviour of cells in their normal state and which modifications undergo during disease process. Nanoscale constructs are smaller than human cells and organelles, whose dimensions are illustrated in Fig.1 and are similar in size to large macromolecules such as enzymes, receptors or the lipid bilayer surrounding cells. This characteristic facilitates the penetration of blood-brain barriers or the stomach epithelium or some fundamental organs in therapy such as spleen and liver (McNeil, 2005). The unprecedented freedom to design and modify size and structure of nanomaterials to the own

liking is the extra gear offered by nanotechnology, which promises to impact several fields of biology: drug development, medical diagnostics, clinical applications and much more (McNeil, 2005, Mahapatro & Singh, 2011).

As concerning drug delivery, nanotechnology may influence medical treatments in multiple ways. Advance in nanoscale design and fabrication gives new options for drug delivery and therapy, for example all the new molecules which are not water-soluble and difficult to be delivered, at the nanosized level, overcome these limits (Picraux, 2020). Several strategies for passing through the biological barriers are implemented including (a) preventing removal from circulation by cells or reticuloendothelial system (RES), (b) targeting specific cells, (c) internalization into cells, (d) endosomal escape, (e) trafficking to specific organelles and (f) controlling the release of payloads. More important, the possibility to deliver precisely to the right location or to release the therapeutic substance on a predetermined schedule, for optimizing treatments, for example by attaching a carrier which is able to release medicine when triggered to do so. The surface modification of nanomaterials allows the bond of biological ligands: folate, arginine-glycine-aspartate (RGD) peptides, aptamers, transferrin, antibodies or small antibody fragments. Monoclonal antibodies (mAbs) have been the most used targeting molecules for membrane proteins, receptors and glycol-antigens on tumor cells. Over time, many small antibody fragments or alternative molecular scaffolds to mAbs have been investigated and developed (Fig. 2), mostly to overcome the limitations of the very large complexes formed with mAbs (Nagamune, 2017).

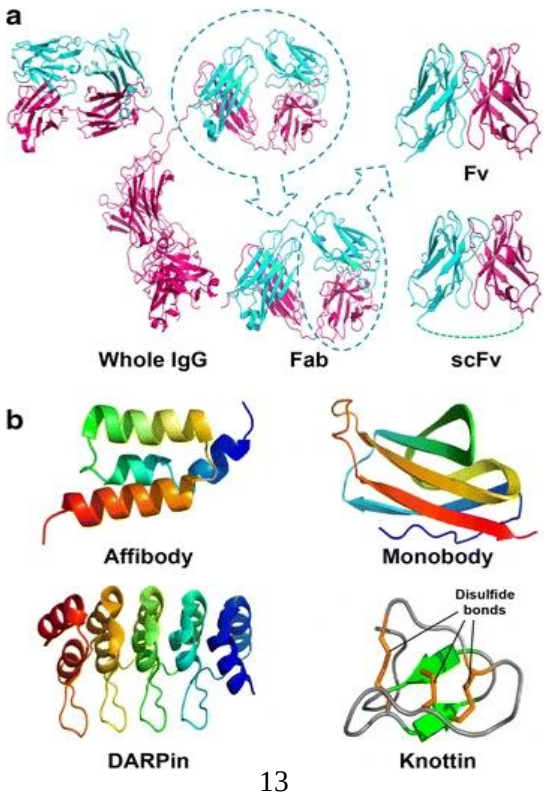

Fig. 2. Targeting molecules. (a) Whole IgG (150-170 kDa) and its small fragments: antigen-binding fragment (Fab: ~ 55 kDa), variable fragment (Fv: ~ 27 kDa) and single-chain variable fragment (scFv: ~ 28 kDa). (b) small molecular binding scaffolds: affibody, which is a three-helix bundles structure derived from the Z domain protein A; DARPin, with three or more repeated small domains consisting of two α-helices separated by a β-turn derived from ankyrin repeated proteins; monobody, with seven β-sheets forming a β-sandwich and three exposed loops from the 10th human fibronectin extracellular type III domain; knottin, involving a triple-disulfide stabilized knot motif. (Nagamune, 2017)

Another important area of nanotechnology application is the developing of new diagnostic tools. Much diagnostic effort now focuses on detecting specific biological "signature" thanks to the advances in molecular biology. Nanomaterials and nanofabrication technologies play significant roles in constructing bioassays, such as biosensors and biodevices. The unique properties of biomaterial-conjugated nanostructures give the great advantage of signal amplification in assays for the detection of a broad range of biomarkers with ultrahigh sensitivity and selectivity and rapid response. A wide range of nano-based bioassays has been developed: colorimetric, fluorescent, surface-enhanced Raman scattering, electrochemical, magnetic resonance imaging (MRI), quartz crystal microbalance and much more (Nagamune, 2017, Picraux, 2020). Several promising nanomaterials with biomolecule-modified surfaces are used in the field of diagnostics. One of the first nanomaterials which had a wide impact on biosensing was carbon nanotubes (CNTs), which have the advantage of a large surface to volume ratio, an excellent electron transfer ability and easy biomolecule immobilization. Several nanomaterials have been directed on imaging thanks to their intrinsic characteristics, such as quantum dots (QDs) as brilliant fluorescent agents, magnetic NPs in MRI or colloidal AuNPs. Microfluidics systems and microarrays, or "labs-on-chips", have enabled the simultaneous analysis of many disease biomarkers for cancer, infectious diseases, Alzheimer's disease, diabetes and cardiovascular diseases. Finally, the manipulation of many biomolecules, such as nucleic acids, peptides, proteins and lipids, enabled to exploit their functions and characteristics in several fields of application, like therapy, diagnosis, bioanalysis and biocatalysis. All this has been possible thanks to the development of biomolecular engineering, gene engineering, chemical and enzymatic conjugation technologies and linker engineering (Nagamune, 2017).

1.2 Nanomaterials

In 2011 the European Commission defined a nanomaterial a *"natural, incidental, or manufactured material containing particles, in an unbound state or as an aggregate or as an agglomerate and where, for 50% or more of the particles in the number size distribution, one or more external dimensions is in the size range 1–100 nm"*. A plethora of nanostructured materials (nanorods, nanotube, nanoparticles, nanofiber, nanowires, nanocapsules, etc.) have been produced during decades, consequently with a large scale of applications in several fields. Nanomaterials (NMs) have drawn attention based on the properties they exhibit like the large surface-to-volume ratio and the new physical-chemical properties associated with quantized effects (such as melting point, wettability, electrical and thermal conductivity, catalytic activity, light absorption and scattering) (Jeevanandam et al., 2018, Picraux, 2020). Furthermore, the possibility to control composition, size, shape, and morphology of nanomaterials is an essential cornerstone for the development and application of nanoscale devices. NMs could be categorized depending on their size, composition, shape and origin. As concerning their origin, NMs can be classified as natural or synthetic. Natural nanomaterials are produced in nature either by biological species (like bacteria, algae, yeasts and fungi), by combustion (natural fire or volcanos) or through anthropogenic activities. Synthetic (engineered) nanomaterials can derive from engine exhaust, mechanical grinding and smoke, or are manufactured by physical, chemical, biological or hybrid methods (Jeevanandam et al., 2018). Many manufacturing approaches have been developed for the synthesis of nanostructures which were gathered in two categories (schematically represented in Fig. 3): top-down and bottom-up (Mendes, 2013, Bayda et al., 2020). The former approach is basically the breaking down or etching away bulk materials to achieve nano-sized particles by employing advanced techniques such as precision engineering and lithography. The bottom-up approach, instead, refers to the building-up of nanostructures atom-by-atom or molecule-by-molecule, using controlled manipulation or spontaneous self-assembly of atoms or molecules, in much the same way that nature does (Mendes, 2013, Bayda et al., 2020). Due to the increase amount of nanomaterials produced and their industrial applications, studying on their effects on health and toxicity is inevitable (Jeevanandam et al., 2018).

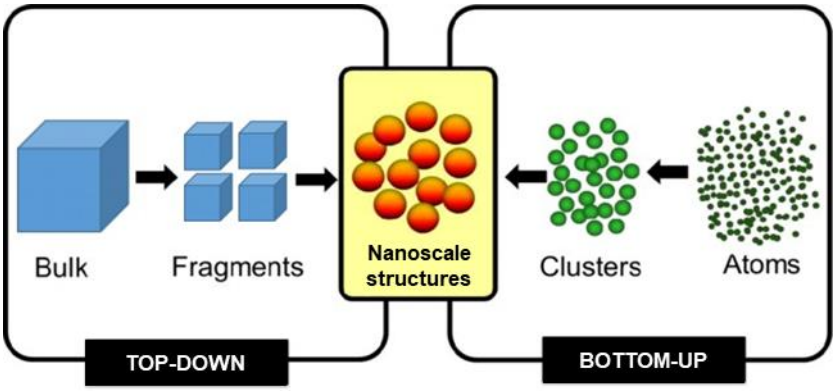

Fig. 3 "Top-down" and "bottom-up" schematic representation of nanofabrication approaches. [Adapted from Rawat, 2015]

2 Nanoparticles

Among the variety of new nanomaterials investigated and developed during last decades, nanoparticles (NPs) provide a particularly useful platform, showing unique properties with wide-ranging applications. As a result, NPs are by far the most versatile and heavily studied class of nanomaterials (Gubala et al., 2020). NPs are a class of material defined as particulate dispersions or solid particles, which have at least one dimension between 1 and 100 nm (Mohanraj and Chen, 2007). However, despite the definitions gave by several national and international regulatory bodies, many researchers habitually use the term “nano” to refer to material with dimensions below 1 μm (Gubala et al., 2020). Thanks to the great attributes of the size similar to biomolecules which enhances their interaction and the possibility to engineer size, shape, materials and surface properties (Fig. 4), NPs result a versatile technique in a wide range of biological applications (Wang & Wang, 2014).

The NP surface is the first part with which cells interact. Electric charge plays an essential role in the NP adsorption and translocation across the cell membrane. Positively charged NPs exhibited higher cell uptake, thanks to the increased entropy. Because of the formation of highly ordered membrane regions that are entropically unfavourable, on the contrary, negatively and neutral charged NPs are poorly internalized (Villanueva-Flores et al., 2020). NP surface charge does not only influence cell uptake and intracellular trafficking, but it has also been demonstrated that can have an effect on the cellular phenotype of differentiated cells. A very interesting example was the use of chemically modified carbon nanotubes (CNT) as a substrate for cultured neurons. Hu et al. showed that longer neurites and more elaborate

branching were observed on positively-charged carbon nanotubes substrates. highlighting the possibility to control the outgrowth and branching pattern of neuronal processes, by manipulating the charge of the functionalized nanomaterial. A similar effect can be achieved by changing the functional groups exposed on NP surface to control differentiation of mesenchymal stem cells. These findings suggest that modulating NP physical properties allow to control cell behaviour and this could have a huge biomedical potential (Hu et al., 2004, Li et al., 2015). Another key parameter is the NP surface hydrophobicity because it is closely related to cell membrane properties. Surface modification with polyethylene glycol (PEG), for example, can increase the hydrophilicity and diminish opsonization. Binding of opsonins (plasma proteins and other blood components) on NP surface, otherwise, leads to a rapid internalization and clearance *in vivo*, and hence decreases the circulation time in the blood stream. Surface modification with hydrophilic polymers/surfactants or biodegradable copolymers with hydrophilic segments can, thus, lead to a long circulating "stealth" NP. In particular, PEG has been extensively employed to make NP invisible to phagocytic cells and to protect them from the immune system (Heinz et al., 2017, Villanueva-Flores et al., 2020).

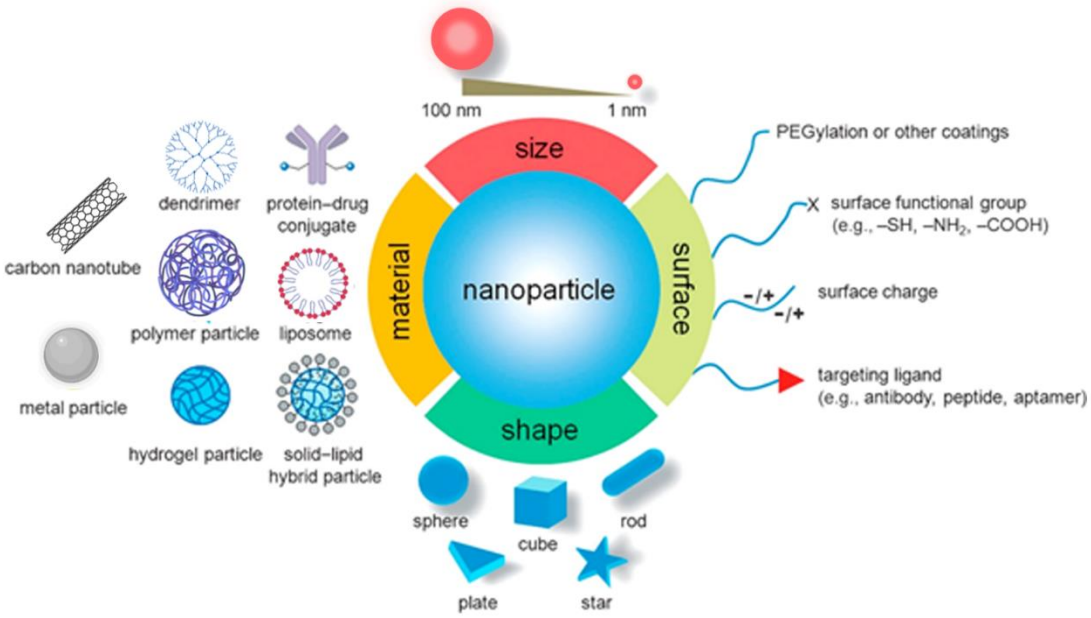

Fig. 4 Several types of nanoparticles, composed of different materials, that have been explored as drug delivery in cancer therapy and their biophysicochemical properties. Size, shape and surface play a major role for their characteristics and properties. [Adapted from Heinz et al., 2017]

Control over size and shape can improve their performance in specific applications and have an essential role as concerning biodistribution, internalization rate, uptake mechanism and toxicity. Which method to measure NP size remains to be standardized and this is still a challenging task of determining the effect of NP size on the interaction with biological components. Several techniques are used to measure this parameter, each one with intrinsic limitations. The medium/solvent used in the biological experiments could be the same for the NP resuspension prior the measurement because every solvent has different ionic strength and pH, and influences NP surface charge, aggregation, stability, but especially the protein corona formed over the NP surface. Regarding biodistribution, for example, NPs >200 nm were filtered by spleen beds and could not easily pass through interendothelial slits to reach the venous circulation. On the contrary, quantum dots (QDs) with a hydrodynamic diameter <5.5 nm were rapidly cleared from the body by renal filtration. Particles with dimension between 40 and 50 nm exhibited the highest cell membrane receptor uptake (Heinz et al., 2017, Villanueva-Flores et al., 2020). On the other hand, a recent study with surface-modified polystyrene nanoparticles demonstrated that particles between 100 and 200 nm had higher cellular uptake efficiency across the gastrointestinal barrier and the blood-brain barrier than 20–100 nm sized particles (Kulkarni and Feng, 2013). Several studies show that there is not a universal size for optimal NP internalization, as the optimal size is different for each cell type. Cellular plasma membranes are dynamic and selectively permeable components that not only border the cellular perimeter but also control trafficking into cells. A size-dependent interaction exists between NPs and the required signaling for their uptake by cells (Villanueva-Flores et al., 2020). The vast literature on this topic highlights that the underlying mechanisms that mediate the non-targeted NP uptake are not fully understood. NP size may affect the uptake efficiency and kinetics, the internalization mechanism and also the subcellular distribution. Elucidation of the endocytic pathway involved in NP uptake has a crucial relevance for enhancing their internalization by cells, manipulating their intracellular trafficking and minimizing possible toxic effects (Huang, Ma, Khor, and Lim, 2002). Cells internalize exogenous materials through various endocytic pathways, that could be generally classified into five mechanistically different classes: clathrin-mediated endocytosis (a), caveolae-mediated endocytosis (b), clathrin- and caveolae-independent endocytosis (c), macropinocytosis (d) and phagocytosis (e) (Panariti et al., 2012, Kou et al., 2013, Oh & Park, 2014, Donahue et al., 2019). Each one of these mechanisms strictly depends on the cell type and differentiation state, then it has been recently demonstrated that different pathways are also activated depending on NP size with which cells interact, as summarized in Fig. 5. Elucidating

the NP uptake mechanisms is necessary to evaluate how they are incorporated into cells and NP size-dependent toxicity. NPs with diameters between 1 and 100 nm showed an alteration of processes essential for basic cellular functions, including active and passive cell death. The smallest nanoparticles investigated, with diameters below 2 nm, have been identified in most papers as toxic for cells. The hypothesized mechanisms proposed to explain the toxicity of these very small NPs could be mainly three: their perfect fit in the major grooves of DNA, the increased ROS production and the blockage of membrane ion channels (Villanueva-Flores et al., 2020). Furthermore, sublethal effects upon exposure of NPs have been observed and are related to size. For example, Senut et al. examined the effects on pluripotency, neuronal differentiation, DNA methylation of human embryonic stem cells (Senut et al., 2016).

The shape is another important factor that determines the structural, physical, and chemical properties of NPs. Different NP shapes show different electronic, optical, and magnetic properties. Nowadays, the advancement in nanotechnology has made it possible to obtain nanomaterials of all types of shape (for example flower-like, ellipsoid, octahedra, 2D- triangles, star like, etc.). These technological developments on NP synthesis can undoubtedly enlarge the spectrum of solutions to improve the function and targeting of nanodevices, but also to provide tools for understanding the effects at different length scales (vascular, cellular and subcellular levels) (Villanueva-Flores et al., 2020). The shape, therefore, could affect NP toxicity, route of internalization and intracellular fate. Many studies suggest that cytotoxicity and apoptosis increase with the decreasing NP aspect ratio. Nevertheless, sharp and edges of anisotropic structures may damage blood vessels. All these findings emphasize that shape is an important parameter to consider for efficiency and safety of NPs and, depending on the application we desire, we can choose a certain shape (Vácha et al., 2011). For example, spherical-, star- and flower-shaped AuNPs are highly efficient in internalization experiments and can be applied for designing delivery nanosystems. Furthermore, spheres were the least cytotoxic and the stars the most (Steckiewicz et al., 2019). In general, spherical and ovoidal particles are more easily internalized compared to elongated particles that orient parallel to the cell membrane and are less easily internalized. Several studies observed that NP uptake depends on their shape, with a higher rate of internalization for sphere > flower >cube > rod >disk. It may be due to the ease of bending of cell membrane around particles. Researcher also observed that cell membrane quickly wrapped star-shaped NPs, similarly to the spherical counterparts (Barua et al., 2013, Li et al., 2015).

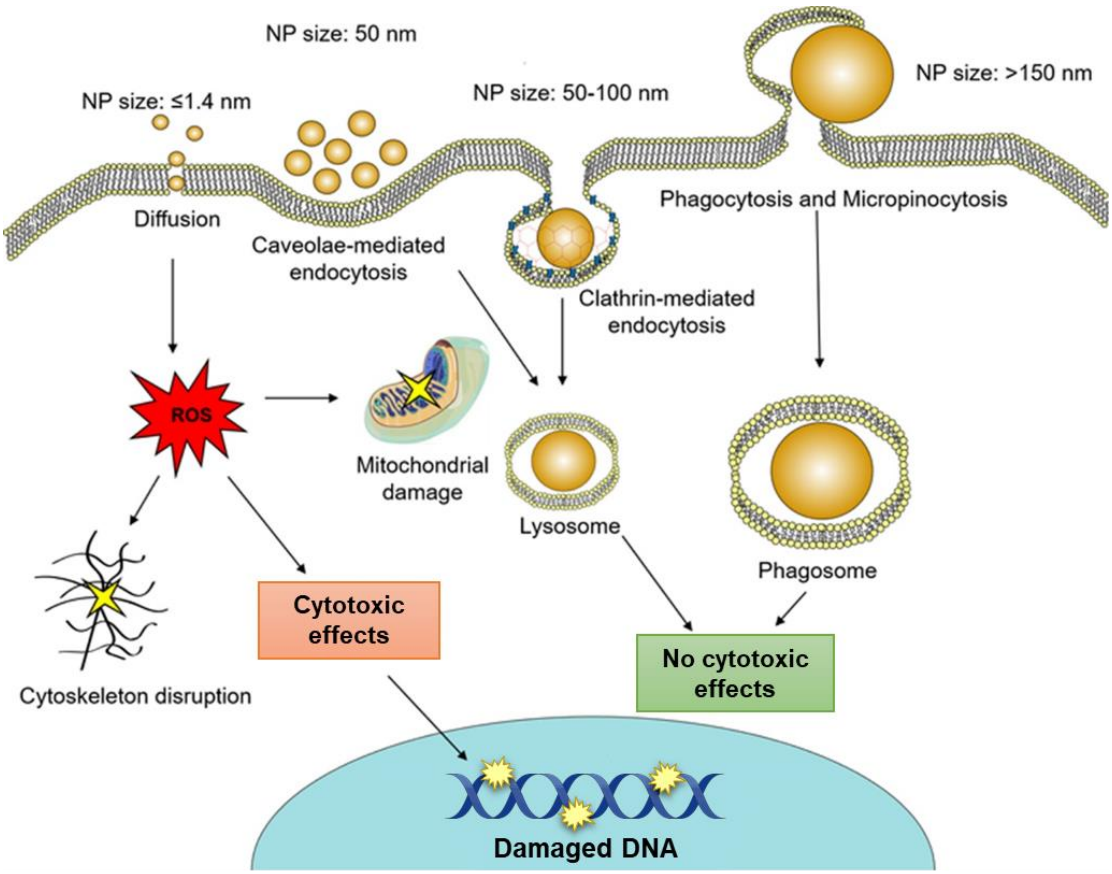

Fig. 5 Size-dependent NP uptake mechanisms and cytotoxicity. The figure summarizes observations regarding the role of NP size on cellular internalization mechanisms. Small NPs (≤ 1.4 nm) have been typically reported as cytotoxic due to oxidative stress induction (ROS) that disrupts the cytoskeleton and damages mitochondria and DNA. NPs with intermediate sized (≈50–100 nm) can be internalized by caveolae-mediated or clathrin-mediated endocytosis depending on the cell line and NP material, and finally, bigger NPs (150–500 nm) can be internalized by macropinocytosis. It is important to consider that both the NP material and the cell line influence internalization. [Adapted from Villanueva-Flores et al. 2020].

2.1 Types of nanoparticles

As presented in Fig. 4, there are many types of NP platform with different size, shape, composition and functionalities. The plethora of NP compositions and architecture reported in literature has get the term "nano-Particle Zoo", housing a myriad of nanomaterials (including nanoparticles, nanobubbles, nanotubes, nanoclusters, nanostars, etc.) fabricated using different techniques with exciting ranges of applications (Moore et al., 2015). This "Zoo" contains, as a matter of fact, several materials, as gold, carbon, quantum dots, silica, liposomes and iron oxide, with different shapes (spheres, plates, cages, stars, worms, etc.) and, as a consequence, different properties (plasmonic, fluorescent, magnetic, etc.) (Gubala et al., 2020). NPs are

divided into various categories depending on their morphology, size and chemical properties (Fig. 6). Based on the physicochemical characteristics, some of the well-known classes of NPs are presented below.

Lipid-based NPs

These NPs contain lipids as building blocks and have characteristically spherical shape with diameter ranging from 10 to 1000 nm. Among several lipid-based formulations, the most famous examples are "liposomes," which were the first NP platform. In 1965 liposomes were described for the first time as model of cellular membranes. Since that moment, they moved from a model in biophysical area to one of the main NP forms which have been applied in several biomedical applications, such as gene and drug delivery (Puri et al., 2009, Wang & Wang, 2014). The principal components of these NPs are phospholipids, which are organized in a bilayer structure and self-assemble in presence of water. Generally, surfactants or emulsifiers are employed to stabilize the external core of these NPs. They are able to encapsulate either hydrophobic or hydrophilic drugs. Furthermore, in addition to phospholipids, other compounds could be added to their formulations, such as cholesterol, which decreases the fluidity of NPs and increases the permeability of hydrophobic drugs through the bilayer membrane, improving the stability of these nanostructure in blood. Therefore, liposomes have the great advantages to carry and protect many types of molecules and biomolecules, as well as their biocompatibility and biodegradability (E. C. Wang and Wang, 2014). Currently, there are numerous liposome-based formulations that have been clinically approved as therapeutic drugs to combat cancer and infectious diseases, while others await clinical trial outcomes (Puri et al., 2009).

Polymeric NPs

Polymeric NPs are formed from biocompatible and biodegradable polymers and have been extensively studied as therapeutic carriers in nanomedicine applications depending on their simple and fast preparation techniques and biosafety. They are composed of block-copolymers of different hydrophobicity which spontaneous assemble in the core-shell structure in an aqueous environment. Polymeric NPs are mainly nanospheres, whose overall mass is generally solid and the other molecules are adsorbed on the spherical surface, or nanocapsules, in which the solid mass is encapsulated within the particle. Polymeric nanomedicines commonly belong to two main categories: polymer-drug conjugates (for increase drug bioavailability and half-

life) and degradable polymeric structures (for controlled-release formulations). They usually improve the efficacy of the drug they carry, thanks to the controlled release in the target site, by exploiting targeting ligands on functionalized polymeric NPs, and the increased uptake along with their cargo, leading to enhanced therapeutics effects (Wang & Wang, 2014, Çalış et al., 2019).

Dendrimers

Dendrimers are a unique class of nano-sized polymers, with a well-defined, homogeneous, and monodisperse structure consisting of tree-like arms or branches whose size and shape can be precisely controlled. These hyperbranched molecules were first discovered by two separated research groups in the early 1980s and called "arborols" that, in latin, means "trees". They might also be called "cascade molecules" but this term is not as much established as "dendrimers" (Abbasi et al., 2014). Dendrimers are produced from monomers using either convergent or divergent steps of growth polymerization. As a consequence, the size of these polymeric nanostructures is dependent on the number of branching which, clearly, can be controlled. Thus, they are monodispersed macromolecules that have a typically symmetric core, an inner shell (branches), and an outer shell (surface). The term "dendrimer" refers to an architectural motif and not a compound (Abbasi et al., 2014, Bhatia, 2016). These nanostructures arise several branches from the core in shape of a spherical structure by means of polymerisation, resulting in the formation of cavities within the dendrimer molecule, which can be useful for drug transport or other bioactive molecules. Furthermore, free ends of dendrimers can be exploited for the binding of several molecules, e.g. branches or end groups can be tailored or modified into biocompatible compounds with low cytotoxicity and high biopermeability. Such interesting properties make dendrimers attractive drug carrier candidates. Moreover, they have a well-defined structure with surface functionalization capability, monodispersity of size, and stability properties (Bhatia, 2016). Finally, a variety of dendrimers exists, and each has biological properties such as polyvalency, self-assembling, electrostatic interactions, chemical stability, low cytotoxicity, and solubility. These varied characteristics make dendrimers ideal in various distinct applications, besides drug delivery, such as gene therapy, immunoassays, sensors, solubilization and MRI contrast agents (Abbasi et al., 2014, Bhatia, 2016).

Nanogels

Nanogels are three-dimensional hydrogel materials in the nanoscale size range formed by crosslinked swellable polymer networks with the capability to imbibe water when placed in an aqueous environment, without actually dissolving into it (Rigogliuso et al., 2012). Nanogels can be composed of a variety of naturally or synthetic polymers or a combination of the two. By changing their chemical composition, all their characteristics of size, charge, porosity, amphiphilicity, softness, and degradability can be adapted according to the needs. They are mostly spherical particles, but the efforts done in the synthetic strategies allow for the fabrication of nanogels with different shapes (Soni et al., 2016). Thanks to their hydrophilic nature, the inertness in the blood stream and biocompatibility nanogels result very interesting for several biomedical applications, compared to other nanomaterials. A great advantage of these hydrogel nanoparticles is the high loading capacity for guest molecules and the possibility to obtain an elevated degree of encapsulation, that make them ideal candidates for uptake and delivery of DNA, proteins, peptides and other biological compounds or chemical drugs. Moreover, owing to their molecular size (between 100-700 nm), nanogels can escape renal clearance and have prolonged serum half-life time, which is a main feature in drug delivery systems. Often, they cannot pass through the endothelial junctions of normal blood vessels. But, notably, the vascular endothelium in pathological sites (e.g. solid tumors, inflammation tissues and infracted areas) is discontinuous with large fenestrations, which allow the nanoparticle passage Nanogels not only protect their cargo from degradation and elimination but also participate actively in the delivery process. Thanks to their distinctive properties such as sweeling, softness and stimuli-responsive behaviour nanogels help to reach a controlled and triggered response in the target site. Nanogels are developed also as *in vivo* diagnostic and imaging tools due to their optical, electrical and magnetic properties. Nevertheless, they suffer from some limitations such as poor colloidal stability, low aqueous solubility and rapid elimination by the mononuclear phagocyte system (MPS). For this reason, to date a few nanogel-based formulations have reached clinical trials (Rigogliuso et al., 2012, Soni et al., 2016).

Metal NPs

Metal NPs are, obviously, made of metals precursors, i.e. silver (Ag NPs), gold (Au NPs), copper (Cu NPs), palladium (Pd NPs), titanium dioxide (TiO_2 NPs) and zinc oxide (ZnO NPs). Metals are characterized by bright shine, solidity, ability to vibrate sound, and are excellent

conductors of electricity and heat. Owing to well-known localized surface plasmon resonance (LSPR) characteristics, these NPs have unique optical properties. Thanks to all these characteristics metal NPs find applications in many scientific fields such as medicine, physics, mechanics, pharmaceutics and others (Sharma et al., 2019, Khan et al., 2019). For example, for gold, silver, and copper NPs by using thiol ligand molecules, which can attach on the particle surface as a self-assembled monolayer, the plasmon color NPs can work as good detection materials because NPs aggregation changes their color (Yonezawa, 2018). Among metal NPs, Au NPs are widely used in several biomedical fields thanks to their size- and shape-dependent optical and chemical properties, biocompatibility and easy surface modification. Au NPs are applied for the delivery of numerous drugs as doxorubicin, paclitaxel, and methotrexate, for genetic disease or tumor diagnosis, photothermal therapy and photoimaging. Iron oxide NPs are studied in particular as passive and active targeting imaging agents as are mainly superparamagnetic. These NPs have been mostly used for magnetically responsive drug delivery therapy and magnetic resonance (MR) imaging (MRI). Also, Ag NPs have been used for several treatments in particular as antimicrobial, anti-inflammatory and anticancer applications (Wang & Wang, 2014, Sharma et al., 2019, Shnoudeh et al., 2019).

Quantum dots

Quantum dots (QDs), first discovered in 1980, are nanocrystals of semiconducting materials measuring around 2-10 nm which display unique size-dependent electronic and optical properties. Mostly, QDs consist of a cadmium selenide (CdSe) core and an aqueous organic zinc selenide (ZnS) shell. Core of the QDs determines the color emitted and outer aqueous shell is available for conjugation with biomolecules. The adsorption spectra of these particles are very broad and emission results in a narrow band. Owing to their properties originating from their physical size, QDs emit bright colours, have high photostability and long lifetime and are stable against photobleaching (Wang & Wang, 2014, Bhatia, 2016). They can be produced to have different biochemical specificities and can be simultaneously excited and detected. As a consequence, QDs have various advantages over many fluorophore dyes for different optical applications. As a result, they are extensively employed in biological research as fluorescent imaging tools for applications such as cell labelling and biomolecule tracking. Thanks to their small size, QDs are also used in biomedical areas such as a diagnostic as well as a therapeutic tool, e.g. the development of non-viral vectors for gene delivery or therapeutic tools for cancer treatments and transport vehicles for DNA, proteins or drugs. However, their utilization in

clinical practise or diagnostic has some limitations because of elimination problems which cause extreme toxicity. Their size is larger than the pore size of endothelium and renal capillaries by reducing their elimination and, furthermore, very little is known about QD metabolism and excretion consequently limiting their use (Bhatia, 2016).

Carbon-based NPs

Generally, these nanomaterials contain carbon and are found in morphologies such as hollow tubes, ellipsoids or spheres. Fullerenes and carbon nanotubes (CNTs) represent two major classes of carbon-based NPs. Fullerenes are made of globular hollow cage such as allotropic forms of carbon. They have some typical properties, as electrical conductivity, high strength, structure, electron affinity, and versatility, which gave them notable commercial interest. Fullerenes present pentagonal and hexagonal carbon units while each carbon is sp^2 hybridized. CNTs are elongated, tubular structures with a 1-2 nm diameter, which resemble to graphite sheet rolling up upon itself. Due to their unique characteristics, these types of materials are useful in many commercial applications as fillers, efficient gas adsorbents for environmental remediation and support medium for different inorganic and organic catalysts (Jeevanandam et al., 2018, Khan et al., 2019).

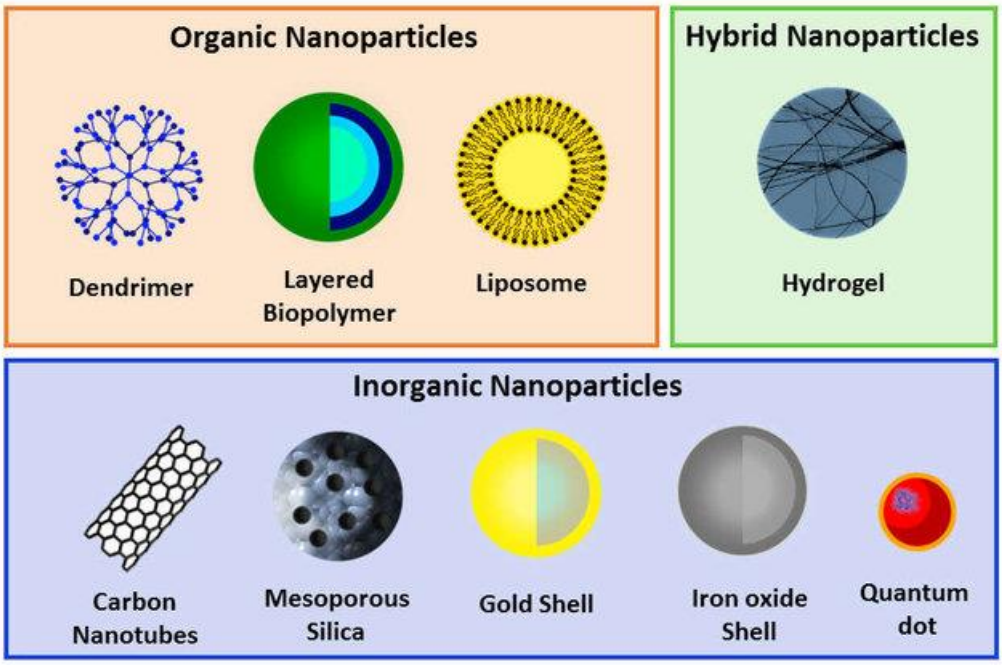

Fig. 6 Schematic representation of different types of nanoparticles (NPs) classified into three groups: organic, inorganic and hybrid NPs. (Silva, Almeida, and Vale, 2019)

2.2 AcZon nanoparticles

AcZon NPs are core-shell dye doped silica nanoparticles synthesized through a micelle-assisted method, where a surfactant is used to create a nanoreactor within which all the hydrophobic reagents arrange (Fig. 7) (Pellegrino et al., 2018). Thanks to the addition of ammonia and silane precursor, the base-catalysed hydrolysis of all the trialkoxysilanes takes place and leads to the formation of fluorescent monodisperse nanoparticles. Shell is composed by two different polyethylene glycols (PEG), both terminating with a trialkoxysilane:

- H_3CO-PEG-$Si(OR)_3$, main component of the shell which induces stability and solubility in water;
- H_2N-PEG-$Si(OR)_3$, the functionalized form in order to have the amine reactive groups on the external shell.

Fluorochromes are themselves components of silica core, thanks to a covalent modification with trialkoxysilane group.

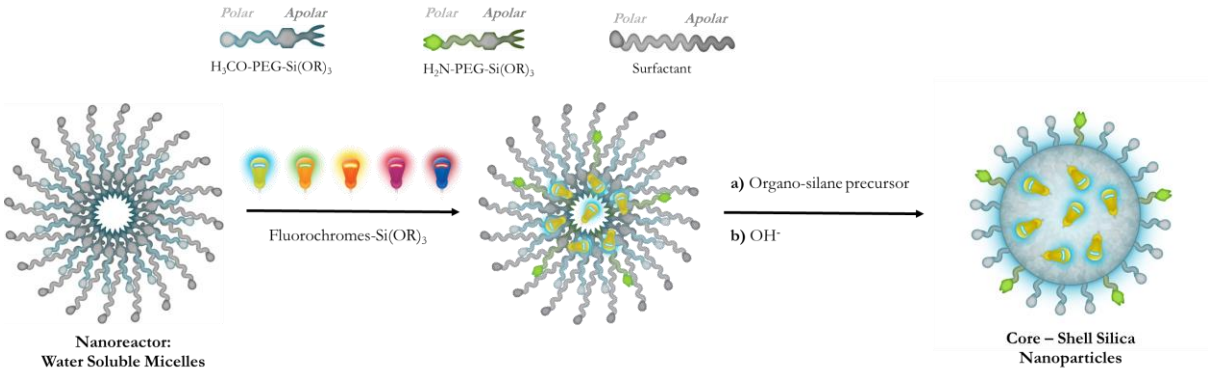

Fig. 7 Schematic representation of the synthesis of AcZon core-shell silica nanoparticles, through a micelle-assisted method, where a surfactant is used to create a nanoreactor within which all reagents arrange. The base-catalysed hydrolysis of a silane precursor, along with different dyes and two different forms of PEG (H_3CO-PEG and H_2N-PEG) all functionalized with a trialkoxysilane group, able to covalently link to the silica matrix, leads to the formation of fluorescent monodisperse NPs. (Pellegrino et al., 2018)

While traditional fluorochromes are still affected by lack in stability and low intensity emission in water solution, these fluorescent NPs are emerging as promising probes allowing to

overcome these limits. The most innovative feature of AcZon NPs is the ability to be a platform where the fluorescence energy transfer process, known as FRET, occurs at a high efficiency rate. Besides being the most used "stealth" polymer in the drug delivery field, PEG allows to modulate the type and number of functional groups (e.g. amine, thiol, carboxyl or methacrylate) exposed on the external shell of NPs. Therefore, PEG properties lead to the conjugation of several biomolecules on AcZon NPs. Amine reactive groups, for instance, can be linked to monoclonal antibodies via crosslinkers, through a site-specific conjugation, preserving antibodies biological activity. The main and more interesting properties of AcZon nanoparticles are presented below.

2.2.1 Silica nanoparticles

Among several nanomaterials, silica nanoparticles represent one of the most widespread systems employed in nanotechnology research and development, and hold great practical applications (Chu et al., 2011). In the field of fluorescence, silica has proven to be an excellent platform, thanks to the fact that it is photophysically inert, i.e., it does not adsorb visible light, and it is not involved in energy or electron transfer processes. Consequently, all the photochemical properties of silica nanoparticles are conferred by the molecules doped inside the system or grafted on their surface. Another advantage of silica is that it is intrinsically non-toxic, in particular if compared to other nanomaterials such as quantum dots (which are generally classified as toxic), which are still widely employed in bioanalytical applications (Gubala et al., 2020). If on the one hand crystalline silica NPs are often reported to be carcinogens, on the other hand amorphous silica NPs are commonly considered biocompatible and harmless, based on their toxic effects evaluated in various *in vitro* studies (Chu et al., 2011, Blechinger et al., 2013). Lastly, from a synthetic point of view, besides the fact that it is rather inexpensive, silica is a very appealing material: the preparation of nanoparticles usually requires mild conditions and does not involve complicated purification procedures, the synthesis is straightforward and versatile enough to allow for different dyes and drugs to be entrapped in the silica matrix and for control over the resulting NP size and shape. In addition, silica chemistry, which is adaptable and well-understood, allows a simple and linear modification of NP surface in order to provide reactive sites for further functionalisation (Gubala et al., 2020). Generally, the most used synthetic strategies for silica NPs are the Stöber method modified by van Blaaderen, the reverse microemulsion method and the one based on

direct micelles as template, all of which have their own advantages and disadvantages (Fig. 8) (Bonacchi et al., 2011).

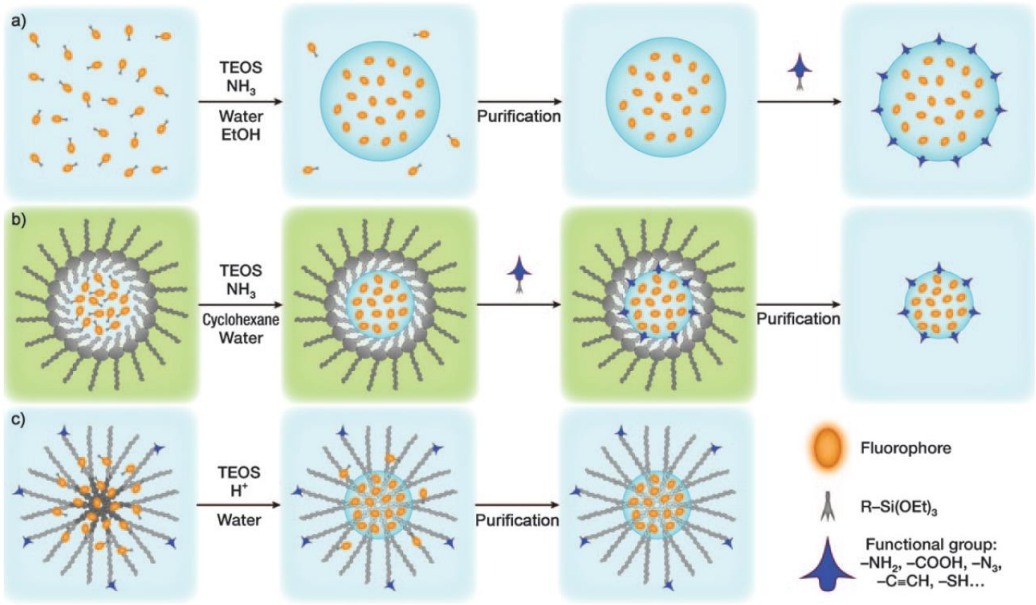

Fig. 8 Common strategies for silica nanoparticle synthesis. All cases involve the controlled hydrolysis of tetraethyl orthosilicate (TEOS) molecules and their catalysed condensation. The three methods, basically, differ in their reaction medium. a) Stöber –van Blaaderen method: involves the hydrolysis and condensation of TEOS, in a water/alcohol mixture catalysed by the addition of ammonium hydroxide. b) Reverse microemulsion or water-in-oil method: surfactant-stabilised water droplets are dispersed in an oil phase to create micelles that serve as a "nanoreactor" for the confined nucleation and growth of silica NPs; TEOS diffuses into the water phase (which also contains ammonia catalyst), and undergoes hydrolysis and condensation. c) Silica-core/PEG-shell nanoparticles: hydrolysis and condensation are confined inside the aqueous nuclei of the inverted microemulsion, where TEOS and the organic precursors diffuse during the reaction. [Adapted from Bonacchi et al. 2011]

2.2.2 Dye doped nanoparticles and fluorescence resonance energy transfer (FRET)

As previously introduced, small molecules organic dyes present several drawbacks, as their susceptibility to photobleaching (especially under stressing conditions), many species could interfere and quench their fluorescence, most of them are highly hydrophobic species (limiting their use in aqueous systems) and, moreover, the synthesis of a supramolecular system could be demanding, time-consuming and expensive. For these reasons, many researchers decide to dope NPs with one or more dyes. The silica matrix, indeed, can protect them from the interfering species present in the external environment (such as oxygen, certain solvents and soluble species in buffer solutions), thus increasing their (photo) stability and, in many cases,

their luminescence quantum yield Φ. Dye doped NPs, furthermore, contain a large quantity of dye molecules housed inside their matrix, giving up a great signal enhancement respect to organic fluorophores (Fig. 9). In general, NPs with maximal brightness and signal enhancement is important to facilitate ultrasensitive analyte detection and the determination of rare biological events that are otherwise difficult to be detected. Thus, dye doped silica NPs are particularly suitable materials for producing bright labels, which are of great interest in diagnostic techniques, such as histology and flow cytometry. There are two ways to incorporate dye molecules into the silica matrix: entrapment or covalent attachment (Wang et al., 2006, Bonacchi et al., 2011). The optimal NP brightness is largely associated with the concentration of dye molecule inside the silica matrix. Therefore, it is necessary to balance the correct amount of fluorophores inside NPs in order to avoid, on the one hand, an insufficient brightness due to few fluorophores, on the other, a self-quenching phenomenon if too many are densely packed inside the silica core, resulting in an reduced overall brightness (Gubala et al., 2020). The mutual disposition of the fluorophores inside the silica matrix, besides, may impact on the formation of aggregates and on the efficiency of homo- and hetero-energy transfer processes inside the system, thus determining a reduce NP fluorescence intensity (Bonacchi et al., 2011).

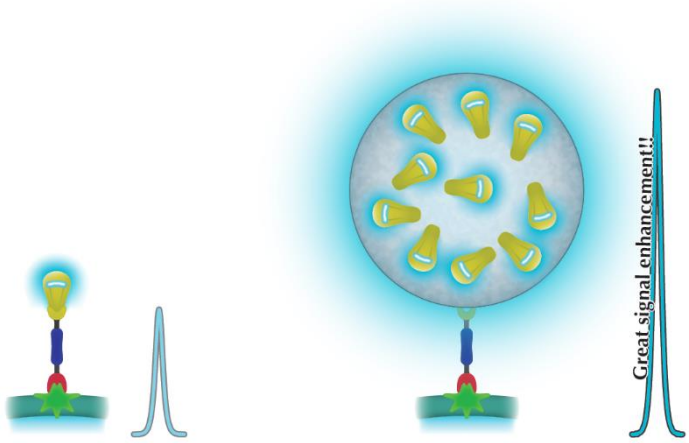

Fig. 9 Schematic comparison between a single molecular fluorophore and fluorescent nanoparticles containing more dyes molecules inside the silica matrix and the corresponding signal enhancement.

Silica NPs are an excellent platform where the energy transfer process occurs at highly efficient rates, thanks to the close proximity of the molecules grafted onto the silica matrix. This non-radiative transfer mechanism was first described by Theodor Förster and it is known as Förster

resonance energy transfer or fluorescence resonance energy transfer. It is a bimolecular process between a donor molecule (D) in the excited state and an acceptor molecule (A) in the ground state. Donor absorbs energy at shorter wavelength whereas acceptor has energy absorption at longer wavelength. There are some conditions under which FRET occurs. The two molecules, donor and acceptor, must be in the near field, in a range between 1 and 10 nm. The emission spectrum of the donor must overlap with the absorption spectrum of the acceptor. Finally, the donor emission and acceptor absorption dipole moments must be oriented in favourable directions (Shrestha, et al., 2015). Multiple dye doped silica NPs exploit FRET by encapsulating different fluorophores with overlapping excitation and emission wavelengths inside the silica matrix allowing for large Stokes shift to be produced, thus improving the signal to noise ratio. The generation of multicolour silica NPs made them suitable for multiplex analysis by exploiting different dyes combination in order to have several wavelengths (Fig. 10). However, it is important to consider the desired application of NPs since it is necessary to choose dyes and the most appropriate synthetic route. Covalent binding of dyes inside the silica matrix will hold fluorophores inside the particle core longer than those physically entrapped. Stabilising dye doped silica NPs against dissolution in aqueous media is therefore advised before biological experimentations as the release of free dye can lead to confusing experimental outcomes and not the efficacious application of the NPs (Gubala et al., 2020).

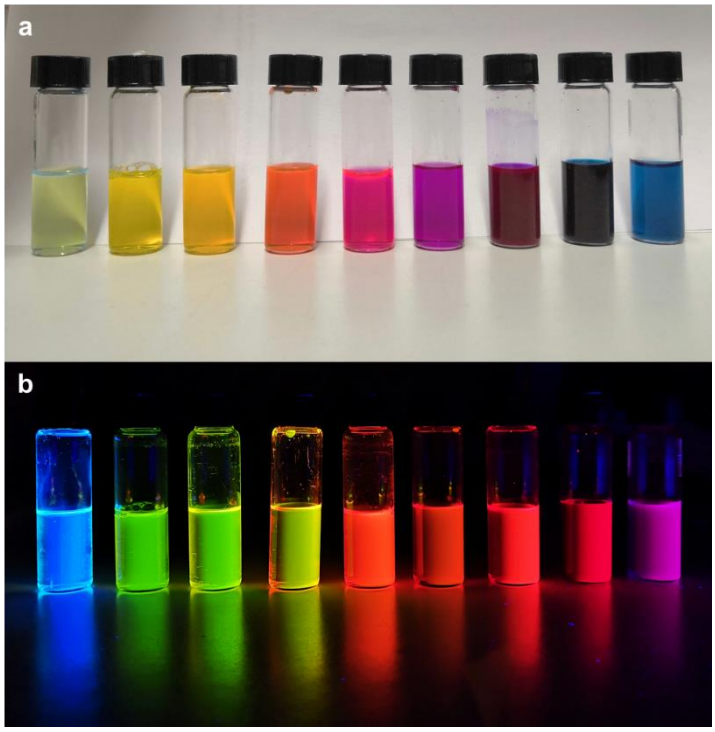

Fig. 10 Images of multiple dye doped silica nanoparticles with different fluorochromes produced in AcZon under ambient light (a) and under 365 nm UV lamp (b).

2.2.3 PEG shell

As previously introduced, AcZon NPs are core-shell nanoparticles, in which the core is composed of a silica matrix whereas the shell is made up of two different PEGs, one main component and the other one with terminal amine groups. With the aim of using NPs in various biomedical applications such as drug delivery, imaging or diagnostic, it is important to protect them from the immune system attack. In general, the use of therapeutic drugs in clinical applications has some limitations including poor solubility as well as adverse pharmacokinetics and biodistribution. Regarding the therapeutic purpose, NPs, that serve as drug reservoirs, can potentially improve the drug solubility and prolong the blood circulation half-life, releasing the drug in a controlled manner to minimize the systemic side effects and further improve the pharmacokinetics (Fam et al., 2020). Despite the interesting features of NPs, their potential antigenicity and immunogenicity often limit their applications as nanocarriers because of their interaction with the mononuclear phagocyte system (MPS) or complement system that led to the rapid clearance of NPs. One approach to avoid it is to coat the surface of the carriers with an inert polymer that resists to the interactions with the components of the bloodstream, imparting "stealth" properties. Polyethylene glycol is one of the most widely used "stealth" polymer, due to its long history of safety in humans and it has been classified as Generally Regarded as Safe (GRAS) by the FDA. Thus, PEG is considered the gold standard and has been extensively employed, in particular, in drug delivery systems in the past decades. The term PEGylation refers to the addition of PEG on the particle surface (Suk et al., 2016, Fam et al., 2020). The MPS, previously known as the reticuloendothelial system (RES), is composed of dendritic cells, monocytes, granulocytes, and tissue-resident macrophages in the liver, spleen, and lymph nodes that are responsible for clearing, processing, and degrading exogenous materials in the blood stream. Thus, the MPS provides an essential defence mechanism that protects from foreign pathogens, but, at the same time, rapidly removes therapeutic NPs from the blood stream, preventing their goal. Unprotected NPs are readily recognized by serum proteins called opsonins, such as the immunoglobulins, complement proteins, or receptors present on the surface of macrophage plasma membrane. Adsorption of opsonins on NP surfaces (called opsonization) causes NPs to become more susceptible to phagocytosis by cells in the MPS. Of note, macrophages can also directly capture NPs by opsonin-independent scavenger receptors. Circulating serum proteins interact with NPs, thereby forming a protein corona on NP surface which make easier NP uptake by cells encountered during their circulation, including endothelial cells. Furthermore, aggregation of circulating NPs can also

weaken their circulation time, because of the uptake by MPS or other non-target cells (Suk et al., 2016, Fam et al., 2020). The most accepted theory on the stealth properties of PEG is based on the hypothesis that PEG chains exhibit an extended and plastic surface barrier layers, due to their flexible and hydrophilic nature, that sterically prevent the adhesion of opsonin proteins by allowing NPs "invisible" for phagocytic capture (Gubala et al., 2020). Moreover, due to their hydrophilic nature, PEG chains on NP surface generate a hydrated cloud with a large excluded volume that sterically precludes NPs from interacting with neighbouring NPs and/or blood components (Suk et al., 2016). Several studies have shown that PEG-modified NPs presented an extended life-time circulation and are passively targeted to tumor tissues. Passive targeting exploits the characteristic enhanced permeation and retention (EPR) effect of solid tumors. Fig. 11 schematically shows the fate of PEG-modified or non-PEGylated NPs after intravenous administration. Opsonin proteins in the blood torrent recognize non-PEGylated nanoparticles, once injected, targeting them for rapid clearance from the circulation. Most of these NPs are moved to the mononuclear MPS organs, such as liver and kidney resulting in poor accumulation in their target. Conversely, stealthed NPs avoid opsonization for a prolonged period of time, resulting in enhanced tumor accumulation. For example, Choi et al. investigated the tumor-targeting ability of self-assembled PEGylated hyaluronic acid nanoparticles. These NPs displayed enhanced tumor uptake with a concomitant reduction in accumulation in the liver. Interestingly, the tumor uptake of PEGylated NPs was around 1.6-fold higher than the counterpart non-PEGylated, indicating a higher extravasation of PEGylated NPs into tumoral tissues (Choi et al., 2011). Hence, by applying a camouflaging technique on NPs, the blood circulation half-life can be improved by escaping the recognition and clearance mechanisms just described by the MPS and/or complement system (Babu et al., 2014).

Finally, PEG is commercially available in a variety of forms (short chained, polymeric or hyper-branched) with a wide range of functionalities and therefore allows for biomolecule binding, thus combining "stealth" and targeting ability into the same system (Gubala et al., 2020). It is also possible to utilise different types of PEG for NP surface to exploit their properties end construct a multifunctional tool by bioconjugating different molecules on NPs. Despite the numerous biomedical applications exploiting PEG properties (many of which FDA approved), some studies have reported that some PEGylated products can generate anti-PEG antibodies, which induce rapid elimination and liver uptake upon repeated doses of PEGylated NPs. This unexpected immunogenic response has commonly referred to as the "accelerated

blood clearance" (ABC) phenomenon. Interestingly, it has also been reported the innate existence of anti-PEG antibodies in 20–25% of normal individuals who have never been treated with PEGylated deliveries. In spite of these critical shortcoming of PEG, which lead to the search for potential alternative stealth coating for drug delivery systems, PEG is still widely employed (Fam et al., 2020, Gubala et al., 2020).

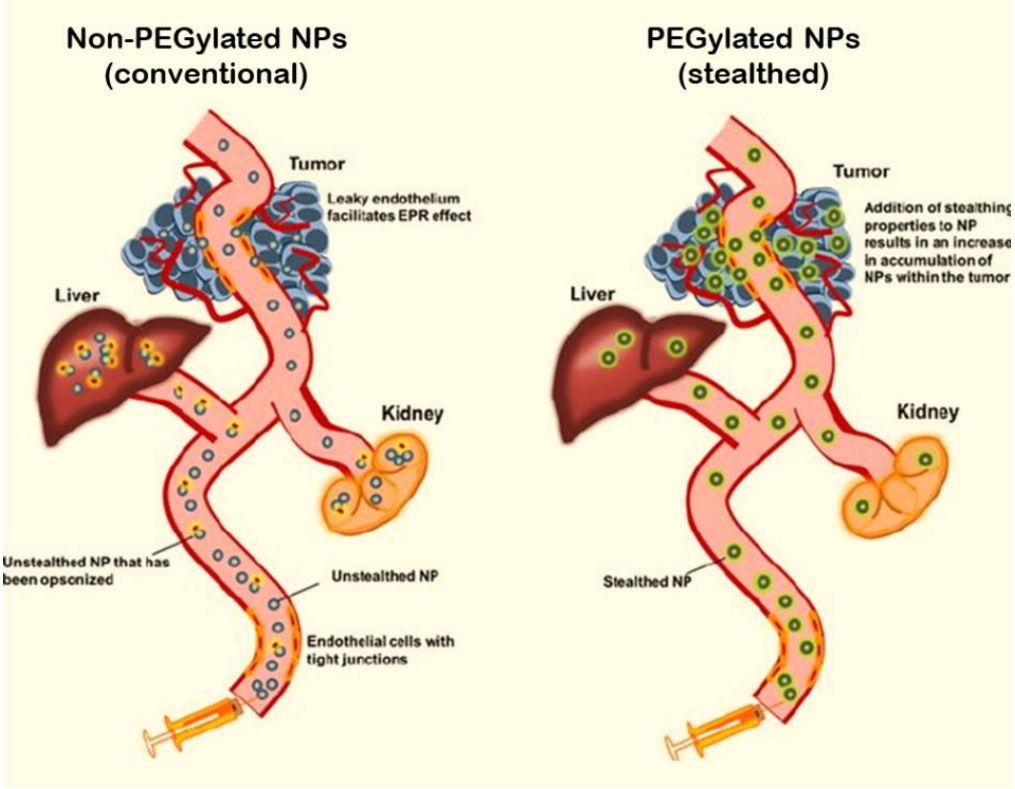

Fig. 11 Schematic image showing the fate of PEG-modified (stealthed) or non-PEGylated (conventional) NPs after intravenous administration. Stealthed NPs (on the right) are poorly recognized by opsonin proteins in blood torrent allowing NPs to rapid elude the phagocytic clearance, resulting in enhanced tumor accumulation, thanks to the enhanced permeability and retention (EPR) effect. On the contrary, conventional NPs (on the left) are rapidly opsonized and cleared from the circulation resulting in poor tumor accumulation and, in reverse, are moved to the mononuclear MPS organs, liver and kidney. [Adapted from Babu et al. 2014]

2.3.Multifunctional nanoparticles

As seen above, NPs are a very versatile technology, in term of size, material, surface properties and shape, with multiple and different application areas. Recent advances in nanotechnology and, in particular, growing needs in biomedical employments have driven the development of multifunctional nanoparticles. Whereas monofunctional NPs provide a single function (e.g. imaging, therapy, diagnostic *in vitro* or *in vivo*, drug delivery, etc…), multifunctional NPs, as the name says, have the potential to integrate, in the same stable tool, various functionalities. For example, a targeting molecule that recognises the surface signature of a specific target cell could be bound to a NP. Simultaneously, the same NP can be modified with an imaging agent (or the NP itself might be an imaging or contrast agent) and/or linked to a drug and, so, monitoring the drug transport process up to the target, which is a function to evaluate the therapeutic efficacy (Sanvicens & Marco, 2008, Bao et al., 2013). Many efforts have been done to advance this technology in diagnosis and treatment of cancer. Multifunctional NP systems can integrate, mostly, imaging, targeting and delivering drug payload, both on the surface and in the core of the particles. Compared to traditional diagnosis and therapeutic methods, this system presents some advantages which give multifunctional NPs great potential as innovative diagnostic and therapeutic systems for the clinical field. (1) NPs can easily integrate more than one kind of imaging or therapeutic agents, allowing to combine more functions together for both diagnosis and therapy. (2) Thanks to their properties, such as large surface area or interior cargo volume, considerable amounts of drugs or imaging agents can be inserted into NPs o conjugated on their surface; (3) NPs can target disease sites for diagnosis or drug delivery with specific targeting moieties or physicochemical optimization of size and surface properties. Moreover, compared to single targeting molecules, more than one, on NP surface, can greatly enhance target-binding and specificity. (4) Proper surface modifications or appropriate size of NPs can lead to improved circulation time in blood torrent (Lee et al., 2012).

Table 1 - A summary of the strategies for constructing multifunctional nanoparticles [Adapted from Sanvicens & Marco 2008]

Functionalities	Benefits	Examples
Stability, biocompatibility	Maintain drug levels in the blood, therefore improving specificity	PEG Modified acrylic acid polymers Phospholipids micelles Polypeptides
Specific targeting	Increase efficiency and reduce toxicity	Antibodies Peptides Aptamers Carbohydrates Folic acid
Intracellular penetration	Modify nanoparticle pharmacokinetics and biodistribution, increasing drug efficiency	Peptides Trans-activator of transcription (TAT) Ligands Transferrin Positively charged moieties Cationic lipids Cationic polymers
Imaging	Report real-time nanoparticle biodistribution	Quantum dots Fluorescent nanoparticles Magnetic nanoparticles
Stimulus-sensitive drug release	Control bioavailability and reduce toxicity	pH-labile Photosensitive Thermosensitive Magnetic sensitive Photothermal sensitive Redox sensitive

In Table 1 are summarized some of the common functionalities that are considered when developing multifunctional nanocarriers and their respective advantages. The goal is to build NPs including all the underlying listed properties, but it still represents a challenge. A wide range of features, besides the encapsulated drugs or therapeutic genes, are linked to the nanoparticle to make it multifunctional. Such as targeting ligands to improve specificity, cell penetrating agents to improve cell uptake, stealth providing molecules to avoid the immune systems and prevent opsonization, protective layers to prevent the degradation of biologic cargo (e.g. proteins or DNA), imaging agents to assess delivery and dosing, target-dependent assembly or disassembly to control drug release, microenvironment sensors (pH, protease, phospholipases) to trigger drug release and cell uptake, and intracellular targeting moieties to direct drugs to specific intracellular compartments (Fig. 12). These different features have to be well included so they can operate in an orchestrated way and indeed give the desired functions. Therefore, it is first necessary to choose the more suitable structure and integration

methods prior to the synthesis of multifunctional NPs, depending on the functions needed and starting materials. The choice of structure is critical because several properties of NPs, such as surface plasmon resonance and drug loading function, are affected by the size and shape of NPs. On the other hand, integration method is restricted by the properties of the single components and their chemical reactivity and steric size. Non-covalent bindings, such as electrostatic interactions or hydrophobic adsorption, do not allow to control over the size, composition and multifunctionality of NPs. In reverse, chemical bonds guarantee more control over the different functionalities. However, new chemical strategies are constantly developed to improve reproducibility and better controlled and coordinated properties all together. Lots of multifunctional NPs, that have been reported, indeed show unique designs (Sanvicens & Marco, 2008, Kim et al., 2018). Bifunctional NPs are the simplest approach and there are already numerous examples in literature. Many others examples are currently available pertaining to the use of multifunctional nanoparticle systems in cancer drug delivery and imaging with different types of NPs, such as liposomes, solid lipid NPs, polymeric NPs, QDs, iron oxide NPs, gold NPs, dendrimers, micelles, and carbon nanotubes. For example, Aurimune® (CYT-6091) is the first multifunctional NP system to enter the clinic and is composed of a colloidal- gold NP conjugated to the tumor growth inhibitor tumor necrosis factor α (TNF- α), carrying both imaging and therapeutic functionalities (Babu et al., 2014). Sahoo and co-workers developed a dual (temperature and pH) responsive polymeric magnetic NP system with encapsulated doxorubicin and folic acid tethered to the surface, as well as conjugated with rhodamine B for the monitoring. This smart nanodrug delivery system was capable targeted specific release of doxorubicin in response to pH and temperature causing significant cytotoxicity toward the human cervical cancer cell line HeLa. These results may provide a potential drug carrier for future *in vivo* applications (Sahoo et al., 2013). Farokhzad et al., with a similar approach, developed biocompatible and biodegradable polymeric NPs for the specific delivery of docetaxel to prostate cancer. The targeting functionality, in this case, was achieved using RNA aptamer that recognised the extracellular domain of the prostate-specific membrane antigen (PSMA), a well characterized antigen expressed on the surface of prostate cancer cells (Farokhzad et al., 2006). Recently, Eliasof et al. constructed a multifunctional nanoparticle, denoted CRLX101, which was investigated in phase 2 clinical trials for cancer. CRLX101 was composed of a cyclodextrin backbone with covalently linked PEG polymer and camptothecin linked via a spacer molecule and had a diameter of 20-30 nm. This multifunctional system targeted to solid tumors resulted in enhanced tumor uptake and controlled release of camptothecin over several days to inhibit tumor growth. Their results,

both on animals and humans, demonstrated similar mechanism of action suggesting that CRLX101 behaviour was translatable to humans and could reach the clinic (Eliasof et al., 2013). These are just a few examples of the many multifunctional NPs studied and developed over the last years; there are with many and different combination of functionalities and applications, not only for cancer treatment. Multifunctional NP systems offer several advantages, nevertheless, it is important to consider that each new functionality elevates the complexity and cost of the final system, e.g. multi-step synthesis, purification and characterization, and regulatory barriers arise, owing to multi-components that are present and heterogeneous formulations. Furthermore, the addiction of several functional modalities may result in issues related also to toxicity and scalability of the final product. Multifunctionality may also correlate with unpredictable NP behaviour *in vivo* and another important challenge is the reproducibility of the final product, in terms of synthesis, identification of the appropriate targeting molecules and their optimal density on NP surface. Thus, in conclusion, it is imperative to employ a cautious approach in the development of multifunctional NPs for translational studies, concerning all the possible troubles and challenges that are, as included in their name, multiple in this type of systems (Cheng et al., 2012, Babu et al., 2014).

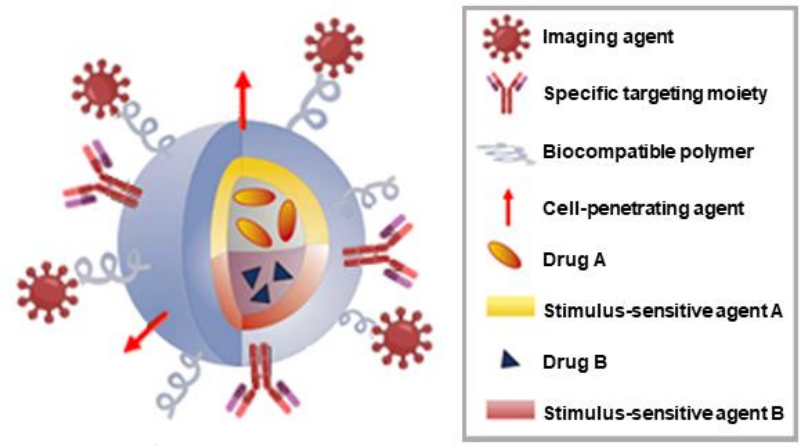

Fig. 12 Schematic example of a multifunctional nanoparticles for drug delivery. Multifunctional nanocarriers can combine a specific targeting agent (usually an antibody or peptide) with nanoparticles for imaging (such as quantum dots or magnetic nanoparticles), a cell-penetrating agent (e.g. the polyArg peptide TAT), a stimulus-sensitive element for drug release, a stabilising polymer to ensure biocompatibility (PEG most frequently) and the therapeutic compound (also two or more therapeutic agents) [Adapted from Sanvicens & Marco 2008]

2.3.1. Antibody conjugated nanoparticles (ACNPs)

In the last years, a new approach has been developed which combine the success and potential of both antibody drug conjugates (ADCs) and nanotechnology: antibody conjugated nanoparticles (ACNPs). They represent a novel strategy for the development of therapies exploiting antibodies to enhance the delivery of drug payloads. Conceptually, ACNPs are similar to ADCs, because antibodies are exploited to specifically target diseased cells, by delivering encapsulated cargo drug (Fig. 13). The aim of ADCs was, indeed, to selectively deliver toxic compounds to diseased tissue, a concept first described by Paul Ehrlich as "Magic Bullets" in the early 1900s to improve the therapeutic index (maximum tolerated dose or toxic dose/minimum efficacious dose). ADCs were first evaluated in the late 1950s using antibodies which targeted leukaemia cells conjugated with the anti-cancer drug methotrexate and represented a new approach that builds on the success of both ADCs and nanotechnology. The first ADC in human clinical trial was reported in 1983 with encouraging results. As concerning ACNPs, they appeared in the literature in 1980 and the first which entered clinical trials was in 2011 (Panowski et al., 2014, Johnston & Scott, 2018). When compared with ADCs, ACNPs, present some advantages concerning therapeutic molecules, such as the delivery of the drug in a controlled way, the preservation of the chemical structure, the reduced risk of secondary metabolites (if metabolism is unpredictable) and, finally, the potentially reduced side effects. Furthermore, it is also possible a combination of chemotherapeutics in the same system, offering the opportunity to potentiate or provide synergistic therapeutic effects. Lastly, no direct drug linker is always required with ACNPs and, hence, this avoids the disruption of the payload efficacy (Fig. 13A). Drug to antibody ratio (DAR) is another important factor that influence the effectiveness of ADCs and ACNPs can potentially offer DARs over 100 (for an ADC is approximately only 4:1 for the optimal balance between cytotoxicity and acceptable pharmacokinetic profiles), ensuring a much higher concentration of therapeutics (Johnston & Scott, 2018, Juan et al., 2020). The mechanisms of action of both targeted therapies (ADCs and ACNPs) are very similar. After binding to the target, the complexes are internalized into the cell through receptor-mediated endocytosis, resulting in the formation of endosomes. Later, endosomes fuse with lysosomes and release the drug into the cytoplasm (Fig. 13B). Though, NP cargo could also directly diffuse through the cellular membrane, enhancing the cellular dispersion of the compound (Juan et al., 2020).

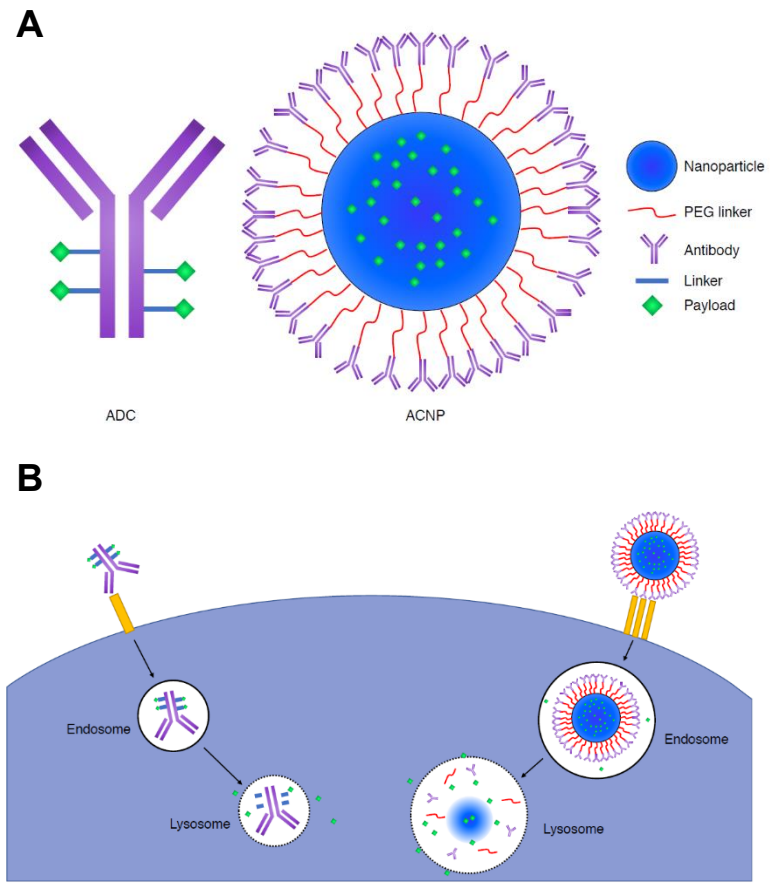

Fig. 13 Schematic representation of antibody drug conjugate (ADC) and antibody conjugated nanoparticle (ACNP) and their mechanism of action on the cell. (A) Schematic representation highlighting the conceptual structure of an ADC and ACNP. (B) Schematic representation of ADC and ACNP mechanism of internalisation, breakdown and drug release into the target cell. (N.B. Antibodies illustrated at different scales). [Adapted from Johnson et al. 2018]

2.3.2. Multimodal imaging

An accurate diagnosis of diseases requires much detailed data and information, and no single imaging technique can provide complete or comprehensive data with the optimum combination of properties (e.g. resolution, sensitivity, cost, availability). The traditional clinical imaging techniques generally include optical imaging, magnetic resonance imaging (MRI), ultrasound (US), computed tomography (CT) and positron emission tomography (PET) or single photon emission computed tomography (SPECT). Each technique has its own unique advantages besides intrinsic limitations. To overcome this problem and improve the currently used imaging

instruments, the combination of multiple imaging modalities has gained more attention, for example PET/CT or PET/MRI. Multimodal imaging, which carries more than two imaging agents, is thus a powerful method that can help in having more informative images of the disease sites through targeted delivery. Furthermore, this new hybrid technology could provide complementary information from distinct imaging modalities by using a single injection of contrast agent (Lee et al., 2012, Li et al., 2016). Multimodal imaging could, additionally, be considered an excellent tool to obtain absorption, distribution, metabolism and excretion (ADME) and pharmacokinetics qualities of novel molecules that are studied for the development of new therapeutics (Burke et al. 2017). NPs possess unique optical effects, electricity properties and magnetic effects and are ideal for these types of applications. Moreover, NPs have large surface areas that can be functionalized to introduce multiple moieties for the development of nanoprobes for molecular imaging. Some inorganic NPs show intrinsic imaging capabilities, such as quantum dots for optical imaging, gold NPs for CT and iron oxide NPs for MR and these could be combined by co-encapsulation or conjugation. In addition, traditional organic NPs (e.g., liposomes, micelles, and polymeric NPs) can integrate more than two imaging agents on the surface or inside and it is possible to make different combinations (Lee et al., 2012, Burke et al., 2017). Even though these combinations are expected to provide more detailed information for a clear diagnosis than a single imaging technique, it is necessary to avoid the overlap of advantages and rather compensate for the weak points of each modality in order to maximize the cooperative outcome. This is the reason why the imaging modalities with high sensitivity (PET, optical, etc.) are commonly fused with other imaging modalities with high spatial resolution (MR, CT, etc.). Even though, on the one hand, the multiple techniques can compensate each other, on the other it is extremely important to consider the different sensitivity of each one. For example, PET tracers must be used in extremely low concentrations, whereas MR or CT agents request high dosages. Thus, it is necessary to pay attention to the amount of the combined imaging agent into NP systems (Lee et al., 2012).

Aim of the study

The research was aimed to investigate multiple dye doped core-shell silica nanoparticles behaviour in some biological models, both tumoral and normal counterpart, in order to exploit this new technology for future applications, in particular for imaging and drug delivery. The study was divided into three main parts and two appendices, as following. The data presented into the first two chapters have been accepted for publication in Nanotechnology, Science and Applications journal (Sub ID: 290867), enriched with unpublished data, while the last one is an article in preparation.

The first chapter objective was the synthesis and physicochemical characterization of NT_B700 NPs. Since more fluorophores are encapsulated into silica core, a detailed photochemical characterization was first assessed. Afterwards, we employed a combinatorial approach for NP size characterization with different techniques to provide more reliable information about this feature. Subsequently, in the second chapter, we focused on NP interaction with some biological models (lymphoid and myeloid cells), as understanding how NPs enter the cells is a key factor in determining their biomedical functions, biodistribution and toxicity. In order to apply NPs in drug delivery or imaging fields, it is also essential to study their clearance mechanisms in target cells. We characterized how NT_B700 NPs were taken up by cells, the triggered biological response and the interaction with some organelles through flow cytometry, coupling quantitative data with qualitative analysis performed by confocal microscopy. The third chapter outcome was the application of silica NPs for drug delivery of doxorubicin, with the aim to overcome some limitations of the anticancer drug, in a breast cancer cell line. We assessed cytotoxicity and the effect on the expression of CD44 antigen, a molecule involved in adhesion, therefore in tumour invasion, cell spreading and metastatic process, both on cell surface and on extracellular vesicles. Finally, in Appendix A, we presented some additional data about the more detailed characterization of NP localization into mitochondria and the impact on these organelles, involved in main cellular activities. Moreover, for future applications for both diagnostic and drug delivery, the targeting skill is required. Thus, in Appendix B, we presented the conjugation of some monoclonal antibodies to NPs. The flow cytometric results on whole blood highlighted the targeting ability of our nanoconstruct, essential for future application as multifunctional system, by combining both imaging and therapeutic tools.

CHAPTER 1

Nanoparticle synthesis and physicochemical characterization

Data accepted in

Sola et al. (2021) Nanotechnol Sci Appl.

Sub ID: 290867

Article in Press

And unpublished data

Materials and Methods

Materials

All reagents were purchased from Sigma Aldrich (St Louis, MO, USA), whether most of solvents from Carlo Erba Reagents s.r.l. (Cornaredo, MI, Italy).

1.1 PEG and fluorophore silanization

H_2N-PEG-Sil

The product was obtained as described by Rio-Echevarria et al.[1]. Briefly, a two-necked flask was dried with a heat gun under a flow of nitrogen.168.5 mg of H_2N-PEG-NH_2 (1751 g/mol; 96.25 mol), dissolved in 1685 µL of dichloromethane (DCM) anhydrous, and 48.1 µL of 2-(4-chlorosulfonylphenyl)ethyltrimethoxysilane (96.25 µmol) were added to the flask and made to react overnight. The product was used without further purifications.

H_3CO-PEG-Sil

Also this other silanized PEG was produced as described by Rio-Echevarria et al.[1]. O-(2-aminoethyl)-O0-methylpolyethylene glycol (H_3CO-PEG-NH_2, 0.5 mmol) was dissolved in 10 mL of DCM. Then 87 mL of triethylamine (1.26 mmol, 2.5 equiv) and 406 mg of 2-(4-chlorosulfonylphenyl)ethyltrimethoxysilane (1.26 mmol, 812 mL of 50% solution in DCM) were added. The mixture was stirred for 3 h at 40°C, the solvent was evaporated and the residue was then dissolved in 10 mL of ethanol (EtOH). This solution was added drop wise into an ice-bath cooled flask containing 200 mL of tert-butyl methylether. A white precipitate was formed and filtered under vacuum (yield 84%).

Rhodamine B-Sil

Synthesis of silanized rhodamine B was made of two reaction steps. The first step was made according to Nguyen and Francis [2] (supporting info-compound number 5) to obtain the product number 2 in the scheme as a purple solid.

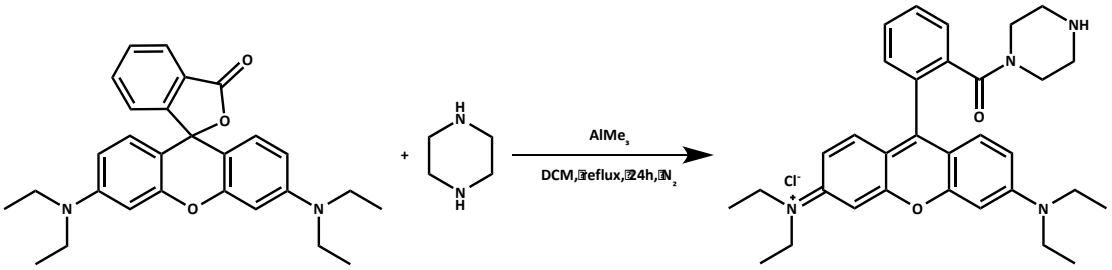

(1) (2)

The second step of reaction is showed in the following scheme:

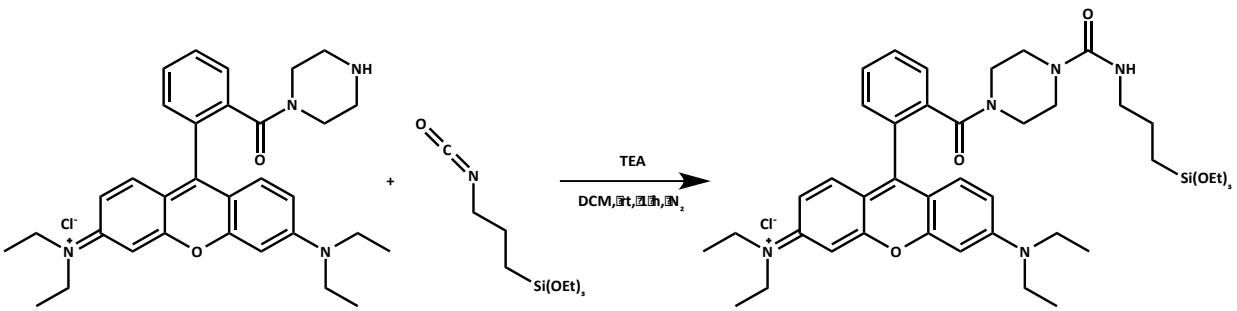

(2) (3)

Briefly, a two-necked flask is dried with a heat gun under a flow of nitrogen. Compound 2 (200 mg, 0.366 mmol), dissolved in 8 mL of DCM, 384 µL of triethiamine (7.5 equiv, 2.74 mmol) and 1429 µL of 3-(Triethoxysilyl)propyl isocyanate (15 equiv, 5.48 mmol) were added to the flask and made to react for one hour. This solution was added drop wise into an ice-bath cooled flask containing 20 mL of di-ethylether. The purple solid obtained was purified trough chromatography on silica gel. Product 3 was obtained with a yield of 60%.

TMB-Sil and DEB-Sil

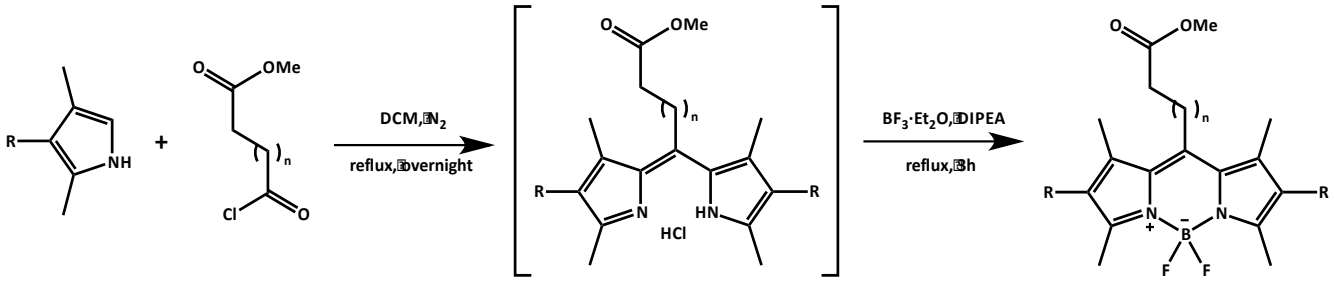

(1)

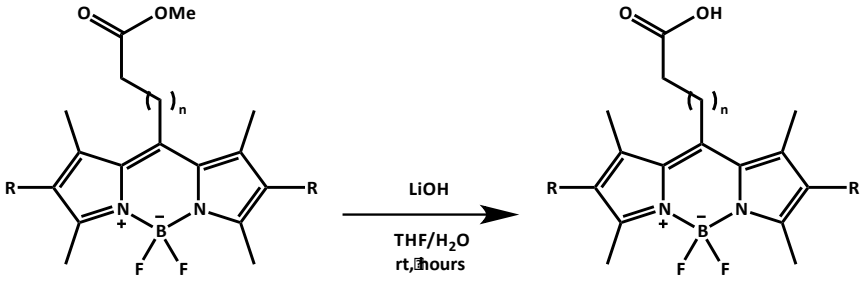

(1) (2)

Product 1 and 2 were obtained as described by Boldyrev et al. [3].

TMB and DEB has n=2. Otherwise for TMB, R=H while for DEB, R=CH_3.

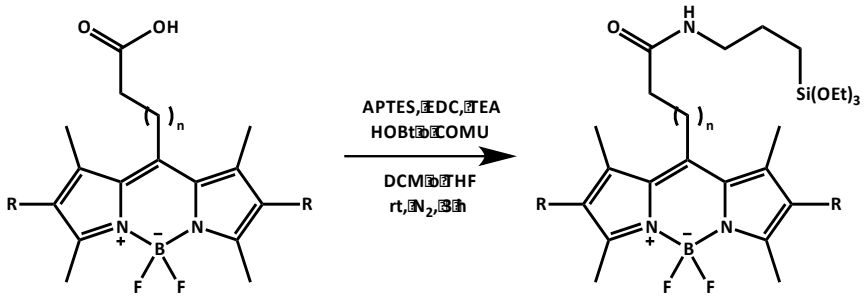

(2) (3)

Synthesis of product 3 was made as described below. A two-necked flask was dried with a heat gun under a flow of nitrogen. 100 mg of product 2 was dissolved in 40 mL of DCM. Subsequently, it was added to the solution in the described order: 3-aminopropyltrietoxysilane (2 equiv), triethylamine (3 equiv), 1-ethyl-3-(3-dimethylaminopropyl)carbodiimide (EDC, 3 equiv) and COMU® (3 equiv).

Cy5-Sil and Cy5.5-Sil

Cyanine5-NHS (product 1, R= CH_2CH) and Cyanine5.5-NHS (product 1, R= CH_3) were purchased from Lumiprobe Corporation (Hunt Valley, Maryland, USA) and used without further purification. The synthesis of the corresponding silanized forms were obtained following the same procedure, illustrated below.

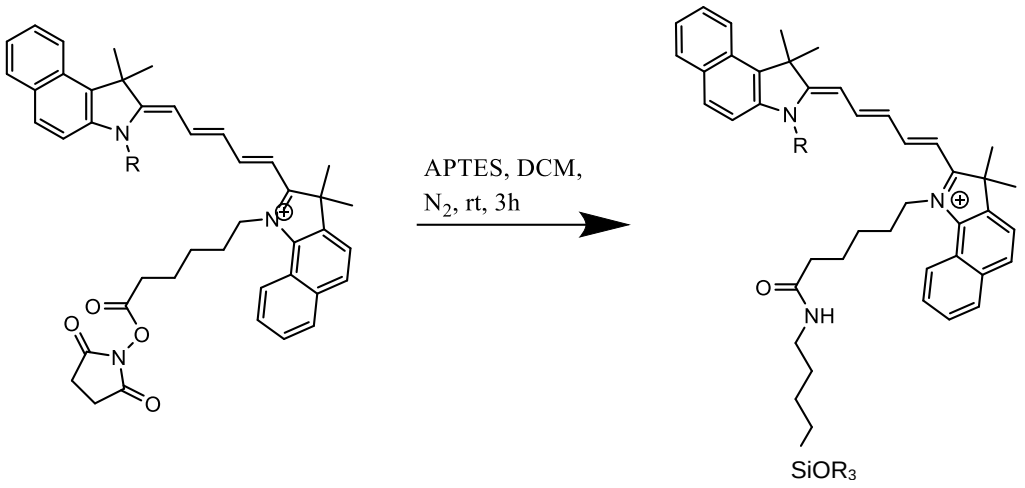

(1) (2)

A two-necked flask was dried with a heat gun under a flow of nitrogen. A solution of 5 mg of dye dissolved in 2 mL of DCM 3-aminopropyltrietoxysilane (1.1 equiv) was slowly added to the flask. The mixture was stirred for 3 h at room temperature (RT). The reaction product was used without further purifications.

1.2 Nanoparticle synthesis

Multiple dye-doped nanoparticle (NT_B700) preparation was carried out as described by Pellegrino et al. [4], with the addition of a fifth fluorophores, Cy5.5, to the others (TMB, DEB, Rhod and Cy5) to reach an emission wavelength of about 700 nm. 0.75 nmol of surfactant and 0.075 mmol of H_3CO-PEG-Sil were mixed with the desired amount of silanized fluorophores, prepared as previously reported. Then, 25 mL of ddH_2O and 375 µL of 1-butanol were added to the flask and mixed under magnetic stirring for 1 h at RT. The sample was then transferred into a heating bath at 40°C. A 2.5 mmol of trimethoxymethylsilane solution, prepared with 178 mg of H_2N-PEG-SiO_3 (0.0875 mmol) 0,3 M in dimethyl sulfoxide (DMSO, Sigma-Aldrich, St Louis, MO, USA) and 375 µL of a 2,8% solution of ammonia in water (0.555 mmol), was added to the mixture and the reaction was kept under stirring for at least 48 h.

For the purification step, 10 g of Bio-Beads (Bio-Rad, Hercules, CA, USA) were added to nanoparticle suspension and left stirring for 3 h at RT. Bio-Beads were then removed by filtration and the whole sample was dialyzed against ddH_2O using regenerated cellulose membrane tubing (*cut-off* 12 kDa) (VWR, Radnor, PA, USA) for at least 24 h. The sample was collected and passed at least twice through hydrophilic PVDF membrane filters (Merck Millipore Ltd., Tullagreen, Ireland) with decreasing pore size (0.45, 0.22 and 0.1 μm). Nanoparticles were finally centrifuged at 1000 rpm for 30 min at RT, discarding the pellet, if any.

1.3 Photochemical characterization

NT_B700 were analysed spectrophotometrically to obtain the molar extinction coefficient (ε) of each included dye. We constructed a 5-points calibration curve, by plotting the concentration of each dye against its absorption at the maximum wavelength. Preliminary experiment showed that there was no loss of dyes during the preliminary purification procedures (Bio-bead and dialysis). Therefore, we could assume that the inclusion of dyes has a reaction yield of 100% and that the fluorophore concentration we had in the final sample was equal to the one we have used during the synthesis.

For the construction of the calibration curve: NPs were first diluted 1:20 in ddH_2O and then we performed a serial dilution in ddH_2O (dilution factor 1:2) in order to obtain 5 samples. Each dilution was analysed by Agilent Cary 60 UV-Vis spectrophotometer (Agilent Technologies, Santa Clara, CA, USA), recording the whole spectrum using the following setup:

Start (nm)……...	1100.0
Stop (nm)……	190.0
X Mode……...……...	Nanometers
Y Mode..……	Abs
UV-Vis Scan Rate (nm/min)…..	1200.00
UV-Vis Data Interval (nm)……	1.00
UV-Vis Ave. Time (sec)……	0.0500
Beam Mode…..……...	Dual Beam
Baseline Type...…….…….	Baseline correction

It must be considered that the ε calculated is that of the dye when inside NPs. On the contrary, to calculate the NP ε we need to consider the number of dyes per NP that has to be multiplied for the ε calculated. From the recorded spectrum we also define the maximum absorption wavelength of each fluorophores.

One of the dilutions used for the calibration curve was also analysed by using a FP-6200 spectrofluorometer (JASCO EUROPE s.r.l., Cremella, Co, Italy). Specifically, in order to avoid auto-absorption phenomenon, we chose the sample whose absorption of the first donor is equal/under 0.1. The selected dilution was analysed at the spectrofluorometer using the following setup:

Measurement Mode……..	Emission
Band Width (Ex)……	5 nm
Band Width (Em)……..	5 nm
Response……	Medium
Excitation Wavelength……..	460.0 nm
Start……	470.0 nm
End…….	900 nm
Data Pitch……..	1 nm
Scanning Speed…….…….	250 nm/min
Sensitivity……..	Low

From emission spectrum we define the maximum emission wavelength of each dye.

1.4 Amine quantification

To quantify the amount of amine reactive groups on nanoparticles, we used a colorimetric assay. NPs are able to react with fluorescein isothiocyanate (FITC, Abs max=494 nm, Em max= 518 nm) (Sigma-Aldrich, St Louis, MO, USA), exploiting $–NH_2$ groups on their surface. Molar ratio between the two species was chosen considering the theoretical amount of PEG-NH_2 used during the synthesis. The reaction conditions, optimized in our laboratory, ensured that the whole $–NH_2$ on nanoparticles surface were able to react with fluorescein. Therefore, the quantification of FITC was directly proportional to amine groups on NP surface.

In order to have a control, each purification was simultaneously made on NPs, treated in the same way, with (positive control) and without (negative control) the addition of FITC.

Positive control: 108 µL of NT_B700 diluted 1:2 in Carbonate/Bicarbonate 2X (pH=9) were mixed with FITC (10 mg/mL in DMSO, Molar Ratio=10) and incubated 1h at RT in the dark. The reaction mixture was applied on size exclusion chromatography column (Sephadex G25, GE Healthcare, Chicago, Il, USA) and eluted with Carbonate/Bicarbonate 1X (pH=9). Selected fractions were collected and diluted with Carbonate/Bicarbonate until 3 mL of volume.

Negative control: 108 µL of NT_B700 diluted 1:2 in Carbonate/Bicarbonate 2X (pH=9) were made to react with the same volume of DMSO added at the positive control and incubated 1h at RT in the dark. The reaction mixture was applied on size exclusion chromatography column (Sephadex G25, GE Healthcare, Chicago, Il, USA) and eluted with Carbonate/Bicarbonate 1X (pH=9). Selected fractions were collected and diluted with carbonate/Bicarbonate until 3 mL of volume.

Positive and negative controls were then analysed by the spectrophotometer (Agilent Technologies, Santa Clara, CA, USA), recording the whole spectrum. To calculate the moles of reacted FITC, directly proportional to $-NH_2$ groups on NP surface, we considered the different absorption between NPs (pool -) and NPs-FITC (pool +) at 494 nm. This wavelength was found to be the FITC absorption maximum at the pH used for the reaction (pH=9.5; ε=80600 $M^{-1}cm^{-1}$; 1/ ε= 12.4 µM*cm).

1.5 FRET efficiency

From emission spectrum we defined the maximum emission wavelength of each dye and the FRET efficiency, which was calculated considering the emission intensity of the final acceptor and average intensity of all four donors.

$$FRET\ efficiency = \left[1 - \left(\frac{\frac{\sum_{i=1}^{N}(Donor\ emission)_i}{N}}{Acceptor\ Emission}\right)\right] \times 100$$

1.6 Nanoparticle concentration

1 mL of NT_B700 were dispensed in a vial whose tare has been precedent calculated. Sample was dried in a SpeedVac Concentrator, Heto VR-1 vacuum Centrifuge (Heto-Holten A/S, Alleroed, Denmark) and the mass (mg) obtained measured in an analytical balance (Sartorius, Göttingen, Germany).

1.7 Nanoparticle size

1.7.1 Nanoparticle Tracking Analysis (NTA)

NT_B700 size was measured by Nanoparticle Tracking Analysis (NTA): each sample was suspended in 1 mL of PBS pH 7.4 (dilution 1:1000) and loaded into the sample chamber of an LM20 unit (NanoSight, Malvern Instruments Ltd, UK). The samples were injected in the sample chamber with sterile syringes until the liquid reached the tip of the nozzle. All measurements were performed at RT.

1.7.2 Size-exclusion chromatography (SEC)

Size-exclusion chromatography is one of the HPLC separation modes, which allows the separation of different analytes according to their size in solution (hydrodynamic volume) measured by how deeply they penetrate the pores of the stationary phase [5]. In order to obtain information about NT_B700 size, we first utilized two calibration kits as standards, which contained species with known molecular weights, to construct a calibration curve:

a) Gel filtration Standard (Bio-Rad, Hercules, CA, USA) (Fig. 1.1) which contains:
    - Thyroglobulin (670 kDa)
    - γ-globulin (158 kDa)
    - Ovalbumin (44 kDa)
    - Myoglobulin (17 kDa)
    - Vitamin B12 (1.35 kDa)

b) Gel Filtration Cal Kit High Molecular Weight (HMW) (GE Healthcare, Chicago, Il, USA), which contains the same proteins with the addition of Blue Dextran (2000 kDa)

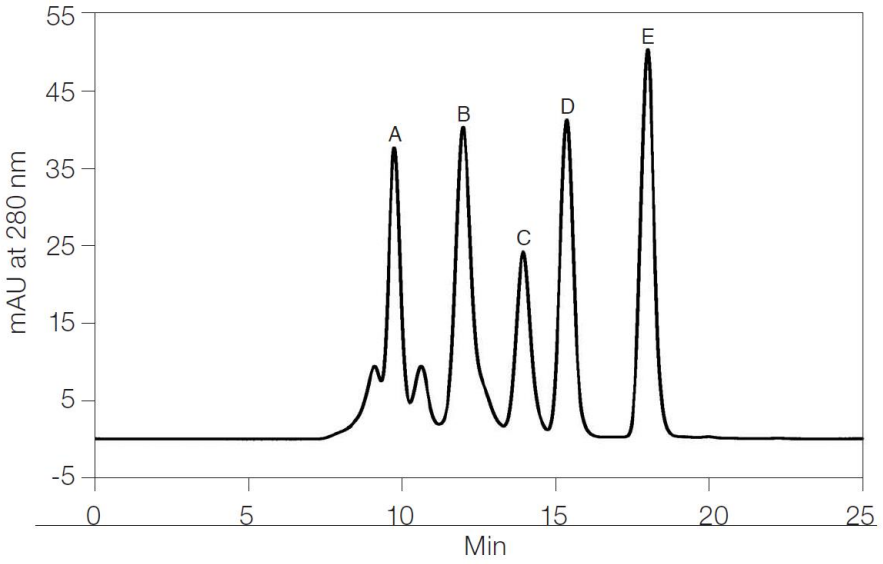

Fig. 1.1 Typical chromatograms of Gel filtration Standard (Bio-Rad) at 280 nm. Peaks: A, thyroglobulin; B, γ globulin; C, ovalbumin; D, myoglobin; E, vitamin B12.

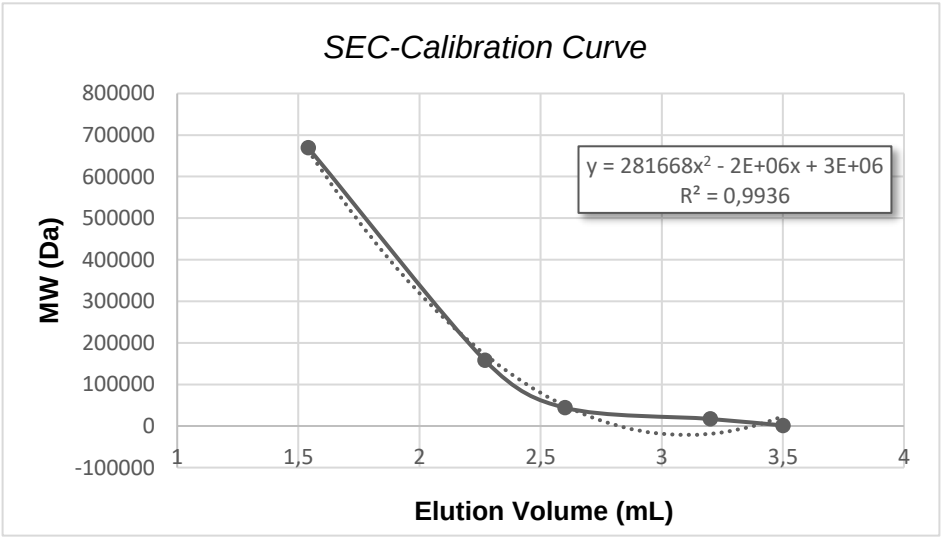

Fig. 1.2 SEC calibration curve with standards.

We took a quantity of NT_B700 sample equal to 0.6% of the column volume with a 25 µL syringe (Hamilton, Reno, NV, USA), injected it in HPLC system (ÄKTA purifier 10, Amersham Pharmacia Biotech, Little Chalfont, UK) with a Tricorn column (GE Healthcare, Chicago, Il, USA) packed with a Superose 6 resin (fractionation range for molecules between 5000 to 5000000 Da) (GE Healthcare, Chicago, Il, USA), by applying the following instrument set-up:

Flow	0.1 mL/min
Pressure	< 3 MPa
UV1	280.0 nm
UV2	498.0 nm
UV3	685.0 nm
Column Volume	3.14 mL
Diameter	5 mm

Finally, we interpolate the elution volume of our sample into the curve (Fig. 1.2) to obtain the molecular weight of NT_B700 NPs.

1.7.3 Transmission Electron Microscopy (TEM)

For a detailed morphological analysis, NPs were processed for transmission electron microscopy (TEM) observation using the conventional negative staining procedure. NPs isolated and diluted at three different concentrations (1:10, 1:100, 1:1000) were adsorbed to formvar carbon-coated 200 mesh grids (Agar Scientific Ltd., Stansted, UK) for 10 min. Subsequently the grids were incubated with 2% (w/v) sodium phosphotungstate for 1 min and the liquid excess was removed with filter paper. After negative staining, specimens were observed by means of a Philips CM10 transmission electron microscope at 80 kV.

1.7.4 Atomic Force Microscopy (AFM)

Atomic Force Microscopy imaging was performed in PeakForce™ tapping-mode on a Nanoscope Multimode 8 (Bruker, Billerica, MA, USA) with ScanAsyst Fluid+ probes (Bruker, Billerica, MA, USA). Nanoparticles were deposited by spreading the solution on freshly-cleaved glass both dried and in liquid (ddH_2O) and imaged at room temperature.

1.8 Nanoparticle pH reactivity

1.8.1 Photochemical characterization

NT_B700 NPs were diluted 1:100 in four solutions at different pH (7.2, 5.5, 4.5 and 2.5) to simulate the various conditions inside the cellular compartments. NP suspensions were removed at different time points (0, 30 min, 4 h, 24 h and 48 h) and analysed by Agilent Cary 60 UV-Vis spectrophotometer, recording the whole spectrum (with the same set up of the *1.3 Photochemical characterization* section). Moreover, the same dilutions were also analysed by using the FP-6200 spectrofluorometer with the same set up but with two different excitation wavelengths, respectively 480 nm and 630 nm, to simulate two lasers typically used in flow cytometry.

	Blue laser	**Red laser**
Measurement Mode	Emission	Emission
Band Width (Ex)	5 nm	5 nm
Band Width (Em)	5 nm	5 nm
Response	Medium	Medium
Excitation Wavelength	480.0 nm	630.0 nm
Start	490.0 nm	640.0 nm
End	900 nm	900 nm
Data Pitch	1 nm	1 nm
Scanning Speed	250 nm/min	250 nm/min
Sensitivity	Low	Low

1.8.2 Flow cytometry analysis

NT_B700 NPs were diluted 1:100 in four solutions at different pH (7.2, 5.5, 4.5 and 2.5) to simulate the various conditions inside the cellular compartments. NP suspensions were removed at different time points (0, 30 min, 4 h and 24 h) and analysed by flow cytometry for both physical (FSC and SSC) and fluorescent properties (PerCP-Cy5.5 and APC-Cy7 channels).

Results and discussion

NT_B700 synthesis and photochemical characterization

As presented in the Introduction section of the thesis, based on van Blaaderen's idea, NT_B700 are core-shell dye doped silica nanoparticles synthesized through a one-pot, two-steps reaction, known as micelle-assisted method, where a surfactant is used to create a nanoreactor within which all the hydrophobic reagents arrange (Fig. 1.1A). After the addition of ammonia and silane precursor (methyltrimethoxysilane, MTMS), the base-catalysed hydrolysis of all the trialkoxysilane groups on PEGs and fluorophores takes place and leads to the formation of fluorescent monodisperse nanoparticles [4]. To obtain NPs excitable with blue laser and emitting in the near-IR, called NT_B700, five different dyes, summarised in Table 1.1, were selected to be simultaneously and covalently entrapped into the silica core, so that they are not released over time. The strong interconnection reached inside the core leads to Florescence Resonance Energy Transfer (FRET). The photochemical characterization of NT_B700 NPs, analysed both by spectrophotometer and spectrofluorometer, allow to obtain the molar extinction coefficient (ε) of each fluorophore part of the nanotandem, their respective maximum absorption and emission wavelengths (Table 1.1). Fig. 1.1B shows the absorbance and fluorescence emission spectra of NT_B700 NPs, which are able to be excited with blue laser (~ 488 nm) and emit in the near-IR (~ 700 nm) exploiting FRET phenomenon. The amount of fluorophores was modulated to obtain the maximum efficiency of the cascade transfer without inducing the self-quenching phenomenon, NT_B700 reached about 80% of FRET efficiency. This value has been calculated considering the emission intensity of the final acceptor and the average of donors as described in the Material and Methods session. Interestingly, the graphs in Fig. 1.2 exhibits more in details, what is present under the emission spectrum that we registered with the spectrofluorometer, showing the peaks of all fluorophores which contribute to make the final spectrum (the solid red line). Above, the normalized spectra of all the five dyes (TMB, DEB, Rhod, Cy5 and Cy5.5) embedded in NT_B700 NPs. Below, the real contribute of each dye into the nanotandem. The dotted black line represents the mathematical simulation of how the spectrum must be once calculated with the mathematical operation, deconvolution, which allow to calculate the theoretical FRET efficiency. Basically, the difference between the solid red line (the real spectrum) and the dotted black line (the calculated one) represents how much NPs are close to the mathematical simulation (R^2 = 0,99643). As it can be seen from the graph, the obtained spectrum matches a lot with the theoretical one, as they are almost practically overlapped.

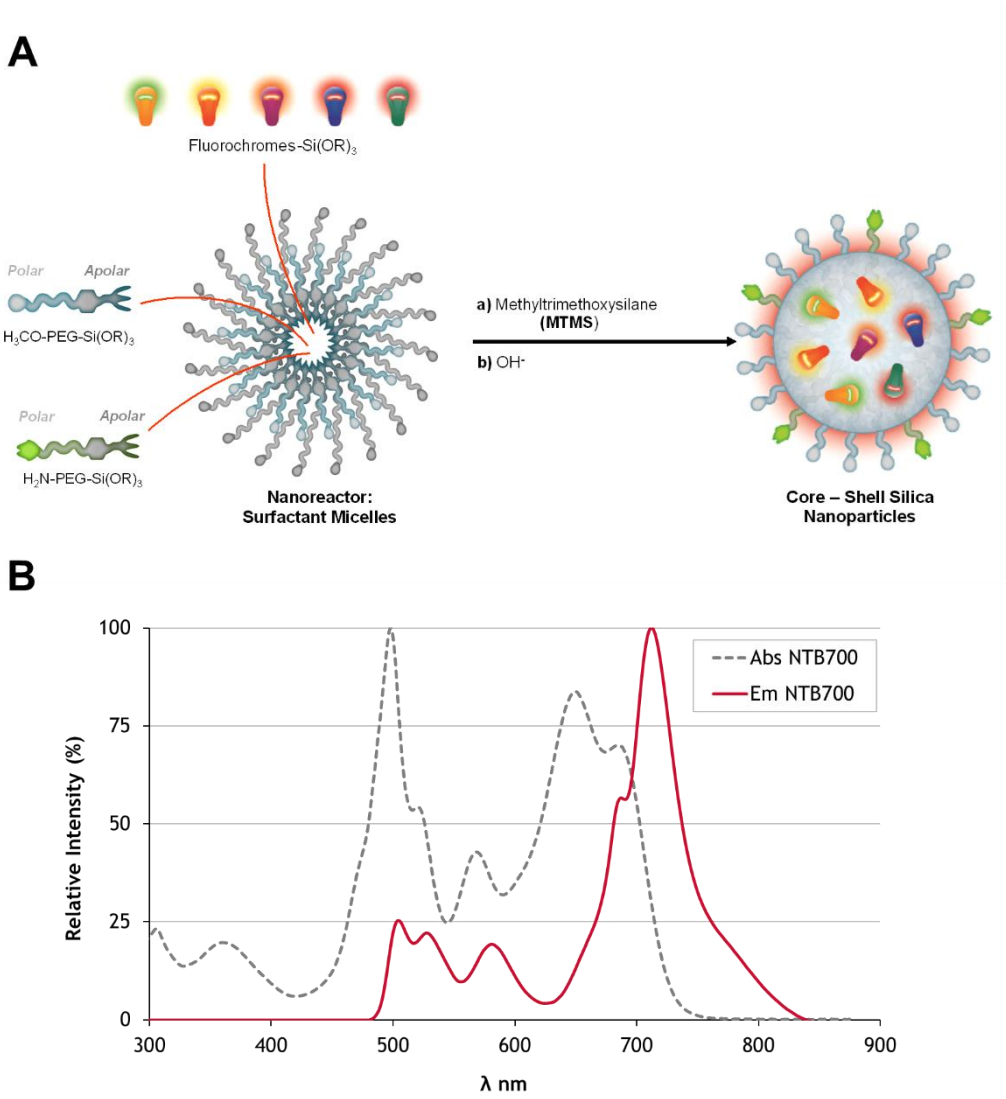

Fig. 1.1 NT_B700 synthesis and photochemical characterization. (A) Schematic representation of the synthesis of the core-shell silica nanoparticles, through a micelle-assisted method, where a surfactant is used to create a nanoreactor within which all reagents arrange. The base-catalysed hydrolysis of a silane precursor (MTMS), along with five different dyes functionalized with a trialkoxysilane group, able to covalently link to the silica matrix, leads to the formation of fluorescent monodisperse NPs. (B) Absorption (dotted grey line) and emission spectra (solid red line) of NT_B700 nanoparticles.

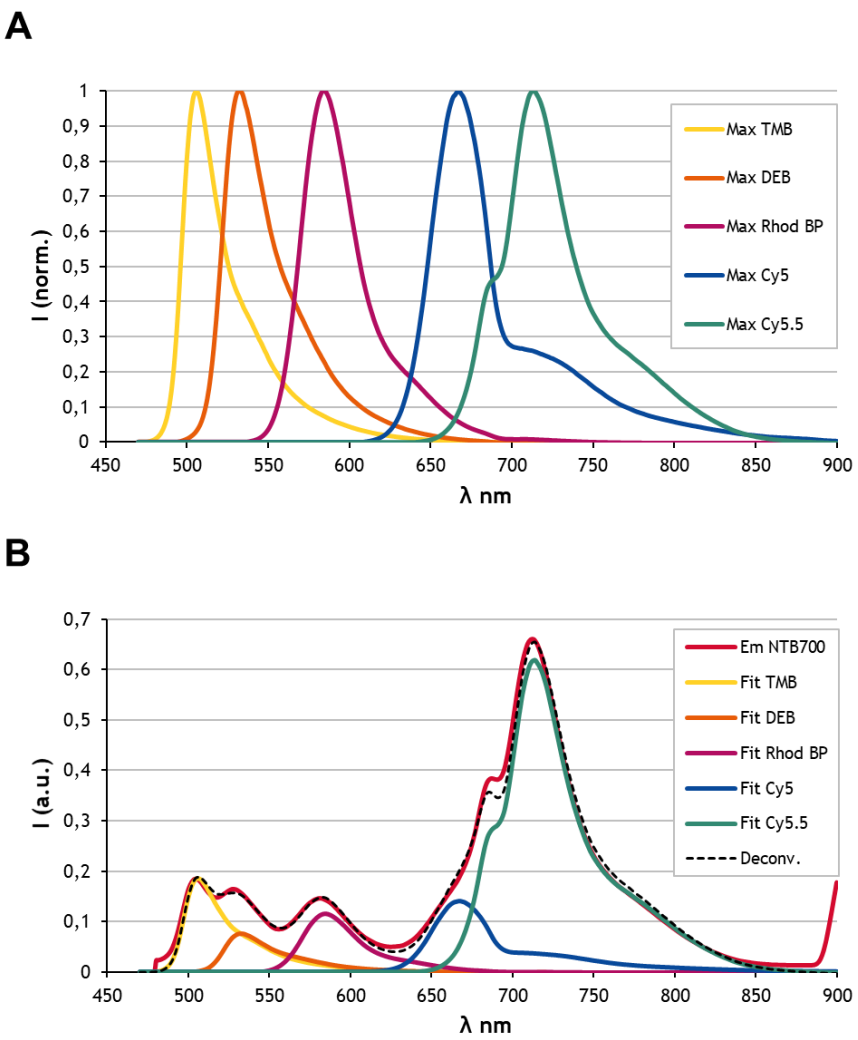

Fig. 1.2 NT$_B$700 photochemical characterization more in detail. (A) Normalized emission spectra of the five fluorophores which compose NT$_B$700 nanotandem: TMB (yellow), DEB (orange), Rhod (purple), Cy5 (blue) and Cy5.5 (green). (B) NT$_B$700 emission spectrum (solid red line) of the selected dilution, whose absorption of the first donor was equal/under 0.1, during NP titration, compared to the deconvolution, which represents the mathematical simulation (dotted black line). The peaks of all fluorophores inside the silica core are shown with same colours of the previous graph, but without normalization.

	λ max Abs (nm)	*ε (M^{-1}cm^{-1})*	*λ max Em (nm)*	*[Dye](μM)/lost*
TMB	498	66900	505	286.3/4.6%
DEB	520	74600	528	135.7/9.6%
Rhod	569	84000	583	94.5/5.5%
Cy5	650	163600	667	97/3.0%
Cy5.5	684	110100	713	119,5/4.4%

Table 1.1 Final photochemical characteristics of the five fluorophores included into NT$_B$700 nanoparticles

Abbreviations: Cy5, cyanine 5; Cy5.5, cyanine 5.5; DEB, diethynylbenzene; Rhod, rhodamine B; TMB, tetramethylbenzidine.

The PEG-NH_2, which composes NT_B700 shell, will be exploited for subsequent binding of different molecules, depending on the applications of use. Thus, it is necessary to quantify the amount of amine reactive groups on NT_B700 NPs. For this quantification we used a colorimetric assay, optimized in our laboratory. NPs are able to react with fluorescein isothiocyanate (FITC) exploiting $–NH_2$ groups on their surface. The reaction conditions ensured that the whole $–NH_2$ on NP surface were able to react with fluorescein. Therefore, the quantification of FITC was directly proportional to amine groups on NP surface. In order to have a control, each purification was simultaneously made on NPs, treated in the same way, with (positive control) and without (negative control) the addition of FITC. Therefore, the amount of amine groups was estimated through the subtraction of the absorbance contribute of negative pool from positive one (Fig. 1.3) (Table 1.2).

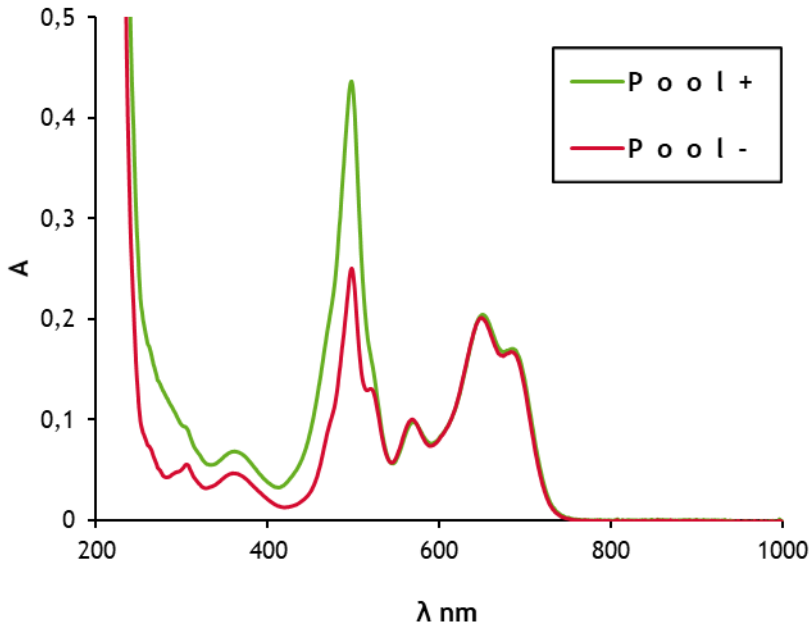

Fig. 1.3 Amine quantification. Absorption spectra of NT_B700 (pool -, red line) and NT_B700-FITC (pool +, green line).

NT_B700 size analysis

Since NPs are an extremely versatile technology and could hire several shapes with different materials and sizes [6], it is essential to characterize nanomaterials from this point of view. NP size could influence their physicochemical properties and, furthermore, with the aim to use NT_B700 in future applications, such as *in vivo* diagnostic or drug delivery, it is indispensable, as first step, to understand how NPs enter the cells. Numerous studies have shown that size,

shape, surface properties and composition of NPs have a great impact on their cellular uptake and intracellular trafficking and these could influence their therapeutic efficacy [7-10]. Nowadays, many types of NPs are synthetised with different approaches and require even more precise techniques for their characterization. Each technique presents several strengths and limitations of use. Moreover, due to the multidisciplinary aspects of nanomaterials in general, a combinatorial characterization approach is often needed, by integrating different protocols in a complementary way. For example, for a specific parameter, such as particle size, the use of two or more techniques is necessary to provide reliable information. Nevertheless, such analysis is sometimes incomplete [11]. Thus, we investigated NT_B700 size with different techniques: some microscopy-based techniques (TEM and AFM), which provide information on the size and morphology of the nanomaterials, NTA, which also investigate size distribution and SEC, that separates molecules based on their size in solution (hydrodynamic volume).

The most commonly used techniques for the analysis of nanoparticles and protein aggregates include dynamic light scattering (DLS), size exclusion chromatography (SEC), gel electrophoresis, scanning electron microscopy (SEM), analytical ultracentrifugation (AUC) and asymmetrical flow field-flow fractionation (AF4). Among them, DLS has become the most chosen technique to routinely determine the size of nanoparticles, thanks to the rapidity of analysis, the user-friendliness and for the accurate and consistent results [12]. Due to the impossibility to DLS analysis for NT_B700 NPs because of the high absorption in red wavelength, we characterized NP size with nanoparticle tracking analysis (NTA), a relatively new technique which has a lower concentration detection limit compared to DLS. This technology utilises the properties of both light scattering and Brownian movement to acquire NP size distribution of samples in liquid dispersion [11]. NTA results (Fig. 1.4) showed NP size around 100 nm, but by reducing the threshold of the instrument, we detected a smaller total average size and, indeed, a new peak on the left of the main one appeared, indicated by the black arrow in Fig. 1.4B. This may depend on the lower detection limit of NTA, which is not able to detect particles of a smaller size and the main peak identified by the instrument might indicate the presence of aggregates.

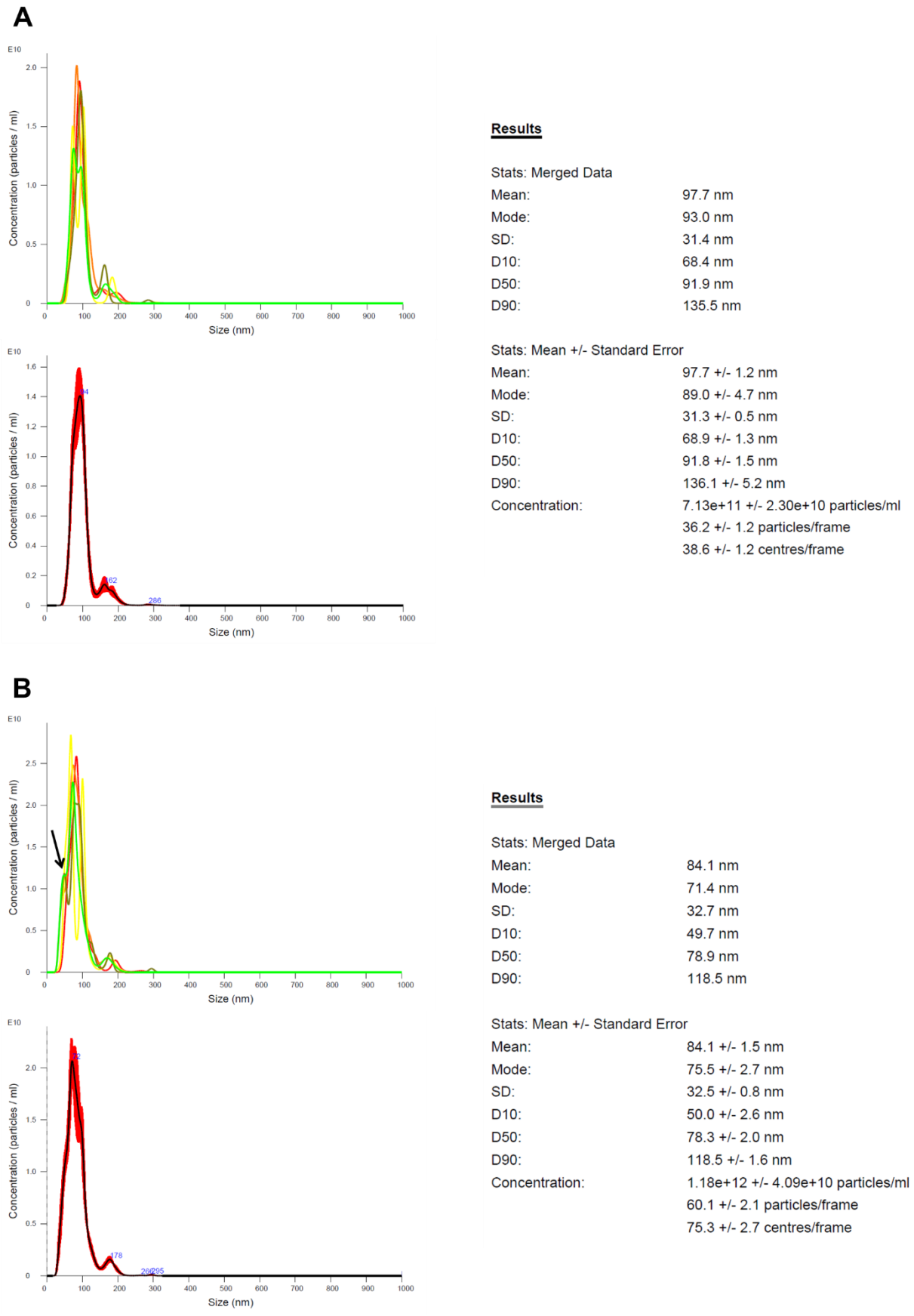

Fig. 14.4 NT_B700 size characterization: nanoparticle tracking analysis (NTA). (A) NT_B700 NPs diluted 1:1000 were analysed using NTA. (B) The same measurement repeated with a lower threshold. NTA measurements were performed by using a NanoSight LM20 (NanoSight, Malvern Instruments Ltd, UK U.K). Results are represented as mean ± sd; n = 5.

The presence of aggregates was supported also by transmission electron microscopy (TEM) analysis. TEM is one of the most common method to analyse NP size and shape, as it provides not only clear images of the sample, but also a valuation of their homogeneity [11]. Insets of TEM images in Fig. 1.5 show the presence of NP aggregates with an average size of 100-150 nm (with some isolated clusters with diameter of 200 nm). The monodisperse form displays an average size of 30 nm. When it comes to nanoparticle fabrication, Robertson and co-workers reported, indeed, that often the production of homogenous batches is challenging [13].

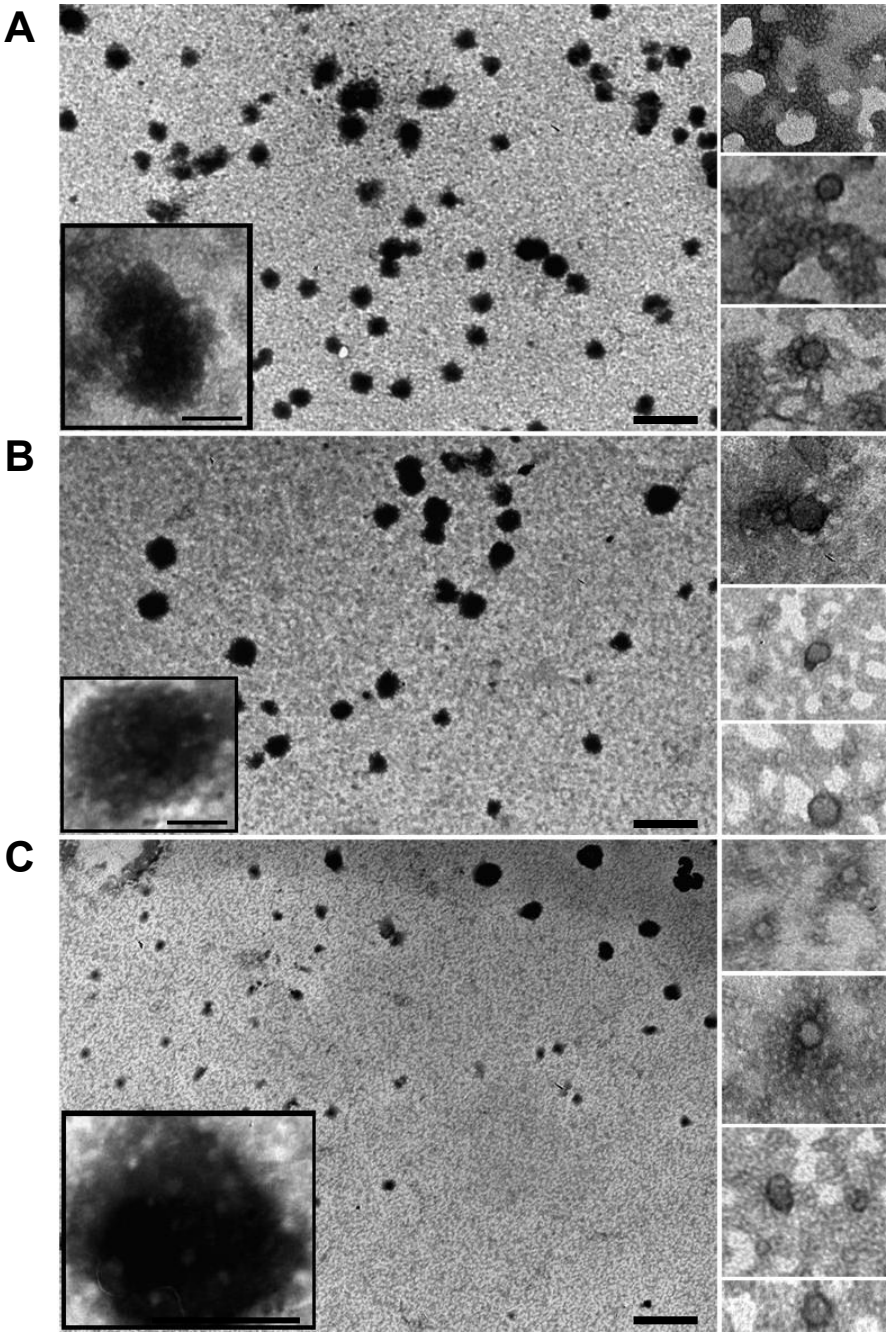

Fig. 1.5 NT_B700 size characterization: transmission electron microscopy (TEM). For a detailed morphological analysis, NPs were processed for TEM observation using the conventional negative staining procedure. Representative TEM images of NPs diluted at three different concentrations: 1:10 (A), 1:100 (B) and 1:1000 (C). Insets are enlargements of NP aggregates. Scale bar = 500 nm; inset scale bar = 100 nm

NT_B700 were additionally characterized by another microscopy-based technique, atomic force microscopy (AFM), thanks to which it is possible to create three-dimensional images of nanomaterial surfaces at high magnification. AFM is based on measuring the interacting forces between a fine probe, a sharp tip coupled to the end of a cantilever, and the sample [11]. AFM on dehydrated specimen results revealed smaller NP size (diameter around 5-10 nm) (Fig. 1.6). These differences probably depended on the tip pressure on the soft PEG shell, which gave us a smaller height, mainly indicating their rigid core of NPs.

Finally, size exclusion chromatography (SEC) is a column liquid chromatographic technique commonly employed for the separation of macromolecules in solution, which separates them according to their hydrodynamic radius, a property determined both by the size and shape of the molecules. The larger molecules elute before the smaller ones because the former enter fewer pores of SEC stationary phase taking less time to cross the path [11,14]. From SEC analysis we obtained the elution volume, that, interpolated in the calibration curve, gave us the molecular weight of NT_B700 NPs (Table 1.2). Moreover, the width of the elution peak shows the degree of polydispersity of the sample and the presence of contaminants. The NT_B700 peak is quite tight indicating a mostly monodisperse form, according to the previous analyses, without excluding the presence of some aggregates (Fig. 1.7). In conclusion, the multiple facets of NPs require a combination of techniques in order to have a complete image of NP size, evaluated from different point of views which gave a more complete information.

All physicochemical characteristics of NT_B700 NPs are summarized in Table 1.2.

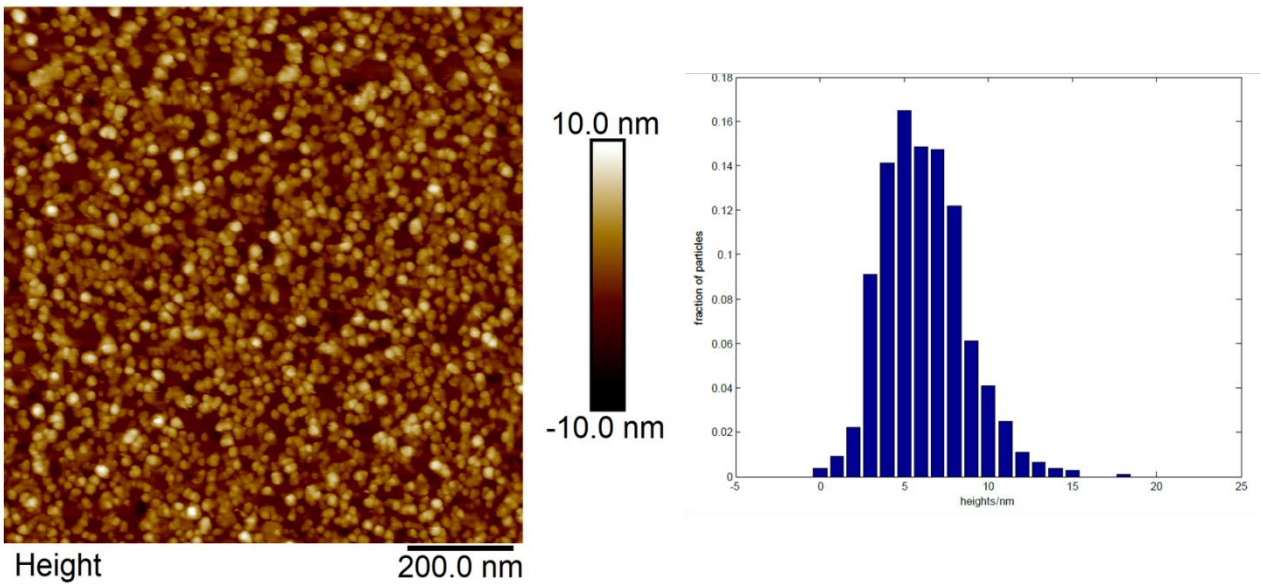

Fig. 1.6 NT_B700 size characterization: atomic force microscopy (AFM). Representative AFM height image of NT_B700 NPs (on the left) and distribution histogram of nanoparticle core (on the right).

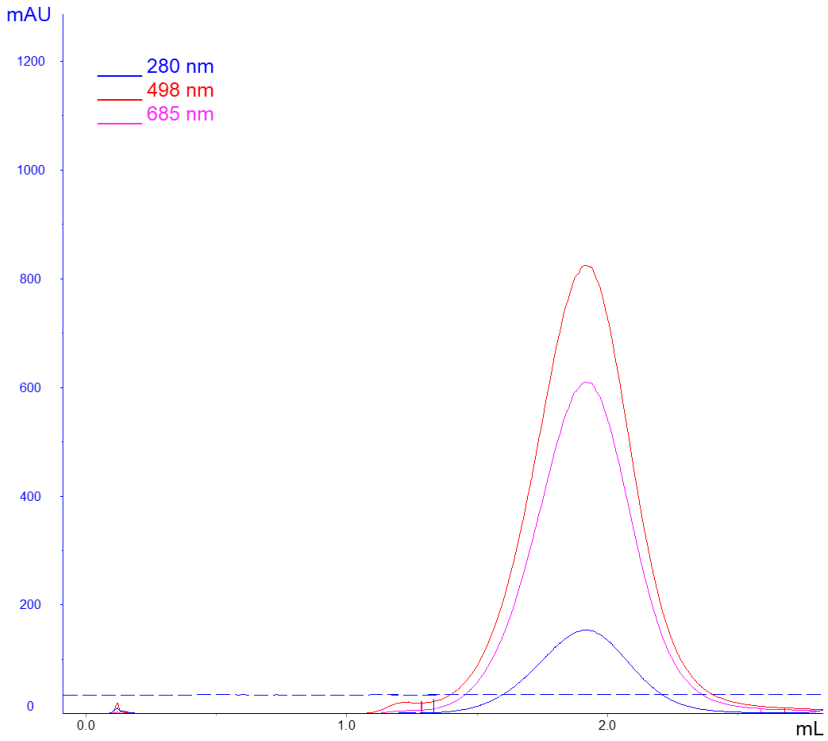

Fig. 1.7 NT_B700 size characterization: size exclusion chromatography (SEC). SEC profile of NT_B700 NPs using a Superose 6 column. The NP profile was monitored at 280 (blue curve), 498 (red curve) and 685 nm (pink curve)

Fluorophores	TMB, DEB, Rhod, Cy5, Cy5,5
λ Maximum absorption wavelength	498 nm
λ Maximum emission wavelength	713/2 nm
FRET efficiency	78,8 %
Concentration	6,4 mg/mL
NH_2 surface content	248,34 µM
Size (NTA)	97,7 ± 1,2 nm
Size (TEM)	30 ± 15 nm
Size (AFM)	5-10 nm (core)
Size (SEC)	377 kDa

Table 1.2 Summary of physicochemical features of NT_B700 nanoparticles

NT_B700 pH reactivity

Thanks to their small size and large surface-to volume ratio, NPs possess exclusive and distinct properties that are useful for their numerous applications, which, mostly, need the interaction of nanomaterials with macromolecules like polymers and proteins. Proteins, notably, are charged molecules, and, in the physiological environment, are known to cover NPs immediately, governed by the resultant electrostatic interactions leading to nonspecific associations that are especially relevant in biological systems. The interaction between NPs and water components may result in the formation, or collapse of aggregates and this is mainly determined by their surface properties (e.g. surface charge) [15], which is controlled by the solution chemistry e.g. pH, ionic strength and surface coating by natural organic matter [16-18].

Kumar et al. examined the effect of pH on the interaction of NPs with medium at different pH values approaching the isoelectric point of protein. Interestingly, they found that at pH 9 a much greater amount of protein was required to aggregate all NPs as compared to that at pH 5.5 [19]. In agreement with such literature, Fig. 1.8 shows that, by decreasing pH, NT_B700 aggregation increased, reaching the maximum aggregation rate at pH 4.5. These data fitted with the fact that with increasing pH the charge on proteins decreases and the surface charge density

of the NPs increases, which means more proteins will be required to mediate NP aggregation. However, we have to take in mind that protein content of RPMI medium, a commonly used culture medium, is moderate in comparison to plasma.

Moreover, we analysed the UV-Vis absorption and fluorescent spectra at the same pH conditions. Concerning the absorption spectra (Fig. 1.9), we observed that the general shape of the spectrum has not significantly changed, even if the maximum absorption slightly reduced in all the investigated conditions across time. As evident from the blue lines in graphs in Fig. 1.9, which represent NT_B700 at pH 2.5, the spectrum shape changed during time, unlike the other conditions. We detected a gradual decrease in the absorption peak between around 600 and 750 nm, until it was almost flat at 48 h. The same behaviour has been observed also in emission spectra, excited both at 480 nm and 630 nm, to reproduce the blue and red lasers of flow cytometer. Regarding the fluorescence intensity at maximum emission wavelength (713 nm), the decrease during time was not significant except for pH 2.5, as observed in flow cytometry (PerCP-Cy5.5 channel) (Fig. 1.10). NT_B700 excited at 630 nm (Fig. 1.11) presented the same trend observed at 480 nm, with the difference that the effect of pH is more evident because the fluorescence intensity of cyanines (the fluorophores excited at this wavelength) is higher than the other dyes included in the tandem. The discrepancies between FC and spectrofluorometer results might depend on the different sensitivity of the two instruments with regard to fluorescence

This pH-NP crosstalk will be interestingly linked to subcellular localization of nanoparticles, since the different intracellular districts and organelles exhibit different pH values [20].

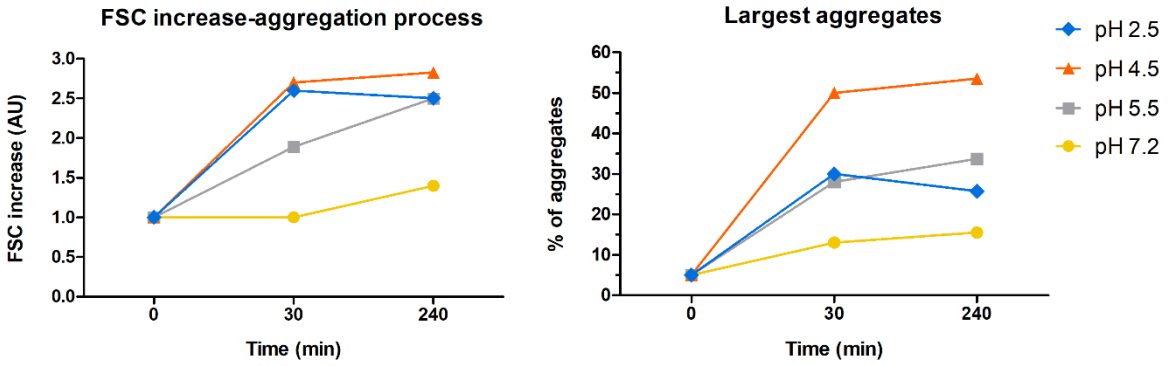

Fig. 1.8 Investigation of pH effect on NT_B700 aggregation in flow cytometry. NT_B700 diluted 1:100 in buffers at different pH (2.5, 4.5, 5.5 and 7.2) and analysed by flow cytometry at three time points (0, 30 and 240 min) for FSC increase to investigate the presence of aggregates (on the left) and percentage of largest aggregates based on physical parameters (on the right).

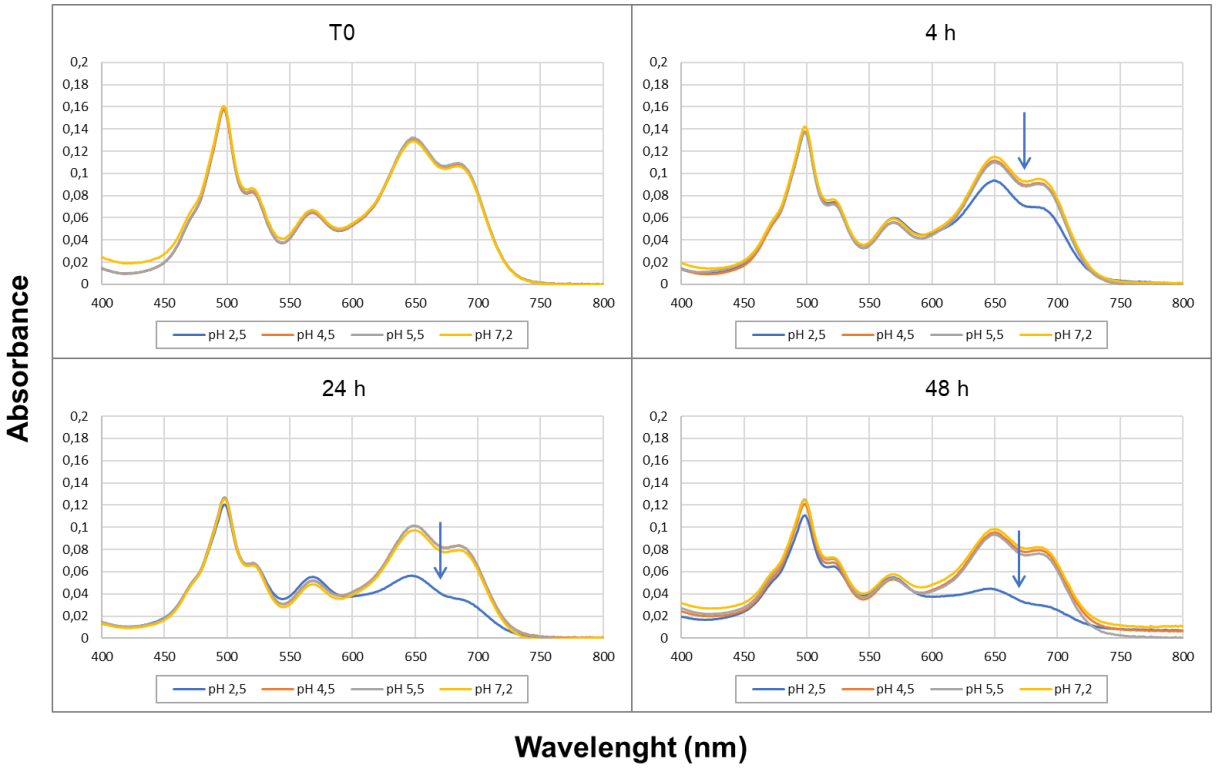

Fig. 1.9 UV-Vis absorption spectra of NT$_B$700 NPs at different pH during time. NT$_B$700 diluted 1:100 in buffers at different pH 2.5 (blue), 4.5 (orange), 5.5 (grey) and 7.2 (yellow) and analysed by spectrophotometer, recording the whole spectrum, at four time points (0, 4, 24 and 48 h). The blue arrows indicate the gradual decrease of absorbance between around 600 and 750 nm, starting at 4 h (at 30 min the decrease was not observed, data not shown) until it was almost flat at 48 h.

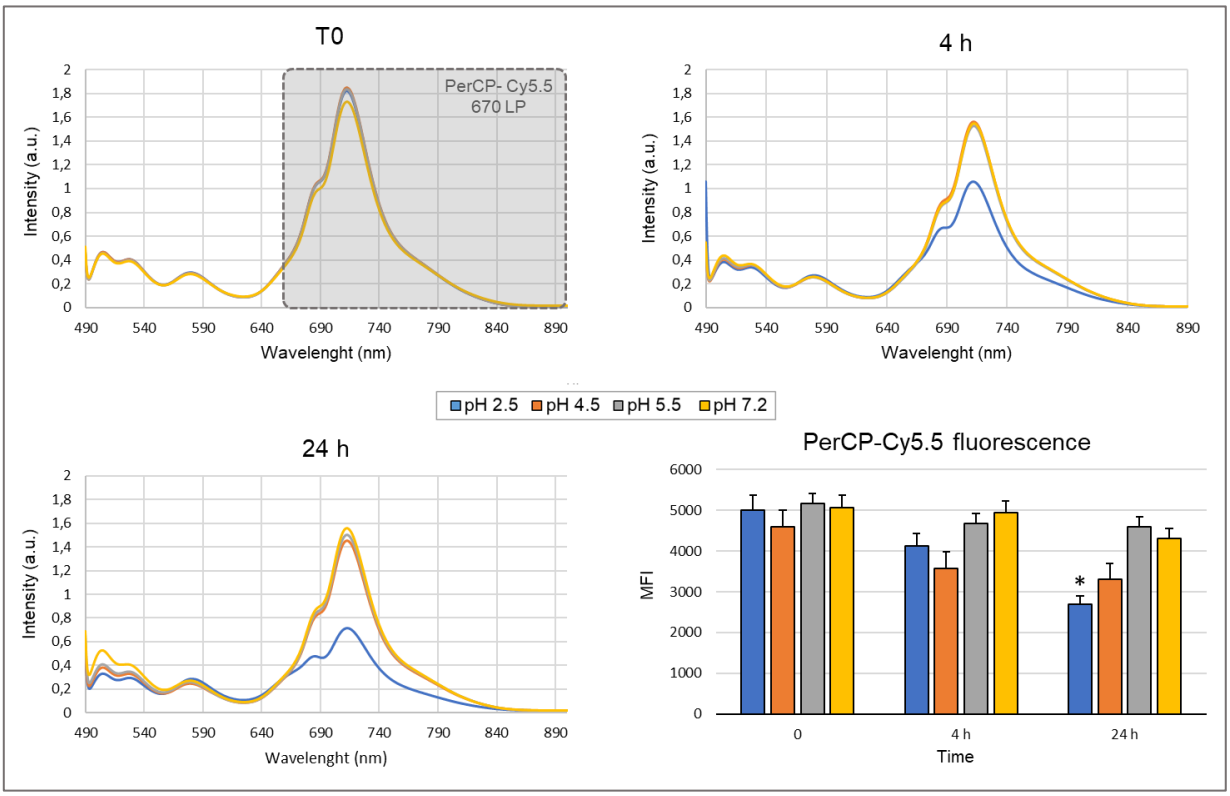

Fig. 1.10 Effect of pH on NT_B700 excited at 480 nm. Fluorescent spectra of NPs diluted 1:100 in buffers at different pH 2.5 (blue), 4.5 (orange), 5.5 (grey) and 7.2 (yellow) and analysed by spectrofluorometer, recording the whole spectrum, at different time points (0, 4 and 24), to simulate the blue laser of the flow cytometer (Excitation wavelength: 480 nm). The grey box simulates the PerCP-Cy5.5 670 Long Pass filter of FacsCanto II flow cytometer. The histograms show the results in FC regarding the effect of pH on NT_B700 fluorescence in PerCP-Cy5.5 filter. Asterisks denote a statistically significant difference (* = $p < 0.05$) between the effect of pH 2.5 at 24 among the starting time and 4h. At least 10000 events were analysed by flow cytometry for each experimental condition.

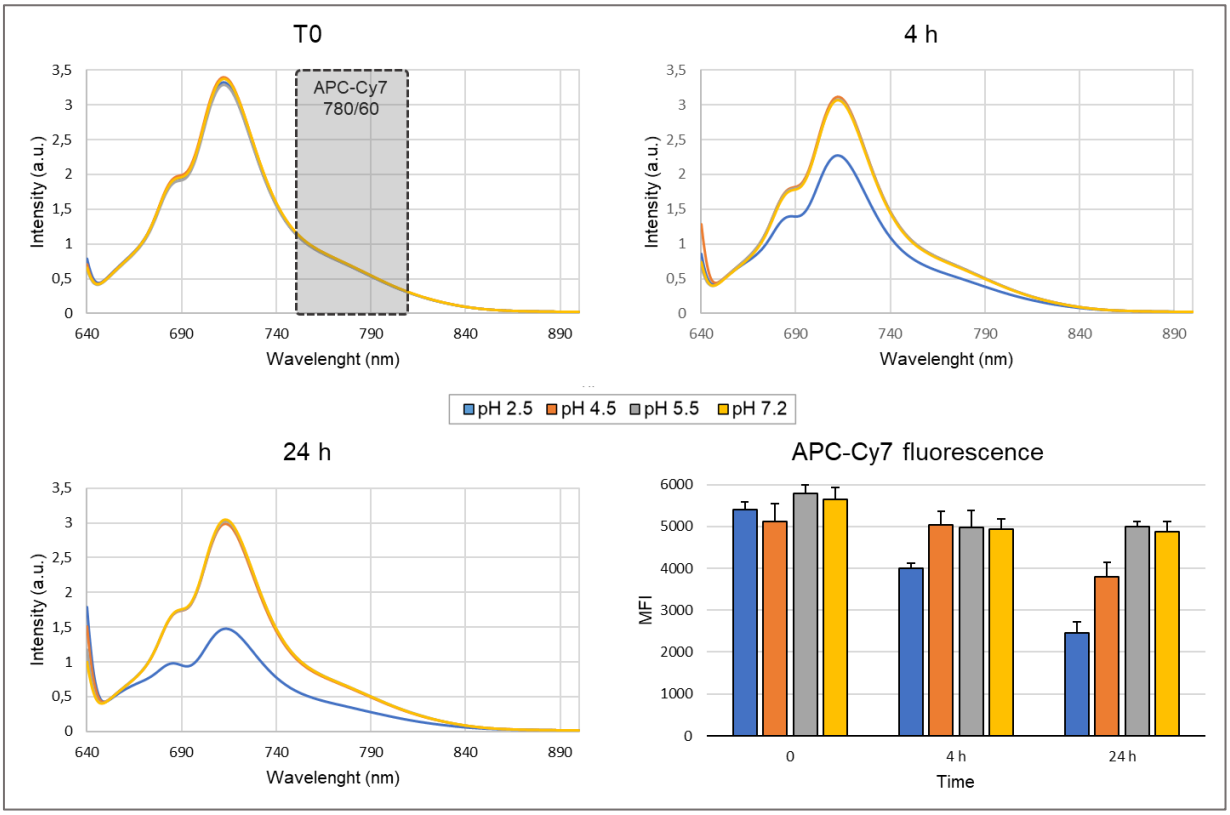

Fig. 1.11 Effect of pH on NT_B700 excited at 630 nm. Fluorescent spectra of NPs diluted 1:100 in buffers at different pH 2.5 (blue), 4.5 (orange), 5.5 (grey) and 7.2 (yellow) and analysed by spectrofluorometer, recording the whole spectrum, at different time points (0, 4 and 24), to simulate the blue laser of the flow cytometer (Excitation wavelength: 630 nm). The grey box simulates the APC-Cy7 (780/60) filter of FacsCanto II flow cytometer. The histograms show the results in FC regarding the effect of pH on NT_B700 fluorescence in APC-Cy7 filter. At least 10000 events were analysed by flow cytometry for each experimental condition.

References

[1] I. M. Rio-Echevarria *et al.*, “Highly PEGylated silica nanoparticles: ‘ready to use’ stealth functional nanocarriers,” *J. Mater. Chem.*, vol. 20, no. 14, pp. 2780–2787, 2010, doi: 10.1039/b921735e.

[2] T. Nguyen and M. B. Francis, “Practical synthetic route to functionalized rhodamine dyes,” *Org. Lett.*, vol. 5, no. 18, pp. 3245–3248, 2003, doi: 10.1021/ol035135z.

[3] I. A. Boldyrev, X. Zhai, M. M. Momsen, H. L. Brockman, R. E. Brown, and J. G. Molotkovsky, “New BODIPY lipid probes for fluorescence studies of membranes,” 2007, doi: 10.1194/jlr.M600459-JLR200.

[4] C. Pellegrino *et al.*, “Multiple Dye Doped Core-Shell Silica Nanoparticles: Outstanding Stability and Signal Intensity Exploiting FRET Phenomenon for Biomedical Applications,” *J. Nanomater. Mol. Nanotechnol.*, vol. s6, pp. 6–11, 2018, doi: 10.4172/2324-8777.s6-003.

[5] K. Nagy and K. Vékey, “Separation methods,” in *Medical Applications of Mass Spectrometry*, Elsevier, 2008, pp. 61–92.

[6] H. Heinz *et al.*, “Nanoparticle decoration with surfactants: Molecular interactions, assembly, and applications,” *Surface Science Reports*, vol. 72, no. 1. Elsevier B.V., pp. 1–58, Feb. 01, 2017, doi: 10.1016/j.surfrep.2017.02.001.

[7] X. Liu *et al.*, “Size Dependent Cellular Uptake of Rod-like Bionanoparticles with Different Aspect Ratios,” *Sci. Rep.*, vol. 6, no. 1, pp. 1–10, Apr. 2016, doi: 10.1038/srep24567.

[8] T. dos Santos, J. Varela, I. Lynch, A. Salvati, and K. A. Dawson, “Effects of transport inhibitors on the cellular uptake of carboxylated polystyrene nanoparticles in different cell lines,” *PLoS One*, vol. 6, no. 9, Sep. 2011, doi: 10.1371/journal.pone.0024438.

[9] J. P. Peñaloza *et al.*, “Intracellular trafficking and cellular uptake mechanism of PHBV nanoparticles for targeted delivery in epithelial cell lines,” *J. Nanobiotechnology*, vol. 15, no. 1, p. 1, Jan. 2017, doi: 10.1186/s12951-016-0241-6.

[10] P. Foroozandeh and A. A. Aziz, “Insight into Cellular Uptake and Intracellular Trafficking of Nanoparticles,” *Nanoscale Research Letters*, vol. 13, no. 1. Springer New York LLC, pp. 1–12, Oct. 25, 2018, doi: 10.1186/s11671-018-2728-6.

[11] S. Mourdikoudis, R. M. Pallares, and N. T. K. Thanh, “Characterization techniques for nanoparticles: Comparison and complementarity upon studying nanoparticle properties,” *Nanoscale*, vol. 10, no. 27. Royal Society of Chemistry, pp. 12871–12934, Jul. 21, 2018, doi: 10.1039/c8nr02278j.

[12] V. Filipe, A. Hawe, and W. Jiskoot, “Critical evaluation of nanoparticle tracking analysis (NTA) by NanoSight for the measurement of nanoparticles and protein aggregates,” *Pharm. Res.*, vol. 27, no. 5, pp. 796–810, May 2010, doi: 10.1007/s11095-010-0073-2.

[13] J. D. Robertson *et al.*, “Purification of Nanoparticles by Size and Shape,” *Sci. Rep.*, vol. 6, pp. 1–9, 2016, doi: 10.1038/srep27494.

[14] L. Pitkänen and A. M. Striegel, “Size-exclusion chromatography of metal nanoparticles and quantum dots,” *TrAC - Trends Anal. Chem.*, vol. 80, pp. 311–320, 2016, doi: 10.1016/j.trac.2015.06.013.

[15] J. J. Stumm, W; Morgan, “Aquatic chemistry: chemical equilibria and rates in natural waters,” *Environ. Sci. Technol. A Wiley-Interscience Ser. Texts Monogr.*, vol. 33, no. 11, pp. 33-6312-33–6312, 1996, doi: 10.5860/choice.33-6312.

[16] M. Baalousha, M. Motelica-Heino, and P. Le Coustumer, “Conformation and size of humic substances: Effects of major cation concentration and type, pH, salinity, and residence time,” *Colloids Surfaces A Physicochem. Eng. Asp.*, vol. 272, no. 1–2, pp. 48–55, Jan. 2006, doi: 10.1016/j.colsurfa.2005.07.010.

[17] B. Nowack and T. D. Bucheli, “Occurrence, behavior and effects of nanoparticles in the environment,” *Environ. Pollut.*, vol. 150, no. 1, pp. 5–22, Nov. 2007, doi: 10.1016/j.envpol.2007.06.006.

[18] P. Christian, F. Von Der Kammer, M. Baalousha, and T. Hofmann, “Nanoparticles: Structure, properties, preparation and behaviour in environmental media,” *Ecotoxicology*, vol. 17, no. 5. Ecotoxicology, pp. 326–343, Jul. 2008, doi: 10.1007/s10646-008-0213-1.

[19] S. Kumar, V. K. Aswal, and P. Callow, “PH-dependent interaction and resultant structures of silica nanoparticles and lysozyme protein,” *Langmuir*, vol. 30, no. 6, pp. 1588–1598, Feb. 2014, doi: 10.1021/la403896h.

[20] J. R. Casey, S. Grinstein, and J. Orlowski, “Sensors and regulators of intracellular pH,” *Nat. Rev. Mol. Cell Biol.*, vol. 11, no. 1, pp. 50–61, 2010, doi: 10.1038/nrm2820.

CHAPTER 2

Uptake and intracellular trafficking studies of multiple dye-doped core-shell silica nanoparticles in lymphoid and myeloid cells

Data accepted in

Sola et al. (2021) Nanotechnol Sci Appl.

Sub ID: 290867

Article in Press

And unpublished data

ORIGINAL RESEARCH

F. Sola et al.

Uptake and intracellular trafficking studies of multiple dye-doped core-shell silica nanoparticles in lymphoid and myeloid cells

Federica Sola[1,2], Barbara Canonico[1], Mariele Montanari[1], Angela Volpe[2], Chiara Barattini[1,2], Chiara Pellegrino[2], Erica Cesarini[1], Michele Guescini[1], Michela Battistelli[1], Claudio Ortolani[1], Alfredo Ventola[2] and Stefano Papa[1]

[1]Department of Biomolecular Sciences, University of Urbino Carlo Bo, 61029 Urbino (PU), Italy; [2]AcZon srl, 40050 Monte San Pietro (BO), Italy

Correspondence: Barbara Canonico

Department of Biomolecular Sciences, University of Urbino Carlo Bo, Via Ca' Le Suore 2-4, 61029 Urbino (PU), Italy

Tel +39 0722 304280

Email barbara.canonico@uniurb.it

Accepted in Nanotechnology, Science and Applications, Sub ID: 290867

Article in Press

Abstract

Introduction: Since most biologically active macromolecules are natural nanostructures, operating in the same scale of biomolecules gives the great advantage to enhance the interaction with cellular components. Noteworthy efforts in nanotechnology, particularly in biomedical and pharmaceutical fields, have propelled a high number of studies on the biological effects of nanomaterials. Moreover, the determination of specific physicochemical properties of nanomaterials is crucial for the evaluation and design of novel safe and efficient therapeutics and diagnostic tools. In this in vitro study, we report a physicochemical characterisation of fluorescent silica nanoparticles (NPs), interacting with biological models (U937 and PBMC cells), describing the specific triggered biologic response.

Methods: Flow Cytometric and Confocal analyses are the main method platforms. However, TEM, NTA, DLS, and chemical procedures to synthesize NPs were employed.

Results: NT_B700 NPs, employed in this study, are fluorescent core-shell silica nanoparticles, synthesized through a micelle-assisted method, where the fluorescence energy transfer process, known as FRET, occurs at a high efficiency rate. Using flow cytometry and confocal microscopy, we observed that NT_B700 NP uptake seemed to be a rapid, concentration-, energy- and cell type-dependent process, which did not induce significant cytotoxic effects. We did not observe a preferred route of internalization, although their size and the possible aggregated state could influence their extrusion. At this level of analysis, our investigation focuses on lysosome and mitochondria pathways, highlighting that both are involved in NP co-localization. Despite the main mitochondria localization, NPs did not induce a significant increase of intracellular ROS, known inductors of apoptosis, during the time course of analyses. Finally, both lymphoid and myeloid cells are able to release NPs, essential to their biosafety.

Discussion: These data allow to consider NT_B700 NPs a promising platform for future development of a multifunctional system, by combining imaging and localized therapeutic applications in a unique tool.

Keywords: nanoparticles, uptake, intracellular trafficking, exocytosis, multifunctional tool

Introduction

Nanotechnology, historically defined as research and technology development at the atomic or molecular scale leading to the study and controlled manipulation of materials, devices and systems within a nanometer range, has achieved the status as one of the key technologies of the twenty-first century [1,2]. Despite not being a newly discovered concept, nanotechnology and nanomaterials in general are, even today, a fascinating research area with multiple application potentials, especially in biomedical fields such as therapy and diagnostics. Since most biologically active macromolecules are natural nanostructures, operating in the same scale of biomolecules gives the great advantage to enhance the interaction with cellular components, as cell membrane and proteins [1,3]. Thanks to their unique features of shape, size and charge, nanoparticles (NPs) appeared to be good candidates in a wide range of applications. Notably, NPs are widely used in biomedical applications as, owing to their small size, they can easily pass through the biological barriers and enter the cells to carry out their function [4]. The development of nano-delivery technology, in particular, yields potential to overcome the blood-brain barrier (BBB), which hampers drugs from reaching their site of action and pose a tough challenge to drug delivery into brain. Therefore, NPs bring hope for neurodegenerative diseases, by encapsulating therapeutic molecules might increase the drug transport through the BBB and target relevant regions in the brain for regenerative processes [5,6].

In order to apply NPs in drug delivery or imaging fields and reduce their toxicity, it is essential to study their specific endocytosis, exocytosis and clearance mechanisms in target cells [4,7,8]. Understanding how NPs enter the cells is a key factor in determining their biomedical functions, biodistribution and toxicity [4,9]. Several regulated processes with complex biomolecular interactions are involved in NP cellular uptake. Extracellular material could exploit multiple different cellular entry routes to cross cell plasma membrane, from passive diffusion to active transport. The latter, generally known as endocytosis, is an energy-dependent process used to describe various pathways and mechanisms of how cells communicate with biological environments. The interest for this field of study, currently evolving, is still high and researchers seek to further elucidate how NPs entry into cells and which mechanisms are employed [10]. The endocytic pathways are generally classified into five mechanistically different classes: clathrin-mediated endocytosis, caveolae-mediated endocytosis, clathrin- and caveolae-independent endocytosis, macropinocytosis and

phagocytosis [10-13]. Furthermore, NP intracellular trafficking and fate have a remarkable importance for their success as carriers designed to reach a specific target inside the cell and deliver specific biomolecules such as contrast agents, genes or drugs [4]. Once inside the cells, NPs are generally enclosed in intracellular vesicles and delivered through the cytoplasm, maybe trafficked along the endolysosomal network or shuttled with the help of motor proteins and cytoskeletal structures to reach some organelles.

Among sundry nanomaterials, silica NPs showed several advantages (hydrophilicity, stability in biological environment, optical transparency, ease of synthesis and low cost) and many fields of applications, such as cosmetics, food, pharmaceutical and medicine [14-16]. Several studies have examined the toxicity of these NPs in different cell lines and amorphous silica NPs are generally considered biocompatible and harmless [15]. In particular, the observed adverse effects are size and cell type dependent [17]. NT_B700 NPs, employed in this study, are fluorescent core-shell silica nanoparticles, synthesized through a micelle-assisted method. The most innovative feature of NT_B700 NPs is the ability to be a platform where the fluorescence energy transfer process, known as FRET, occurs at a high efficiency rate [18]. Besides being one of the most used "stealth" polymers in the drug delivery field, polyethylene glycol (PEG), part of NP shell, allows to modulate the type and number of functional groups exposed on NP surface. As a consequence, PEG properties lead to the conjugation of several biomolecules on NT_B700 NPs in addition to being the primary interface between NPs and cells, by influencing bio-distribution and toxicity [19,20].

The present study provides insights about the characterization of fluorescent NP routes of internalization and exocytosis in lymphoid and myeloid cells. Furthermore, these mechanisms are related to the possible detection of cell death features. The use of U937 cells guarantees the possibility to collect data on a homogeneous, numerically plentiful, myeloid population, whereas PBMC cells allow for the simultaneous analysis of NP effects on many and varied important immune cells like B-cells, T-cells, monocytes and natural killer (NK) cells. Studying nanomaterial behaviour in these types of cells is fundamental since they will interact with NPs once introduced into the blood torrent [21].

Materials and Methods

2.1. Human tumour myeloid cells (U937) and peripheral blood mononuclear cell (PBMC)

2.1.1. Ethic statement

PBMCs (peripheral blood mononuclear cells) were isolated from whole blood of anonymous donors obtained from the Transfusion Centre of Urbino Hospital. No specific approval from an institutional review board was required for the use of whole blood for the following reasons: (1) no personal patient information was made available; (2) whole blood could not be used for treatment of patients and were waste products for the blood transfusion centre and (3) blood donors were verbally informed that parts of the donation that cannot be used for patient treatment may be used for scientific research.

2.1.2. PBMC isolation

Peripheral blood mononuclear cells (PBMCs) were isolated from fresh whole blood of healthy donor. The method for mononuclear cell isolation was first developed by Boyum in 1968 [22]. PBMCs were separated by density gradient centrifugation, since the different components of the blood have different densities and can be separated accordingly. 20 mL of whole blood, previously diluted 1:2 with sterile phosphate saline buffer 1X (PBS, 10 mM NaPi, 150 mM NaCl, pH 7.3-7.4), was gently layered on top of an opportune volume of the Ficoll-Paque^{TM} Plus solution (GE Healthcare, Little Chalfont, UK) into a 50 mL centrifuge tube and centrifuge at 400 g without brake for 30 min at room temperature (RT). The solution is denser than lymphocytes, monocytes, and platelets (meaning these will remain above it), but less dense than granulocytes and erythrocytes, which will drop below it. The white ring of PBMCs, which was located between the two phases, was collected with a serological pipette and then transferred to a 50 mL centrifuge tube and washed three times with PBS 1X to eliminate any remaining platelets (the first centrifuge at 300g for 15 min, the following at 200 g for 10 min). Finally, the pellet was resuspended in in Roswell Park Memorial Institute Medium (RPMI) 1640 (Sigma-Aldrich, St Louis, MO, USA) with stable L-glutamine supplemented with 10% v/v heat-inactivated fetal bovine serum (FBS; Gibco; Thermo Fisher Scientific, Inc., Waltham, MA, USA) and 1% v/v penicillin/streptomycin (Sigma-Aldrich, St Louis, MO, USA).

2.1.3. Cell culture

U937 (human myelomonocytic cell line) cells were grown at 37°C in humidified incubator with 5% CO_2 in RPMI 1640 complete medium, with stable L-glutamine supplemented with 10% v/v heat-inactivated fetal bovine serum (FBS) and 1% v/v penicillin/streptomycin.

PBMCs were cultured in RPMI 1640 complete medium and incubated at 37°C in humidified incubator with 5% CO_2.

2.2.Nanoparticle uptake assessment

2.2.1. Nanoparticle uptake

NP dispersions were prepared by diluting the stock solution, previously filtered with a 0.22 μm membrane filter (Euroclone SpA, Milan, Italy) under sterile environment, into complete medium used for cell culture at room temperature (to ensure better NP dispersion), immediately prior to the experiments on cells. U937 and PBMCs (5×10^5 cells/well) were seeded separately into 6 or 12-well plates. To assess time-dependent NP internalization, a solution of NT_B700 (64 μg/mL) was added to culture medium for different time points. Different concentrations (6.4, 12.8, 64 and 640 μg/mL) of NT_B700 NPs were added and incubated for 1 h, to evaluate concentration-dependence. Once estimated the better conditions of concentration and time (64 μg/mL for 1 h), all subsequent evaluations were carried out under these conditions. After the incubation time, cells were collected by centrifuging (1200 rpm, 5 min) to remove the NP-containing medium and washed twice with PBS 1X. The quantification of NP incorporation into cells was carried out by measuring the mean fluorescence intensity (MFI) with flow cytometer (for instrument details see the corresponding paragraph). In addition to the quantitative analysis carried out in flow cytometry, a qualitative analysis was carried out by confocal microscopy (for instrument details see the corresponding paragraph). For negative control, cells were incubated with medium only.

2.2.2. Morphological feature evaluation

To evaluate changes in cell morphology and size both cytometry and microscopy were used. As suggested by Suzuki et al., in flow cytometry the intensity of the side scatter (SSC) could be an index that NPs are taken up into cells [23], since incorporated NPs change the SSC signal standing for cell granularity. Therefore, in flow cytometry the differences in size and

morphology were distinguished by using their physical characteristics: forward scatter (FSC, cell size) and side scatter (SSC, cell granularity). Although a quantitative analysis was carried out in flow cytometry, a qualitative analysis of NP effect on cells was performed in microscopy by evaluating cell morphology and density, compared to control cells, under an inverted phase-contrast microscope (Nikon, Japan).

2.2.3. Investigation of PBMC subsets

PBMCs were stained with different monoclonal antibodies (mAbs) to define cell subsets in order to highlight the differences in NP uptake among cell populations:

- anti CD5 (CRIS-1) for T lymphocytes,
- anti-CD14 (CB14) for monocytes,
- anti-CD16 (CB16) for natural killer (NK) cells
- anti-CD19 (CB19) for B lymphocytes.

All mAbs were produced and conjugated in AcZon (AcZon s.r.l., Monte San Pietro, BO, Italy) with different fluorophores, FITC or RPE, in order to have different emission channels compared to NT_B700 NPs and perform a multiparametric analysis by flow cytometry. Fluorochrome-conjugated monoclonal antibodies were added to 50 µL of cell pellet, vortexed and then incubated for 20 min at RT. After the incubation time 1 mL of PBS was added and samples were acquired by flow cytometry.

2.2.4. Cell viability assays

2.2.4.1.Trypan Blue exclusion assay

This test was used to determine the number of viable cells in cell suspension. An aliquot of cell suspension was mixed with an equal volume of 0.4% Trypan Blue solution (Life Technologies Corporation, Eugene, Oregon, USA), incubated for approx. 3 min at room temperature and then counted with a Neubauer chamber. Cells were visually examined, with a light microscopy, to determine whether cells took up or excluded dye: viable cells typically show a clear cytoplasm (unstained) whereas nonviable cells show a blue cytoplasm (stained) [24]. Percentage of viable cells was calculated as following:

$$\text{Viable cells (\%)} = \frac{\text{number of viable cells}}{\text{number of total cells}} \times 100$$

2.2.4.2.Flow cytometry detection of cell death

NP toxicity was evaluated using propidium iodide (PI) staining, that is capable of binding and labelling DNA. Live cells, with intact cell membranes, are distinguished by the ability to exclude the dye that easily penetrate dead or damaged cells [25]. Cells pellets were resuspended with 300 µL of PBS, 5 µL of 1 mg/mL PI (Sigma-Aldrich, St Louis, MO, USA) were added per sample, incubated for 5 min in the dark at room temperature and analysed on flow cytometer. The % of PI positive cells was calculated using the following equation = [% of PI positive cells (cells exposed to NP or drugs) - % of PI positive cells (cells untreated)].

2.2.5. Cell cycle analysis

The distribution of DNA in the cell cycle was investigated by flow cytometry. 5×10^5 cells/well were seeded 6-well plates and cells were exposed to a solution of NT_B700 (64 µg/mL), whereas control cells were incubated with medium only, harvested at different time points (1, 4, 24, 48 and 72 h), centrifuged at 1200 rpm for 5 min. and washed with PBS 1X. The pellets were fixed drop by drop with ice-cold ethanol (70%) and stored at +4°C until the analysis. For cell cycle analyses, samples were washed twice with PBS 1X and each pellet was resuspended in 440 µL of PBS 1X, to which 10 µL of 1 mg/mL PI (Sigma-Aldrich, St Louis, MO, USA) and 50 µL of 1 mg/ml RNAse (Sigma-Aldrich, St Louis, MO, USA) were added, to reach a final volume of 500 µL. The samples were well resuspended and incubated at 37°C for at least 30 min or at +4°C until analysis by flow cytometry.

2.2.6. Inhibition of endocytosis

To investigate the energy-dependence of uptake mechanism, cells (5×10^5 cells/well) were pre-incubated at +4°C and with a sodium azide (NaN_3) solution (1 mg/mL) for 30 min, followed by the addition of NPs (64 µg/mL) for 2 h and, finally, cells were prepared and analysed by flow cytometry as previously described. The quantification of NP uptake into cells was carried out by measuring the mean fluorescence intensity (MFI) with flow cytometer.

Known inhibitors of various endocytic processes were used to elucidate the mechanism of cellular uptake of NT_B700 NPs. Each pharmaceutical inhibitor was previously titrated with a Trypan Blue exclusion assay (performed as previously described) in order to use a non-cytotoxic concentration. The titration concentrations, pre-diluted in medium, tested: nocodazole (2.5, 5, 10, 20 40 µg/mL), genistein (2.5, 5, 10, 20 40 µg/mL), amiloride (5, 10, 25, 50, 100 µg/mL) and chlorpromazine (1.25, 2.5, 5, 10, 20 µg/mL). Cells ($5x\ 10^5$ cells/well) were pre-incubated with inhibitors of endocytosis: amiloride (30 µg/mL) chlorpromazine (5 µg/mL), genistein (20 µg/mL) and nocodazole (7.5 µg/mL) for 30 min, followed by the addition of NPs (64 µg/mL) for 2 h and, then, samples analysed by flow cytometry. The quantification of NP uptake into cells was carried out by measuring the mean fluorescence intensity (MFI) with flow cytometer. Negative controls, i.e. cells without the presence of drugs and/or NPs were also carried out by incubating with medium only. Moreover, cell viability was assessed after 2 h of exposure to each of the different inhibitors, including the energy-dependent conditions of +4°C and NaN_3, by PI staining. All inhibitors were purchased from Sigma-Aldrich.

2.3.Intracellular trafficking studies

Cells (5×10^5 cells/well) were exposed to NT_B700 NPs (64 µg/mL) at different time points (1-48 h), washed and then stained with various cellular markers to investigate the effect of NP uptake in several cellular compartments.

Lysosomal involvement

To label and trace lysosomes the acidotropic dye LysoTracker™ Green (LTG) (Thermo Fisher Scientific, Waltham, MA, USA) was used. LysoTracker probes, in general, are fluorescent acidotropic dyes for labeling and tracking acidic organelles in live cells: it means that the amount of fluorescence obtained from staining with LTG is directly related to the volume of lysosome-related organelles in a cell [26]. Cells were resuspended in pre-warmed (37°C) medium containing 100 nM LysoTracker (diluted in RPMI). After 45 min incubation green lysosomal fluorescence was detected by flow cytometry and confocal microscopy.

Determination of mitochondrial potential (ΔΨm) and reactive oxygen species (ROS)

Mitochondrial features were investigated by TMRE, DCFH-DA and MitoSOX staining.

Tetramethylrhodamine ethyl ester perchlorate (TMRE) (Sigma-Aldrich, St. Louis, MO, USA) is a cell permeable, positively charged red-orange dye (Abs max=488 nm, Em max= 580 nm) that accumulates in active mitochondria due to their relative negative charge. The level of TMRE fluorescence in stained cells can be used to determine mitochondrial membrane potential ΔΨm [27]. TMRE 40 nM was added to the samples 15 min before the acquisition time. Samples were analysed by confocal microscopy and flow cytometry using the appropriate fluorescence channel.

5-(and-6)-chloromethyl-2,7'-dichlorodihydrofluorescein diacetate acetyl ester (CM-H_2DCFDA, DCFH-DA) (Molecular Probes, Eugene, OR), is a cell permeable, non-fluorescent precursor of DCF which can be used as probe for intracellular reactive oxygen species (ROS). Intracellular esterases cleave at the two ester bonds DCFH-DA, producing a cell membrane-impermeable product, H_2DCF which is a non-fluorescent molecule that accumulates intracellularly (Fig. 2.1). Subsequent oxidation yields the highly fluorescent product DCF and the redox state of the sample can be monitored by detecting the increase in fluorescence [28]. DCFH-DA 5μM was added to the samples, incubated for 30 minutes at 37°C and then acquired. Samples were analysed by flow cytometry using the appropriate fluorescence channel.

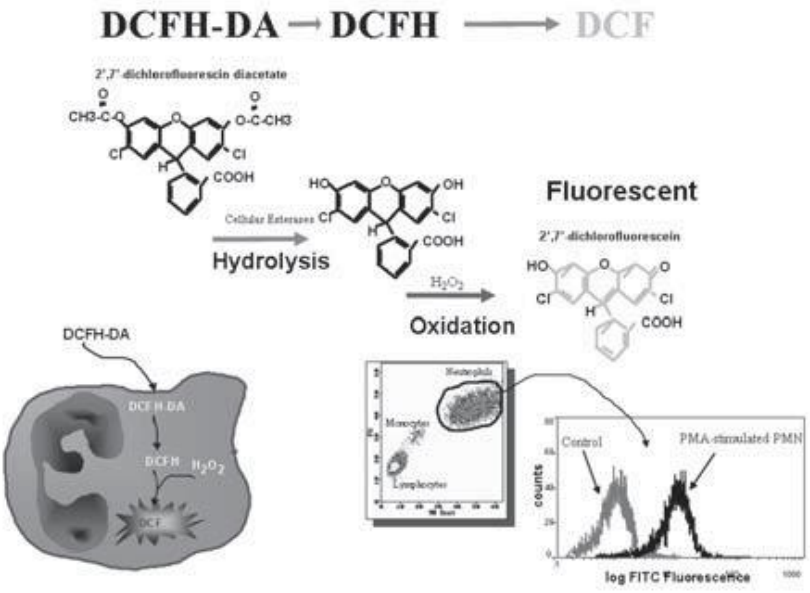

Fig. 2.1 Schematic representation of fluorescence emission of 2′-7′-Dichlorodihydrofluorescein diacetate (DCFH-DA) after oxidation due to intracellular reactive oxygen species (ROS), in particular H_2O_2. [29]

MitoSOX Red (Thermo Fisher Scientific, Waltham, MA, USA) is a florigenic dye specifically targeted to mitochondria in live cells and its oxidation by superoxide (O_2-), that is contained in mitochondria, produces a red fluorescence [30]. MitoSOX 5μM was added to the sample 10 min before the time of acquisition. Samples were analysed by flow cytometry using the appropriate fluorescence channel.

Autophagic vacuole detection

Autophagic vacuoles were detected in flow cytometry by monodansylcadaverine (MDC) (Sigma-Aldrich, St Louis, MO, USA) staining, a specific autophagolysosomes marker typically used to investigate the autophagic machinery [31]. Cells were incubated with 50μM MDC at 37°C for 10 minutes and then acquired by flow cytometry.

2.4.Nanoparticle release

2.4.1. Spectrofluorimetric analysis

One of the most common approach to study NP release is to seed cells, previously incubated with NPs, with fresh medium (NP-free) [32].

Since NP release was investigated in complete medium, the presence of phenol red, which had a specific absorbance spectrum, could interfere with the analysis. Furthermore, during the incubation time with cells, the pH indicator could vary, proportionally with the medium acidification, so it was necessary to standardize its influence.

By analysing the absorbance spectra of phenol red at different pH (Fig. 2.2), we chose a pH<5 in order to standardize all the analysis and exclude the contribute of phenol red.

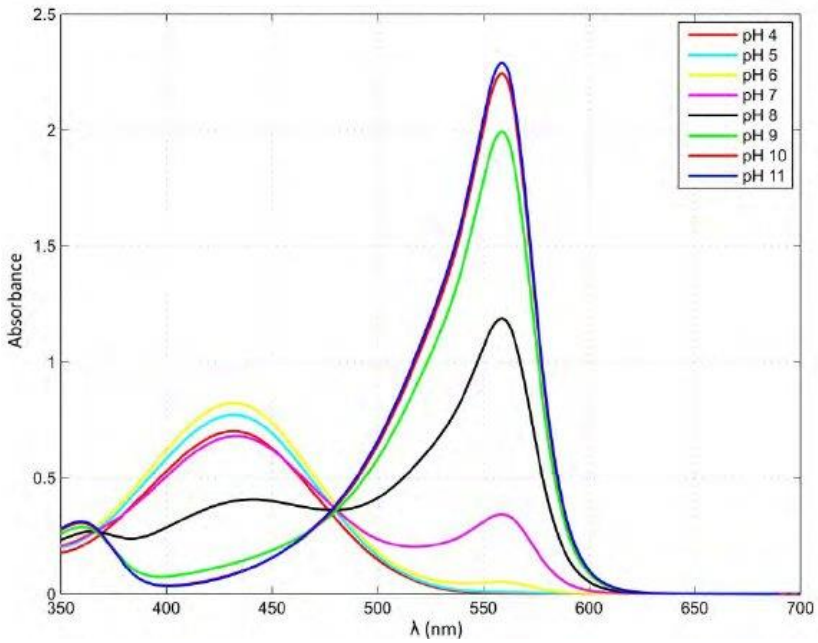

Fig. 2.2 Absorbance spectra of phenol red at different pH values. [33]

We prepared a buffering solution AcOH/NaOAc 500 mM for the dilutions and work for all samples with a pH<5:

- 2,43 mL di AcOH (Carlo Erba, Cornaredo, Milan, Italy)
- 0,619 g NaOAc (Sigma-Aldrich, St Louis, MO, USA)
- brought to a final volume of 100 mL with ddH_2O (Carlo Erba, Cornaredo, Milan, Italy)

For the construction of the calibration curve: NPs were first diluted 1:50 in complete medium, then 1:2 (final dilution 1:100 for the first point of the curve) in buffering solution AcOH/NaOAc 500 mM and then we performed a serial dilution (dilution factor 1:2) in order to obtain at least 5 samples. Each dilution was analysed by using a FP-6200 spectrofluorometer (JASCO EUROPE s.r.l., Cremella, Co, Italy), recording the whole spectrum with the following setup:

Measurement Mode……..	Emission
Band Width (Ex)……	5 nm
Band Width (Em)……..	5 nm
Response……	Slow
Excitation Wavelength……..	480.0 nm

Start……	490.0 nm
End…….	900 nm
Data Pitch……...	1 nm
Scanning Speed…….…….	250 nm/min
Sensitivity……...	High

We considered the entire area of the spectrum for each point, up to the sensitivity limit of the instrument, subtracted the area value of buffered medium and plot these values (y-axes) with NP concentrations (x-axes) to obtain the calibration curve illustrated in Fig. 2.3

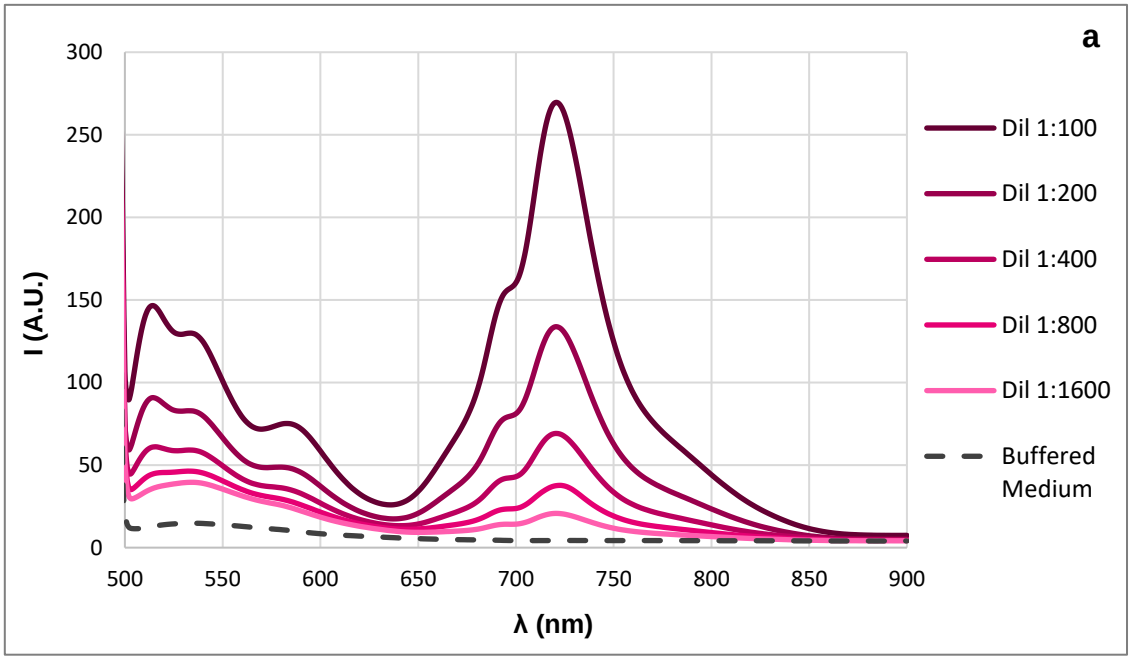

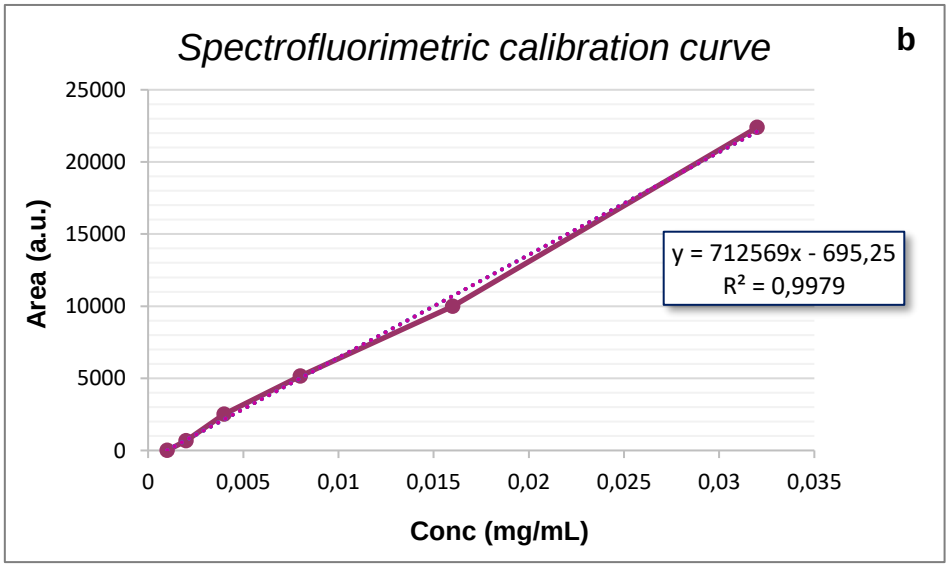

Fig. 2.3 Spectrofluorimetric calibration curve. (a) Emission spectra of the buffered medium (dashed line) and all points of the calibration curve, corresponding to serial dilution of NT_B700 in buffered medium. (b) Calibration curve showing NT_B700 concentration related to emission area.

Cells (5×10^5 cells/well) were exposed to NT_B700 NPs (64 μg/mL) for 1 h, harvested by centrifuging (5 min at 1200 rpm) and then seeded again with 1 mL of RPMI 1640 complete medium to investigate NP extrusion. At different times (0.5, 1, 4, 24, 48 and 72 hours) cells, incubated in NP-free medium, were collected by centrifuging and supernatants were analysed with spectrofluorometer (JASCO EUROPE s.r.l., Cremella, Co, Italy) in order to detect NPs in media. To quantify the NPs released by cells in culture medium, we considered the area of each sample, subtracted the area value of buffered medium and interpolated it in the calibration curve to obtain NP concentration, by applying the formula of the calibration curve. Whereas, the cells were analysed by flow cytometry to investigate the residual fluorescence within them.

2.4.2. Flow cytometry detection of particle release

Cells (5×10^5 cells/well) were exposed to NT_B700 NPs (64 μg/mL) for 1 h, harvested and then seeded again with 1 mL of RPMI 1640 complete medium to investigate NP extrusion after 24 h of incubation with fresh medium (NP-free). Cells were collected by centrifuging and both cells and supernatants analysed by flow cytometry, the former with the intracellular probes previously described, the latter with Dako CytoCountTM beads (Thermo Fisher Scientific, Waltham, MA, USA) for the evaluation and count of extracellular vesicles (EVs) released by cells [30]: 300 μL of medium for each sample was carefully dispensed at the bottom of the tube and 25 μL of beads were added. Supernatants were also stained with anti-CD63-FITC (clone TEA3/18) (Immunostep, Spain), a classical marker of exosomes [34].

2.5.Cytometric investigations

Cytometric experiments were carried out with a FACSCanto™ II flow cytometer (BD Biosciences, San Jose, CA, USA), equipped with an argon laser (Blue, Ex 488 nm), a helium-neon laser (Red, Ex 633 nm) and a solid-state diode laser (Violet, Ex 405 nm). For each sample, at least 10.000 events were acquired. Data analyses were performed with Kaluza Analysis 2.1 (Beckman Coulter, Brea, CA, USA) and FACSDiva™ softwares (BD Biosciences, San Jose, CA, USA).

In alternative, cytometric experiments were carried out with a CytoFLEX S flow cytometer (Beckman Coulter, Brea, CA, USA), equipped with three lasers: Violet laser (405 nm, 80 mW power), Blue laser (488 nm, 50 mW power) and Red laser (638 nm, 50 mW power). Fluorescence and side scatter light delivered by fiber optics to Avalanche Photo Diode detector arrays. At least 10.000 events were acquired for each sample. Data analyses were performed with Kaluza Analysis 2.1 (Beckman Coulter, Brea, CA, USA) and CytExpert software (Beckman Coulter, Brea, CA, USA).

Cytometric experiments were also carried out with a NovoCyte® 3000 flow cytometer (ACEA Biosciences, San Diego, CA, USA), equipped with three lasers (Violet Ex 405 nm, Blue Ex 488 nm and Red Ex 640 nm) and fifteen fluorescent channel detection. At least 10.000 events were acquired for each sample. Data analyses were performed with Kaluza Analysis 2.1 (Beckman Coulter, Brea, CA, USA) and NovoExpress Software (ACEA).

2.6.Confocal microscopy analysis

Confocal microscopy analyses were applied by a Leica TCS SP5 II confocal microscope (Leica Microsystem, Germany) with 488, 543 and 633 nm illuminations and oil-immersed objectives. For confocal imaging, cells were seeded on MatTek glass bottom chambers (MatTek Corporation Slovak Republic). The images were further processed and analysed in ImageJ software (National Institutes of Health, Bethesda, MD, USA). Colocalization analyses were performed using JACoP plugin in ImageJ software (NIH, Bethesda, MD, USA) [35]. Pearson's correlation coefficient (PCC) was used as the parameter to measure colocalization in our samples.

2.7. Statistical analysis

Data are shown as mean (or percentage, as indicated) ± standard deviation (sd) of at least three independent experiments. Analyses of variance (ANOVA) approaches were used to compare values among more than two different experimental groups for data that met the normality assumption. One-way ANOVA or two-way ANOVA were followed by a Bonferroni post-hoc test. The means of two groups were compared by using a T test. The p values less than 0.05 were considered statistically significant. All statistical analyses were performed using GraphPad Prism 8.4.2 (GraphPad software, San Diego, CA, USA).

Results and discussion

Time- and concentration-dependence of NT_B700 nanoparticle uptake

To characterize how NT_B700 nanoparticles are taken up by cells, we quantified their incorporation through flow cytometry, measured by mean intensity fluorescence (MFI) and variation in side scatter (SSC), supported by a qualitative analysis performed by confocal microscopy. The measurements were performed under different conditions: variation of the incubation time in order to see a time-dependence of NP uptake, the use of different concentrations for dose-dependence and by modifying energy conditions of cell culture (next paragraph). NT_B700 NPs were already internalized after 30 min of incubation at 37°C (Fig. 2.1C), which demonstrated that these NPs translocate rapidly into the cells. The intensity of the side scatter (SSC) could be an index that NPs are taken up into cells, time-, dose- and size-dependently [23], since incorporated NPs change the SSC signal standing for cell granularity in flow cytometry [36]. As suggested by Suzuki et al., we observed a variation of U937 SSC during investigated times and a simultaneously slight decrease of FSC values, without a correlation with cell death (Fig. 2.1A and 2.1B). U937 cells showed a good tolerance of the uptake process with only the higher NP concentration (> 64 µg/mL) presenting high percentage of PI positive cells (Fig. 2.1E). We did not observe a significant change in cell viability and morphology for the cells treated with NT_B700 nanoparticle compared to control during time (Fig. 2.2). Although the percentage of Trypan Blue positive cells, i.e. nonviable cells, were comparable to control, we observed an inhibition of cell growth, confirmed also by cell cycle analysis with a stop in G1 phase, associated with a related reduction in S and G2/M phases (Fig. 2.3). Confirming the non-toxicity of NT_B700, we did not observe an increase of sub-G1 peak, one of the hallmarks of apoptosis. It has been known that NP concentration can impact uptake efficiency [8], therefore the effects of concentration on NP uptake were investigated by applying several concentrations, ranging from 0 to 640 µg/mL, to the cells. As shown in Fig. 2.1D the internalization of NT_B700 increased in a concentration-dependent manner when incubated at 37°C.

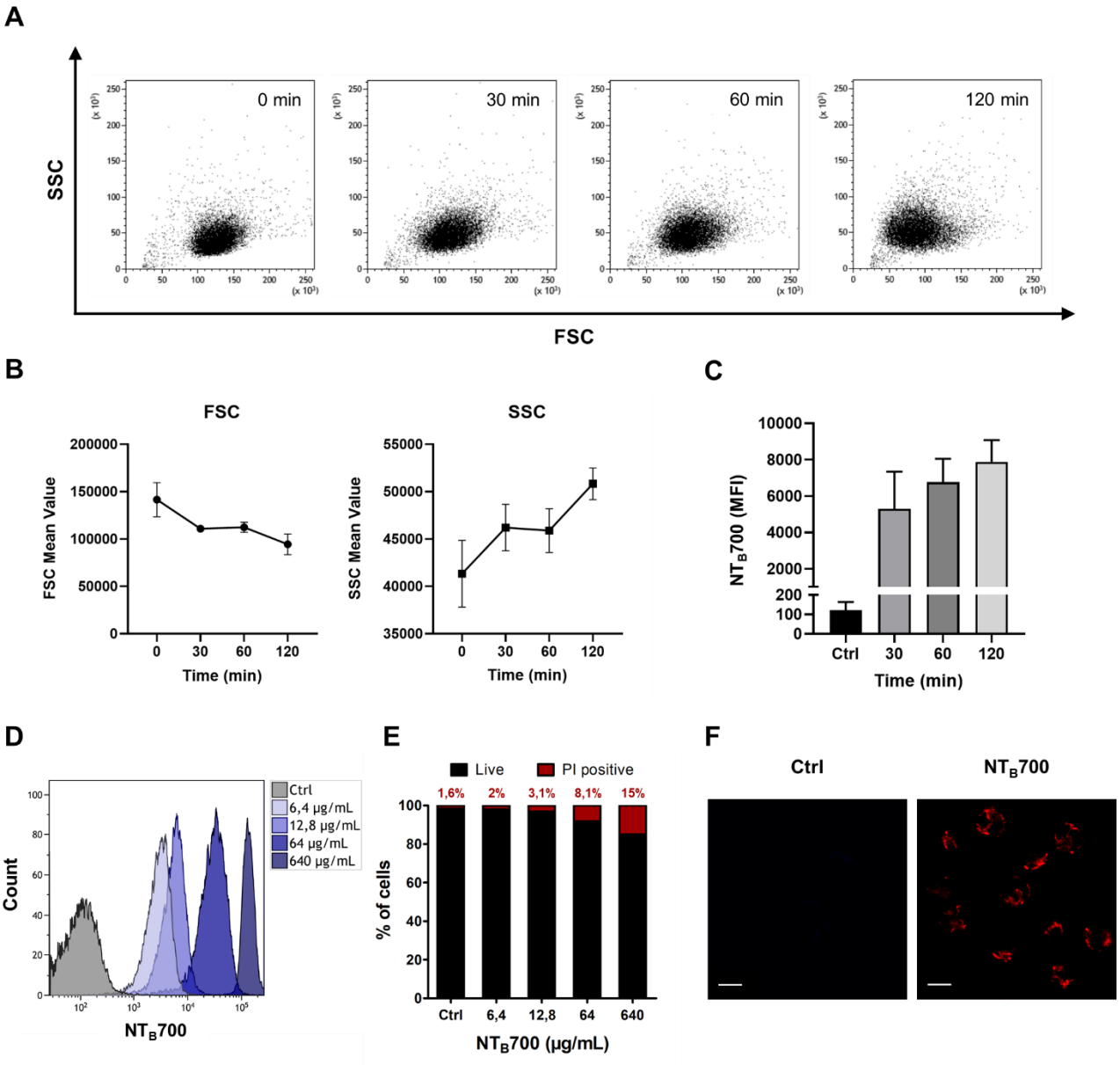

Fig. 2.1 Kinetics NT_B700 nanoparticle uptake in U937 cells. (A) U937 were incubated with 64 µg/mL NT_B700 at several time points (0, 30, 60 and 120 min). Dot plots (FSC vs. SSC) representing U937 treated with 64 µg/mL NT_B700 nanoparticles during time. (B) FSC slightly decreased during time (on the left); cellular granularity (SSC values) increased in a time-dependent manner (on the right). (C) Time-dependence of NT_B700 nanoparticle uptake in U937 cells. Mean Fluorescence Intensity (MFI) from the flow cytometry histograms is shown as a function of time. (D) Flow cytometry histogram overlay for cells treated for 1 h with different concentrations of NT_B700 nanoparticles (0, 6.4, 64 and 640 µg/mL) (E) Cell viability of U937 loaded with increasing doses of NT_B700 nanoparticles (0, 6.4, 64 and 640 µg/mL) determined by membrane permeability assay using Propidium Iodide (PI) and flow cytometry analysis to calculate the percentage of PI positive cells, indicating cell death. (F) U937 incubated for 1 h at 37°C with NT_B700 nanoparticles (64 µg/mL), turned out best experimental conditions. Representative confocal images of NT_B700 nanoparticles uptake in U937 cell line compared to control cells in which no fluorescence could be detected. NT_B700 in red. Scale bar = 10 µm. At least 10000 events were analysed by flow cytometry for each experimental condition

NT_B700 NP uptake into cells was further confirmed by confocal microscopy. Fig. 2.1F shows U937 untreated (Ctrl) and treated with nanoparticles, depicted in red, and no fluorescence was detectable in the nuclei. NP fluorescence did not appear diffuse into cytoplasm but seems to be more internalized in round shapes, as indicating their localization into vesicles or organelles inside the cells. Flow cytometry data and images collected at different times allowed us to select the best experimental conditions (1 h incubation time and a concentration of 64 µg/mL) to be used in further studies.

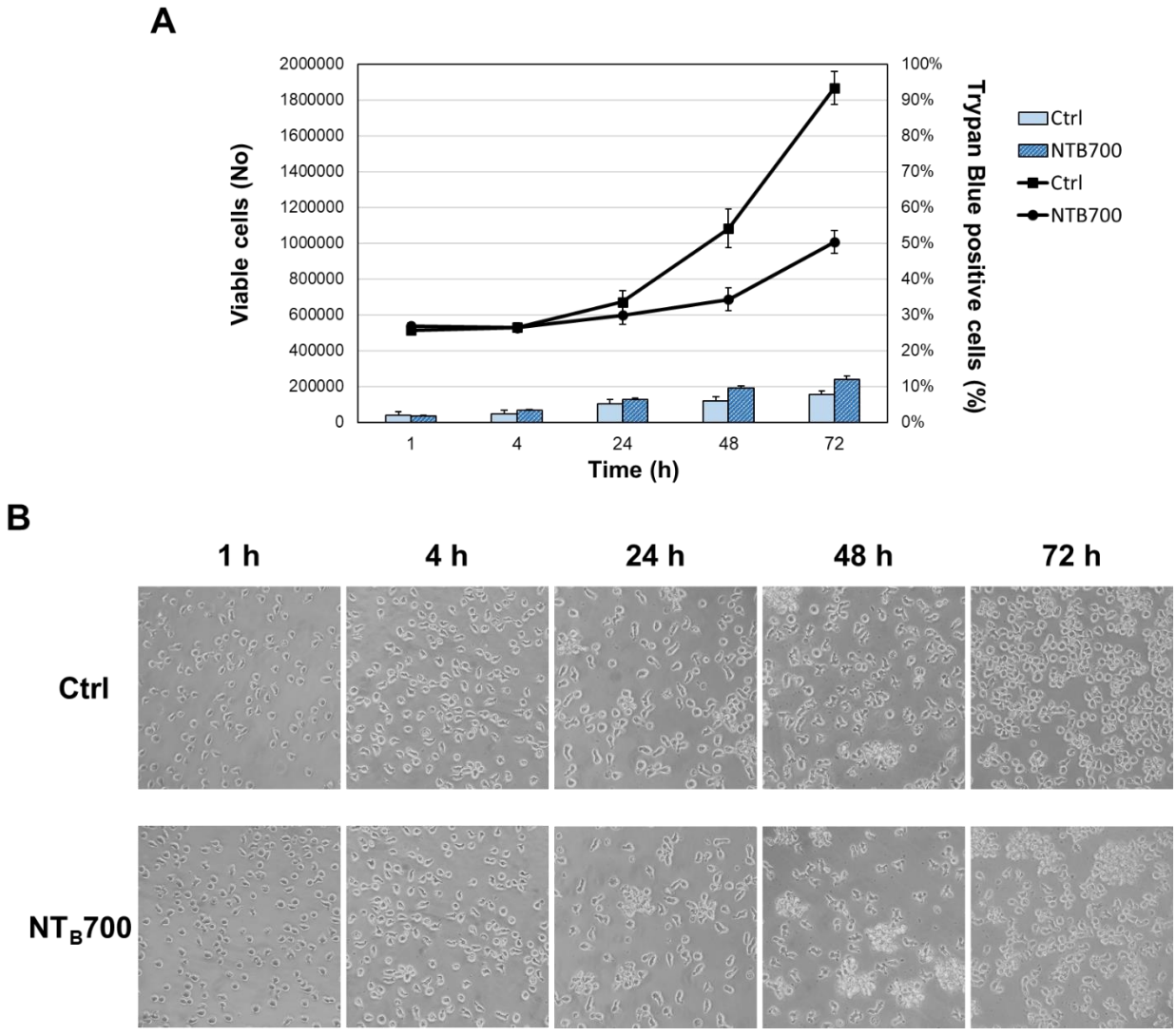

Fig. 2.2 Cell viability and morphology of U937 treated with NT_B700 nanoparticle. U937 were incubated with 64 µg/mL NT_B700 for different time points (1-72 h). (A) The cell viability was measured using Trypan Blue exclusion assay. Growth curves are expressed with black lines (■ for control cells, ● for treated cells), whereas the histograms indicate the percentage of Trypan Blue positive cells. Data are expressed as means ± sd of three experiments. (B) Representative phase contrast images of U937 cells (Ctrl and treated incubated with NT_B700) to observe cell morphology and density. Magnification 40X.

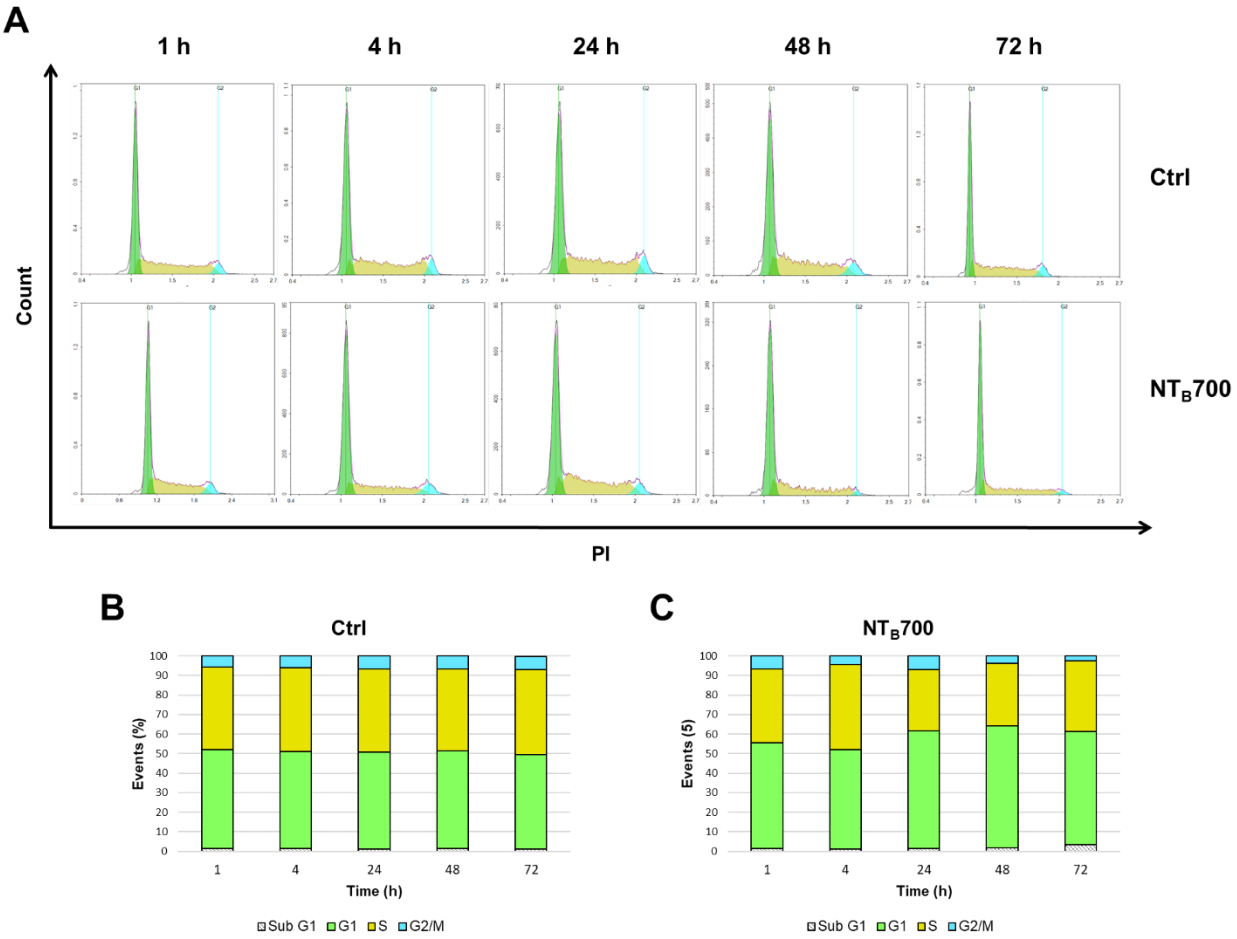

Fig. 2.3 Cell cycle progression analysis of U937 cells after exposure to NT_B700 nanoparticle. (A) Representative DNA histograms (obtained by PI staining) of control and treated cells with NT_B700. Bar graphs indicating the percentages of cell distribution in different phases of cell cycle (sub-G1, G1, S and G2/M) for control cells (B) or after treatment with NT_B700 (C) for different times (1-72 h).

Temperature- and energy-dependence of NT_B700 nanoparticle uptake

NP entry and headway into cells is an active process, which requires energy to be performed [8], and it is widely known that active processes, in general, are inhibited at low temperature, because several proteins and enzymes are sensitive to temperature [36,37]. In order to investigate whether NT_B700 NP uptake was energy-dependent, the internalization of NPs was measured by flow cytometry at either 37°C (control) or +4°C. As expected, NP uptake in U937 at +4°C resulted in a very strong inhibition (greater than 90%), as shown in Fig. 2.4. Several research groups with different types of NPs have reported the same behaviour [7-8,38-39]. E.g. Dos Santos et al. observed a stronger reduction of carboxylated-modified polystyrene (PS-COOH) NPs in different cell lines, in particular for those with smaller diameter [7]. Zeng and

co-workers showed a clear reduction of NP accumulation in MDA-MB468 cells [40]. Furthermore, pre-treatment of cells with sodium azide (NaN_3), which disturbs the production of ATP by blocking the electron transport chain, resulted in a clear reduced NP internalization. Nevertheless, NT_B700 uptake decrease is less significant compared to the effect of temperature we observed. Other researchers obtained similar results [8,40]. As proposed by Penaloza et al., NaN_3, by inhibiting the ATP synthesis, reduces the intracellular content of ATP but cells could compensate by using exogenous ATP and allow NP entry [8]. Nonetheless, our data, in agreement with earlier studies, indicated that NT_B700 nanoparticles are internalized by an active energy-dependent process.

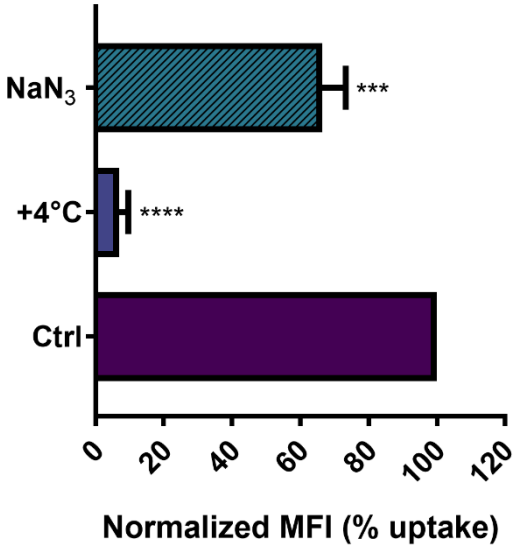

Fig. 2.4 Effect of temperature and energy depletion on NT_B700 nanoparticle internalization in U937. Cells were incubated with NT_B700 (64 µg/mL) under different condition: control (NPs incubated at 37°C), +4°C and sodium azide (NaN_3). The percentage of nanoparticle uptake was measured by MFI, determined through flow cytometry (2 independent replicas of 3 experiments), normalized with NP MFI values in normal condition at 37°C (Ctrl is 100% uptake). Asterisks denote a statistically significant difference effect of temperature and energy with their respective control (*** = $p < 0.001$, **** $p = < 0.0001$). At least 10000 events were analysed by flow cytometry for each experimental condition.

Investigation of NT_B700 nanoparticle uptake mechanism and intracellular fate: U937 tumoral cells

Future applications of fluorescent nanoparticles could be live cells labelling agents or drug carriers and both require knowledge of nanoparticle entry route and intracellular fate. Given the temperature- and energy-dependence of NT_B700 uptake in U937 cells, we hypothesized that an endocytosis mechanism was responsible of their internalization. Furthermore, the images of NT_B700 nanoparticles inside cells (Fig. 2.1F) suggested that the intracellular fluorescence was contained in vesicles, likely endosomes, compatible with cell entry through one of the possible endocytic mechanisms. In order to study how NT_B700 NPs gain access into cells, we pre-incubated cells with some inhibitors of the main routes of endocytosis, before the addition of NPs. Based on what is reported in literature and according to the manufacturer's protocols, we titrated each pharmaceutical inhibitor (chlorpromazine, genistein, amiloride and nocodazole). Through a cell viability assay, we assessed the best concentration for each one on U937 cells, summarized in Table 2.1 (Fig. 2.5). NP uptake inhibition was measured only at short time, to avoid triggering the activation of other endocytic mechanisms to compensate the blockage of specific uptake pathways [7,41]. In the course of this type of experiments, it is also required to assess the cellular toxicity of each pharmacological inhibitor employed, as a quality step prior to their co-incubation with NPs [7]. Hence, we performed a cell viability assay through a PI staining after 2 h 30 min of exposure (by miming 30 min of pre-incubation with the inhibitor and 2h of co-incubation with both, inhibitor and NPs) to each different inhibitor, including the beforehand studied conditions of temperature and energy depletion with NaN_3. The flow cytometry results (Fig. 2.6A) showed the percentage of PI positive cells: this measurement highlighted the absence of a significant cell damage, ($\leq$ 10% cytotoxicity).

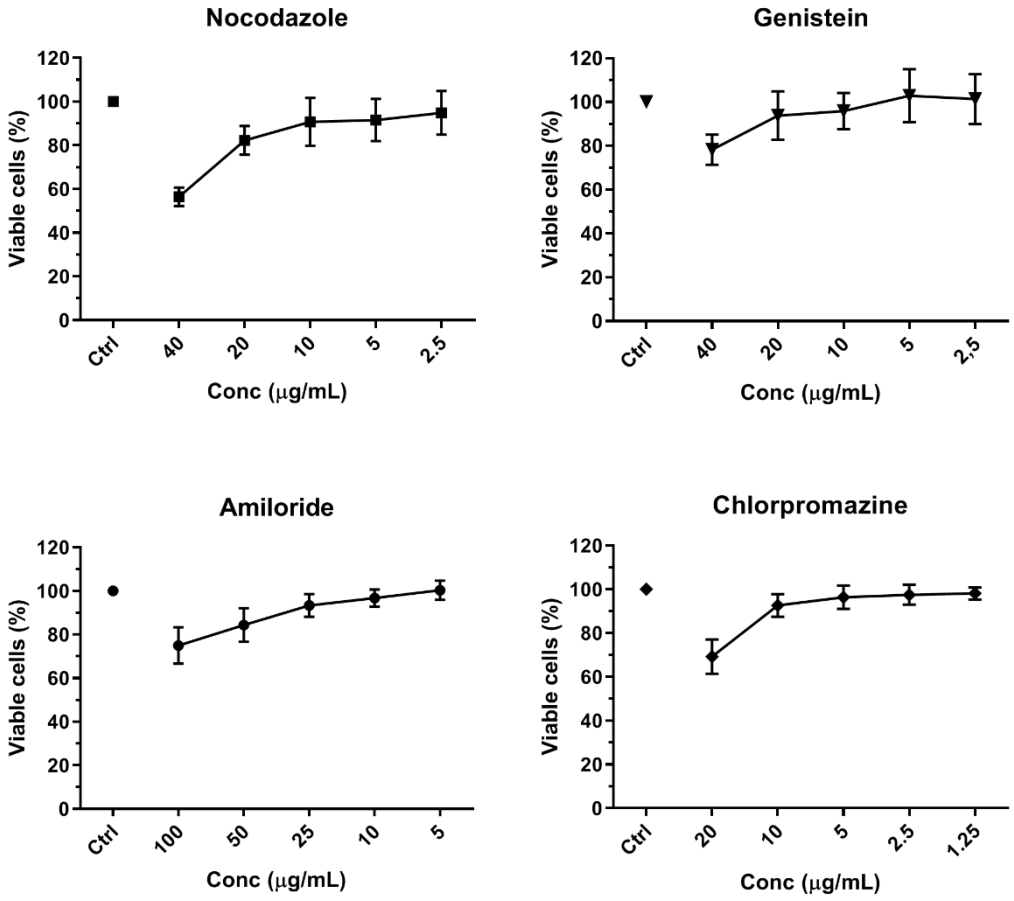

Fig. 2.5 Titration of the four pharmaceutical inhibitors on U937 cells to determine the best concentration for experimental use. Cells were treated for 2,5 h with different concentration of each inhibitors: Nocodazole (2.5, 5, 10, 20 40 µg/mL), Genistein (2.5, 5, 10, 20 40 µg/mL), Amiloride (5, 10, 25, 50, 100 µg/mL) and Chlorpromazine (1.25, 2.5, 5, 10, 20 µg/mL). Trypan Blue exclusion assay was employed to evaluate the toxicity of the inhibitors and decide the best concentration of use. The number of viable cells was normalized compared to control cells (untreated), which represent 100% of viability. The experiment was run in triplicate for each pharmaceutical inhibitor.

Pathway	Inhibitor	Conc.	Mechanism	References
Clathrin-mediated endocytosis	Chlorpromazine hydrochloride	5 µg/mL	AP2 inhibitor; blocks endosome recycling	[43]
Caveolae-mediated endocytosis	Genistein	20 µg/mL	Tyrosin-kinase inhibitor and blocks the recruitment of dynamin II, by interfering with lipid rafts	[7] [44]
Macropinocytosis	Amiloride	30 µg/mL	Na^+/H^+ exchanger pump inhibitor and prevents Rac1 and Cdc42 signaling	[43] [45]
Microtubules	Nocodazole	7.5 µg/mL	Binds to tubulin, blocking microtubule polymerization	[7] [43]

Table 2.1 Uptake pathways and inhibition conditions. The table shows the transport inhibitors selected for this study, their mechanism of action, pathways involved and condition of use.

Chlorpromazine is a cationic amphiphilic drug which interferes with clathrin-mediated endocytosis at multiple levels, as reported in Table 2.1 [43]. Genistein is a tyrosin-kinase inhibitor that blocks the recruitment of dynamin II and causes local disruption of actin filaments, by interfering with lipid rafts, and disturbs the caveolae-mediated endocytosis [7,43]. NT_B700 uptake and its inhibition was evaluated by measurement of intracellular fluorescence by flow cytometry and was compared to that for control cells, that had been exposed to NT_B700 in the absence of inhibiting drug (Fig. 2.6B). Results showed no significant reduction of NP uptake for either chlorpromazine and genistein, thus indicated that NT_B700 do not enter the cells *via* clathrin- and caveolae-mediated endocytosis. Similarly, we observed a lack of inhibition upon amiloride treatment, which is an inhibitor of macropinocytosis by blocking the Na^+/H^+ exchanger pump and the resulting acidification interferes with the cytosolic pH close to the cell membrane where macropinosomes form and blocks other signaling essential for macropinocytosis [42,44]. A statistically significant inhibition was instead observed for nocodazole treatment, which is a microtubule disruptor by blocking their polymerization. It is notably known that the cytoskeleton plays an important role in several cellular events, including endocytosis and trafficking of vesicles inside the cell [7]. Our results showed that NT_B700 enter the cells probably exploiting several routes of internalization, because no one of these investigated vias was more involved than the others, and once inside the cells, free or entrapped in vesicles, NPs are translocated along microtubule-depending shuttles. Among all

methods employed to study NP internalization, the use of pharmacological inhibitors is often chosen thanks to their fast action and ease of use. Nevertheless, inhibitors have shown several limits such as poor specificity, toxicity and many researchers reported that their efficacy could be highly cell line dependent [43-46].

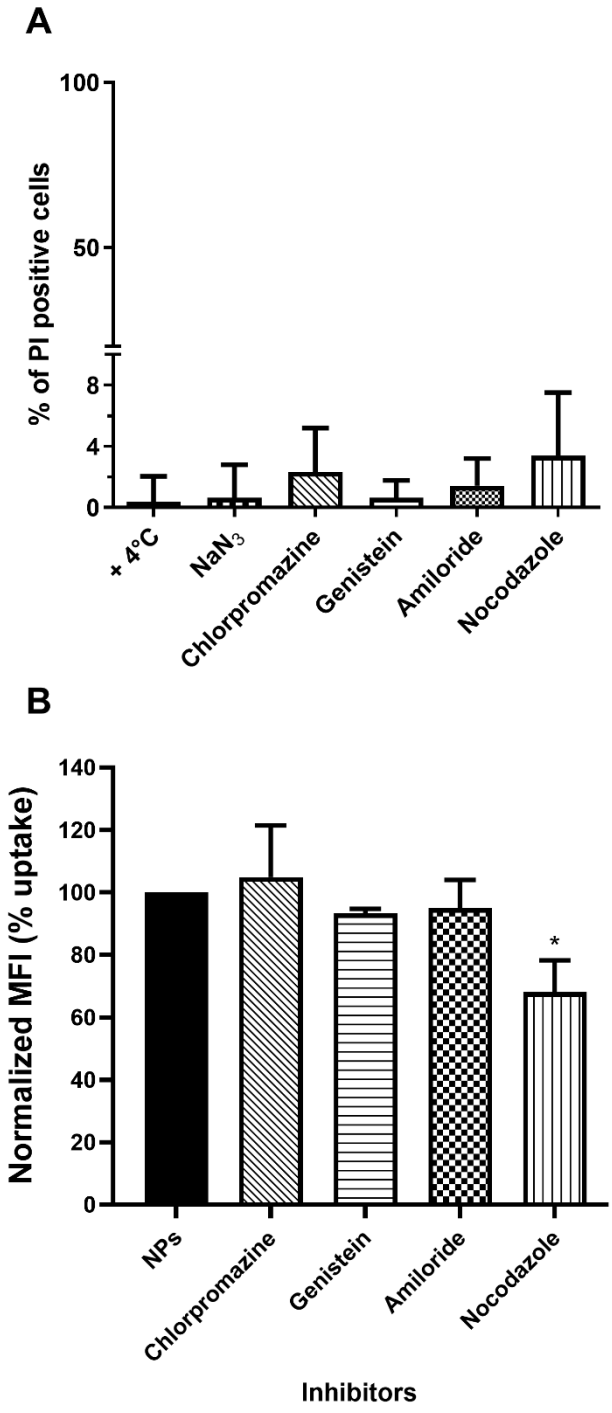

Fig. 2.6 Effect of pharmacological inhibitors on cell viability and NT_B700 endocytosis in U937 cells. (A) Cell viability assay performed through propidium iodide (PI) staining, analysed by flow cytometry, after 2 h 30 min of exposure to each one of the different inhibitors. Percentage of PI positive cells was calculated respect to control (untreated). (B) Effect of inhibitors on NT_B700 internalization in U937. Cells were pre-treated with each one of the inhibitors (chlorpromazine, genistein, amiloride, nocodazole) for 30 min, followed by 2 h of exposure to NPs, in the presence of the same inhibitor, then washed and analysed by flow cytometry. Normalized MFI (mean fluorescence intensity) was calculated compared to "NPs" which is reported as 100% uptake (cells incubated with NPs in normal condition, at 37°C without inhibitors). Mean values and sd of 2 independent replicas of 3 experiments. Asterisks denote a statistically significant difference (* = $p < 0.05$) between nocodazole and NPs. At least 10000 events were analysed by flow cytometry for each experimental condition.

After internalization *via* one or more of the endocytic pathways, nanoparticles are transported and trafficked along the endolysosomal network within plasma-membrane bounded compartments, vesicles, to reach their destination. These vesicles travel in complex trafficking patterns and it is a hard goal to completely detail the intracellular events that take place once nanoparticles are inside the cells [10,11]. Since lysosomes deal with the digestion of the foreign material taken up by the cells from outside, it's important to understand their involvement in NP uptake and management [47]. To confirm that NP reached lysosomes, we investigated whether nanoparticles colocalized with LysoTracker^{TM} green (LTG), a permeable dye which stains acidic compartments in live cells (i.e. lysosomes), by confocal microscopy. As shown in Fig. 2.7A, NT_B700 partially colocalized with these organelles, to indicate that NPs were internalized and trafficked to lysosomes.

Interestingly, we observed an almost complete colocalization with other important organelles, which have unique features and participate to numerous cell functions [48]: mitochondria. We stained U937, previously loaded with NPs, by using TMRE (tetramethylrhodamine ethyl ester perchlorate), which is a cell-permeant and cationic dye sequestered by active mitochondria. We performed a colocalization analysis, by using JACoP plugin in ImageJ [35], and Pearson's correlation coefficient (PCC) was used as a standard to measure colocalization between NT_B700 NPs fluorescence and fluorescence of LTG and TMRE, respectively. Histogram in Fig. 2.7B shows an almost complete colocalization of NPs with mitochondria, with a PCC value of about 0.91 ± sd. This behaviour is quite evident in the colocalization masks in which pixels with positive signals for both probes are shown in white. Since the observed marked involvement of mitochondria after NT_B700 internalization, we decided to further investigate the effect of NPs on these organelles, which also participate in the production and management of reactive oxygen species (ROS). After 1 h of incubation with NT_B700 we observed a substantial stability in ROS content (mainly H_2O_2), detected by CM-H_2DCFDA (DCF), whereas after 4 h, we could observe a moderate ROS increase, combined with a mild drop of mitochondrial membrane potential (MMP), this drop was further accentuated at 24 h and then rose again after 48 h, the last time of our analyses (Fig. 2.7C). Besides mitochondria status, DCF fluorescence informed us that H_2O_2 had turned approximately to the starting values. The contemporary evaluation of the contribute of O_2- to the ROS pool by MitoSOX is shown in Fig. 2.7D and depicted a scenario in which during the first phase of NP uptake and the concomitant mitochondria internalization, the main produced component of ROS was O_2-. After 4 h, this oxygen radical significantly dropped, highlighting an increased level of hydrogen

peroxide. Superoxide and/or hydrogen peroxide can be generated from the major sites at high rates both in the mitochondrial matrix and on the cytosolic side of the mitochondrial inner membrane [49]. Therefore, U937 cells exposed to NT_B700 NPs (at this concentration) showed to have antioxidant defences capable of overcoming oxidative stress and recovering the redox balance, minimizing cytotoxicity (as demonstrated by PI test). Usually, the amount of ROS generated, and the related oxidative stress, are correlated with the nanomaterial concentration to which cells are exposed. Generally, the mitochondrial membrane hyperpolarization is associated with ROS production, although, a part of literature about NP uptake reveal a decrease in ROS production, as effect of the size of foreign material internalized by the cells [50].

LTG (specific for lysosome network) and MDC (labelling acidic endosomes, lysosomes, and, particularly, late-stage autophagosomes) demonstrated an almost complementary trend, during the time-course investigated (Fig. 2.7C). Of note, data collected after 48 h for these two parameters, confirmed a restoration of a balanced intracellular status (data not shown). Furthermore, the cross-evaluation of these data, allowed us to ascribe the increase of MDC fluorescence to acidic endosomes, and late-stage autophagosomes, since LTG fluorescence did not peak, but it reached a plateau already at 24 h, lasting up to 48 h. Such scenario suggested the involvement of the secretory/autophagic pathway, including the exosome release. In fact, exosome biogenesis occurs during the process of endosomal maturation. This process starts with endocytosis and ends with the degradation of the endosomal content by fusion with lysosomes. However, during endosomal maturation, endosomes no longer fuse with small endocytic vesicles. These multivesicular endosomes are also called late endosomes or multivesicular bodies (MVB). At this point, intraluminal vesicles can be degraded by lysosomes or released to the extracellular environment as exosomes [51]. NP release in the extracellular medium was analysed in tumour myeloid cells, whereas specific step of the process was investigated on normal counterparts: peripheral blood mononuclear cells (PBMCs) (see next paragraphs).

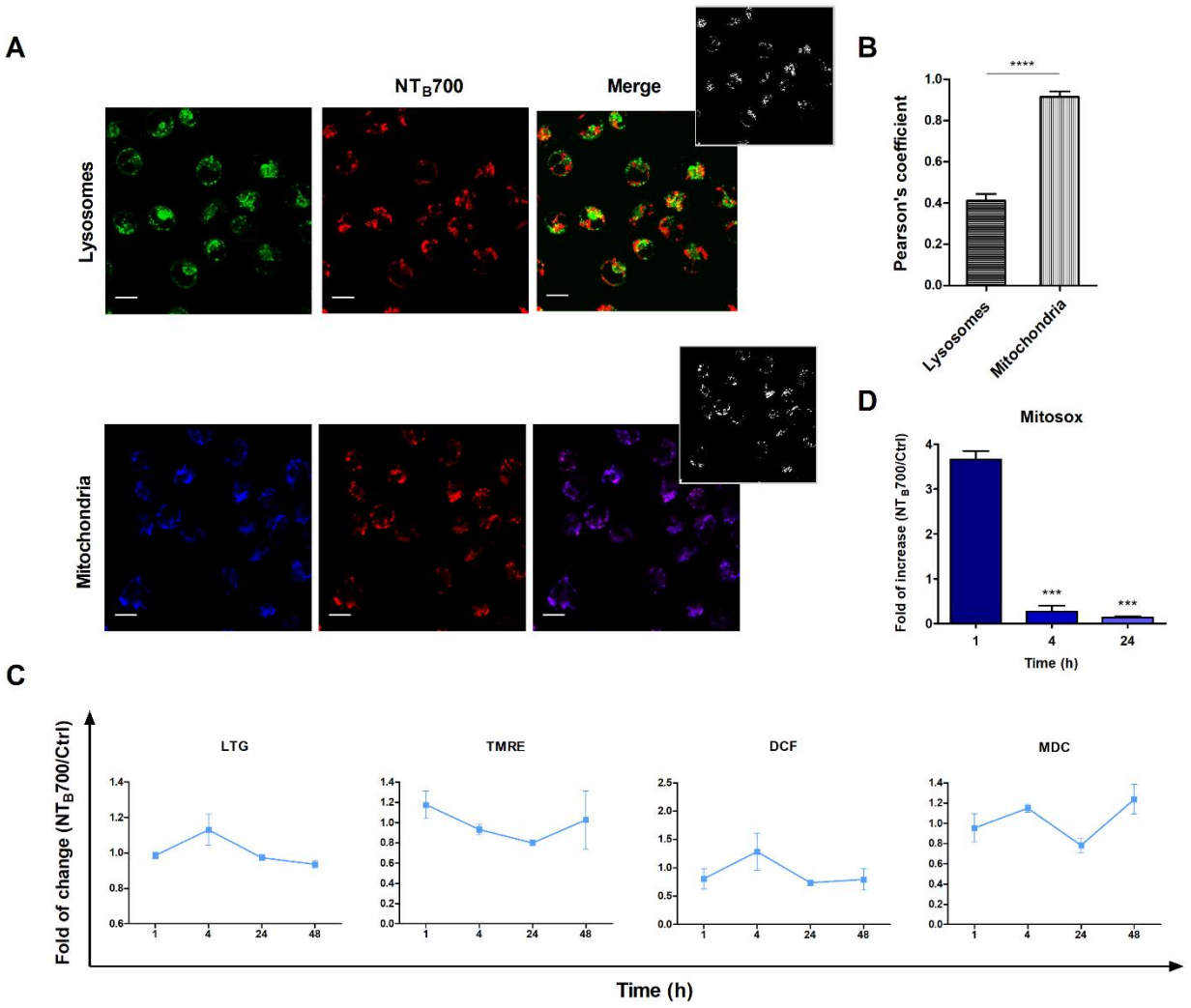

Fig. 2.7 Lysosomes and mitochondria involvement in NT_B700 uptake in U937 cells. (A) Representative confocal images of lysosomal (above) and mitochondria (below) involvement in U937 cells incubated for 1 h at 37°C with NT_B700 (64 µg/mL) and then stained with LTG and TMRE. Figure shows LTG (green), TMRE (blue), NT_B700 nanoparticles (red) and merged images (on the right); yellow and violet indicate colocalization. Scale bars: 10 µm. Insert: binary version of merged images. The colocalization mask was generated by Image J software to show colocalization pixel. (B) Pearson's colocalization coefficient (PCC) of LTG and TMRE with NT_B700 in U937 cells. Pearson's coefficients were derived from three completely independent experiments with >10 fields per experiment contributing to the cumulative result. Each value is expressed as PCC ± sd; asterisks denote a statistically significant difference (**** = $p < 0.0001$) between strains. (C) Flow cytometry analysis of lysosomes (LTG), mitochondria (MTG), ROS production (DCF) and autophagolysosomes formation (MDC) expressed as fold of change calculated as the ratio between cells incubated with NPs (64 µg/mL) and control cells. 1 value indicates no differences between treated and untreated. (D) Flow cytometry analysis of O_2- production (MitoSOX) expressed as fold of change calculated as the ratio between cells incubated with NPs (64 µg/mL) and control cells at different time points (1, 4 and 24 h). Asterisks denote a statistically significant difference (*** = $p < 0.001$) between strains. At least 10000 events were analysed by flow cytometry for each experimental condition.

Investigation of NT_B700 nanoparticle uptake mechanism and intracellular fate: peripheral blood mononuclear cells (PBMCs)

Working with peripheral blood mononuclear cells (PBMCs) gives the great advantage to perform a simultaneous analysis of NP effects on several important immune cells such as B-cells, T-cells, monocytes and natural killer (NK) cells. Furthermore, studying nanomaterial behaviour in these types of cells is crucial since they will interact with NPs once introduced into the blood torrent [21]. We investigated NT_B700 behaviour in PBMC, based on results previously obtained on tumoral U937 cell line. Firstly, we incubated PBMCs with NT_B700 (64 µg/mL, as best beforehand condition) for different times, from 1 h to 48 h. We observed that fluorescence (=internalized NPs) increased in a time-dependent manner, both for lymphocytes and monocytes (gating strategy based on morphological features on FSC vs. SSC dot plot depicted in Fig. 2.8), as for U937 cells (Fig. 2.9A), even if for lymphocytes was not so evident because of the lower fluorescence signal. NPs are foreign agents and monocytes, which are described as "professional" phagocytic cells, are expected to directly participate in NP internalization, degradation and removal from bloodstream and tissues, thanks to their immune activity [36,52]. As expected, monocytes showed, indeed, the strongest fluorescent signal increase, therefore a much larger NP entry (Fig. 2.9A). Interestingly, after 48 h of incubation with NPs, both lymphocyte and monocyte populations showed a decreased fluorescence. The maximum NPs uptake was at 24 h and then, after a plateau, the exocytic pathway started to overbear the endocytic one and NPs were released from the cells. The various cell types were identified by staining with monoclonal antibodies, specific for PBMC subpopulations: CD5 for T lymphocytes, CD19 for B lymphocytes, CD16 for NK cells and CD14 for monocytes [53]. Among lymphocyte subpopulations, NK cells (CD16+) showed the highest NP internalization (Fig. 2.9B). Confocal analysis confirmed NP internalization in PBMC cells (Fig. 2.9C), and after 4 h of incubation we didn't observed different intensity of fluorescence (data not shown). Given that each NP has its own characteristic and each cell type reacts differently to external influences, interactions between NPs and one cell type cannot be generalized. Studying immunomodulatory effects of engineered NPs is challenging and of high importance [54].

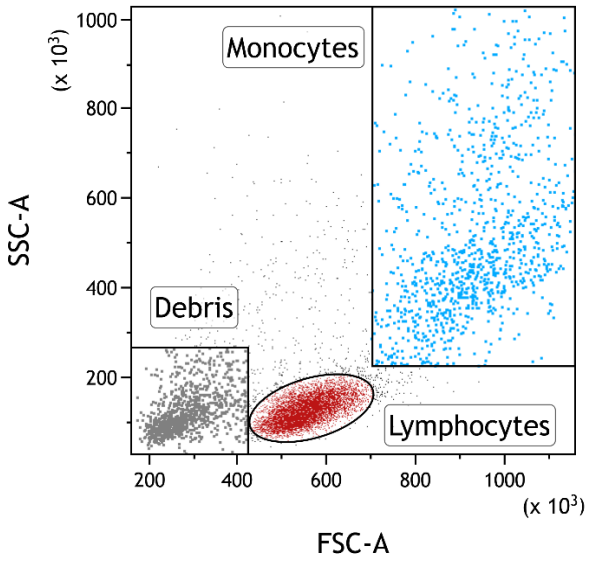

Fig. 2.8 Gating strategy for subsequent analysis on PBMC. Dot plot FSC vs. SSC presenting gating strategy for PBMC to evaluate NT_B700 effect on lymphocyte (red) and monocyte (light blue) populations.

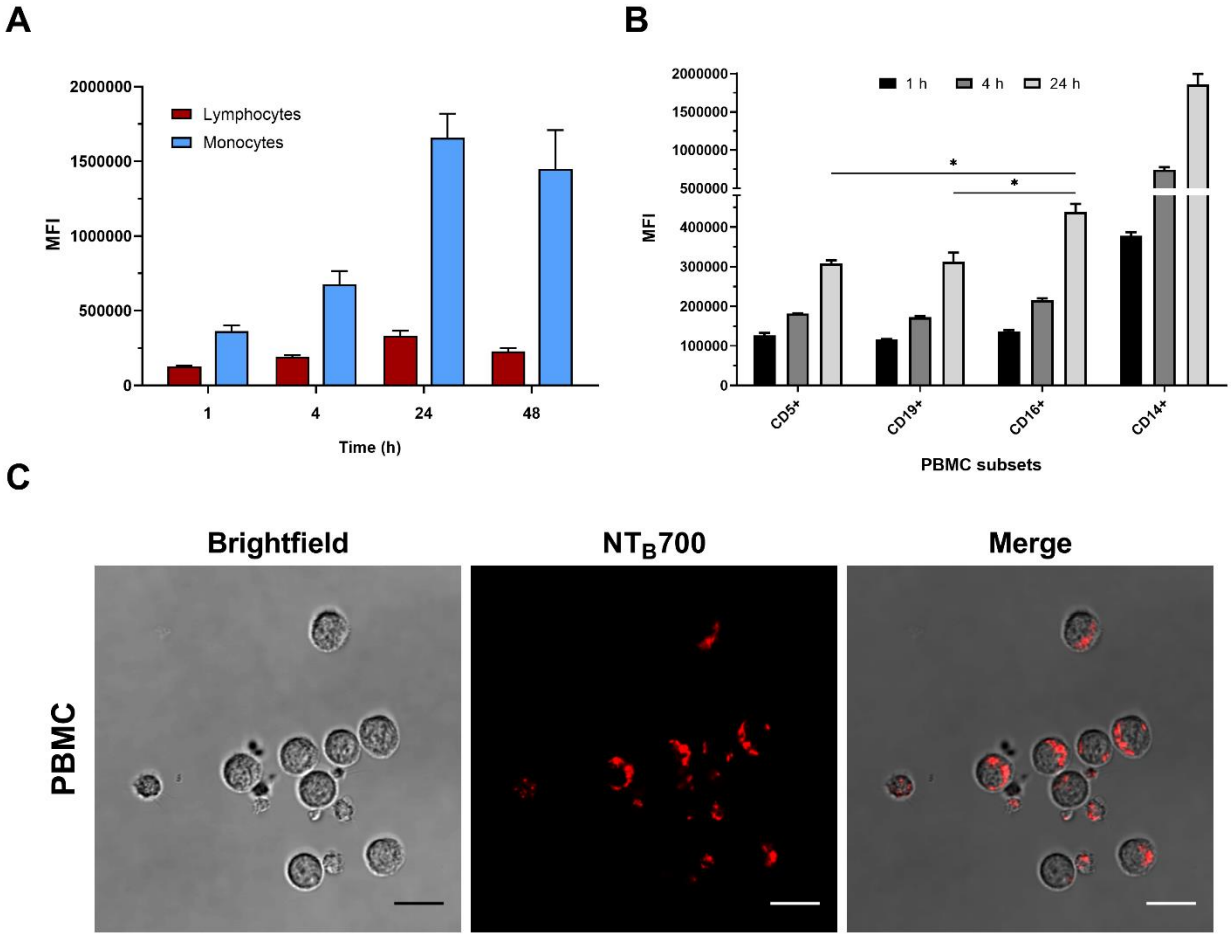

Fig. 2.9 Kinetics of NT_B700 uptake and confocal images of NP internalized in peripheral blood mononuclear cells (PBMCs). (A) PBMCs were incubated at 37°C with 64 µg/mL NT_B700 at different time points (1, 4, 24 and 48 h). Lymphocyte (red) and monocyte (light blue) populations were selected through a gating strategy on FSC vs. SSC dot plot. Mean Fluorescence Intensity (MFI) from the flow cytometry histograms is shown as a function of time in hours. (B) PBMCs were incubated at 37°C with 64 µg/mL NT_B700 at different time points (1, 4 and 24 h), washed and then stained with several mAbs to identify four PBMC subsets: CD5+ (T lymphocytes), CD19+ (B lymphocytes), CD16+ (NK cells) and CD14+ (monocytes). Asterisks denote a statistically significant difference (* = $p < 0.05$) between 24 h strains. (C) Light and fluorescent images of PBMCs incubated for 1 h at 37°C with NT_B700 nanoparticles (64 µg/mL). Representative confocal images of NT_B700 nanoparticles uptake in PBMCs: brightfield (on the left), fluorescent nanoparticles inside cells (in the middle) and merged images (on the right). NT_B700 in red. Scale bar = 10 µm. At least 10000 events were analysed by flow cytometry for each experimental condition. Error bars represent sd.

Among the different PBMC subsets we observed a higher amount of NPs and a contemporary increase autophagosome formation/single cell in monocytes (Fig. 2.10B). Monodansylcadaverine (MDC) staining, a specific autophagolysosome marker, was used to investigate the involvement of the autophagic machinery in NT_B700 uptake to investigate whether NPs/cell incubation may trigger autophagy. Wu et al. observed that induction of autophagy by Superparamagnetic Iron Oxide Nanoparticles (SPIONs) had an important role in the survival and function of human monocyte cells, as they form the first line of defence in the body's immune system and the door for NPs into the human body [55]. In monocytes we also had a contemporary decrease of MMP during time and a higher production of ROS compared to lymphocytes (Fig. 2.10B and 2.10C), more evident at 4 h of incubation with NT_B700. Furthermore, the ROS decrease after 4 h may depend on the clearance of damaged mitochondria, where NPs colocalized. These findings correlate with those ones from TMRE and LTG fluorescence and suggested an ongoing mitophagic pathway (that further investigations will clarify). In Fig. 2.11 a representative sequence of contour plots shows the simultaneously evaluation of ROS level (DCF), and MMP (TMRE), on PBMCs. High ROS level, low MMP and NP uptake do not direct cells to death, based on physical parameters in FSC vs SSC contour plots (violet events). On the contrary, the orange events, lacking DCF fluorescence, with low MMP and absence of NP fluorescence, are mainly located in typical area of shrunken apoptotic cells. The figure highlights different topics emerged in this study: 1) NP cellular uptake induces, at short times (1-4 h) an increase in H_2O_2 content; 2) H_2O_2 has both beneficial and negative effects; 3) NP uptake and H_2O_2 increase are contemporary to a

slight decrease of MMP that are, all, no prodromal of cell death; 4) all these features are evident on myeloid cells, whereas lymphocytes are almost unaltered.

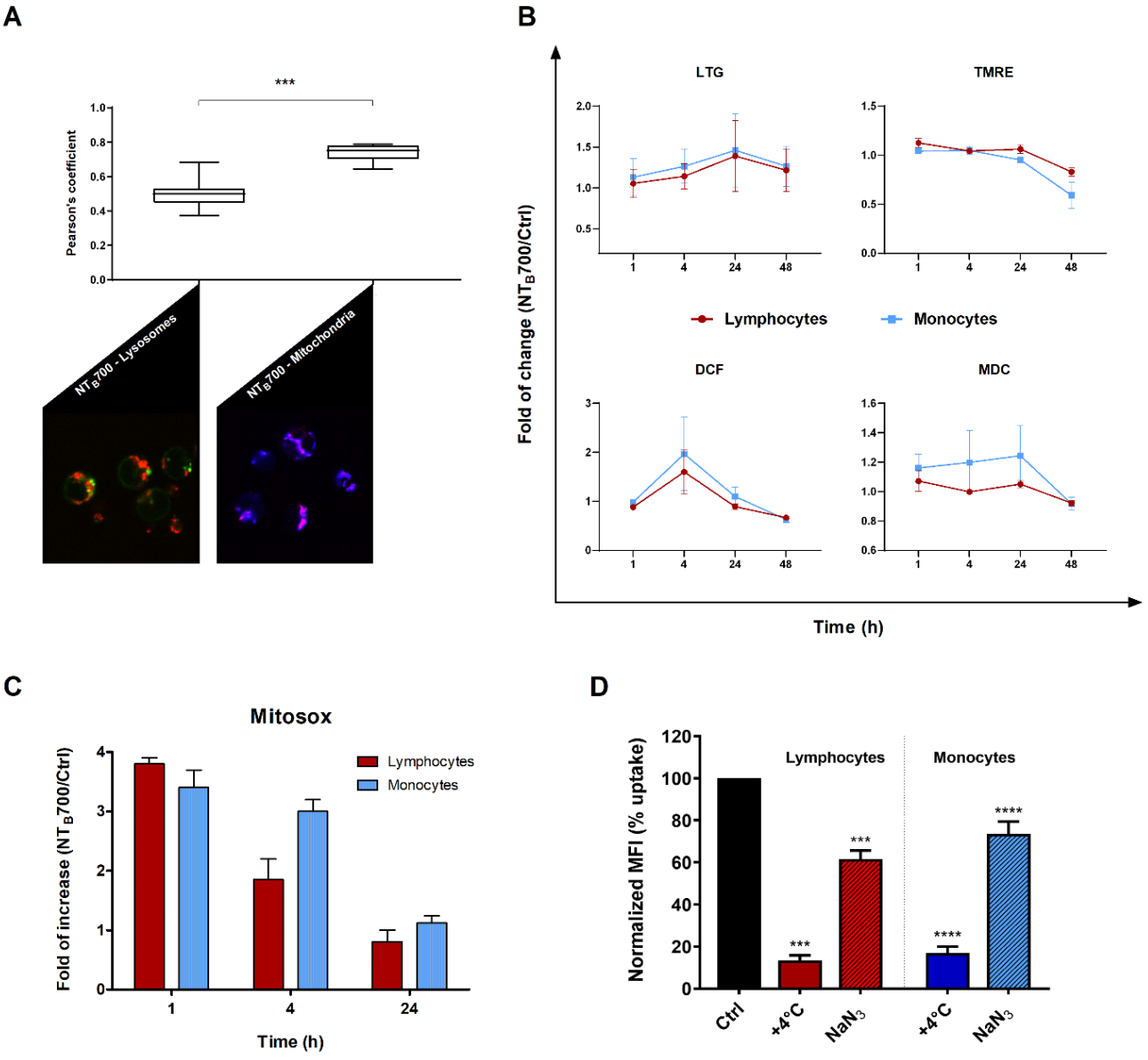

Fig. 2.10 Assessment of lysosomes and mitochondria involvement in NT_B700 uptake in PBMCs. (A) Pearson's colocalization coefficient (PCC) of lysosomes (LTG) and mitochondria (TMRE) with NT_B700 in PBMC cells. Pearson's coefficients were derived from three completely independent experiments with >10 fields per experiment contributing to the cumulative result. Each value is expressed as PCC ± sd; (*** = $p < 0.001$). Below representative confocal images of lysosome (left) and mitochondria (right) colocalization in PBMC cells incubated for 1 h at 37°C with NT_B700 nanoparticles (64 µg/mL) and then stained with LTG and TMRE. Figure shows LTG (green), TMRE (blue), NT_B700 nanoparticles (red) and, respectively, orange and violet indicate colocalization. (B) Flow cytometry analysis of PBMCs incubated at 37°C with 64 µg/mL NT_B700 at different time points (1, 4, 24 and 48 h) washed and then stained LTG, TMRE, DCF and MDC. Fold of change, calculated as the ratio between cells incubated with NPs and control cells (w/o NPs), from the flow cytometry histograms is shown as a function of time in hours. 1 value indicates no differences between treated and untreated. (C) Flow cytometry analysis of O_2- production (MitoSOX) expressed as fold of change calculated as the ratio between cells incubated with NPs (64 µg/mL) and control cells at different time points (1, 4 and 24 h). Mean values and sd of 2 independent replicas of 3 experiments. Asterisks denote a statistically significant difference (*** = $p < 0.001$) between strains. (D) Effect of temperature and energy depletion on NT_B700 nanoparticle internalization in PBMC. Cells were incubated with NT_B700 (64 µg/mL) under different condition: control (NPs incubated at 37°C), +4°C and sodium azide (NaN_3). The percentage of nanoparticle uptake was measured by MFI, determined through flow cytometry (2 independent replicas of 3 experiments), normalized with NP MFI values in normal condition at 37°C (Ctrl is 100% uptake). In red (on the left) lymphocyte data and in blue/light blue (on the right) monocyte data. Asterisks denote a statistically significant difference (*** = $p < 0.001$; **** = $p < 0.001$) compared to control. At least 10000 events were analysed by flow cytometry for each experimental condition.

As previously investigated on U937, we observed a different amount of colocalization of NPs with two important organelles, such as lysosomes and mitochondria, in PBMCs (Fig. 2.10A). The colocalization was higher with mitochondria but not as much as we stated for U937 (PCC value of about 0.74 ± sd), where we showed an almost complete colocalization with a PCC value near 1. The pharmacological inhibitors we used for U937 cells, to investigate NP endocytosis, did not give significant results for PBMC (data not shown), maybe because the heterogeneity of the populations made this analysis more complicated. On the contrary, the effect of temperature and energy depletion on NT_B700 entry in PBMC gave the results we guessed: a strong inhibition depending on temperature and a lower decrease in internalized fluorescence concerning NaN_3 treatment (Fig. 2.10D). Our data indicated that NT_B700 nanoparticles in myeloid and lymphoid cells are internalized by an active energy-dependent process, as for the monocyte immortalized tumour cell line beforehand investigated.

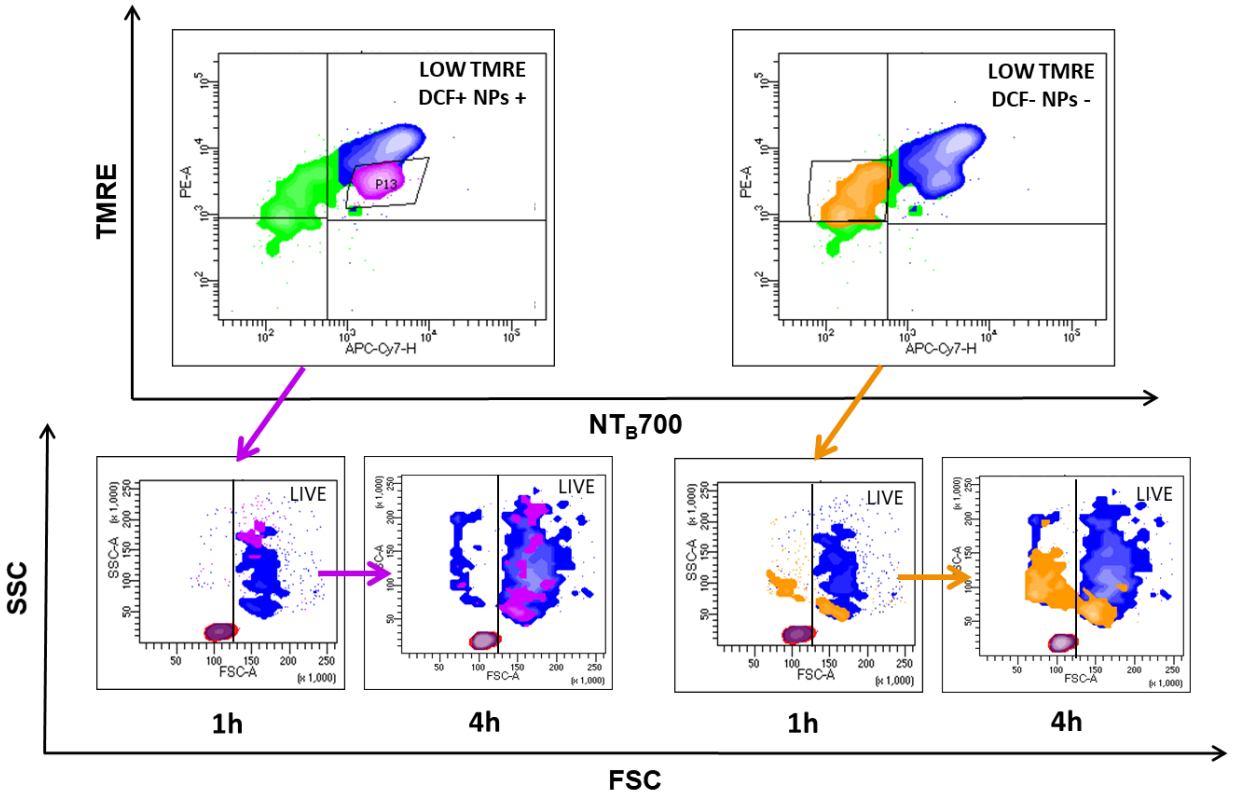

Fig. 2.11 Confirmation of prevalent cell viability in normal myeloid cells, after NP uptake. Sequences of representative contour plots of PBMC stained with DCF and TMRE after 1h and 4h of NP uptake. (on the left) High ROS level (DCF+), low MMP (LOW TMRE) and NP uptake (NPs+) do not direct cells to death, as FSC vs SCC dot plots illustrate below (violet events). On the contrary, the orange events (on the right), lacking of DCF (DCF-), low MMP (LOW TMRE) and no NPs (NPs-) are located in typical characteristic shrunken apoptotic cells, in dot plots of physical features, and this may depend on the clearance of damaged mitochondria. Lymphocytes are pictured in red, while monocytes in blue.

NT_B700 nanoparticle release: from tumoral to normal counterparts

Compared to the investigations of NP endocytic pathways, relatively little effort has been done to study NP excretion from cells. How NPs evolve inside the cells before the extrusion is less discussed, although such information would provide fundamental guidance in their design for practical drug/imaging applications to evaluate their biosafety [13,32]. NPs may be excreted from cells due to a dynamic intracellular transport and trafficking process, through vesicles, or directly translocated from the cytoplasm across cell membrane into the extracellular space, which is much less favoured than vesicles-mediated exocytosis [10]. It is known that both endo- and exocytosis processes occur simultaneously. As suggested by Sakhtianchi et al., the most common approach to study NP release is to seed cells, previously incubated with NPs, with fresh medium (NP-free) [32]. U937 were exposed to NT_B700 (64 µg/mL) for 1 h, harvested and then seeded again with NP-free medium. The supernatants removed after 1 h of incubation and after 24 h of incubation with NP-free medium were then analysed by flow cytometry, following the addition of Dako CytoCount™ beads as internal control (Fig. 2.12A) [56]. Results showed that there is always an amount of extracellular vesicles (EVs) secreted by the cells (without treatment) and also in medium without cells, as it is well known FBS contains a significant amount of EVs [57]. Cells treated with NT_B700 and then exposed to NP-free medium had higher number of EVs compared to control cells, maybe because the presence of NPs inside the cells stimulated the exocytic process. The analysis of the fluorescence of the extruded vesicles confirmed that NPs were released from cells after 24 h (Fig. 2.12B). The fluorescence of NT_B700 released from U937 cells was also investigated and confirmed with another technique. The supernatants after centrifugation, once harvested the cells, were analysed with spectrofluorometer. To quantify the NPs released by cells in culture medium, we considered the area of each sample, that is characteristic of these NPs, subtracted the area value of buffered medium and interpolated it in the calibration curve to obtain NP concentrations at different time points (Fig. 2.12C). At the same time, the collected cells were analysed by flow cytometry to investigate the residual fluorescence within them and it was evident a clear reduction in NT_B700 fluorescence (Fig. 2.12D).

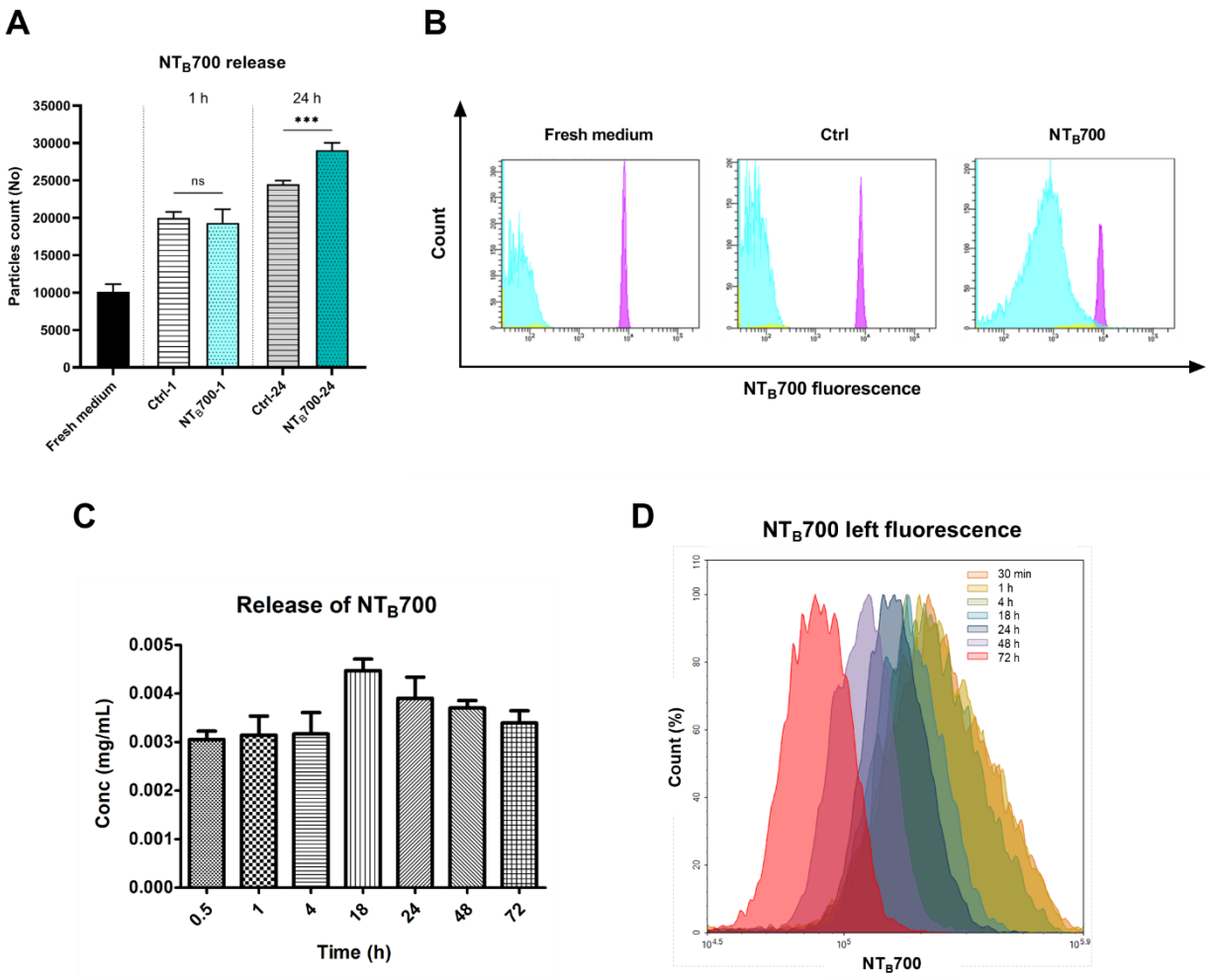

Fig. 2.12 NT_B700 release studies in U937. U937 were incubated with NT_B700 (64 µg/mL) for 1 h, harvested and then seeded again with fresh medium (NP-free). The supernatants of all conditions (treatment of 1 h and 24 h after incubation in fresh medium following 1 h of NT_B700 treatment) have been analysed by flow cytometry. (A) Histogram shows the quantification of extracellular vesicles (EVs) counted by using Dako CytoCount™ beads in fresh medium and released by the cells in 1 h of treatment or after 24 h of incubation in fresh medium following 1 h of NT_B700 treatment or control cells, in the same experimental conditions. Asterisks denote a statistically significant difference (*** = $p < 0.001$) between 24 h strains. (B) Flow cytometry histograms showing the fluorescence of particles in NT_B700 channel (violet peak represents Dako Cyto Count™ beads, light blue peak represents particles released based on gates in FSC vs SSC dot plot). Cells incubated with NPs presented a marked peak in NT_B700 fluorescence channel (histogram on the right) compared to fresh medium and control cells (without NPs), which showed the ability of cells to excrete NPs after their internalization. (C) Histogram shows NP release in fresh medium (NP-free), after 1 h of incubation with NT_B700 (64 µg/mL), quantified by spectrofluorometer. The whole area of the supernatants at several time points (from 30 min to 72 h) was calculated and interpolated in the calibration curve to obtain the concentration of NP in the mediums. (D) Flow cytometry histogram overlay for cells treated for 1 h with NT_B700 (64 µg/mL) and incubated in fresh medium (NP-free) for the indicated time points. (30 min-72 h) to investigate the residual NP fluorescence within them. At least 50000 events were analysed by flow cytometry for each experimental condition for (A) and (B) flow cytometer analysis; at least 10000 events for each experimental condition of (D).

Also PBMC after NT_B700 exposure for different time points (1, 4 and 24 h), were seeded with fresh medium to investigate more in deep NP release on normal counterparts Media were stained both with Dako CytoCount™ and CD63 monoclonal antibody, a typical exosome marker to study the EVs secreted by the cells during the incubation in fresh medium (w/o NPs) [34]. Results in Fig. 2.13B showed that NT_B700 were partially released partially by the endosomal route (CD63+), visually evident in contour plots in Fig. 2.13A, and directly into the extracellular space (EVs with only NT_B700 fluorescence). Furthermore, the confocal images colocalization studies between NT_B700 and LTG (lysosomal dye) of PBMCs loaded with NPs and then incubated in fresh medium, indicated that the colocalization varied during time. After 24 h the colocalization between NT_B700 and lysosomes increased compared to early time points (Fig. 2.13C), suggesting that NPs are taken up into endocytic compartments, which are firstly transported and only later fused with lysosomal compartments. Hsiao et al. and Al-Rawi et al. reported similar kinetics in their studies [17,58]. These results indicated that also the lysosomal exocytosis was involved in NP extrusion from cells. In terms of biosafety these data indicated the ability of cells (both tumoral and normal) to remove NPs once internalized. It has a considerably importance in the perspective of NT_B700 future employments, such as imaging or drug delivery, in particular for *in vivo* applications.

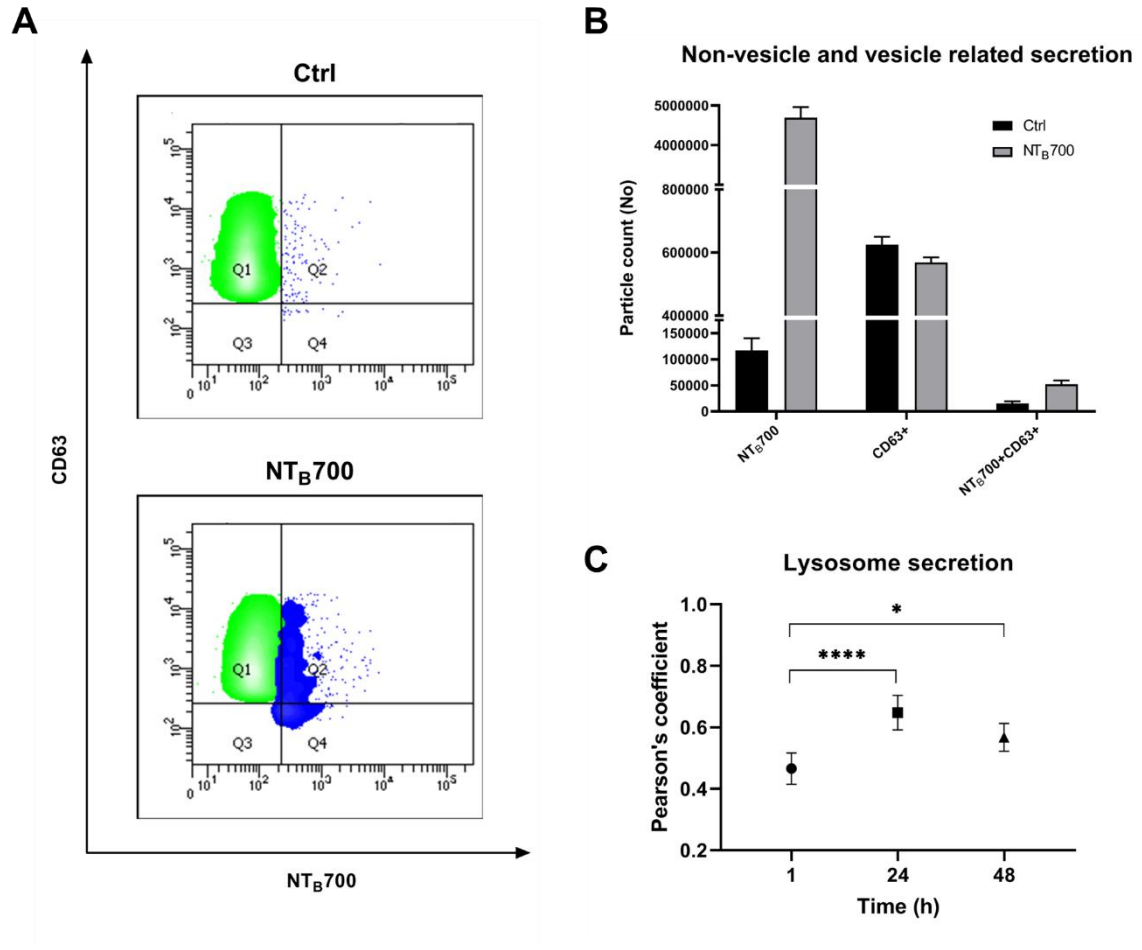

Fig. 2.13 NT_B700 release studies in PBMC. (A) Flow cytometry contour plots (fluorescence of particles in NT_B700 channel vs. CD63 fluorescence) of supernatants of control (above) and NP-treated cells (below) after 24 h in fresh medium, presenting in green CD63+ particles and in blue NT_B700+ particles. (B) Non-vesicle and vesicle related secretion. PBMCs were incubated with NT_B700 (64 µg/mL) for 1 h, harvested and then seeded again with fresh medium (NP-free). The supernatants have been analysed by flow cytometry. Histogram shows the quantification of extracellular vesicles (EVs) counted by using Dako CytoCount™ beads and CD63+ particles released by the cells after 24 h of incubation in fresh medium following 1 h of NT_B700 treatment or control cells in the same experimental conditions w/o NPs. (C) Pearson's colocalization coefficient (PCC) of LTG with NT_B700 in PBMC varying during time to investigate lysosome particle secretion. Pearson's coefficients were derived from three completely independent experiments with >10 fields per experiment contributing to the cumulative result. Each value is expressed as PCC ± sd; Asterisks denote a statistically significant difference (* = $p < 0.5$, **** = $p < 0.0001$) between strains. At least 50000 events were analysed by flow cytometry for each experimental condition.

References

[1] S. E. McNeil, "Nanotechnology for the biologist," *J. Leukoc. Biol.*, vol. 78, no. 3, pp. 585–594, Sep. 2005, doi: 10.1189/jlb.0205074.

[2] T. Nagamune, "Biomolecular engineering for nanobio/bionanotechnology," *Nano Convergence*, vol. 4, no. 1. Korea Nano Technology Research Society, p. 9, Dec. 01, 2017, doi: 10.1186/s40580-017-0103-4.

[3] A. Mahapatro and D. K. Singh, "Biodegradable nanoparticles are excellent vehicle for site directed in-vivo delivery of drugs and vaccines.," *Journal of nanobiotechnology*, vol. 9. BioMed Central, p. 55, 2011, doi: 10.1186/1477-3155-9-55.

[4] P. Foroozandeh and A. A. Aziz, "Insight into Cellular Uptake and Intracellular Trafficking of Nanoparticles," *Nanoscale Research Letters*, vol. 13, no. 1. Springer New York LLC, pp. 1–12, Oct. 25, 2018, doi: 10.1186/s11671-018-2728-6.

[5] C. Saraiva, C. Praça, R. Ferreira, T. Santos, L. Ferreira, and L. Bernardino, "Nanoparticle-mediated brain drug delivery: Overcoming blood-brain barrier to treat neurodegenerative diseases," *Journal of Controlled Release*, vol. 235. Elsevier B.V., pp. 34–47, Aug. 10, 2016, doi: 10.1016/j.jconrel.2016.05.044.

[6] Y. Luo, H. Yang, Y. F. Zhou, and B. Hu, "Dual and multi-targeted nanoparticles for site-specific brain drug delivery," *Journal of controlled release : official journal of the Controlled Release Society*, vol. 317. NLM (Medline), pp. 195–215, Jan. 10, 2020, doi: 10.1016/j.jconrel.2019.11.037.

[7] T. dos Santos, J. Varela, I. Lynch, A. Salvati, and K. A. Dawson, "Effects of Transport Inhibitors on the Cellular Uptake of Carboxylated Polystyrene Nanoparticles in Different Cell Lines," *PLoS One*, vol. 6, no. 9, p. e24438, Sep. 2011, doi: 10.1371/journal.pone.0024438.

[8] J. P. Peñaloza *et al.*, "Intracellular trafficking and cellular uptake mechanism of PHBV nanoparticles for targeted delivery in epithelial cell lines," *J. Nanobiotechnology*, vol. 15, no. 1, p. 1, Jan. 2017, doi: 10.1186/s12951-016-0241-6.

[9] X. Liu *et al.*, "Size Dependent Cellular Uptake of Rod-like Bionanoparticles with Different Aspect Ratios," *Sci. Rep.*, vol. 6, no. 1, pp. 1–10, Apr. 2016, doi: 10.1038/srep24567.

[10] N. D. Donahue, H. Acar, and S. Wilhelm, "Concepts of nanoparticle cellular uptake, intracellular trafficking, and kinetics in nanomedicine," *Advanced Drug Delivery Reviews*, vol. 143. Elsevier B.V., pp. 68–96, Mar. 15, 2019, doi: 10.1016/j.addr.2019.04.008.

[11] A. Panariti, G. Miserocchi, and I. Rivolta, "The effect of nanoparticle uptake on cellular behavior: Disrupting or enabling functions?," *Nanotechnology, Science and Applications*, vol. 5, no. 1. Dove Press, pp. 87–100, 2012, doi: 10.2147/NSA.S25515.

[12] L. Kou, J. Sun, Y. Zhai, and Z. He, "The endocytosis and intracellular fate of nanomedicines: Implication for rational design," *Asian J. Pharm. Sci.*, vol. 8, no. 1, pp. 1–10, Feb. 2013, doi: 10.1016/j.ajps.2013.07.001.

[13] N. Oh and J. H. Park, "Endocytosis and exocytosis of nanoparticles in mammalian cells," *International Journal of Nanomedicine*, vol. 9, no. SUPPL.1. Dove Medical Press Ltd., pp. 51–63, May 06, 2014, doi: 10.2147/IJN.S26592.

[14] Z. Chu, Y. Huang, Q. Tao, and Q. Li, "Cellular uptake, evolution, and excretion of silica nanoparticles in human cells," *Nanoscale*, vol. 3, no. 8, pp. 3291–3299, 2011, doi: 10.1039/c1nr10499c.

[15] J. Blechinger, A. T. Bauer, A. A. Torrano, C. Gorzelanny, C. Bräuchle, and S. W. Schneider, "Uptake kinetics and nanotoxicity of silica nanoparticles are cell type dependent," *Small*, vol. 9, no. 23, pp. 3970–3980, Dec. 2013, doi: 10.1002/smll.201301004.

[16] D. Sriramulu, E. L. Reed, M. Annamalai, T. V. Venkatesan, and S. Valiyaveettil, "Synthesis and Characterization of Superhydrophobic, Self-cleaning NIR-reflective Silica Nanoparticles," *Sci. Rep.*, vol. 6, no. 1, pp. 1–10, Nov. 2016, doi: 10.1038/srep35993.

[17] H. A. Hsiao I-L, Gramatke AM, Joksimovic R, Sokolowski M, Gradzielski M, "Size and Cell Type Dependent Uptake of Silica Nanoparticles," *J. Nanomed. Nanotechnol.*, vol. 05, no. 06, 2014, doi: 10.4172/2157-7439.1000248.

[18] C. Pellegrino *et al.*, "Multiple Dye Doped Core-Shell Silica Nanoparticles: Outstanding Stability and Signal Intensity Exploiting FRET Phenomenon for Biomedical Applications," *J. Nanomater. Mol. Nanotechnol.*, vol. s6, pp. 6–11, 2018, doi: 10.4172/2324-8777.s6-003.

[19] J. V. Jokerst, T. Lobovkina, R. N. Zare, and S. S. Gambhir, "Nanoparticle PEGylation for imaging and therapy," *Nanomedicine*, vol. 6, no. 4. NIH Public Access, pp. 715–728, Jun. 2011, doi: 10.2217/nnm.11.19.

[20] R. M. Zucker, J. Ortenzio, L. L. Degn, J. M. Lerner, and W. K. Boyes, "Biophysical comparison of four silver nanoparticles coatings using microscopy, hyperspectral imaging and flow cytometry," *PLoS One*, vol. 14, no. 7, p. e0219078, Jul. 2019, doi: 10.1371/journal.pone.0219078.

[21] G. G. De *et al.*, "Interaction of Nanoparticles with Blood Components and Associated Pathophysiological Effects Provisional chapter Interaction of Nanoparticles with Blood Components and Associated Pathophysiological Effects," 2016, doi: 10.5772/intechopen.69386.

[22] A. Böyum, "Isolation of leucocytes from human blood. A two-phase system for removal of red cells with methylcellulose as erythrocyte-aggregating agent.," *Scand. J. Clin. Lab. Investig. Suppl.*, vol. 97, pp. 9–29, 1968.

[23] H. Suzuki, T. Toyooka, and Y. Ibuki, "Simple and easy method to evaluate uptake potential of nanoparticles in mammalian cells using a flow cytometric light scatter analysis," *Environ. Sci. Technol.*, vol. 41, no. 8, pp. 3018–3024, Apr. 2007, doi: 10.1021/es0625632.

[24] W. Strober, "Trypan Blue Exclusion Test of Cell Viability," *Curr. Protoc. Immunol.*, vol. 111, no. 1, p. A3.B.1-A3.B.3, Nov. 2015, doi: 10.1002/0471142735.ima03bs111.

[25] S. Johnson, V. Nguyen, and D. Coder, "Assessment of Cell Viability," *Curr. Protoc. Cytom.*, vol. 64, no. 1, pp. 9.2.1-9.2.26, Apr. 2013, doi: 10.1002/0471142956.cy0902s64.

[26] B. Chazotte, "Labeling lysosomes in live cells with lysotracker," *Cold Spring Harb. Protoc.*, vol. 6, no. 2, Feb. 2011, doi: 10.1101/pdb.prot5571.

[27] B. Canonico *et al.*, "Rapamycin re-directs lysosome network, stimulates er-remodeling, involving membrane CD317 and affecting exocytosis, in Campylobacter Jejuni-lysate-infected U937 cells," *Int. J. Mol. Sci.*, vol. 21, no. 6, 2020, doi: 10.3390/ijms21062207.

[28] E. Eruslanov and S. Kusmartsev, "Identification of ROS using oxidized DCFDA and flow-cytometry," *Methods Mol. Biol.*, vol. 594, pp. 57–72, 2010, doi: 10.1007/978-1-60761-411-1_4.

[29] B. Canonico *et al.*, "Indagini citofluorimetriche nella vitalità e morte cellulare. II. Studio di altre funzioni cellulari," *Biochim. Clin.*, vol. 33, no. 2, pp. 93–103, 2009.

[30] B. Canonico *et al.*, "Defective Autophagy, Mitochondrial Clearance and Lipophagy in Niemann-Pick Type B Lymphocytes," *PLoS One*, vol. 11, no. 10, p. e0165780, Oct. 2016, doi: 10.1371/journal.pone.0165780.

[31] C. L. Vázquez and M. I. Colombo, "Chapter 6 Assays to Assess Autophagy Induction and Fusion of Autophagic Vacuoles with a Degradative Compartment, Using Monodansylcadaverine (MDC) and DQ-BSA," *Methods in Enzymology*, vol. 451, no. C. Academic Press, pp. 85–95, Jan. 01, 2009, doi: 10.1016/S0076-6879(08)03606-9.

[32] R. Sakhtianchi, R. F. Minchin, K. B. Lee, A. M. Alkilany, V. Serpooshan, and M. Mahmoudi, "Exocytosis of nanoparticles from cells: Role in cellular retention and toxicity," *Advances in Colloid and Interface Science*, vol. 201–202. Elsevier, pp. 18–29, Dec. 01, 2013, doi: 10.1016/j.cis.2013.10.013.

[33] L. Rovati, P. Fabbri, L. Ferrari, and F. Pilati, "Plastic Optical Fiber pH Sensor Using a Sol-Gel Sensing Matrix," in *Fiber Optic Sensors*, InTech, 2012.

[34] F. Luchetti, B. Canonico, M. Arcangeletti, M. Guescini, and E. Cesarini, "Fas Signalling Promotes Intercellular Communication in T Cells," *PLoS One*, vol. 7, no. 4, p. 35766, 2012, doi: 10.1371/journal.pone.0035766.

[35] S. Bolte and F. P. Cordelières, "A guided tour into subcellular colocalization analysis in light microscopy," *Journal of Microscopy*, vol. 224, no. 3. Blackwell Publishing Ltd, pp. 213–232, 2006, doi:

10.1111/j.1365-2818.2006.01706.x.

[36] W. Busch *et al.*, “Internalisation of engineered nanoparticles into mammalian cells in vitro: Influence of cell type and particle properties,” *J. Nanoparticle Res.*, vol. 13, no. 1, pp. 293–310, Jan. 2011, doi: 10.1007/s11051-010-0030-3.

[37] B. J. Iacopetta and E. H. Morgan, “The kinetics of transferrin endocytosis and iron uptake from transferrin in rabbit reticulocytes,” *J. Biol. Chem.*, vol. 258, no. 15, pp. 9108–9115, 1983, doi: 10.1016/S0021-9258(17)44637-0.

[38] J. Saraste, G. E. Palade, and M. G. Farquhar, “Temperature-sensitive steps in the transport of secretory proteins through the Golgi complex in exocrine pancreatic cells,” *Proc. Natl. Acad. Sci. U. S. A.*, vol. 83, no. 17, pp. 6425–6429, 1986, doi: 10.1073/pnas.83.17.6425.

[39] O. Faklaris *et al.*, “Photoluminescent diamond nanoparticles for cell labeling: study of the uptake mechanism in mammalian cells,” *ACS Nano*, vol. 3, no. 12, 2009, doi: 10.1021/nn901014jï.

[40] X. Zeng, Y. Zhang, and A. M. Nyström, “Endocytic Uptake and Intracellular Trafficking of Bis-MPA-Based Hyperbranched Copolymer Micelles in Breast Cancer Cells,” vol. 13, p. 17, 2012, doi: 10.1021/bm301281k.

[41] P. Bozavikov, D. Rajshankar, W. Lee, and C. A. McCulloch, “Particle size influences fibronectin internalization and degradation by fibroblasts,” *Exp. Cell Res.*, vol. 328, no. 1, pp. 172–185, Oct. 2014, doi: 10.1016/j.yexcr.2014.06.018.

[42] I. Fiorentino *et al.*, “Energy independent uptake and release of polystyrene nanoparticles in primary mammalian cell cultures,” *Exp. Cell Res.*, vol. 330, no. 2, pp. 240–247, Jan. 2015, doi: 10.1016/j.yexcr.2014.09.017.

[43] V. Francia, C. Reker-Smit, G. Boel, and A. Salvati, “Limits and challenges in using transport inhibitors to characterize how nano-sized drug carriers enter cells,” *Nanomedicine*, vol. 14(12), pp. 1533–1549, 2019, doi: 10.2217/nnm-2018-0446.

[44] D. Vercauteren *et al.*, “The use of inhibitors to study endocytic pathways of gene carriers: Optimization and pitfalls,” *Mol. Ther.*, vol. 18, no. 3, pp. 561–569, Mar. 2010, doi: 10.1038/mt.2009.281.

[45] T. G. Iversen, T. Skotland, and K. Sandvig, “Endocytosis and intracellular transport of nanoparticles: Present knowledge and need for future studies,” *Nano Today*, vol. 6, no. 2. Elsevier, pp. 176–185, Apr. 01, 2011, doi: 10.1016/j.nantod.2011.02.003.

[46] S. E. Lehman, A. S. Morris, P. S. Mueller, A. K. Salem, V. H. Grassian, and S. C. Larsen, “Silica nanoparticle-generated ROS as a predictor of cellular toxicity: Mechanistic insights and safety by design,” *Environ. Sci. Nano*, vol. 3, no. 1, pp. 56–66, Feb. 2016, doi: 10.1039/c5en00179j.

[47] G. M. Cooper, “Lysosomes,” *Cell A Mol. Approach. 2nd Ed.*, 2000, [Online]. Available: https://www.ncbi.nlm.nih.gov/books/NBK9953/.

[48] R. K. Pathak, N. Kolishetti, and S. Dhar, “Targeted nanoparticles in mitochondrial medicine,” *Wiley Interdisciplinary Reviews: Nanomedicine and Nanobiotechnology*, vol. 7, no. 3. Wiley-Blackwell, pp. 315–329, May 01, 2015, doi: 10.1002/wnan.1305.

[49] M. D. Brand, “Mitochondrial generation of superoxide and hydrogen peroxide as the source of mitochondrial redox signaling,” *Free Radical Biology and Medicine*, vol. 100. Elsevier Inc., pp. 14–31, Nov. 01, 2016, doi: 10.1016/j.freeradbiomed.2016.04.001.

[50] N. Hao, H. Yang, L. Li, L. Li, and F. Tang, “The shape effect of mesoporous silica nanoparticles on intracellular reactive oxygen species in A375 cells,” *New J. Chem.*, vol. 38, no. 9, pp. 4258–4266, Aug. 2014, doi: 10.1039/c4nj00736k.

[51] F. G. Ortega *et al.*, “Interfering with endolysosomal trafficking enhances release of bioactive exosomes,” *Nanomedicine Nanotechnology, Biol. Med.*, vol. 20, p. 102014, Aug. 2019, doi: 10.1016/j.nano.2019.102014.

[52] T. Pfaller *et al.*, “The suitability of different cellular in vitro immunotoxicity and genotoxicity methods for the analysis of nanoparticle-induced events,” *Nanotoxicology*, vol. 4, no. 1, pp. 52–72, Mar. 2010, doi:

10.3109/17435390903374001.

[53] L. Lai, N. Alaverdi, L. Maltais, and H. C. Morse, “Mouse Cell Surface Antigens: Nomenclature and Immunophenotyping,” *J. Immunol.*, vol. 160, no. 8, 1998.

[54] G. J. Oostingh *et al.*, “Problems and challenges in the development and validation of human cell-based assays to determine nanoparticle-induced immunomodulatory effects,” *Part. Fibre Toxicol.*, vol. 8, p. 8, Feb. 2011, doi: 10.1186/1743-8977-8-8.

[55] Q. H. Wu *et al.*, “Iron oxide nanoparticles and induced autophagy in human monocytes,” *Int. J. Nanomedicine*, vol. 12, pp. 3993–4005, May 2017, doi: 10.2147/IJN.S135189.

[56] B. Canonico, F. Luchetti, M. Arcangeletti, M. Guescini, M. Degli Esposti, and S. Papa, “Flow cytometric analyses disclose intercellular communications in FasL-stimulated T cells: Results and trouble shooting,” *Cytometry Part A*, vol. 81 A, no. 1. Cytometry A, pp. 5–8, Jan. 2012, doi: 10.1002/cyto.a.21151.

[57] G. V. Shelke, C. Lässer, Y. S. Gho, and J. Lötvall, “Importance of exosome depletion protocols to eliminate functional and RNA-containing extracellular vesicles from fetal bovine serum,” *J. Extracell. Vesicles*, vol. 3, no. 1, 2014, doi: 10.3402/jev.v3.24783.

[58] M. Al-Rawi, S. Diabaté, and C. Weiss, “Uptake and intracellular localization of submicron and nano-sized SiO 2 particles in HeLa cells,” *Arch. Toxicol.*, vol. 85, no. 7, pp. 813–826, Jul. 2011, doi: 10.1007/s00204-010-0642-5.

CHAPTER 3

Fluorescent silica nanoparticles targeting mitochondria as delivery system for doxorubicin

In preparation

Original Article

Fluorescent silica nanoparticles targeting mitochondria as delivery system for doxorubicin

Sola F. et al

Department of Biomolecular Sciences, University of Urbino Carlo Bo, Urbino (PU), Italy

AcZon s.r.l., Monte San Pietro (BO), Italy

In preparation

Abstract

Since fluorescent silica nanoparticles (SiNPs) appeared a promising imaging platform, showing a specific subcellular localization, we decided to conjugate one of the most commonly used anticancer drug, doxorubicin (DOX). As anticancer agent, DOX has both a high efficacy but also an elevated systemic toxicity and causes multiple side effects. Nanostructures are usually employed to increase the drug circulation time and accumulation in target tissues, reducing undesired cytotoxicity. The DOX loading level was determined to be 25%. We tested these functionalised NPs (DOX-NPs) on breast cancer cell line MCF-7, since DOX is currently one of the most effective agents in the treatment of this disease. We evaluated DOX-NP cytotoxicity, the effect on cell cycle and the impact on the expression of CD44 antigen, a molecule involved in adhesion, therefore in cell spreading in tumour invasion, compared to free DOX and stand-alone NPs. We did not find an increased cytotoxic effect, as we expected, but, beside an opposite trend of CD44 on cell surface, we found the ability to release a minor amount of CD44+ extracellular vesicles (EVs), from both CD81 negative and CD81 positive pools. Further experiments are needed to confirm this significant issue and to consider the employment of specific linkers, maybe pH sensitive, to ensure the total release of the drug from the internalized NPs and increase the toxicity of the fluorescent DOX nanocarrier.

Graphical abstract

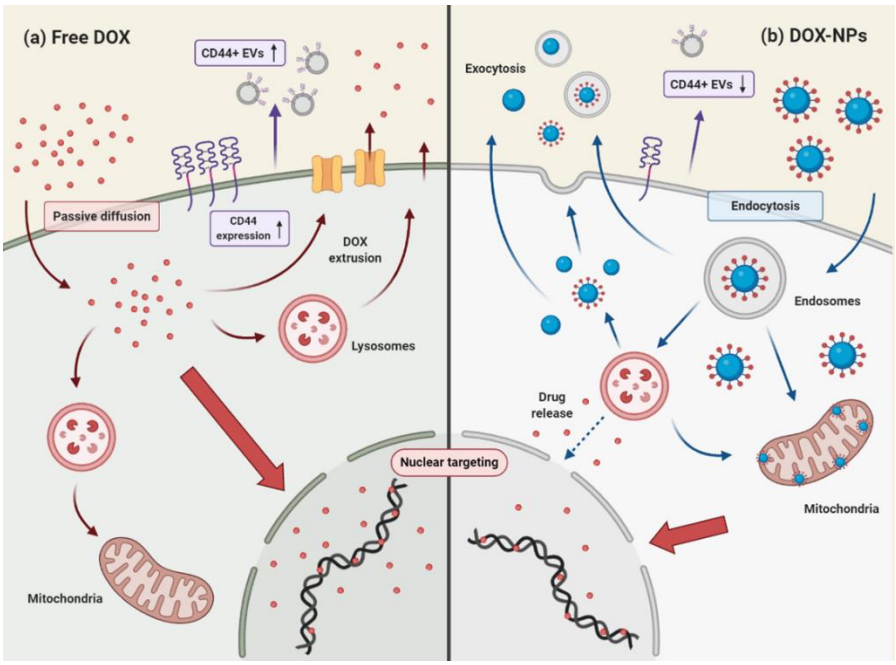

Keywords: breast cancer, doxorubicin, fluorescent silica nanoparticles, extracellular vesicles

Introduction

Doxorubicin (DOX) is an antibiotic deriving from the anthracycline family that is widely employed in breast cancer therapy. The proposed mechanism of action includes the intercalation into DNA disrupting gene expression and macromolecule biosynthesis, production of reactive oxygen species (ROS) and inhibition of topoisomerase II (topo II), a key enzyme in DNA synthesis and replication [1,2]. Nevertheless, one of the most essential problems of DOX-based chemotherapy is the lack of specificity to target cells and the affections of healthy tissues as well. Like all the other anticancer agents, indeed, DOX has both a high efficacy but also an elevated systemic toxicity and causes multiple side effects [1,3]. In particular, the most serious long-term adverse effect of DOX treatment is an irreversible cardiomyopathy, which occasionally does not respond to common therapies and can progress to biventricular failure and even to death [2]. Furthermore, the development of drug resistance in DOX treatment leads to the failure of this therapy. Hence, in the last year many researchers studied new approaches to overcome all these limitations, in particular by exploiting the multiple advantages of nanotechnology. The application of nanotechnology, in particular in medicine, have spread rapidly and could bring significant advances in the diagnosis and treatment of diseases. Currently, many substances, also used in the past, are newly under investigation for drug delivery and, in particular, for cancer cure. Among the multitude of nanomaterials, nanoparticles (NPs) showed interesting and unique features which made them particularly attractive for medical purposes, such as their quantum properties, their surface to mass ratio and the ability to carry other molecules [4]. Moreover, a suitable NP system may improve the efficacy of chemotherapy, using the pathophysiology of tumors, especially the enhanced permeability and retention (EPR) effect and delivering drugs to the target through an active targeting strategy due to the receptor-mediated endocytosis mechanisms [1,5,6]. Owing to their small size, NPs have the great ability to pass through the biological barriers, as the blood brain barrier (BBB), the pulmonary system and the tight junctions of endothelial cells of the skin, thus increasing the systemic bioavailability of the drugs [7]. Generally, NP-based drug delivery systems are constructed by the incorporation of active drugs via entrapment, conjugation or encapsulation into NPs, depending on the peculiar characteristics of the system [6]. Several research groups worked on the development of NPs for DOX delivery and many systems were already approved by FDA, most of which are based on liposomes (e.g. Doxil®, Lipodox® or Myocet®) [2]. Fluorescent silica nanoparticles (SiNPs) synthetized through a micelle-assisted method, as presented by Pellegrino et al. [8], exhibited exciting results in term

of cytotoxicity and intracellular localization, as we presented in our previous study. SiNPs showed interesting features, mostly regarding the versatility of the technology, which makes them potentially interesting for several applications, including drug delivery. SiNPs are core-shell system where the core is made of a silica matrix in which are entrapped fluorophores and one of the most used "stealth" polymers in the drug delivery field, polyethylene glycol (PEG), composes the shell, which is the first interaction with the external environment and allows the modulation of functional groups exposed on NP surface. In the present study, we changed the amine functional groups ($-NH_2$) present on NP shell to carboxyl groups(-COOH) in order to bind doxorubicin. Concerning fluorescence, silica has proven to be an excellent platform, thanks to the fact that it is photophysically inert, i.e., it does not adsorb visible light, and it is not involved in energy or electron transfer processes. Furthermore, another advantage of silica is that it is intrinsically non-toxic [9]. PEG is considered the gold standard and has been extensively employed, in particular, in drug delivery systems in the past decades owing to the ability to avoid opsonization and phagocytosis by cells of the mononuclear phagocyte system (MPS), leading to an extended life-time circulation of the system [10]. The present study provides insights about the effects of this nanocarrier, DOX-NPs, on breast cancer cell line MCF-7, compared to free DOX and stand-alone NPs, since DOX is currently one of the most effective agents in the treatment of breast cancer [1]. Previous data allow to consider SiNPs promising platform for future development of multifunctional systems [8]. In this study we assessed the first step by conjugating a therapeutic molecule to a well-known imaging platform. In future, other steps will be necessary to add a targeting molecule, by exploiting the functional groups on the shell surface, in order to achieve a specific cellular targeting and intracellular drug delivery via receptor-mediated endocytosis. Shi et al. presented, for example, the benefits of Doxorubicin-conjugated immuno-nanoparticles, a polymeric core-shell NP system where both DOX and antibody targeting ligands were coupled on NP surface through a simple conjugation chemistry, on SKBR-3 cell line, compared to healthy HMEC-1 cells [3]. Khutale and co-workers developed a multifunctional NP system based on gold NPs (AuNPs), which are extensively used for drug delivery, by exploiting a pH-dependent release of DOX once inside the cells to increase the availability of the drug and avoiding its efflux [6]. Even Aryal et al. constructed pH-responsive Au-NPs conjugated with DOX which have the multiple potential for future applications to simultaneously enhance computed tomography (CT) imaging contrast or facilitate photothermal cancer therapy while delivering anticancer drug to the target [11].

Materials and Methods

3.1. DOX-NP synthesis and physicochemical characterization

Modification of surface functional group: COOH-NPs

As depicted in Scheme 1, the conjugation of doxorubicin (DOX) required different steps. Firstly, we changed the functional group on the NP surface from -NH_2 to COOH, in order to bind DOX. 2 mL of NPs were diluted with 222 µL of Carbonate/Bicarbonate 10X pH 9.5 and 1.2 mL di Carbonate/Bicarbonate 1X pH 9.5 and 10.9 mg of succinic anhydride (200 eq., 10 mg/mL in DMSO). The mixture was stirred for 1 hour at 40°C, in the dark and then concentrated with Amicon ultra 50 kDa (Merck Millipore, Burlington, MA, USA) and purified by means of size exclusion chromatography (Sephadex G25, GE Healthcare, Chicago, Il, USA) using water as eluent.

Quantification of residual amine groups

Quantification of carboxylic groups on the surface was obtained using a colorimetric indirect method. COOH-NPs were made to react with fluorescein isothiocyanate (FITC, Abs max=494 nm, Em max= 518 nm) (Sigma-Aldrich, St Louis, MO, USA), which bound amine groups left on NP surface. 108 µL of COOH-NPs diluted 1:2 in buffer Carbonate/Bicarbonate 2X (pH=9) were mixed with FITC (10 mg/mL in DMSO, Molar Ratio=10) and incubated 1h at RT in the dark. The reaction mixture was applied on size exclusion chromatography column (Sephadex G25, GE Healthcare, Chicago, Il, USA) and eluted with buffer Carbonate/Bicarbonate 1X (pH=9). Selected fractions were collected and diluted with Carbonate/Bicarbonate to 3 mL of volume. The sample was then analysed at the spectrophotometer (Agilent Technologies, Santa Clara, CA, USA), recording the whole spectrum. The absorption wavelength of FITC, used to calculate the moles of reacted FITC, directly proportional to -NH_2 left on NP surface, was found to be the FITC absorption maximum at the pH used for the reaction (pH=9.5; ε=80600 $M^{-1}cm^{-1}$; 1/ ε= 12.4 µM*cm).

Doxorubicin conjugation to COOH-NPs: DOX-NPs

COOH-NPs were dialyzed against 50mM MES pH=5 for 24 hours at 4°C. 379 µL of NPs-COOH in MES were diluted with 500 µL of 50 mM MES pH=5. 28.6 µL of 1-ethyl-3-(3-dimetilaminopropil)carbodiimide (EDC, 10mg/mL in DMSO), 21.2 µL N-hydroxysuccinimide

(NHS, 10 mg/mL in ddH2O), 0.5 mg of doxorubicin (10 mg/mL in DMSO) (Sigma-Aldrich, St Louis, MO, USA) were added to the solution. The mixture was stirred for 2.5 hours at RT, in the dark. The mixture was concentrated with Amicon ultra 50 kDa (Merck Millipore, Burlington, MA, USA) and purified by means of size exclusion chromatography (Sephadex G25, GE Healthcare, Chicago, Il, USA) using water as eluent. The product was analysed by Agilent Cary 60 UV-Vis spectrophotometer (Agilent Technologies, Santa Clara, CA, USA), recording the whole spectrum with the following setup:

Start (nm)……..	1100.0
Stop (nm)……	190.0
X Mode……...……..	Nanometers
Y Mode..……	Abs
UV-Vis Scan Rate (nm/min)…..	1200.00
UV-Vis Data Interval (nm)……	1.00
UV-Vis Ave. Time (sec)……	0.0500
Beam Mode…..……..	Dual Beam
Baseline Type...…….…….	Baseline correction

Drug conjugation efficiency

The efficiency of drug conjugation was calculated using a direct method by measuring DOX linked to NPs. Quantification of doxorubicin was made using a calibration curve drawn linking absorption at 500 nm to concentration of a set of reference solutions of serial dilutions of free DOX in ddH_2O (Standard 1 to 4). Each dilution was analysed by spectrophotometer (Agilent Technologies, Santa Clara, CA, USA).

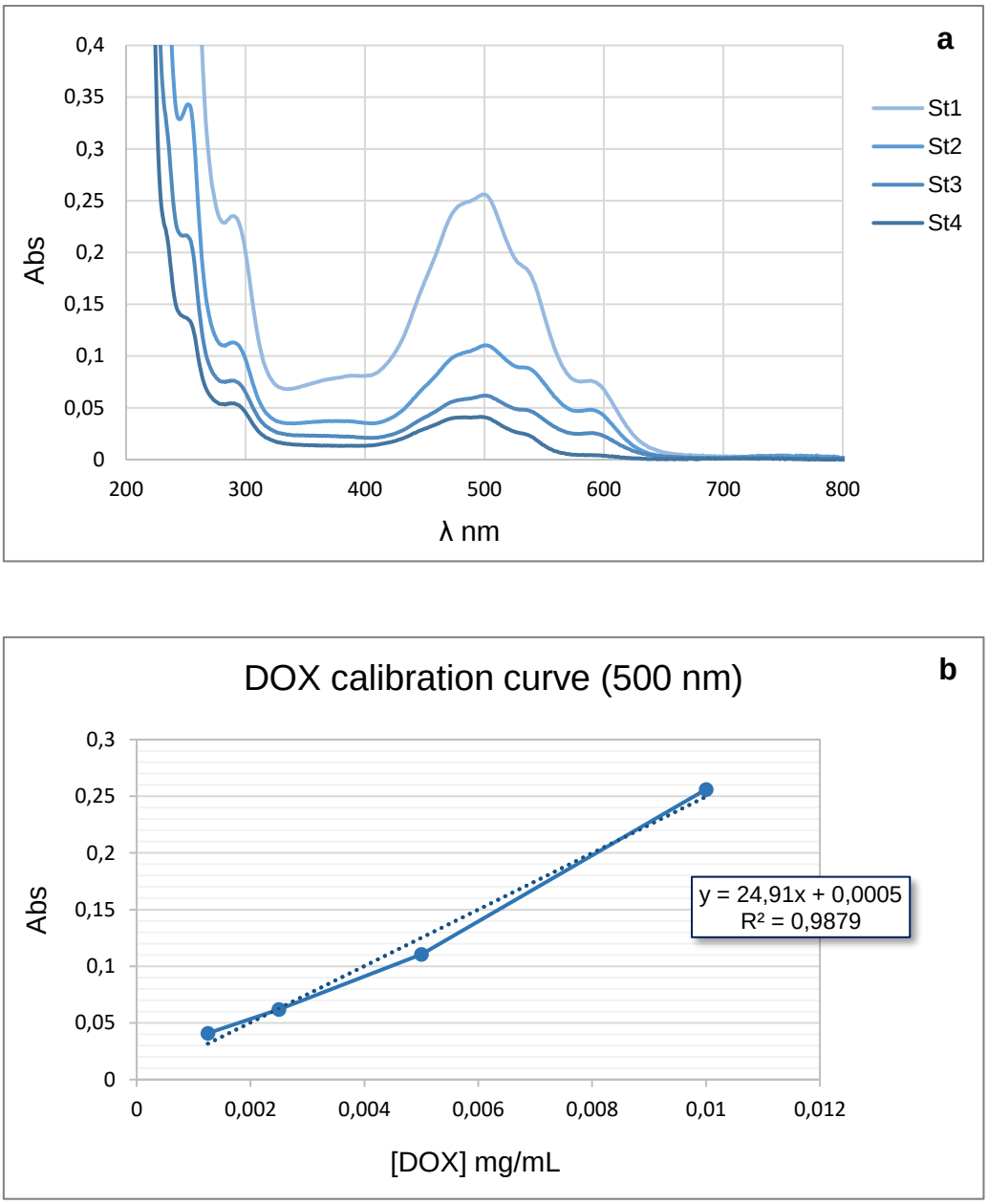

Fig. 3.1 Doxorubicin spectrofluorimetric calibration curve for drug quantification. (a) Absorption spectra of standard dilutions of DOX in ddH_2O. (b) Calibration curve showing DOX concentration related to absorbance at 500 nm.

By interpolating in the calibration curve the absorption value at 500 nm of DOX-NPs sample, it was calculated a 25% of drug linked to nanoparticles.

Scheme 1. Schematic pathway for the synthesis of Doxorubicin-Fluorescent silica nanoparticles in MES buffer, pH 5

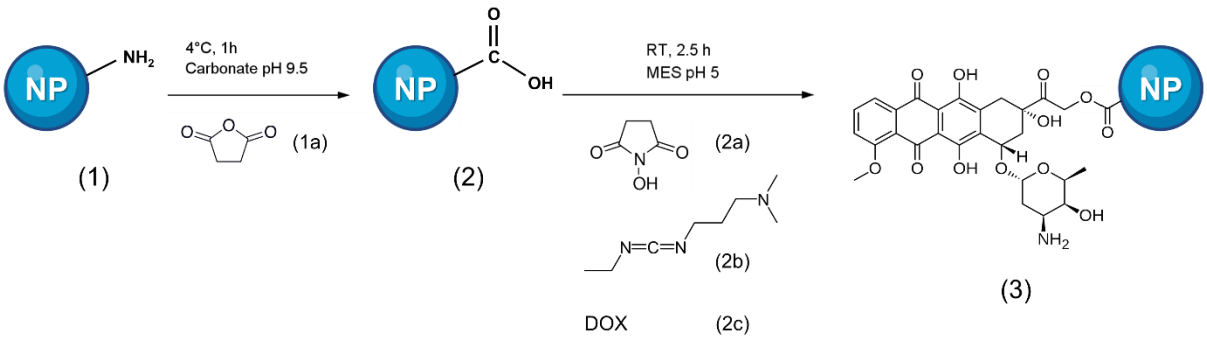

(1) Fluorescent silica NPs (amine functionalization); (1a) Succinic anhydride; (2) Fluorescent silica NPs (carboxylic functionalization); (2a) N-Hydroxysuccinimide (NHS); (2b) 1-Ethyl-3-(3-dimethylaminopropyl)carbodiimide (EDC); (2c) Doxorubicin; (3) DOX-NPs

3.2. Cell culture

MCF-7 (breast cancer cell line) cells were grown at 37°C in humidified incubator with 5% CO_2, in Roswell Park Memorial Institute Medium (RPMI) 1640 (Sigma-Aldrich, St Louis, MO, USA) with stable L-glutamine supplemented with 10% v/v heat-inactivated fetal bovine serum (FBS; Gibco; Thermo Fisher Scientific, Inc., Waltham, MA, USA) and 1% v/v penicillin/streptomycin (Sigma-Aldrich, St Louis, MO, USA).

3.3. Nanoparticle uptake and intracellular localization

To evaluate NP uptake and intracellular localization we firstly defined DOX IC_{50} value on MCF-7 cells. Based on literature, we titrated DOX by exposing cells for 24 h to different concentrations of drug and then assess cell viability through Trypan Blue exclusion assay. We diluted DOX-NPs at the same concentration of drug (1 µg/mL), and, based on the fluorophores concentration of DOX-NPs, we calculated the dilution for COOH-NPs to be used as control. NP dispersions and DOX were prepared by diluting the stock solution, previously filtered with a 0.22 µm membrane filter (Euroclone SpA, Milan, Italy) under sterile environment, into complete medium used for cell culture at room temperature (to ensure better NP dispersion), immediately prior to the treatment of cells. MCF-7 (10^5 cells/well) were seeded in MatTek glass bottom chambers (MatTek Corporation Slovak Republic) and incubated for 24 h at 37°C in humidified incubator with 5% CO_2. Then, the medium was removed and replaced with fresh medium containing free DOX (1 µg/mL), DOX-NPs (1 µg/mL of DOX) and COOH-NPs

(diluted 1:50) and incubated for 4h. The conditioned media were removed and cells were then washed twice with PBS 1X (10 mM NaPi, 150 mM NaCl, pH 7.3-7.4) and stained with different cellular markers. 100 nM of the acidotropic dye LysoTracker™ Green (LTG) (Thermo Fisher Scientific, Waltham, MA, USA) incubated for 45 min was used to investigate the involvement of lysosomal compartment [12], whereas mitochondrial features were investigated by Tetramethylrhodamine ethyl ester perchlorate (TMRE) (Sigma-Aldrich, St. Louis, MO, USA) 40 nM, which is a ΔΨm-specific stain able to selectively enter active mitochondria, was added to the samples 15 min before the acquisition [13]. Confocal microscopy analyses were applied by a Leica TCS SP5 II confocal microscope (Leica Microsystem, Germany) with 488, 543 and 633 nm illuminations and oil-immersed objectives. The images were further processed and analysed in ImageJ software (National Institutes of Health, Bethesda, MD, USA). Colocalization analyses were performed using JACoP plugin in ImageJ software (NIH, Bethesda, MD, USA) [14]. Pearson's correlation coefficient (PCC) was used as the parameter to measure colocalization in our samples.

For quantification of NPs internalized into cells through flow cytometry, 10^5 cells/well were seeded in 12-well plates and incubated for 24 h at 37°C with 5% CO_2, to let them adhere. MCF-7 were then treated and incubated for different time points (24, 48 and 72 h). After trypsinization cells were harvested, centrifuged at 1200 rpm for 5 min, washed twice with PBS 1X and analysed with NovoCyte® 3000 flow cytometer (ACEA Biosciences, San Diego, CA, USA), equipped with three lasers (Violet Ex 405 nm, Blue Ex 488 nm and Red Ex 640 nm). At least 10.000 events were acquired for each sample. Data analyses were performed with NovoExpress Software (ACEA).

3.4. DOX internalization and accumulation

MCF-7 (4.5×10^4 cells/well) were seeded on Millicell EZ slides (Millipore, Burlington, MA, USA) and grown for 24 h at 37°C in 5% CO_2 incubator. The medium was removed and replaced with fresh medium containing free DOX (1 µg/mL), DOX-NPs (1 µg/mL of DOX), COOH-NPs (diluted 1:50) and DMSO (vehicle control). At different time points 24, 48 and 72 h, the treatment was gently aspirated from the left corner of each well and the cells washed twice with PBS 1X. 200µL of 14 µM Hoechst 33342 (Thermo Fisher Scientific, Waltham, MA, USA) has been added to each well and incubated 10 min in the dark. Finally, after the incubation, the slides were washed with PBS 1X and mounted with nail polish on microscope slides. Cells were immediately visualized with Nikon Optiphot 2 fluorescence microscope (Nikon, Tokyo,

Japan), with DM580 and Omega optical INC. XF 1009/25 filters at 20X, 40X and 100X oil immersion magnification. The images were collected using NIS-Elements (Nikon, Tokyo, Japan)

For fluorescence quantification of DOX inside cells through flow cytometry, 10^5 cells/well were seeded in 12-well plates and incubated for 24 h at 37°C with 5% CO_2, to let them adhere. MCF-7 were then treated and incubated for different time points (24, 48 and 72 h). After trypsinization cells were harvested, centrifuged at 1200 rpm for 5 min, washed twice with PBS 1X and analysed with a FACSCanto™ II flow cytometer (BD Biosciences, San Jose, CA, USA), equipped with an argon laser (Blue, Ex 488 nm), a helium-neon laser (Red, Ex 633 nm) and a solid-state diode laser (Violet, Ex 405 nm). For each sample, at least 10.000 events were acquired. Data analyses were performed with Kaluza Analysis 2.1 (Beckman Coulter) and FACSDiva™ softwares (BD Biosciences, San Jose, CA, USA).

3.5. Cytotoxic activity

3.5.1. Trypan blue exclusion assay

The cytotoxicity of DOX and DOX-NPs on MCF-7 cells was determined by Trypan blue exclusion assay, as described by Strober [15]. 10^5 cells/well were seeded in 12-well plates and incubated for 24 h at 37°C with 5% CO_2, to let them adhere. MCF-7 were then treated with free DOX (1 µg/mL), DOX-NPs (1 µg/mL of DOX) and COOH-NPs (diluted 1:50) and incubated for different time points (24, 48 and 72 h). Controls were incubated with fresh medium and, moreover, with DMSO as vehicle control. After trypsinization, an aliquot of cell suspension was mixed with an equal volume of 0,4% Trypan Blue solution (Life Technologies Corporation, Eugene, Oregon, USA), incubated approx. 3 min at room temperature and then counted with a Bürker chamber. Cells were visually examined, with a light microscopy (Nikon, Japan), to determine whether cells took up or excluded dye: viable cells typically show a clear cytoplasm (unstained) whereas nonviable cells show a blue cytoplasm (stained). Percentage of viable cells was calculated, related to control, as following:

$$\text{Viable cells (\%) of control} = \frac{\text{number of viable cells}}{\text{number of viable cells of control}} \times 100$$

3.5.2. Morphological changes

For the analysis of morphological changes, MCF-7 were seeded in 12-well plates and incubated for 24 h, then treated with free DOX (1 µg/mL), DOX-NPs (1 µg/mL of DOX), COOH-NPs (diluted 1:50) and DMSO (vehicle control) and incubated for different time points (24, 48 and 72 h). Finally, the cells were observed under bright field inverted light microscope Nikon eclipse TS100 (Nikon, Tokyo, Japan) at 10X and 40X magnification, to highlight, respectively, the detachment of cells and cell density and morphological changes related to cell death.

3.5.3. Cell cycle analysis

The distribution of DNA in the cell cycle was investigated by flow cytometry. MCF-7 (5×10^5 cells/well) were seeded in 6-well plates, grown for 24h and, finally, exposed to a solution of free DOX (1 µg/mL), DOX-NPs (1 µg/mL of DOX), COOH-NPs (diluted 1:50) and DMSO (vehicle control) and incubated for different time points (24 and 48 h). After trypsinization cells were harvested, centrifuged at 1200 rpm for 5 min and washed twice with PBS 1X. The pellets were fixed drop by drop with ice-cold ethanol (70%) and stored at +4°C, until the analyses. For cell cycle analyses, samples were washed twice with PBS 1X and each pellet was resuspended in 440 µL of PBS 1X, to which 10 µL of 1 mg/mL PI (Sigma-Aldrich, St Louis, MO, USA) and 50 µL of 1 mg/ml RNAse (Sigma-Aldrich, St Louis, MO, USA) were added, to reach a final volume of 500 µL. The samples were well resuspended and incubated at 37°C for at least 30 min or at +4°C until analysis by flow cytometry.

3.5.4. Evaluation of cell surface expression of phosphatidylserine

To investigate cell surface expression of phosphatidylserine (PS), feature of programmed cell death, an aliquot of cells previously treated, was stained with FITC-conjugated Annexin V (Immunostep, Spain). Washed cells were centrifuged at 1200 rpm for 5 min and the pellet resuspended in 50 µL of Annexin V Binding Buffer (10 mM Hepes/NaOH, pH 7,4; 140 mM NaCl; 2,5 mM CaCl2). Finally, 2.5 µL of Annexin V-FITC were added to cell suspension, incubated for 15 min at room temperature and analysed by flow cytometry.

3.6. Flow cytometric analysis of CD44 expression

To evaluate CD44 expression on cells, fluorochrome-conjugated monoclonal antibodies were added to 50 µL of cell pellet. Mouse anti-human antibody anti-CD44 RPE (clone J.173) (Beckman Coulter, Brea, CA, USA) was added at dilutions according to the manufacturer's instructions. After 15 min of incubation at RT in the dark, samples were acquired by flow cytometry.

Media of MCF-7 cells, which have undergone the different treatments, were analysed to study the presence of extracellular vesicles released by cells [16]. 300 µL of medium for each sample was carefully dispensed at the bottom of the tube and 25 µL of Dako CytoCount^{TM} beads (Thermo Fisher Scientific, Waltham, MA, USA) were added. Megamix-Plus beads (Biocytex, Marseille, France) were acquired according to manufacturer's instructions to setup FSC and SSC parameters for EV detection [17]. Supernatants were also stained with mouse anti-human antibody anti-CD81-FITC (clone JS-81) (BD Biosciences, San Jose, CA, USA), a tetraspanin frequently identified in exosomes and considered classical markers of exosomes [18]. Moreover, media were stained with anti-CD44 RPE (clone J.173) (Beckman Coulter, Brea, CA, USA), to evaluate the expression of this tumoral marker, not only on cell surface, but also on the EVs released from cells. After 15 min of incubation at RT in the dark, samples were acquired by flow cytometry.

3.7. Statistical analysis

Data are shown as mean (or percentage, as indicated) ± standard deviation (sd) of at least three independent experiments, when carried out, otherwise two replicates of experiments were running out. The means of two groups were compared by using a paired T test or by one-way ANOVA, followed by a Bonferroni post-hoc test. The p values less than 0.05 were considered statistically significant. All statistical analyses were performed using GraphPad Prism 5 (GraphPad software, San Diego, CA, USA).

Results and discussion

Synthesis and characterization of DOX-NPs

Fluorescent silica nanoparticles (SiNPs) were synthesized as previously reported by Pellegrino et al. [8], through a micelle-assisted method, where a surfactant, which is an amphiphilic long-chain organic compound able to create self-assembled molecular clusters called micelles in a solution, is used to create a nanoreactor. Besides the silica core, SiNP shell is composed by two different polyethylene glycols (PEGs), both terminating with a trialkoxysilane group: a main component which induces stability and solubility in water, and the counterpart functionalized to have amine reactive groups on the shell. For our study we started from this nanoconstruct to obtain fluorescent SiNPs conjugated with doxorubicin (DOX). We choose fluorescent NPs excited by red laser and which emit near 660 nm, in order to have absorption spectra of the two species, DOX (λ max Abs 500 nm) and NPs, quite far and with little influence on each other and, hence, to simultaneously monitor both of them with the aid of the spectrophotometer. To conjugate DOX to SiNPs, first of all, we modified the functional groups on shell surface from amine (-NH_2) to carboxylic (-COOH) groups with the addition of succinic anhydride (Fig. 3.1A). The quantification of carboxylic groups on the surface was obtained using a colorimetric indirect method. COOH-NPs was made to react with fluorescein isothiocyanate (FITC), which bound amine groups left on NP surface (Fig. 3.1B). The reaction yield was, therefore, 89 % of -COOH on NPs. Finally, we made to react COOH-NPs and DOX. The drug linked to NPs was quantified using a calibration curve drawn linking absorption at 500 nm to the concentration of a set of reference solutions of free DOX in ddH_2O. It was calculated a 25% of therapeutic drug bound to NPs. The Fig. 3.1C show the absorption spectra of stand-alone NPs (dotted grey line) and DOX-NPs (solid blue line) in which are distinguishable both species, DOX, with maximum absorption at 500 nm, and NPs, with maximum absorption at 667nm. Moreover, the NP peaks of the two spectra are practically superimposed, while the DOX one is well distinct. In Table 3.1 are synthetized all the physicochemical features of under study DOX-NPs. The fluorescence characteristics, such as maximum absorption and emission wavelength or molar extinction coefficient, had already been investigated, whereas the other data were directly investigated after DOX conjugation.

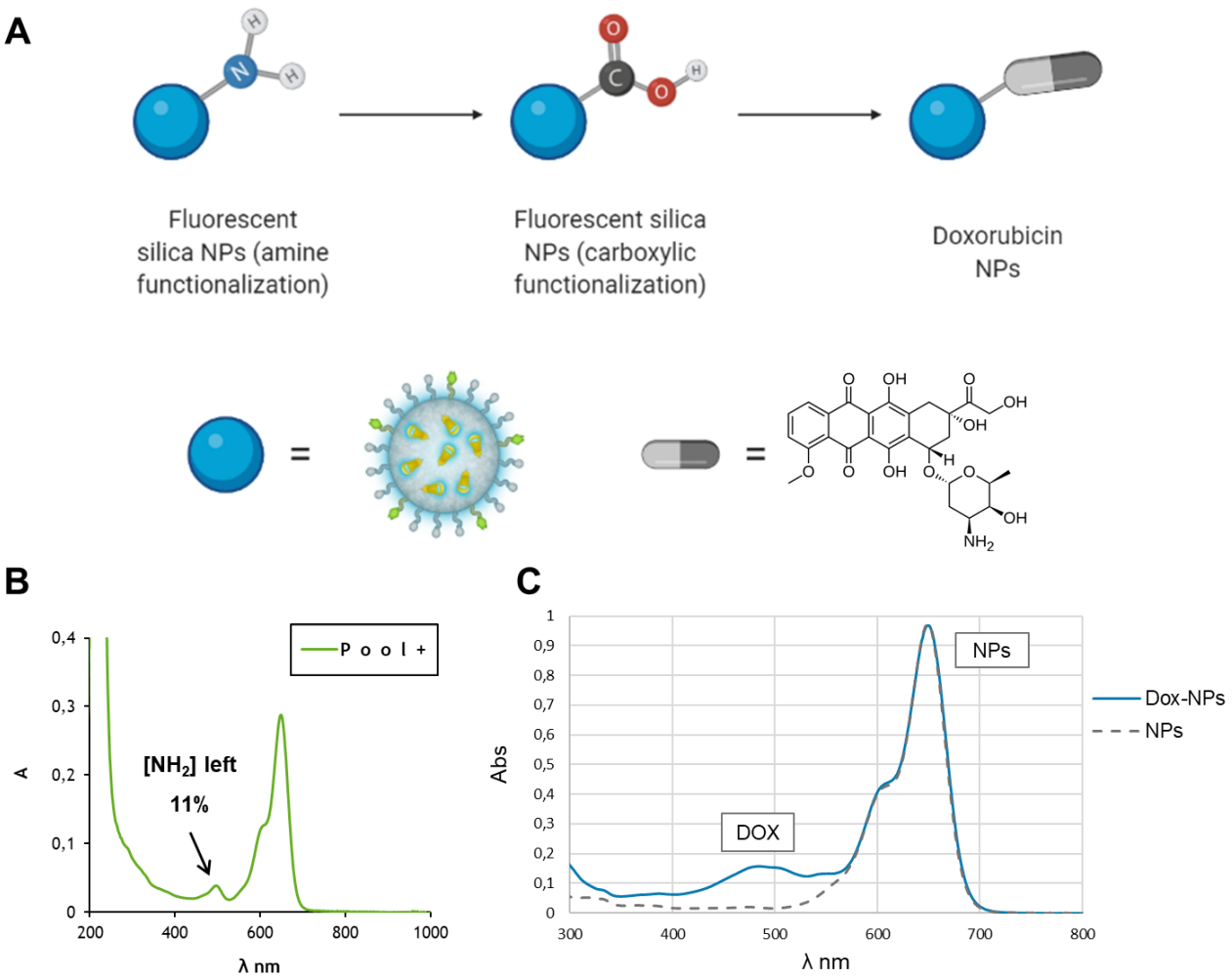

Fig. 3.1 Synthesis and characterization of DOX-NPs. (A) Schematic representation of the synthesis of fluorescent silica nanoparticles conjugated to doxorubicin. The first step was the modification of the functional groups on shell surface with the addition of succinic anhydride from amine (-NH_2) to carboxylic (-COOH) groups. After that, we assessed the conjugation of DOX to COOH-NPs in acid environment in order to obtain the final product: DOX-NPs. (B) Quantification of residual amine groups on COOH-NPs surface. Absorption spectrum of COOH-NPs that were made to react with FITC. The peak highlighted by black arrow refers to the 11% of amine groups left on NP surface. (C) Absorption spectra of DOX conjugated (solid blue line) and stand-alone (dotted grey line) nanoparticles.

DOX-NPs	
Fluorophore	Cy5
[Dye]	18.87 µM
ε ($M^{-1}cm^{-1}$)	102600
λ max Abs (nm)	648 nm
λ max Em (nm)	667 nm
[NH_2] left	11%
COOH surface content	243.78 µM
[DOX]	5.2 µg/mL

Table 3.1 Summary of physicochemical features of DOX-NPs

DOX and NP uptake and intracellular localisation

In our previous study, we investigated the cellular uptake and intracellular fate of multiple dye doped SiNPs into lymphoid and myeloid cells, both tumoral and normal counterparts, in detail U937 cell line and peripheral blood mononuclear cells (PBCMs). Results showed that the internalization process was time-, concentration-, energy and cell type-dependent in all investigated cells. Once inside the cells, NPs were transported within plasma-membrane bounded vesicles along microtubules to organelles, as lysosomes and, in particular, mitochondria, but without affecting cell viability. Interestingly, we observed an almost complete colocalization of NPs with mitochondria, compared to what has been observed with lysosomes. Thus, we started from this data to study the new construct of SiNPs conjugated with DOX. Firstly, we assessed DOX concentration to be used with MCF-7 cells. Based on what was reported in literature, we titrated DOX by exposing cells for 24 h to different concentrations of drug and then assessed cell viability through Trypan Blue exclusion assay (Fig. S1). We diluted DOX-NPs at the same concentration of drug (1 µg/mL), and, based on the fluorophores concentration of DOX-NPs, we calculated the dilution for COOH-NPs to use as control and titrated both NP constructs, with the aid of flow cytometry, confirming to have the same fluorescence intensity (Fig. S2). Through confocal analysis, we examined NP

localization inside the cells, observing in particular the same organelles analysed in the previous work, lysosomes and mitochondria (Fig. 3.2). After 4 h of incubation, we stained cells with LysoTracker^{TM} green (LTG), a permeable dye which stains acidic compartments in live cells for lysosomes, whereas for mitochondria TMRE (tetramethylrhodamine ethyl ester perchlorate), which is a cell-permeant and cationic dye sequestered by active mitochondria, was employed. We performed a colocalization analysis, by using JACoP plugin in ImageJ [14], and Pearson's correlation coefficient (PCC) was used to measure colocalization between NPs fluorescence and fluorescence of LTG and TMRE. Concerning COOH-NPs we detected a higher colocalization with TMRE, as previously observed, whereas for DOX-NPs there was no difference between colocalization with lysosomes or mitochondria, indicating a possible different intracellular reworking of the two types of nanoparticles. Lysosomes, notably, contain the bulk of hydrolases, that, once released into the cytosol, are able not only to induce the apoptotic pathway, but also to amplify the death pathways triggered by other cellular compartments. Furthermore, these organelles receive cargo destined for degradation via the autophagic pathway, by degrading damaged organelles and molecules [19,20]. Thus, the DOX-NP higher colocalization with these organelles may suggest a collaboration with the triggering of cell death or, at longer times, might support the elimination of damaged organelles containing NPs, what mitochondria could be.

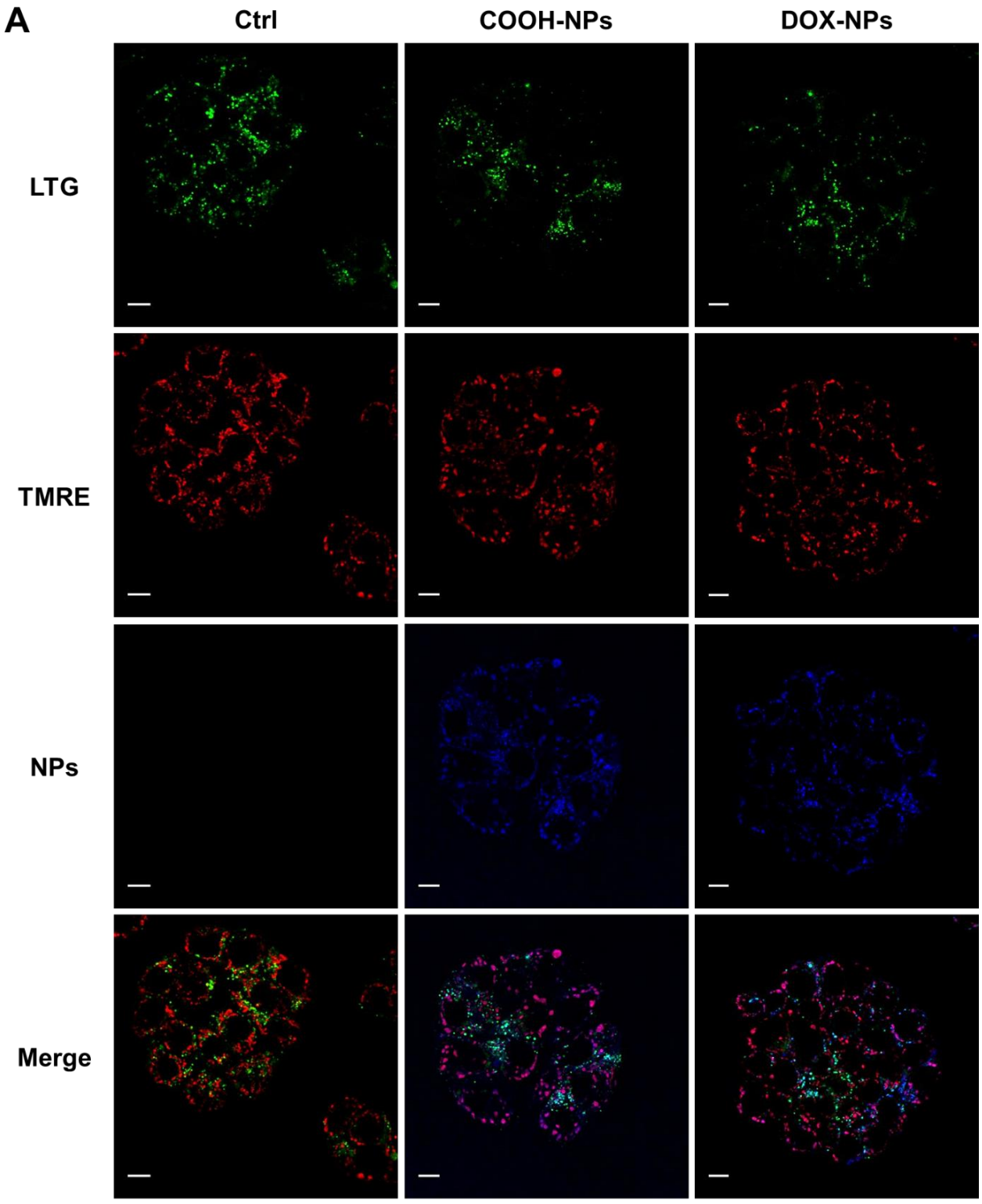
A
Ctrl
COOH-NPs
DOX-NPs
LTG
TMRE
NPs
Merge

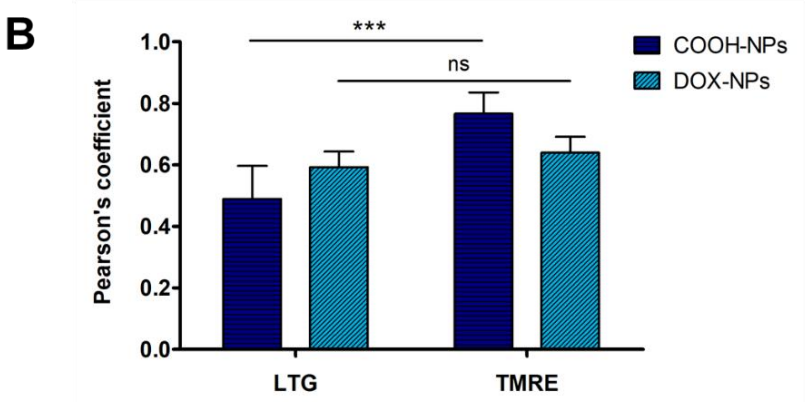
B
***
ns
COOH-NPs
DOX-NPs
Pearson's coefficient
1.0
0.8
0.6
0.4
0.2
0.0
LTG
TMRE

Fig. 3.2 Intracellular investigation of COOH-NPs and DOX-NPs in MCF-7 cells: colocalization with lysosomes and mitochondria (A) Representative confocal images of MCF-7 cells incubated for 4 h at 37°C with medium (ctrl), COOH-NPs (diluted 1:50) or DOX-NPs (1 µg/mL of drug) and then stained with LysoTracker™ green (LTG) and Tetramethylrhodamine ethyl ester perchlorate (TMRE), respectively for lysosomes and mitochondria. Figures show LTG (green), TMRE (red), NPs (blue) and merged images (last line at the bottom). Teal and violet colors indicate colocalization between, respectively, LTG/NPs and TMRE/NPs. Scale bar: 10 µm. (B) Pearson's colocalization coefficient (PCC) of LTG and TMRE with COOH-NPs and DOX-NPs in MCF-7cells. PCCs were derived from two completely independent experiments with 8 fields per experiment contributing to the cumulative result. Each value is expressed as PCC ± sd; asterisks denote a statistically significant difference (*** = $p < 0.001$) between LTG and TMRE colocalization with COOH-NPs.

Moreover, drug release and accumulation *in vitro* were monitored through fluorescent microscopy. Thanks to the doxorubicin characteristic properties, it is notably possible to measure this anticancer drug in biological systems through the employment of fluorescent-based techniques, including microscopy and flow cytometry [21]. We investigated the site of DOX accumulation by tracking the DOX fluorescence and with counter staining the nuclei of MCF-7 cells with Hoechst 33342 (Fig. S2). Our results showed free DOX and DOX conjugated with SiNPs with different cellular localization, suggesting the exploitation of alternative uptake mechanisms by the cells. DOX conjugated to SiNPs accumulated in vesicle-like organelles, probably by following one or some endocytic pathways, while free DOX was more diffused in cytoplasm and inside the nucleus of cells. A nuclear accumulation was clearly visible, in particular at long times of incubation (Fig. 3.3). The internalization of doxorubicin, both free and conjugated, was evaluated also by flow cytometry (Fig. 3.4A). We noticed that, while free DOX fluorescence internalized by MCF-7 cells increased during time until reaching almost a plateau at 72 h, for conjugated DOX, after a slight gain at 48 h, there was a reduction in DOX fluorescence, because the cell might implement release/exocytosis mechanisms, as we observed for unconjugated NPs in our previous study. At the same time, by flow cytometry we also measured NP fluorescence inside the cells. Histograms in Fig. 3.4B illustrate that both COOH-NPs and DOX-NPs had the same fluorescence intensity after 48 h of incubation at 37°C, in their respective fluorescence channel, other than that of DOX.

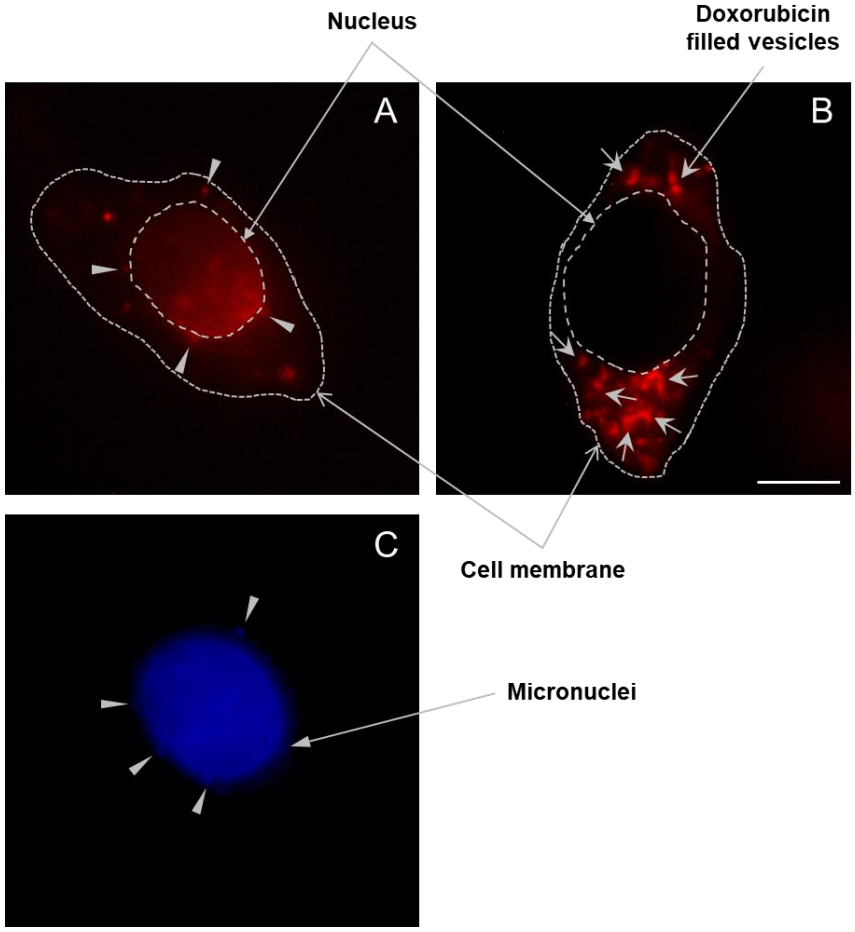

Fig. 3.3 Intracellular accumulation of doxorubicin in MCF-7 cells treated with DOX and DOX-NPs. Representative fluorescent microscopy images of MCF-7 cells incubated for 48 h at 37°C with free DOX (1 µg/mL), mainly localized in the nucleus (A), and respective counter staining of nucleus with Hoechst (C) or with DOX-NPs (1 µg/mL of drug), where red fluorescence results in vesicles into the cytoplasm and in perinuclear region (B). Grey arrows highlight DOX filled vesicles, while small grey triangles micronuclei containing DOX. Magnification 100X oil immersion.

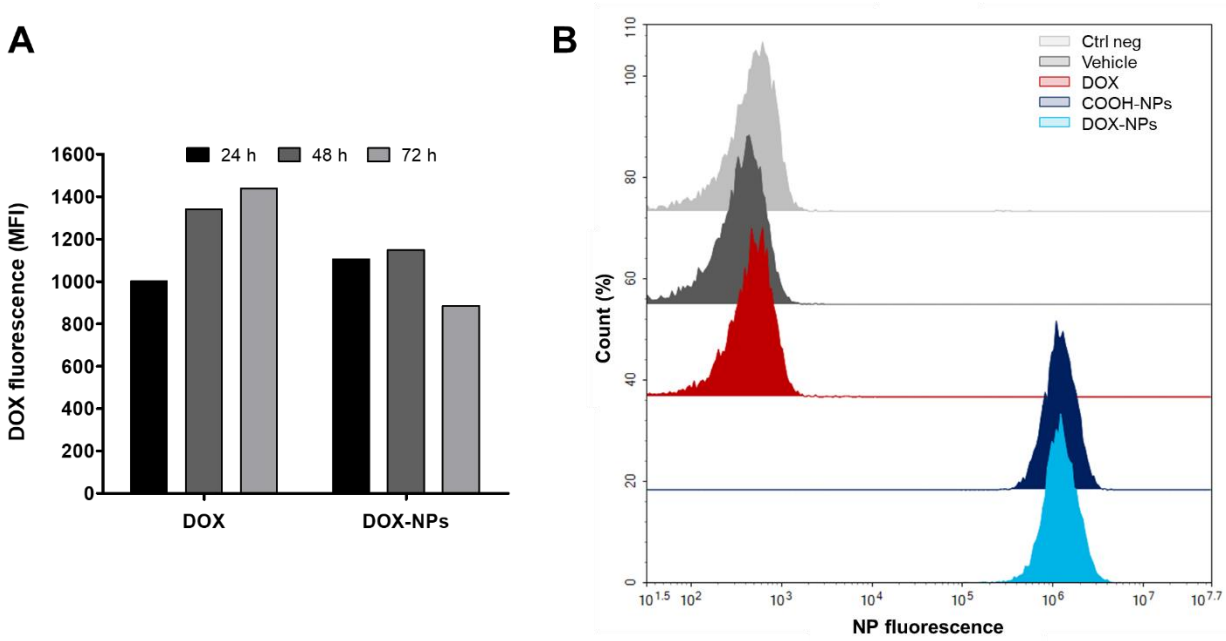

Fig. 3.4 Flow cytometry quantification of doxorubicin and nanoparticle fluorescence inside MCF-7 cells. MCF-7 were incubated with medium (Ctrl neg), DMSO (vehicle), COOH-NPs (diluted 1:50), free DOX (1 µg/mL) and DOX-NPs (1 µg/mL of DOX) for 24, 48 and 72 h at 37° C. (A) Mean Fluorescence Intensity (MFI) of DOX from the flow cytometry data is shown as a function of time (n=2). (B) Flow cytometry histogram overlay shows the NP fluorescence within MCF-7 cells after 48 h of incubation. At least 10000 events were analysed by flow cytometry for each experimental condition.

Investigation of cell death

The cytotoxic effects of the treatment administered were firstly investigated through Trypan Blue exclusion assay. Fig. 3.5A shows cytotoxicity results of MCF-7 cells after incubation with COOH-NPs, DOX-NPs, free DOX or vehicle (DMSO) for 24, 48 and 72 h. We observed that cell viability of MCF-7 after incubation with COOH-NPs was in the range from 85-90% in the longest investigate time compared to control. The 10-15 % decrease in cell viability we hypothesized that was to be attributed to the anionic nature of NPs unlike the SiNPs used in our previous study, which presented amine functional groups on shell surface. These differences may arise to different intracellular trafficking of the changed charge-NPs and/or to the different cellular model. The findings reported in literature concerning the effects of different types of particles functionalized with different chemical groups from numerous research groups did not show a clear trend in term of cytotoxicity related to surface charge of NPs [22]. Our results differed from what Bhattacharjee and co-workers observed about the role of surface charge in cytotoxicity on NR8383 macrophage cells. Positively charged Si NP-NH_2

resulted more cytotoxic, reducing mitochondrial metabolic activity and producing high levels of intracellular ROS, while negatively charged Si NP-COOH induced no toxicity [22]. Furthermore, Riebeling et al. evaluated the effects of 40 nm carboxyl-modified polystyrene and 50 nm amine-modified NPs on several cell lines and they detected no effect of the former in any test they did, whereas the other displayed cytotoxicity in most cell models [23].

As concerning the effect of DOX-NPs on cell viability we did not observe a higher cytotoxicity then free DOX, as expected. With free DOX we reached 50% of cell death, in early investigated time point (24 h), while conjugated DOX showed a slower effect on cell viability (from 75% at 24 h to 30% at 72 h). DOX-NPs are taken into cells *via* an endocytic process and this requires more time compared to passive diffusion across cell membrane. The nuclear localization of the drug may be important due to its intranuclear site of action and its delivery is required for therapeutic effects. However, we did not notice DOX fluorescence into the MCF-7 nuclei, but we observed DOX fluorescence in NP filled vesicles: this evidence suggests that an alternative site of drug accumulation is represented by lysosomes (as demonstrated by major DOX-NP stock in lysosome, in respect of NP alone) (Fig. 3.2B), and this site is able to exert doxorubicin cytotoxic activity. A model of action could be that one described by Wu et al. [24].

As presented by Bar-On et al. DOX is able to arrest MCF-7 cells at G1/S and G2/M checkpoints, whereas another breast cancer cell line, MDA-MB-231, at G 2 /M phase only [25]. We decided to study the effect of DOX and DOX-NPs on cell cycle of MCF-7 through PI staining of ethanol fixed cells by flow cytometry. SiNPs with amine functional groups, showed a stop in G1 phase and related growth inhibition (data not shown). While at 24 h of treatment the analysis displayed the same amount of cells in phase S and similarities in G2/M between controls (both incubated with medium and DMSO as vehicle), and NPs (data not shown). At 48 h, we observed a marked increase of MCF-7 cells in G2/M phase, compared to controls when treated with COOH-NPs (Fig. 3.6A). The same trend of inhibition of cell proliferation was observed also with DOX-NPs. Regarding DOX, our results highlighted a marked decrease of G1 events and concomitant increase in S and G2/M: however, the most relevant feature is the elevated sub-G1 peak, one of the notable hallmarks of apoptosis. While MCF-7 incubated with DOX-NPs showed only a 4% of cells in sub-G1 phase, approximately six times lower than free DOX.

Apoptosis is a well-known process of cell death characterized by specific morphological changes, including cell shrinkage, chromatin condensation and nuclear fragmentation [26].

Micronuclei are chromatin-containing bodies which are results of a DNA damage and may be considered another feature of apoptosis. Hintzsche et al. presented a higher number of micronuclei in HSC and TK6 cells treated with doxorubicin, related to decrease in cell viability and increase apoptosis per cell [27]. Given the large hypodiploid peak observed in cell cycle analysis and cell death related to DOX treatment, we hypothesized the presence of micronuclei (Fig. 3.3C), resulting from the oligonucleosomal DNA cleavage, which also carry the drug molecule intercalated in the DNA. The fluorescence of DOX in Fig. 3.3A, in fact, matches with Hoechst staining in the image below, pointed out from small grey triangles. Another parameter to evaluate apoptosis is the exposure on cell surface of phosphatidylserine from cytoplasmic side [28]. This is an early characteristic, important to highlight a different apoptotic pattern. Caspase-activated DNase is responsible for the oligonucleosomal DNA degradation during apoptosis. DNA degradation is thought to be important for multicellular organisms to prevent oncogenic transformation or as a mechanism of viral defence. It has been reported that certain cells, including some neuroblastoma cell lines such as IMR-5, enter apoptosis without digesting DNA in such a way [29]. Therefore, we evaluated the exposure of phosphatidylserine (PS), another apoptotic feature, through Annexin V staining by flow cytometry [30]. At early time point (24 h) we did not detect substantial differences in PS exposure, although DOX-NPs exhibited the highest percentage (Fig. 3.6C). Continuing in incubation time, DOX showed a much more pronounced effect, reaching about 75% of Annexin V positive cells. The flow cytometry overlay histogram in Fig. 3.6B, already at 48 h of treatment, well displays the effect of DOX in term of PS exposure, compared to other treatments and controls.

Fig. 3.5 In vitro cytotoxicity and cell density of MCF-7 treated with COOH-NPs, DOX and DOX-NPs during time. MCF-7 were incubated with medium (Ctrl neg), DMSO (vehicle), COOH-NPs (diluted 1:50), free DOX (1 µg/mL) and DOX-NPs (1 µg/mL of DOX) for 24, 48 and 72 h at 37° C (n=2). (A) Cell viability was assessed through Trypan Blue exclusion assay and data are expressed as percentage of control. (B) Representative phase contrast images of MCF-7 with several treatments at different time points to effect on morphology, cell density and detachment. Magnification 10X.

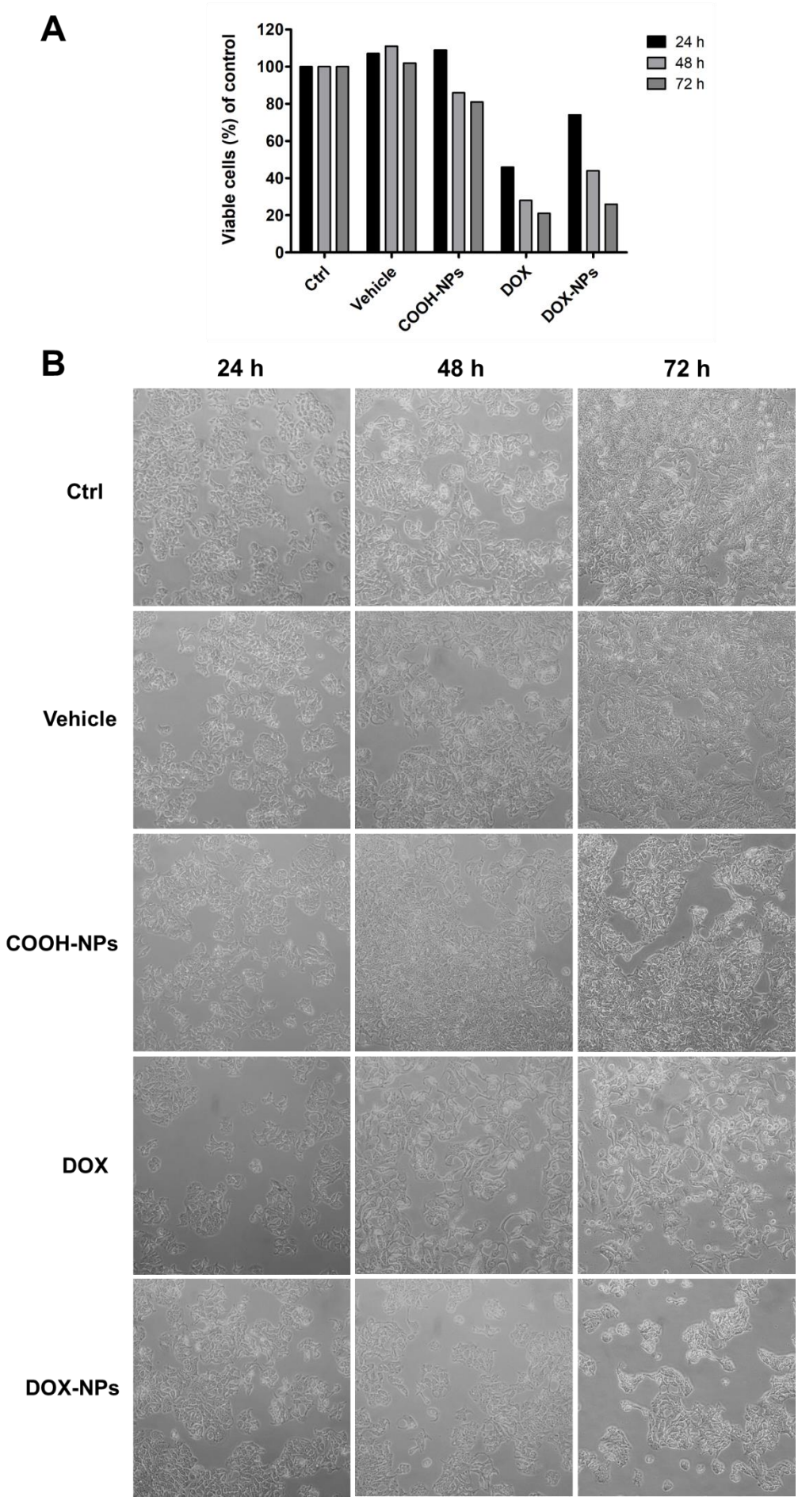
A
Viable cells (%) of control
120
100
80
60
40
20
0
24 h
48 h
72 h
Ctrl
Vehicle
COOH-NPs
DOX
DOX-NPs
B
24 h
48 h
72 h
Ctrl
Vehicle
COOH-NPs
DOX
DOX-NPs

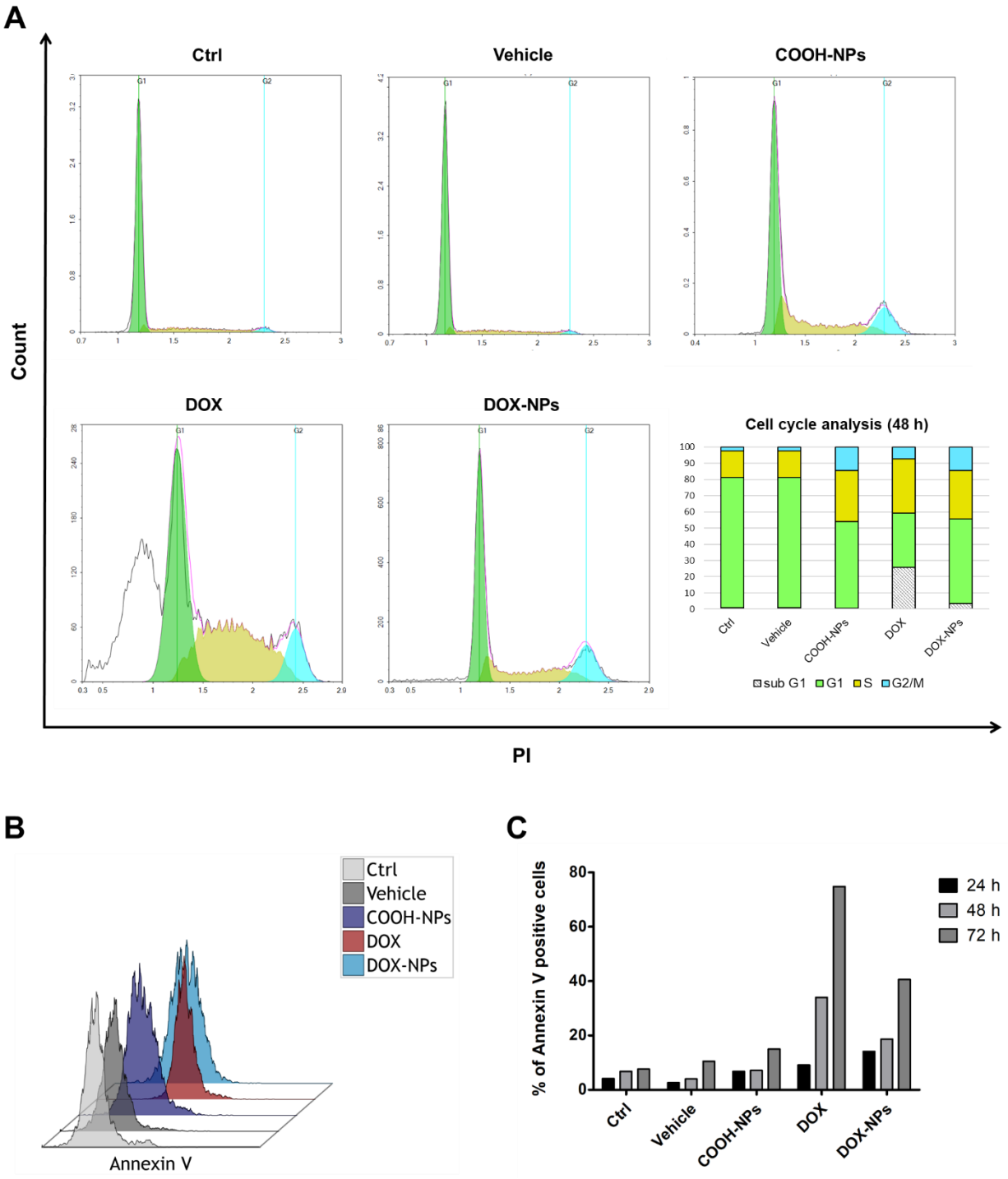

Fig. 3.6 Investigation of cell death features on MCF-7 cells after treatment. MCF-7 were incubated with medium (Ctrl neg), DMSO (vehicle), COOH-NPs (diluted 1:50), free DOX (1 µg/mL) and DOX-NPs (1 µg/mL of DOX) for 24, 48 and 72 h at 37° C. (A) Representative DNA histograms (obtained by PI staining) of MCF-7 cell cycle analysis after 48 h exposure. Bar graph indicates the percentages of cell distribution in different phases of cell cycle (sub-G1, G1, S and G2/M) for control and treated cells after 48 h. (B) Exemplifying flow cytometry histogram overlay for MCF-7 treated for 48 h and stained with Annexin V-FITC to investigate cell surface expression of phosphatidylserine, as marker of apoptosis. (C) The histogram presents the percentage of Annexin V positive cells detected through flow cytometry during time (n=2).

Lastly, apoptosis is most notably recognised by some morphological features that occur during its progression. Early alterations include cell shrinkage and rounding, because of the retraction of lamellipodia and the breakdown of cytoskeleton. Before the apoptotic cell is disposed of, it is possible to observe the process of cell disassembly, characterized by three recognizable steps: (1) membrane blebbing, (2) formation of membrane protrusion and (3) fragmentation [31,32]. By analysing the images obtained under the phase contrast microscope at higher magnification, we detected some of the main morphological-like apoptotic events, both in MCF-7 incubated with DOX (Fig. 3.7A, B) and DOX-NPs (Fig. 3.7C, D). In the early time points we noticed the characteristic cell rounding, later accompanied by surface and dynamic blebbing (on the left and on the right, the respectively in Fig. 3.7C), the typical apoptotic membrane protrusion (Fig. 3.7A, D) and, finally, the characteristic release of subcellular membrane-based vesicles (Fig. 3.7B). In DOX-NP treated cells we noticed more of these typical apoptotic morphological features, maybe because free DOX exhibited a more efficacious treatment with marked cell death on MCF-7, as already observed.

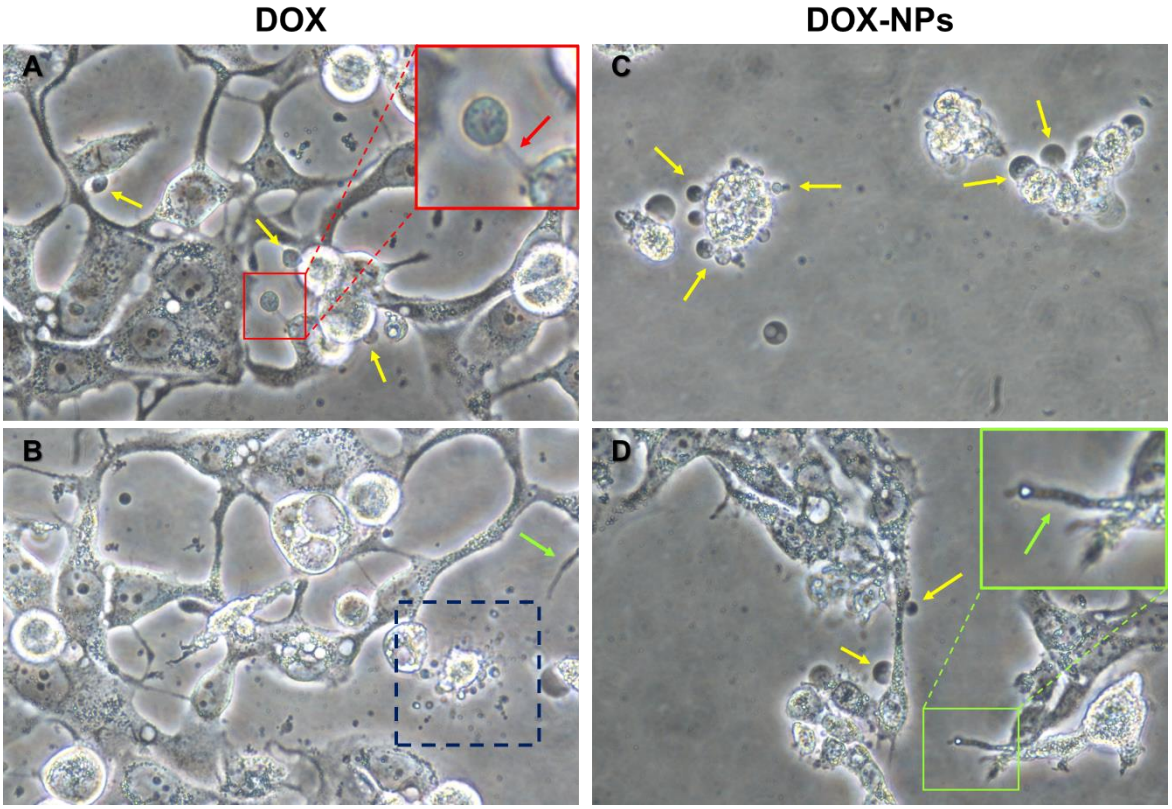

Fig. 3.7 Some peculiar morphologic apoptotic features in MCF-7 cells treated with DOX and DOX-NPs. MCF-7 were incubated with free DOX (1 µg/mL) and DOX-NPs (1 µg/mL of DOX) for 24, 48 and 72 h at 37° C. Here we present some representative phase contrast images (magnification 40X) of MCF-7 treated for 72 h with DOX (A-B) and DOX.NPs (C-D), which present some characteristic aspects of the different stages of apoptotic until cell disassembly. Yellow arrows show apoptotic blebs on cell surface, in particular in frame C we observed two different stages: surface blebbing (on the left) involves the cell periphery while dynamic blebbing (on the right) occurs at a later stage and can lead to drastic changes in cell shape. After apoptotic membrane blebbing, a cell undergoes further morphological changes as generating a variety of membrane protrusions, with subtle differences in morphology, including microtubule spikes, apoptopodia and beaded apoptopodia, which are highlighted with green arrows. Green inset shows the presence of a beaded apoptodia. Lastly, the release of individual membrane-bound apoptotic bodies occurs and leads to the final step of cell fragmentation. The red inset underlines the release of an apoptotic body at the apex of a membrane protrusion, whereas the blue cage contains a cell which is going to fragmentation with the release of subcellular membrane-vesicles.

Effect on tumor spreading and invasion

Cell invasion is the main process for cancer progression and depends on several signaling pathways that control cytoskeletal dynamics and the turnover of cell-matrix and cell-cell junction, followed by cell migration into the adjacent tissues [33]. CD44 is a receptor for extracellular matrix (ECM) components, mainly hyaluronic acid (HA), and a most common cancer stem cell (CSC) marker. Although it is involved in normal physiological events, such as cell-cell interaction and cell-matrix interaction, its high expression has been associated with tumor progression, migration and metastasis. Recently, it has also been linked with anticancer drug resistance, cell proliferation, tumor recurrence and invasion in multiple types of tumors [34-37]. In particular, in breast cancer cell lines several studies reported that CD44+ CSCs have a higher tumorigenicity [35]. Wolf and colleagues, moreover, with the aid of on engineered HA hydrogel-based matrix, have highlighted the importance of CD44 for cell migration and adhesion through the formation of microtentacles on cells [38]. Since in contrast images previously analysed we noticed the presence of structures similar to microtentacles (inset in Fig. 3.8A) and due to the relevance of this surface molecule, we decided to investigate CD44 expression on MCF-7 after treatments, through flow cytometry. Histogram in Fig. 3.8A shows that DOX-NPs induced a gradually decrease of CD44 expression on cell surface, while free DOX-treated cells display a time-dependent opposite trend; in line with Fang et al. data, that observed a dose-dependent increase of CD44 mRNA expression in MCF-7 cells after treatment with DOX at different concentrations [35].

Wang et al. observed that doxorubicin promotes the secretion of CD44+enriched exosomes from MCF-7 cells, which transfer resistance properties by initiating several intracellular signaling pathways [34,38]. Both in normal physiological, as well as pathological conditions, cells release membrane-bound vesicles such as exosomes, microvesicles and apoptotic bodies. These extracellular vesicles (EVs) could facilitate communication between cells though their cargo such as proteins, miRNA, DNA and mRNA [40-42]. As previously introduced, we observed the presence of apoptotic bodies, but in microscopy it was not possible to discriminate among the different types of EVs produced by cells. Thus, we analysed all media, collected before the detachment of MCF-7 cells prior to other analysis on cells, in flow cytometry by Dako CytoCount^{TM} beads (for counting), FSC/SSC Megamix-Plus beads (for appropriately setting) and anti-CD81 monoclonal antibody (for exosome labelling) to investigate the EVs secreted by the cells. Results show that MCF-7 release both EVs (CD81-) and exosomes (CD81+) containing NPs (Fig. 3.8B-upper contour plots), as we presented in our previous study in lymphoid and myeloid cells, thus cells are able to dispose of nanoconstruct, with different intracellular pathways. As depicted in contour plots of Fig. 3.8B at the bottom (gating strategy of negative sample, i.e. w/o CD44 staining in Fig. S4) all media contain both CD44+CD81- and CD44+CD81+ vesicles. We observed a higher amount of events in control sample (data not shown). When these data were related with the corresponding number of cells in the sample (obviously much greater in cells w/o treatment), we noticed a higher number of events per cell-unit in DOX-treated samples, as we expected, but, interestingly, we did not detect the same effect with DOX-NPs (Fig. 3.8C). This finding highlights, besides an opposite trend in CD44 expression on cell surface, the lack of the enrichment in CD44+ exosomes, for DOX-NP treated cells. Taking into account the establishment of drug resistance in other cells, neighbouring or distant in the body, DOX-NPs may represent a vantage in terms of pathology spreading and metastasization process compared to free DOX treatment.

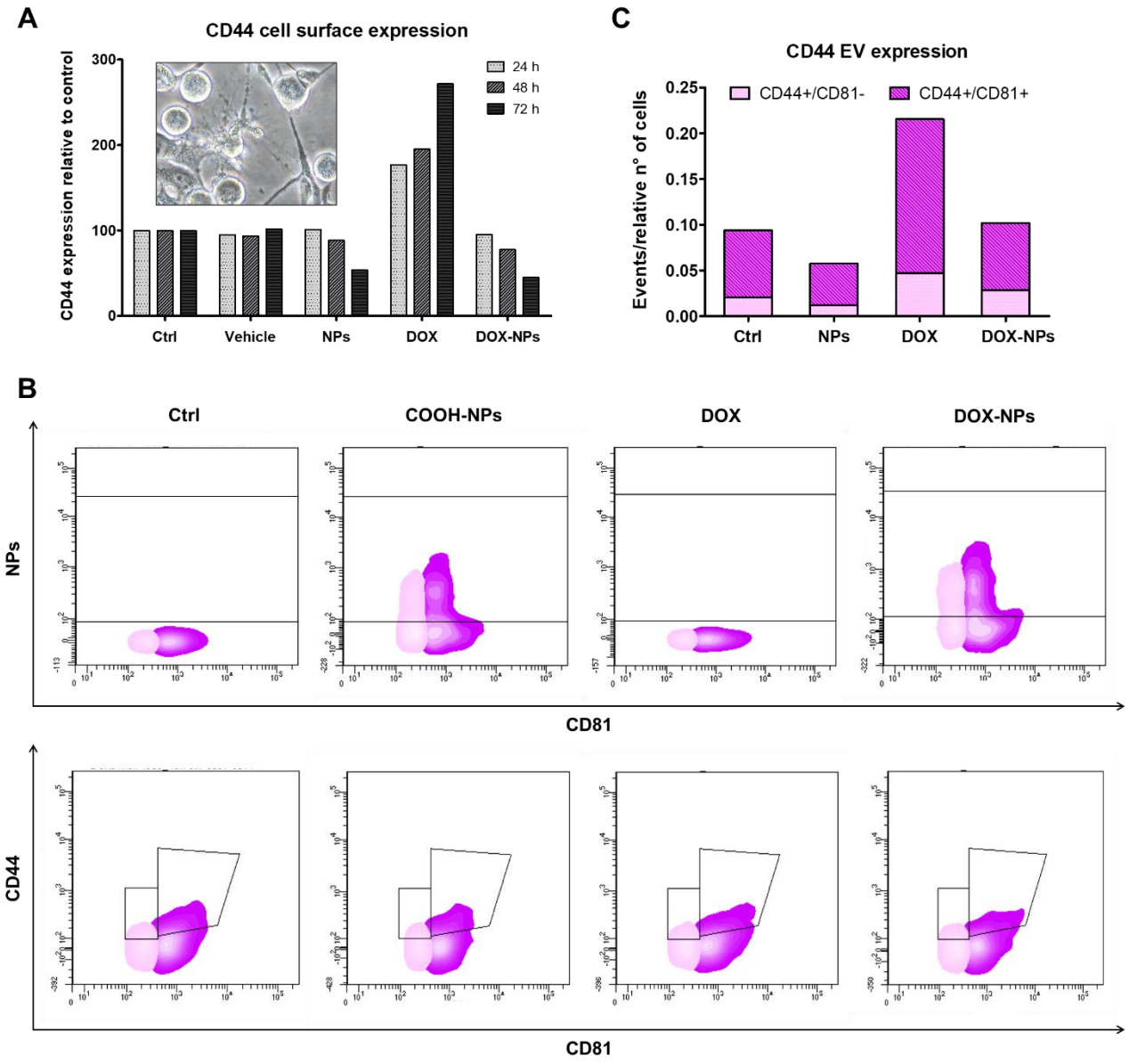

Fig. 3.8 CD44 expression on cell surface and enrichment on extracellular vesicles after DOX treatment. (A) MCF-7 were incubated with medium (Ctrl neg), DMSO (vehicle), COOH-NPs (diluted 1:50), free DOX (1 µg/mL) and DOX-NPs (1 µg/mL of DOX) for 24, 48 and 72 h at 37° C, washed and then stained with CD44 RPE. Mean Fluorescence Intensity (MFI) data were acquired by flow cytometry and normalized to control (n=2). (B) Flow cytometry contouring plots (above: NPs channel vs. CD81 FITC; below fluorescence of particles CD44 RPE vs. CD81 FITC) of supernatants, presenting in pink CD81- particles violet CD81+particles. (C) Histogram shows the quantification of extracellular vesicles (EVs), counted using Dako CytoCountTM beads, in Ctrl, COOH-NP, DOX and DOX-NP media containing CD44+/CD81- and CD44+/CD81+ particles (n=2). The color scheme is the same of contouring plots. At least 10000 events were analysed by flow cytometry for cells and at least 30000 events for EVs for each experimental condition.

References

[1] J. Prados *et al.*, "Doxorubicin-Loaded Nanoparticles: New Advances in Breast Cancer Therapy," *Anticancer. Agents Med. Chem.*, vol. 12, no. 9, pp. 1058–1070, 2012, doi: 10.2174/187152012803529646.

[2] N. Zhao, M. C Woodle, and A. J. Mixson, "Advances in Delivery Systems for Doxorubicin," *J. Nanomed. Nanotechnol.*, vol. 09, no. 05, 2018, doi: 10.4172/2157-7439.1000519.

[3] M. Shi, K. Ho, A. Keating, and M. S. Shoichet, "Doxorubicin-conjugated immuno-nanoparticles for intracellular anticancer drug delivery," *Adv. Funct. Mater.*, vol. 19, no. 11, pp. 1689–1696, 2009, doi: 10.1002/adfm.200801271.

[4] S. Eliasof *et al.*, "Correlating preclinical animal studies and human clinical trials of a multifunctional, polymeric nanoparticle," *Proc. Natl. Acad. Sci. U. S. A.*, vol. 110, no. 37, pp. 15127–15132, Sep. 2013, doi: 10.1073/pnas.1309566110.

[5] W. H. De Jong and P. J. A. Borm, "Drug delivery and nanoparticles: Applications and hazards," *International Journal of Nanomedicine*, vol. 3, no. 2. Dove Press, pp. 133–149, 2008, doi: 10.2147/ijn.s596.

[6] G. V. Khutale and A. Casey, "Synthesis and characterization of a multifunctional gold-doxorubicin nanoparticle system for pH triggered intracellular anticancer drug release," *Eur. J. Pharm. Biopharm.*, vol. 119, pp. 372–380, 2017, doi: 10.1016/j.ejpb.2017.07.009.

[7] S. A. A. Rizvi and A. M. Saleh, "Applications of nanoparticle systems in drug delivery technology," *Saudi Pharmaceutical Journal*, vol. 26, no. 1. Elsevier B.V., pp. 64–70, Jan. 01, 2018, doi: 10.1016/j.jsps.2017.10.012.

[8] C. Pellegrino *et al.*, "Multiple Dye Doped Core-Shell Silica Nanoparticles: Outstanding Stability and Signal Intensity Exploiting FRET Phenomenon for Biomedical Applications," *J. Nanomater. Mol. Nanotechnol.*, vol. s6, pp. 6–11, 2018, doi: 10.4172/2324-8777.s6-003.

[9] V. Gubala, G. Giovannini, F. Kunc, M. P. Monopoli, and C. J. Moore, "Dye-doped silica nanoparticles: Synthesis, surface chemistry and bioapplications," *Cancer Nanotechnology*, vol. 11, no. 1. BioMed Central Ltd., pp. 1–43, Jan. 09, 2020, doi: 10.1186/s12645-019-0056-x.

[10] S. Y. Fam, C. F. Chee, C. Y. Yong, K. L. Ho, A. R. Mariatulqabtiah, and W. S. Tan, "Stealth coating of Nanoparticles in drug-delivery systems," *Nanomaterials*, vol. 10, no. 4, pp. 1–18, 2020, doi: 10.3390/nano10040787.

[11] S. Aryal, J. J. Grailer, S. Pilla, D. A. Steeber, and S. Gong, "Doxorubicin conjugated gold nanoparticles as water-soluble and pH-responsive anticancer drug nanocarriers," *J. Mater. Chem.*, vol. 19, no. 42, pp. 7879–7884, 2009, doi: 10.1039/b914071a.

[12] B. Chazotte, "Labeling lysosomes in live cells with lysotracker," *Cold Spring Harb. Protoc.*, vol. 6, no. 2, Feb. 2011, doi: 10.1101/pdb.prot5571.

[13] B. Canonico *et al.*, "Rapamycin re-directs lysosome network, stimulates er-remodeling, involving membrane CD317 and affecting exocytosis, in Campylobacter Jejuni-lysate-infected U937 cells," *Int. J. Mol. Sci.*, vol. 21, no. 6, 2020, doi: 10.3390/ijms21062207.

[14] S. Bolte and F. P. Cordelières, "A guided tour into subcellular colocalization analysis in light microscopy," *Journal of Microscopy*, vol. 224, no. 3. Blackwell Publishing Ltd, pp. 213–232, 2006, doi: 10.1111/j.1365-2818.2006.01706.x.

[15] W. Strober, "Trypan Blue Exclusion Test of Cell Viability," *Curr. Protoc. Immunol.*, vol. 111, no. 1, p. A3.B.1-A3.B.3, Nov. 2015, doi: 10.1002/0471142735.ima03bs111.

[16] B. Canonico *et al.*, "Defective Autophagy, Mitochondrial Clearance and Lipophagy in Niemann-Pick Type B Lymphocytes," *PLoS One*, vol. 11, no. 10, p. e0165780, Oct. 2016, doi: 10.1371/journal.pone.0165780.

[17] P. Simeone *et al.*, "Diameters and fluorescence calibration for extracellular vesicle analyses by flow cytometry," *Int. J. Mol. Sci.*, vol. 21, no. 21, pp. 1–15, 2020, doi: 10.3390/ijms21217885.

[18] Z. Andreu and M. Yáñez-Mó, “Tetraspanins in extracellular vesicle formation and function,” *Front. Immunol.*, vol. 5, no. SEP, 2014, doi: 10.3389/fimmu.2014.00442.

[19] U. Repnik, M. H. Česen, and B. Turk, “The endolysosomal system in cell death and survival,” *Cold Spring Harb. Perspect. Biol.*, vol. 5, no. 1, p. a008755, Jan. 2013, doi: 10.1101/cshperspect.a008755.

[20] J. Wang *et al.*, “DOX-loaded peptide dendritic copolymer nanoparticles for combating multidrug resistance by regulating the lysosomal pathway of apoptosis in breast cancer cells,” *J. Mater. Chem. B*, vol. 8, no. 6, pp. 1157–1170, 2020, doi: 10.1039/c9tb02130b.

[21] M. Kauffman, M. Kauffman, H. Zhu, Z. Jia, and Y. Li, “Fluorescence-Based Assays for Measuring Doxorubicin in Biological Systems,” *React. Oxyg. Species*, vol. 2, no. 6, p. 432, 2016, doi: 10.20455/ros.2016.873.

[22] S. Bhattacharjee *et al.*, “Role of surface charge and oxidative stress in cytotoxicity of organic monolayer-coated silicon nanoparticles towards macrophage NR8383 cells.,” *Part. Fibre Toxicol.*, vol. 7, no. 1, p. 25, Sep. 2010, doi: 10.1186/1743-8977-7-25.

[23] C. Riebeling *et al.*, “A guide to nanosafety testing : Considerations on cytotoxicity testing in different cell models,” *NANOIMPACT*, 2017, doi: 10.1016/j.impact.2017.11.004ï.

[24] S.-H. Wu *et al.*, “RBC-derived vesicles as a systemic delivery system of doxorubicin for lysosomal-mitochondrial axis-improved cancer therapy,” *J. Adv. Res.*, Nov. 2020, doi: 10.1016/j.jare.2020.11.009.

[25] O. Bar-On, M. Shapira, and D. D. Hershko, “Differential effects of doxorubicin treatment on cell cycle arrest and Skp2 expression in breast cancer cells,” *Anticancer. Drugs*, vol. 18, no. 10, pp. 1113–1121, 2007, doi: 10.1097/CAD.0b013e3282ef4571.

[26] A. Saraste and K. Pulkki, “Morphologic and biochemical hallmarks of apoptosis,” *Cardiovascular Research*, vol. 45, no. 3. Oxford Academic, pp. 528–537, Feb. 01, 2000, doi: 10.1016/S0008-6363(99)00384-3.

[27] H. Hintzsche, G. Montag, and H. Stopper, “Induction of micronuclei by four cytostatic compounds in human hematopoietic stem cells and human lymphoblastoid TK6 cells,” *Sci. Rep.*, vol. 8, no. 1, pp. 1–11, 2018, doi: 10.1038/s41598-018-21680-8.

[28] H. S. Kim, Y. S. Lee, and D. K. Kim, “Doxorubicin exerts cytotoxic effects through cell cycle arrest and fas-mediated cell death,” *Pharmacology*, vol. 84, no. 5, pp. 300–309, 2009, doi: 10.1159/000245937.

[29] V. J. Yuste, J. R. Bayascas, N. Llecha, I. Sánchez-López, J. Boix, and J. X. Comella, “The absence of oligonucleosomal DNA fragmentation during apoptosis of IMR-5 neuroblastoma cells. Disappearance of the caspase-activated DNase,” *J. Biol. Chem.*, vol. 276, no. 25, pp. 22323–22331, Jun. 2001, doi: 10.1074/jbc.M100072200.

[30] H. P. Dong *et al.*, “Evaluation of cell surface expression of phosphatidylserine in ovarian carcinoma effusions using the annexin-V/7-AAD assay: Clinical relevance and comparison with other apoptosis parameters,” *Am. J. Clin. Pathol.*, vol. 132, no. 5, pp. 756–762, 2009, doi: 10.1309/AJCPAVFA8J3KHPRS.

[31] A. Smith, M. A. Parkes, G. K. Atkin-Smith, R. Tixeira, and I. K. Poon, “Cell disassembly during apoptosis,” *WikiJournal Med.*, vol. 4, no. 1, p. 8, 2017, doi: 10.15347/wjm/2017.008.

[32] R. Tixeira *et al.*, “Defining the morphologic features and products of cell disassembly during apoptosis,” *Apoptosis*, vol. 22, no. 3, pp. 475–477, 2017, doi: 10.1007/s10495-017-1345-7.

[33] P. Friedl and S. Alexander, “Cancer invasion and the microenvironment: Plasticity and reciprocity,” *Cell*, vol. 147, no. 5. Elsevier, pp. 992–1009, Nov. 23, 2011, doi: 10.1016/j.cell.2011.11.016.

[34] X. Wang *et al.*, “Enrichment of CD44 in Exosomes From Breast Cancer Cells Treated With Doxorubicin Promotes Chemoresistance,” *Front. Oncol.*, vol. 10, no. July, pp. 1–12, 2020, doi: 10.3389/fonc.2020.00960.

[35] X. J. Fang, H. Jiang, Y. Q. Zhu, L. Y. Zhang, Q. H. Fan, and Y. Tian, “Doxorubicin induces drug resistance and expression of the novel CD44st via NF-κB in human breast cancer MCF-7 cells,” *Oncol. Rep.*, vol. 31, no. 6, pp. 2735–2742, 2014, doi: 10.3892/or.2014.3131.

[36] I. geun Ryoo, B. hyun Choi, S. K. Ku, and M. K. Kwak, “High CD44 expression mediates p62-associated NFE2L2/NRF2 activation in breast cancer stem cell-like cells: Implications for cancer stem cell resistance,” *Redox Biol.*, vol. 17, pp. 246–258, Jul. 2018, doi: 10.1016/j.redox.2018.04.015.

[37] R. Marhaba, P. Klingbeil, T. Nuebel, I. Nazarenko, M. Buechler, and M. Zoeller, “CD44 and EpCAM: Cancer-Initiating Cell Markers,” *Curr. Mol. Med.*, vol. 8, no. 8, pp. 784–804, 2008, doi: 10.2174/156652408786733667.

[38] K. J. Wolf *et al.*, “A mode of cell adhesion and migration facilitated by CD44-dependent microtentacles,” *Proc. Natl. Acad. Sci. U. S. A.*, vol. 117, no. 21, 2020, doi: 10.1073/pnas.1914294117.

[39] S. S. Skandalis, T. T. Karalis, A. Chatzopoulos, and N. K. Karamanos, “Hyaluronan-CD44 axis orchestrates cancer stem cell functions,” *Cell. Signal.*, vol. 63, no. July, p. 109377, 2019, doi: 10.1016/j.cellsig.2019.109377.

[40] R. Kakarla, J. Hur, Y. J. Kim, J. Kim, and Y. J. Chwae, “Apoptotic cell-derived exosomes: messages from dying cells,” *Exp. Mol. Med.*, vol. 52, no. 1, pp. 1–6, 2020, doi: 10.1038/s12276-019-0362-8.

[41] M. Battistelli and E. Falcieri, “Apoptotic bodies: Particular extracellular vesicles involved in intercellular communication,” *Biology*, vol. 9, no. 1. MDPI AG, Jan. 01, 2020, doi: 10.3390/biology9010021.

[42] M. Guescini *et al.*, “Muscle Releases Alpha-Sarcoglycan Positive Extracellular Vesicles Carrying miRNAs in the Bloodstream,” *PLoS One*, vol. 10, no. 5, p. e0125094, May 2015, doi: 10.1371/journal.pone.0125094.

Supplementary information

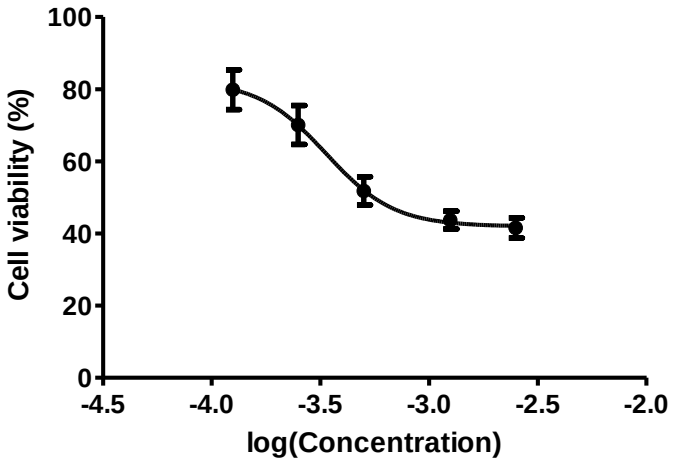

Fig. S1 The logarithmic curve for MCF-7 cells response to different concentration of doxorubicin at 24 h to calculate IC_{50} and use it in the further experiments.

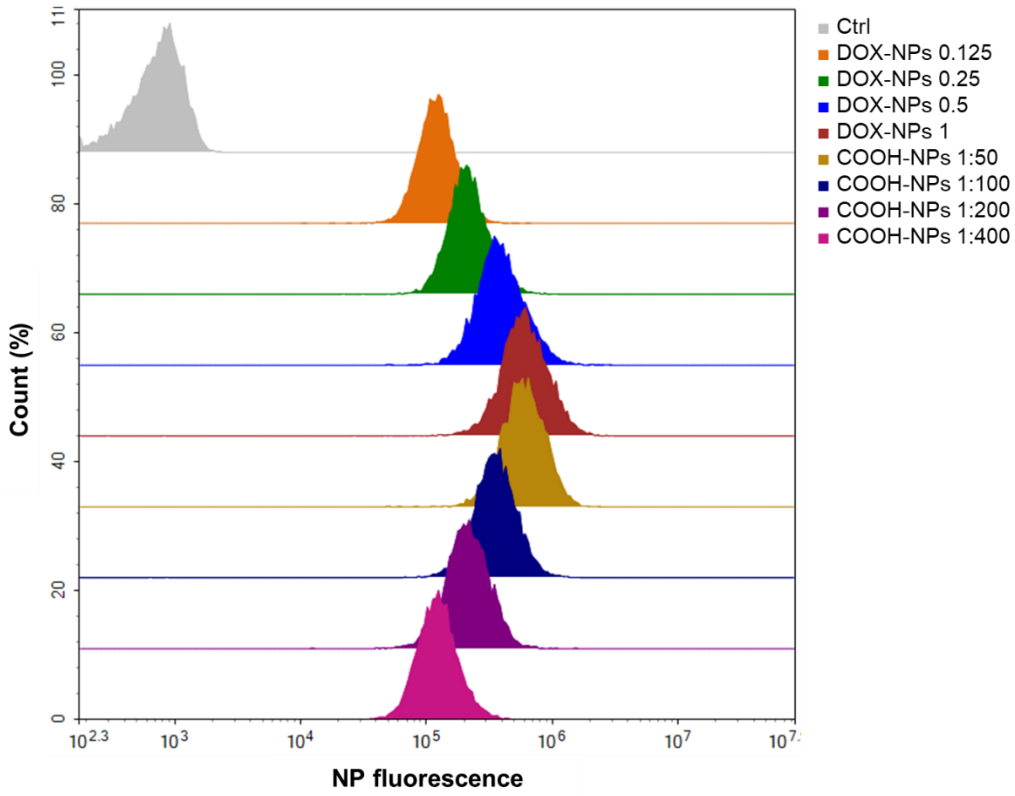

Fig. S2 Flow cytometry histogram overlay of MCF-7 cells incubated for 24 h with different concentrations of DOX-NPs (0.125, 0.25, 0.5 and 1 µg/mL of drug) and COOH-NPs (diluted 1:50, 1:100, 1:200 and 1:400), in order to titrate NPs and utilize stand-alone NP as control with the same fluorescence of DOX-NPs in the NP fluorescent channel.

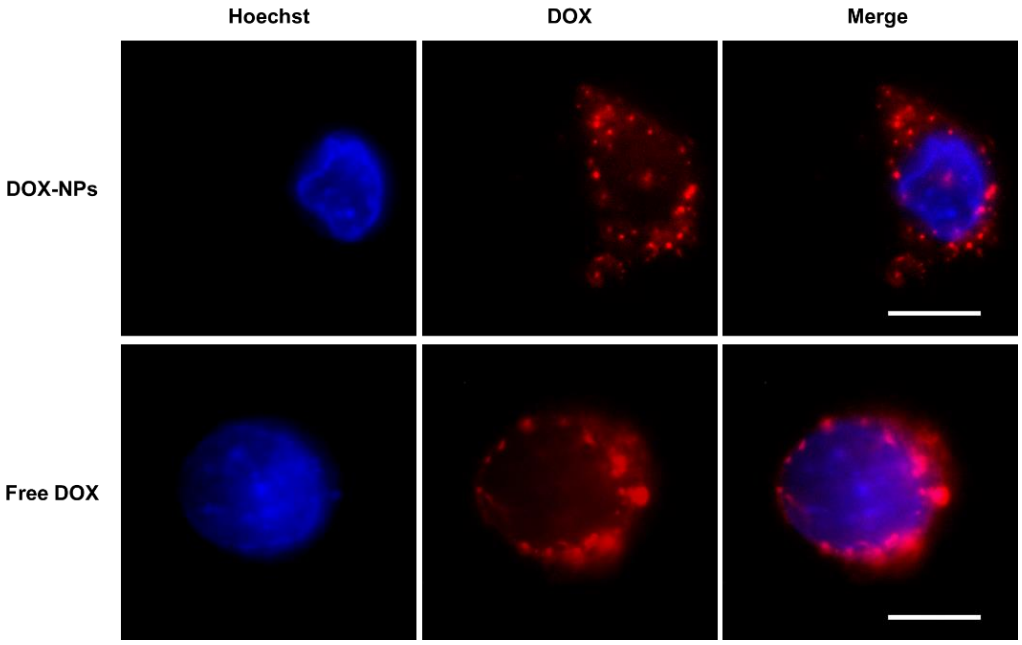

Fig. S3 Fluorescent microscopy images of MCF-7 cells incubated for 48 h with DOX-NPs and free DOX and counter-stained nuclei with Hoechst 33342 to investigate doxorubicin localization inside the cells. Doxorubicin in red, Hoechst 33342 in blue. MCF-7 cells treated with DOX-NPs mainly present DOX fluorescent confined inside vesicle-like organelles (above frames), whereas free DOX is also inside the nucleus and in perinuclear region, besides micronuclei which are being disposed of by the dying cell (below frames). Merged images highlight the presence of free DOX into the nucleus, which results in a more violet color. Scale bar= 10 µm. Magnification 100X oil immersion.

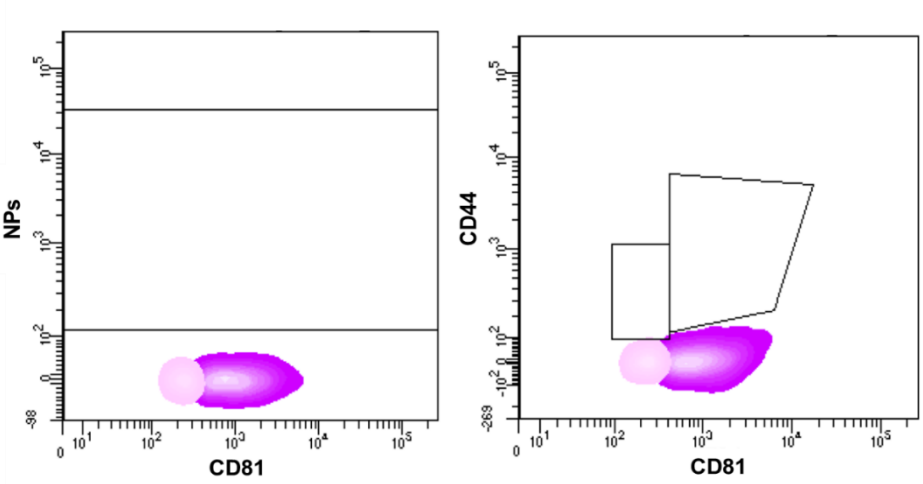

Fig. S4 Flow cytometry contouring plots of negative sample (w/o CD44 RPE) to set the gates for the detection of NPs containing EVs (on the left), by distinguishing CD81- (pink) and CD81+ (violet) among CD44+ events (on the right) of supernatants. In order to count the events in the corresponding gate, media were stained with Dako CytoCount™ beads. At least 30000 events have been acquired by flow cytometry for each experimental condition.

Conclusions

In this study, we investigated the cellular uptake and intracellular fate of multiple dye doped silica NPs, NT_B700, into lymphoid and myeloid cells (U937 tumoral cell line and PBCMs). Results showed that the internalization process is time-, concentration-, energy- and cell type-dependent. Among the immune cells we had examined, monocytes, described as "professional" phagocytic cells, strongly participated in NP internalization. We observed, both with NTA and TEM, a partially aggregated form of NPs, present together with the monodisperse one, which was also influenced by pH. The aggregation increased at low pH, compared to physiological one, and this will influence their internalization, trafficking inside the cells, endosomal escape (to mitochondria) and finally, their release. Our results highlighted, therefore, that NT_B700 NPs did not have a preferred route of internalization; once inside the cells NPs were transported within plasma-membrane bounded vesicles along microtubules to organelles, as lysosomes and, in particular, mitochondria (Fig. 1), but without significantly affect cell viability. Cells did not enter to death but we noticed a slight arrest of cell growth. As previously mentioned, the toxic potential of NPs is dependent on their size and shape, determining their propensity to induce ROS generation. Usually, following exposure to NPs, the intracellular generation of ROS sharply increases but, in our model, although an initial ROS overexpression was detected, mitochondrial functions were not substantially impaired. Cells remained viable after 72 h, and we can affirm that absolutely lack catastrophic consequences of the studied NPs on cells, due to moderate and temporary ROS increase. Further experiments will take into account intracellular antioxidant pool. However, the permanence of mild H_2O_2 content up to 48-72 h propelled us to remind that H_2O_2 might act as a signaling molecule or lead to oxidative damage of biomolecules, depending on the cellular context, its local concentration, and the kinetics of its production and elimination. Finally, both lymphoid and myeloid cells were able to release NPs (Fig 1) and this aspect is essential for their biosafety and future developments, although in an organism extruded NPs represent a material to be filtered and permanently expelled. In conclusion, all these data allow to consider NT_B700 nanoparticles promising platform for future development of multifunctional systems. Exploiting the functional groups on the shell surface, we would conjugate a cytotoxic drug, in addition to the targeting molecule, to combine imaging and therapeutic applications in a unique tool.

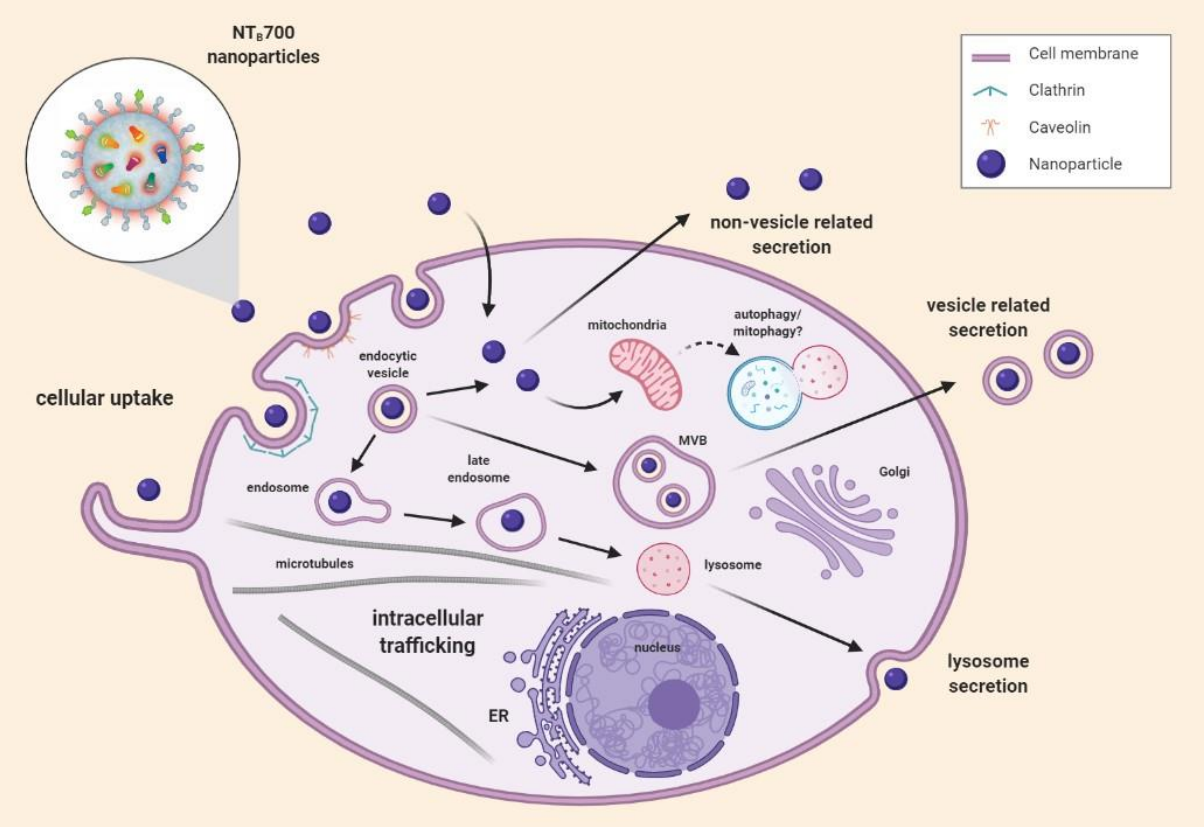

Fig. 1 Representative scheme of supposed NT_B700 uptake, intracellular trafficking pathways and release.

Starting from these good assumptions, we decided to conjugate (by changing functional groups on the shell surface from $-NH_2$ to -COOH) one of the most commonly used anticancer drug, doxorubicin (DOX). As antineoplastic agent, DOX has both a high efficacy but also an elevated systemic toxicity and causes multiple side effects. With the employ of nanostructure, we wished to overcome some well-known limitations. We tested the resulting DOX-NPs on breast cancer cell line MCF-7, since DOX is currently one of the most effective agents in the treatment of breast cancer. We evaluated cytotoxicity, the effect on cell cycle and the impact on the expression of CD44 antigen, a molecule involved in cell-matrix adhesion, therefore in cell spreading in tumour invasion, both on cell surface and the enrichment of CD44 in exosomes. We did not find an increased cytotoxic effect, as we expected, but a different modulation of CD44 expression on MCF-7 cells surface and less release of CD44+ extracellular vesicles (EVs), from both CD81- and CD81+ pools, which has a relevant importance in terms of pathology spreading and metastasization process. These preliminary data allow to consider fluorescent SiNPs a good tool for drug delivery, but it is still necessary to improve the drug doping on NPs, (we reached 25% of drug conjugation yield), in contrast to conjugation of monoclonal antibodies, which is now standardized. To have the same drug concentration of

free DOX (IC_{50}), in fact, too many NPs are currently required. Our data suggest that the delivery system itself works inasmuch it allows the internalization of DOX not from the passive transport but *via* endocytic pathways, reaching some main organelles, such as lysosomes and mitochondria. Since drug nanocarriers, once inside the cells, will encounter a series of endocytic compartments with increasing acidity, the employ of some acid-cleavable linkers between DOX and NPs may raise cytotoxicity. The nanosystem will increase the overall intracellular accumulation of the anticancer drug, through the EPR effect, and DOX will only be released in a pH-dependent controlled manner, by improving the efficacy of the treatment with greatly reduce the side effects to normal tissues. Furthermore, we could take into account the mitochondria localization of fluorescent SiNPs into the peri-mitochondrial space, as deeply illustrated in Appendix A and the effects on such an important organelle Our data suggested that the mitochondrial functionality was not substantially impaired, even if we noticed a slight arrest of cell growth. As concerning ROS formation (both species hydrogen peroxide and superoxide), although we detected an initial ROS overexpression, mitochondrial respiration was not substantially impaired, thanks to higher amount of GSH significant for ROS buffering. In general, we observed that quantitively the ROS produced by PBMCs were in lower amount than U937, which are the tumoral counterparts. This finding might suggest the use of NPs in combination with other drug treatments to potentiate their cytotoxic effect. Moreover, the SiNPs localization might be very interesting for those human illness, including diabetes, neurodegenerative disease as Parkinson's and Alzheimer's, and many types of cancer, which are linked to mitochondrial dysfunctions (Ma et al., 2020). Increasing interest is more and more addressed to mitochondrial targeting for both probes and therapeutics. Thanks to their specific subcellular localization, fluorescent SiNPs might be advantageous in these fields of application.

Finally, besides the intracellular localization that we observed, it is important to study the targeting ability of the under-study fluorescent NPs. In Appendix B, indeed, we presented the high pure systems that we are able to achieve for mAb conjugation to fluorescent SiNPs, thanks to their intrinsic characteristics. NP bioconjugates bind their target with high specificity and enhanced intensity signal, thanks to the multiple dyes within their silica core, as depicted from flow cytometry analysis. Hence, we could conjugate whatever targeting molecules on NP surface to specifically direct the cell population we are interested in, with both diagnostic and therapeutic aims.

To conclude, besides the fluorescent properties as promising imaging tool, SiNPs can be easily modulated in terms of type and numbers of functional groups exposed on their surface. This promising strategy can be suitable for conjugation of different molecules (e.g. mAb, drug, peptides, DNA, radionuclide, …), to devise a multifunctional system which may take place in several applications in therapy and diagnostic in the same tool (Fig. 2), as, for example, antibody conjugated nanoparticles (ACNPs) which represents a novel strategy for the development of therapies exploiting antibodies to enhance the delivery of drug payloads.

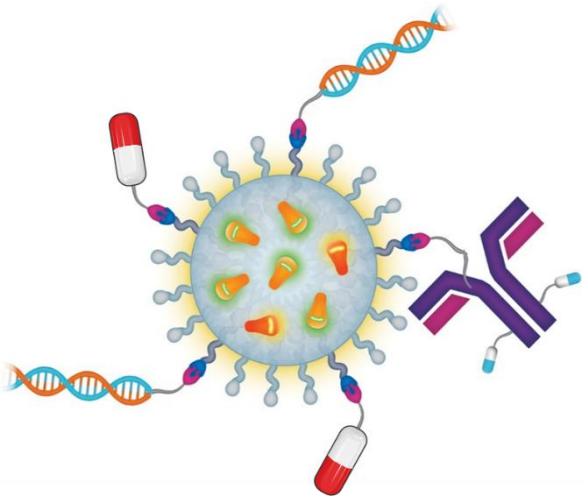

Fig. 2 Schematic representation of multifunctional tool based on fluorescent silica NPs (SiNPs) enabling the conjugation of biologically active molecules for targeting and one or more therapeutic agents, by modulating the types and numbers of functional groups on shell surface and enhancing the delivery of drug payloads

Appendix A

In-depth analysis of NT_B700 nanoparticles localization and effects on isolated mitochondria

To deeply characterize mitochondria uptake of NPs, and their status after NT_B700 internalization, we isolated mitochondria from control and NT_B700 treated U937 cells, by means of the protocol highlighted in the Material and Methods session. Isolated mitochondria were tested by Flow Cytometry and Confocal Microscopy.

In Fig. A1, brightfield images of isolated mitochondria from controls (1 h and 24 h) and NP-treated cells (1 h and 24 h) are visible. In these images we can appreciate a slight reduction in the size of this organelle. Furthermore, fluorescence colocalization highlights rounded, yellow/green, MTG/TMRE labelled mitochondria, with onion-shaped cristae, from control, whereas in NP treated cells, it is evident a light violet fluorescence (originating by overlapping red and green colors with blue of NPs). The fluorescence images put in light the peripheral distribution of NT_B700, certainly located in the peri-mitochondrial space, underlining that inner membrane is a valid barrier against delivery of exogenous material into mitochondrial matrix. The NT_B700 positive mitochondria is more elongated and it seems polarized, suggesting the budding of a mitochondrial derived vesicles: however, these aspects are now under investigations.

The quantitative flow cytometric analyses, show a 2-fold increase of mitochondria NT_B700 positive, (40% after 1 h vs 80% after 24 h), furthermore, NT_B700 fluorescence intensity are 3-fold higher after 24 h than after 1 h, suggesting that in the same cells, NPs tend to accumulate in a specific mitochondrion.

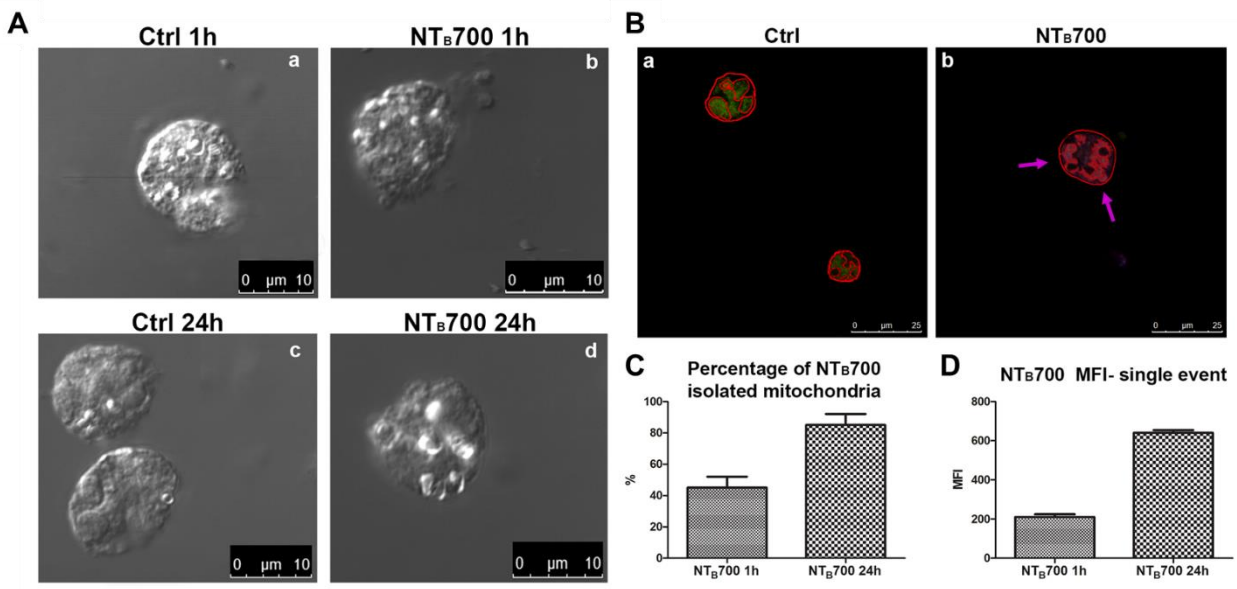

Fig. A1 Isolated mitochondria of U937 cells incubated for 1 or 24 h with NT_B700 nanoparticles. (A) Representative brightfield images of isolated mitochondria from controls (1 h and 24 h, a and c) and NP-treated cells (1 h and 24 h, b and d). Scale bar = 10 µm. (B) Representative fluorescent merged confocal images of isolated mitochondria from control (a) and NP-treated cells (b) for 24 h and then stained with LTG (green) and TMRE (red). Yellow/green and violet indicate colocalization (highlighted in treated cells from violet harrows). Scale bars: 25 µm. (C) Histogram of flow cytometry data indicating percentage of NT_B700 positive cells after 1 h and 24 h of incubation. (D) Histogram of flow cytometry data which illustrate Mean Fluorescence Intensity (MFI) of NT_B700 NPS within isolated mitochondria of U937 cells after 1 h and 24 of treatment. At least 10000 events were analysed by flow cytometry for each experimental condition.

The contour plots and histograms in Fig. A2 illustrate the sequence of analysis and gating strategy by which we quantitate mitochondria NT_B700 uptake. However, inserting MTG and TMRE in this multiparametric panel, we are able to evaluate mass and function of isolated mitochondria. In controls it is evident the absence of any fluorescent signal in the NP fluorescent channel, whereas in NT_B700 positive samples, the right shift of fluorescence is clear and intense. Intriguingly, in the contour plot FSC vs MTG (FITC), in particular after 24 h, a mitochondria population with high MFI MTG values, is observable. A subset of this population displays also higher FSC values: this is a further suggestion for mitochondria fission and/or mitochondrial-derived vesicles (MDVs) budding from mitochondria outer membrane.

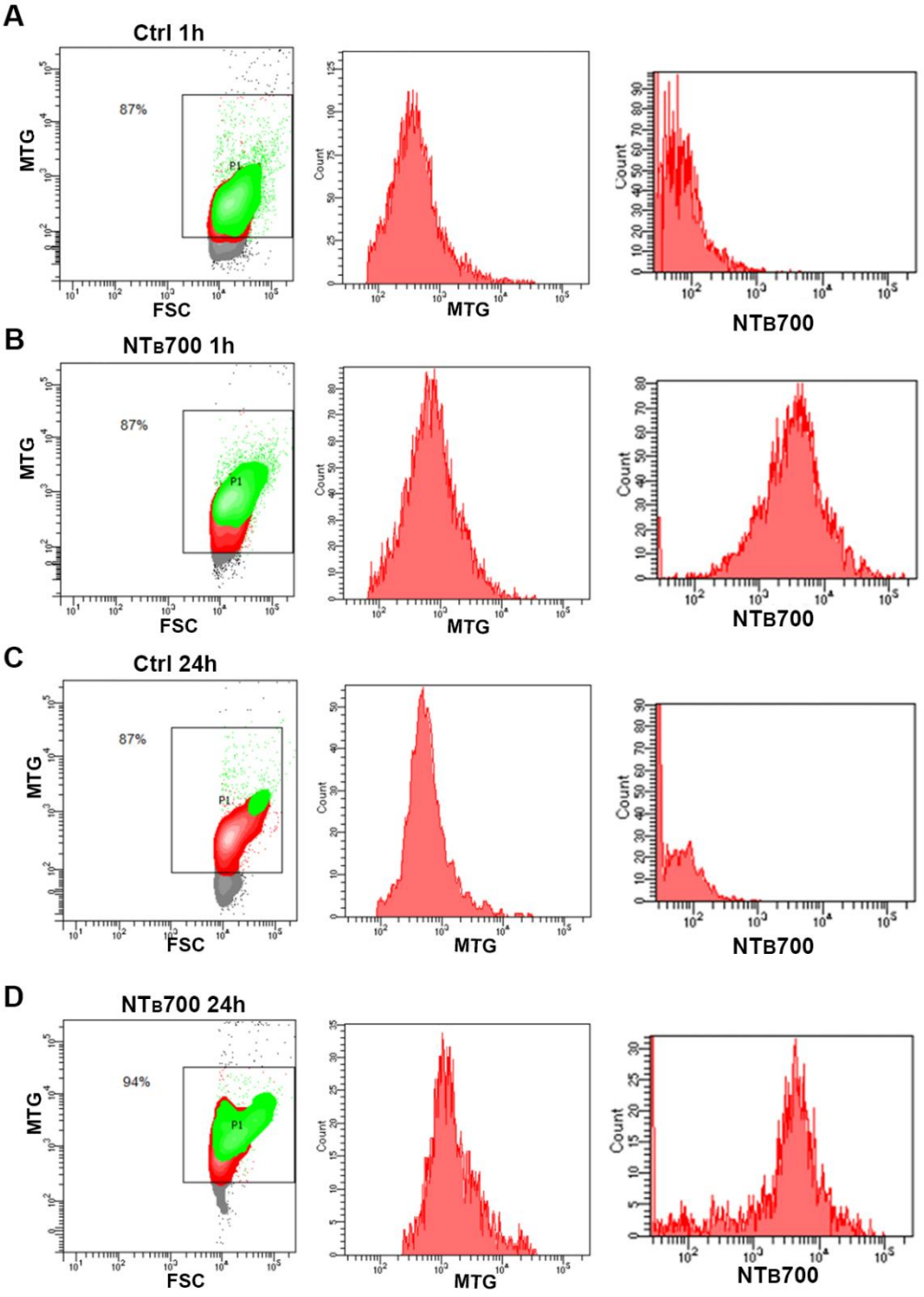

Fig. A2 NT_B700 nanoparticle uptake study of U937 isolated mitochondria and mitochondrial mass investigation. Sequence of analysis by flow cytometry of NT_B700 fluorescence and MTG staining of isolated mitochondria from controls, 1 h and 24 h (A-C) and NP-incubated cells, 1 h and 24 h (B-D). From left to right: contour plots FSC vs. MTG (FITC), histograms of MTG staining of gated population and histograms in NP fluorescent channel. At least 10000 events were analysed by flow cytometry for each experimental condition.

The increase of both MTG and TMRE after 24 h from NT_B700 explains the reduction of mitochondrial GSH content (Fig. A3): In fact, the increase in MTG may account for MDV formation and starting fission process, and it is accompanied by TMRE increase, denoting augmented $\triangle\Psi m$. These sequalae of events leads to inhibition of the levels of mitochondrial glutathione to impair free radical scavenging, leading to further increases in ROS (Duan et al., 2020).

These findings apparently are not in agreement with our previous data on mitochondria, inside cells. However, isolation procedure could exacerbate some mitochondrial damage or lesive process but, more importantly, the total, intracellular GSH content increase after both 1 h and 24 h, leading to ROS buffering and cell homeostasis, since, we did not register significant cell death phenomena, until 72 h of investigations.

Our data, taking into account recent references on the field, seem to depict the following scenario:

1) Cells after 1 h maintain the ability to synthetize GSH in the cytosol and its transport to mitochondria is not compromised, indeed it is increased in respect to control cells, as demonstrated by data on mitochondria GSH.

2) After 24 h, total GSH of NT_B700 treated-cells is higher than control cells and mitochondria GSH is slightly reduced, suggesting that the NP filled peri-mitochondrial space, may impair specific inner mitochondria membrane (IMM) carriers, able to transport GSH.

3) MDVs budding (to deeply characterize) should have the capability to partially free mitochondria from NT_B700 MDVs and this option is absolutely in agreement with viable status of the cells and NT_B700 release in the environment.

In Fig. A4 we have summarized in a schematic illustration all collected data of NT_B700 nanoparticle uptake in U937 cells and their intracellular trafficking, by highlighting, particularly, the impact on mitochondria.

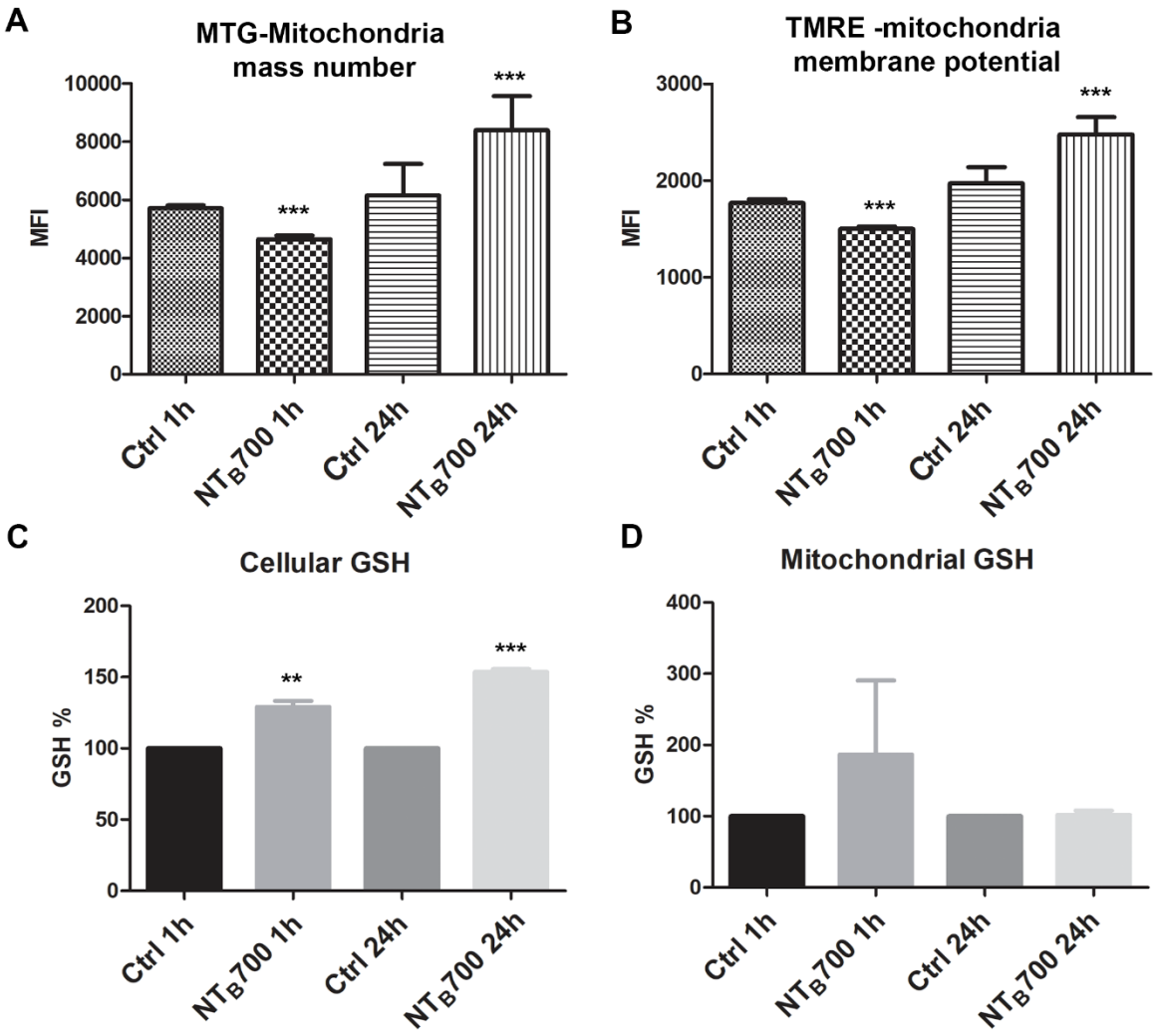

Fig. A3 Assessment of mitochondrial features of isolated mitochondria from U937 cells incubated for short or long time with NT_B700 nanoparticles. Quantification of mitochondrial mass with MTG staining (A) and mitochondrial membrane potential (MMP) $\triangle\Psi m$ with TMRE (B) through flow cytometry analysis of control and treated cells for 1 and 24 h. Determination of cellular (C) and mitochondrial (D) glutathione (GSH) content in U937 cells incubated with NP for 1 h or 24 h by high performance liquid chromatography (HPLC). GSH content of untreated U937 cells was 25.0 ± 5 nmol/mg proteins in cells and 3.55 ± 0.55 nmol/mg proteins in mitochondria. Asterisks denote a statistically significant difference (** = $p < 0.01$, *** = $p < 0.001$) of treated compared to the relative control. At least 10000 events were analysed by flow cytometry for each experimental condition.

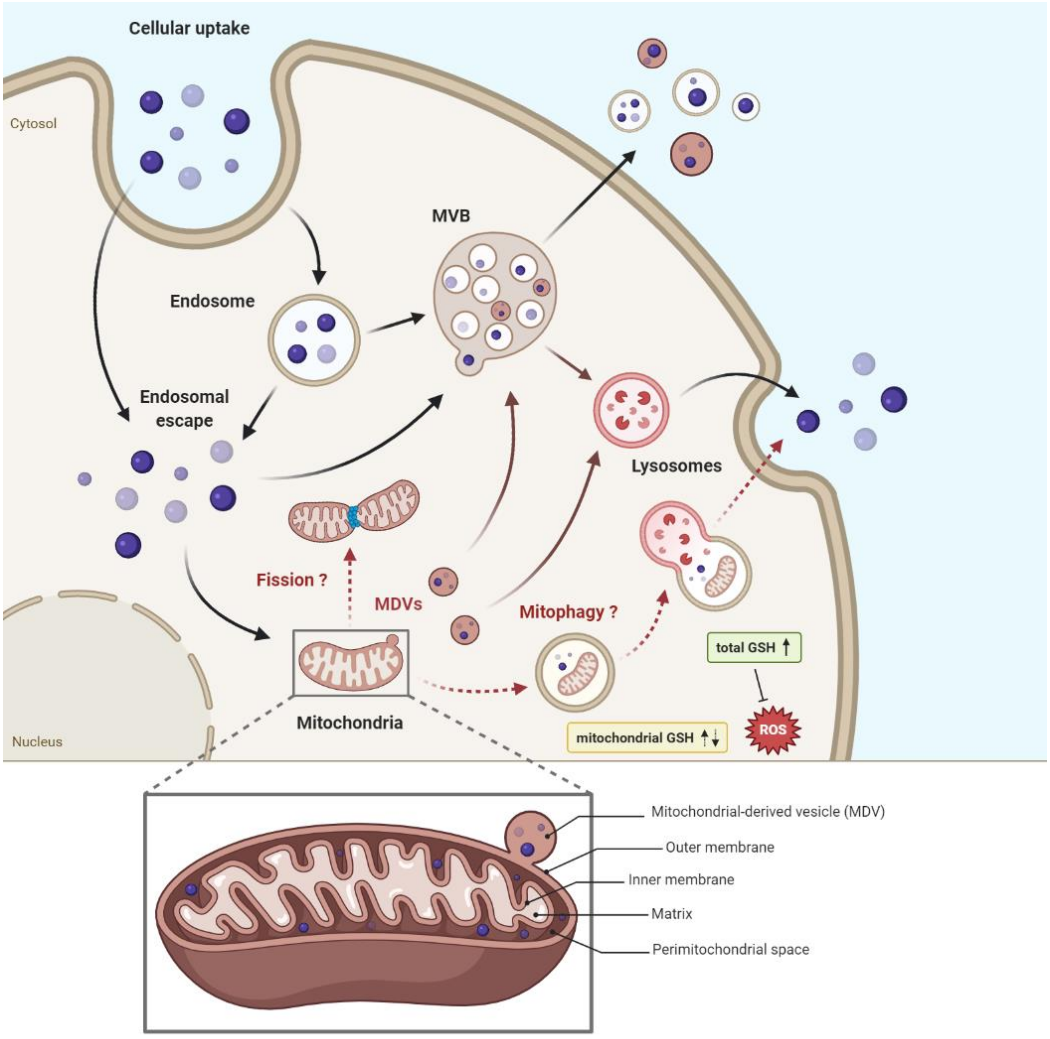

Fig. A4 Schematic representation of NT_B700 nanoparticle uptake in U937 cells and their intracellular trafficking, by highlighting the effects on mitochondria. Our previously data showed a colocalization with both lysosomes and mitochondria in U937 cells, indicating intracellular endocytic rehashing of NPs once inside the cells and transport to other organelles. Confocal analysis depicted the peripheral distribution of NT_B700, located in the peri-mitochondrial space (as illustrate in the enlargement of the mitochondrion) confirmed. Flow cytometric data of entire cells and isolated mitochondria suggested the mitophagic process to eliminate damaged mitochondria full of NPs or either mitochondria fission and/or mitochondrial-derived vesicles (MDVs) budding from mitochondria outer membrane to free mitochondria from NT_B700. Although an initial ROS overexpression was detected, mitochondrial respiration was not substantially impaired. After 1 h, cells maintain the ability to synthetize GSH in the cytosol and its transport to mitochondria is not compromised, as we observed a higher amount of GSH in respect to controls. Nevertheless, after 24 h of incubation with NPs, total GSH is still higher than control cells in order to buffer ROS, while mitochondria GSH is slightly reduced. Finally, cells are able to release NPs both with vesicle or non-vesicle related secretion. (Image created with BioRender.com)

Materials and Methods

GSH, dithiobis-(2-nitrobenzoic acid) (DTNB) as well most of the reagent-grade chemicals were purchased from Sigma-Aldrich (Milan, Italy).

Isolation of mitochondria

Mitochondria were isolated by differential centrifugation, as detailed in (Fiorani et al., 2010). In brief, the U937 cells (40-50 x 10^6) were washed twice in Phosphate Buffered Solution (PBS, 136 mM NaCl, 10 mM Na_2HPO_4, 1.5 mM KH_2PO_4, 3 mM KCl; pH 7.4) and re-suspended (10 x 10^6 cells/ml) in ice-cold homogenizing buffer (HB, 225 mM mannitol, 75 mM sucrose, 0.1 mM EGTA, protease inhibitor cocktail, 5 mM Tris-HCl, pH 7.4). The cells were homogenized with 30-40 strokes, by using a glass potter placed in an ice-bath. The efficiency of the homogenization process was monitored under the microscope, by counting the number of residual trypan blue negative cells. The homogenate was centrifuged at 1000 g for 10 min at +4°C and the supernatant (S1) collected for the final centrifugation. The pellet was re-homogenized and the supernatant (S2) added to S1 and (S1+S2) centrifuged at 12,000 g for 30 min at 4 °C. The pellet, corresponding to the mitochondrial fraction, was carefully resuspended in HB. Aliquots of mitochondrial suspensions were collected to perform further analyses and mitochondrial protein assay. The remaining suspension was centrifuged at 12,000 g for 20 min at +4°C and the mitochondrial pellet processed for the GSH measurement by HPLC, as detailed below.

Measurement of GSH content in cells and mitochondria by high performance liquid chromatography

The determination of GSH content in U937 cells and mitochondria was performed as described in Fiorani et al. (Fiorani et al., 2018). Briefly, the cellular (1×10^6 cells) and mitochondrial pellets were suspended in 100 µl of lysis buffer (0.1% Triton X-100; 0.1 M Na_2HPO_4; 5 mM Na-EDTA, pH 7.5), vortexed and kept for 10 min on an ice bath. Thereafter, 15 µl of 0.1 N HCl and 140 µl of precipitating solution (0.2 M glacial meta-phosphoric acid, 5 mM sodium EDTA, 5 M NaCl) were added to the samples. After centrifugation, the supernatants were collected and kept at −20 °C until the HPLC analyses. Just before analysis, 60 µl of the acid extract were supplemented with 15 µl of 0.3 M Na_2HPO_4 and 15 µl of a solution containing 20 mg of DTNB in 100 ml of sodium citrate (1% w/v). The mixture was stirred for 1 min at room temperature and, after 5 min, filtered through 0.22 µm pore micro-filters. The resulting samples were finally analyzed for their GSH content by an HPLC assay (Guidarelli, Fiorani,

Cerioni, and Cantoni, 2019), using a 15 cm × 4.6 mm, 5 µm Supelco Discovery® C18 column (Supelco, Bellefonte, PA). The UV absorption was detected at 330 nm. The injection volume was 20 µl. The retention time of GSH was approximately 15.7 min.

Flow cytometric and confocal analyses

Isolated mitochondria were further analysed by Flow Cytometry and Confocal Microscopy. For the determination of mitochondrial potential (ΔΨm) and mitochondrial mass we employed two different probes, respectively, tetramethylrhodamine ethyl ester perchlorate (TMRE) and MitoTracker™ Green (MTG). MTG (Thermo Fisher Scientific, Waltham, MA, USA) is a mitochondrial-selective fluorescent label which passively spreads through the plasma membrane and accumulates in active mitochondria where it covalently binds to mitochondrial proteins by reacting with free thiol groups of cysteine residues, measuring the mitochondrial mass (Presley et al., 2003 Canonico et al., 2009). MTG 50 nM was added to the samples, incubated for 30 minutes at 37°C and then acquired. TMRE (Sigma-Aldrich, St. Louis, MO, USA) 40 nM, which is a ΔΨm-specific stain able to selectively enter active mitochondria, was added to the samples 15 min before the acquisition (Canonico et al., 2020). To establish the healthy condition of isolated mitochondria we also used carbonyl cyanide m-chlorophenylhydrazone (CCCP), which is a typical mitochondrial uncoupler, leading to the dissipation of mitochondrial membrane potential (Miyazono et al., 2018). After the incubation of control mitochondria with 10 µM CCCP for 45 min, we observed a decrease of TMRE, resulting in a correct procedure of mitochondria isolation. Thus, we proceeded with TMRE and MTG staining of all samples, with were analysed with a FACSCanto™ II flow cytometer (BD Biosciences, San Jose, CA, USA), equipped with an argon laser (Blue, Ex 488 nm), a helium-neon laser (Red, Ex 633 nm) and a solid-state diode laser (Violet, Ex 405 nm). For each sample, at least 10.000 events were acquired. Data analyses were performed with FACSDiva™ softwares (BD Biosciences, San Jose, CA, USA). Furthermore, a qualitative analysis of morphological features and the localization of NPs within isolated mitochondria was applied by a Leica TCS SP5 II confocal microscope (Leica Microsystem, Germany) with 488, 543 and 633 nm illuminations and oil-immersed objectives. The images were further processed and analysed in ImageJ software (National Institutes of Health, Bethesda, MD, USA).

Appendix B

Site-specific antibody conjugation to fluorescent silica nanoparticles for highly pure systems

Despite the wide use of the traditional fluorochromes, their limits are widely known, such as broad emission spectra, short emission time, susceptibility to photobleaching and to many species in the external environment, which could quench their fluorescence. The field of diagnostic still pays attention in the identification of new technologies allowing to overcome them. Thanks to their unique characteristics, nanoparticles stood out as good candidates in several biomedical applications. Fluorescent silica NPs (SiNPs) are multiple dye doped core-shell nanostructures where fluorophores are entrapped into a silica matrix, which is photophysically inert, not involved in energy or electron transfer processes and intrinsically non-toxic (Pellegrino et al., 2018). Thanks to the nanometric dimension, the silica core can hold multiple dyes resulting in increased signal intensity and where the process of fluorescence resonance energy transfer (FRET) occurs at high efficiency rate. Besides being one of the main "stealth" polymers employed in the drug delivery and FDA-approved, the polyethylene glycol (PEG), which composed NP shell, protects the fluorescent molecules from external stimuli and induces stability and solubility in water. Finally, it allows to modulate the types and number of functional groups (e.g. amine, thiol, carboxyl or methacrylate) exposed on NPs surface and leads the conjugation of several biomolecules. Bioconjugation with PEG (also known as PEGylation) is the covalent conjugation of molecules such as peptides, proteins, or oligonucleotides with PEG (Fam et al., 2020).

The unique structural characteristics of antibody molecules allow several choices for modification and conjugation schemes. The chemistry used to conjugate formation should be chosen to yield the best possible preservation of antigen binding activity. In order to limit the steric hindrance, the site-specific conjugation to SiNPs involves a crosslinker reagent that can specifically react with residues that are only in certain position on the immunoglobulin surface, avoiding the antigen binding sites. The disulfide bridges in the hinge region can be selectively cleaved with a reducing agent such us 1,4-dithiothreitol (DTT). A protein, in its native conformation, is frequently protected from complete reduction. For instance, at a moderate concentration of DTT and without denaturants, limited cleavage of disulphides in antibody molecules results in reducing mainly the bonds between the heavy chains of immunoglobulin. This strategy leads to obtain an exposed sulfhydryl group which can be targeted for conjugation

using a crosslinker with 8.3Å spacer arm and thiol-reactive moieties, to limit the steric hindrance and preserving the antibody biological activity. Our bioconjugation method, indeed, takes advantage of the heterobifunctional crosslinker Succinimidyl-4-(N-maleimidomethyl) cyclohexane-1-carboxylate (SMCC) which contains N-hydroxysuccinimide (NHS) ester and maleimide groups that simultaneously allow covalent conjugation of amines and sulfhydryl containing molecules. NHS reacts with the $-NH_2$ on NP surface, to form amide bonds, while maleimides react with sulfhydryl groups available on the hinge region of monoclonal antibodies (reduced), to form stable thioester bonds (Hermanson, 2008). Conjugation molar ratio (Ab/NP) depends on the biological molecules involved in the bioconjugation process (isotype and consequently sulfhydryl group available on hinge region), spacer arm of crosslinker used and dimensions of SiNPs, which have been standardize in order to obtain the best fluorescence performance and homogeneity of the system. Several molar ratios, in fact, have been tested and the right amount of mAbs and NPs has been bettered to gain one antibody per NP, therefore other binding sites were still suitable for other conjugation. Moreover, we decreased the quantity of free mAb, we improved the uniformity of the process and rose the conjugation yield (from 10% to 30%). To sum up, as illustrated in Fig. B1, the bioconjugation of mAb to fluorescent SiNPs involves the following steps: activation of NPs with SMCC crosslinker, mAb reduction and, finally, the bioconjugation reaction.

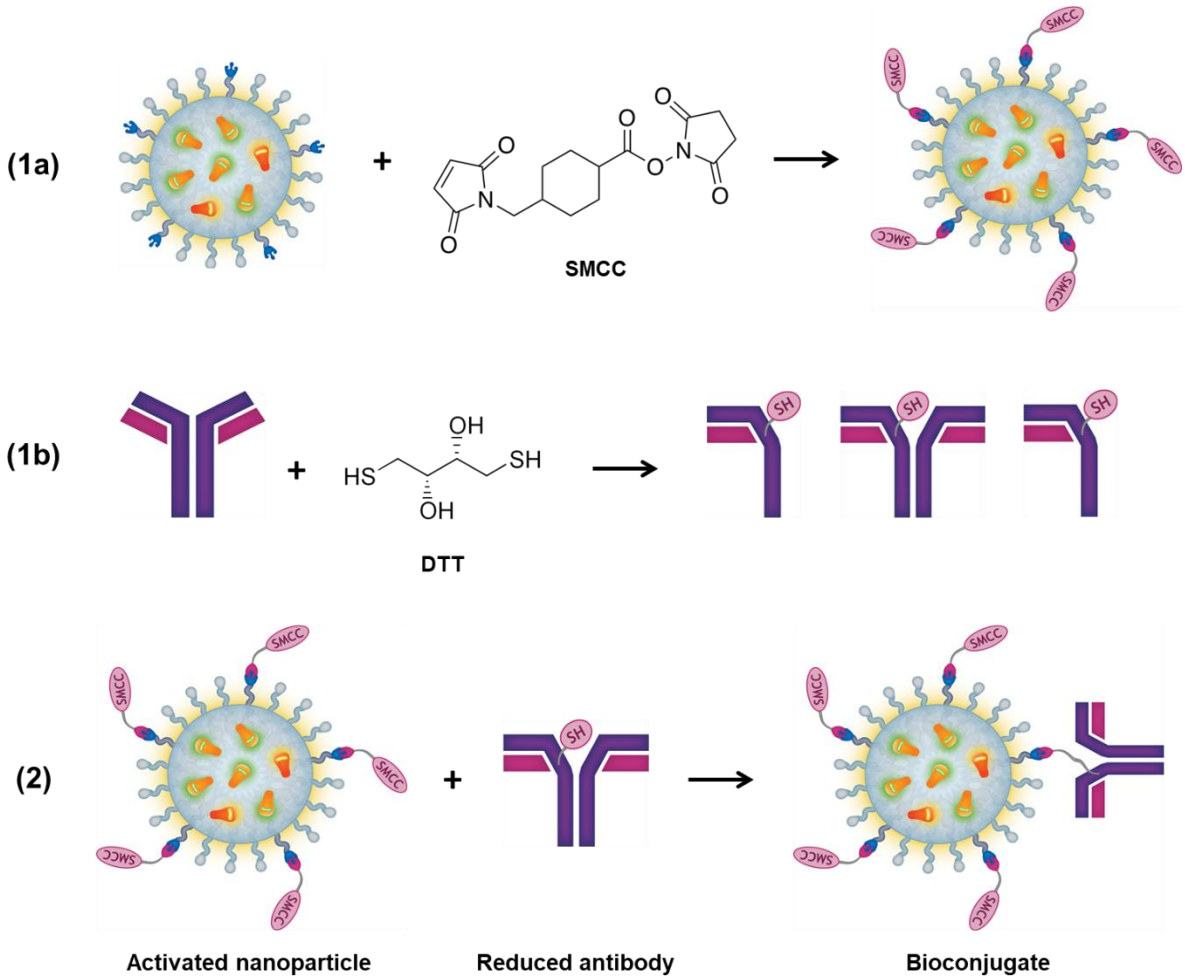

Fig. B1 Schematic representation of fluorescent silica nanoparticles (SiNPs) conjugation to monoclonal antibody (mAb). The process involves different steps: (1a) SiNP activation with the heterobifunctional crosslinker SMCC through the NHS group which reacts with amine groups on NP surface, to form amine bond; (1b) the mAb reduction with DTT, which, at a moderate concentration, is able to cleave the disulphide bonds between the heavy chains of immunoglobulin; (2) finally the bioconjugation of the reduced antibody to the activated SiNP, exploiting the maleimide group of SMCC, which is still free, that reacts with sulfhydryl groups available on the hinge region of reduced mAb, to form stable thioester bonds.

Afterward, to obtain a high pure system, the NP bioconjugate follows two subsequently steps of purification (Fig. B2-A): size-exclusion chromatography (SEC) and affinity chromatography (AC). The former separates the unbound antibody from the bioconjugate, exploiting the pores of the stationary phase and separating the species based on their dimensions (Nagy & Vékey, 2008). Affinity chromatography, instead, eliminates unbound NPs, hence reaching a high degree of purity (more than 96%). Affinity chromatography technique takes advantage of the reversible interaction between the Fc region of monoclonal

IgG-type antibodies and a specific ligand immobilized in a chromatographic matrix (Grodzki & Berenstein, 2010). The stationary phase (protein G) allows us to eluate all the unconjugated NP from the mixture during the binding phase, thanks to the interaction of the conjugate to protein G through the Fc portion. This unique strategy leads to select only the conjugate having intact Fc portion, reducing heterogeneity and not interfering with antibody biological properties.

One of the possible applications in diagnostics of NP-based conjugates is flow cytometry, which also allows to quickly evaluate the quality of products. Fig. B2-B shows cytometric results on whole blood staining of the three products obtained during the purification steps of Ms. anti-human anti-CD4 conjugated to NT_B700: the first product from SEC, the unbound portion from AC and the final conjugate from the purification by AC. The dot plots show that the purification by AC leads to an improvement of the conjugated performance: higher fluorescence (mean positive) and better discrimination between the positive and negative populations. The alongside histogram (Fig. B2-C) illustrates, indeed, the signal-to-noise ratio (S/N= MFI positive cells/MFI negative cells) of each sample, highlighting the higher discrimination of the final biconjugate after all steps of purifications, leading to a high pure system. Besides anti-CD4 antibody, we conjugated another common monoclonal antibody with different antigen density, Ms. anti-human anti-CD8. The brilliant signal of NPs allowed to well discriminate between $CD8_{dim}$ and $CD8_{bright}$, respectively presented in red and orange in Fig. B2-D. Furthermore, thanks to the interesting features of SiNPs regarding fluorescence and the high degree of purity, the final bioconjugate presents better results also compared to commercial traditional conjugate (Fig. B2-E).

To conclude, Ab-NP conjugates lead to overcome the classic drawbacks faced with traditional fluorescent molecules, enhancing system homogeneity, purity and making the best performance for both fluorescence intensity and stability. NP versatility, associates to conjugation technology, allows to consider this system as a promising platform for future developments for targeting tools. Since SiNPs can be easily modulated in terms of type and numbers of functional groups exposed on their surface, this promising strategy can be suitable for conjugation of different molecules (e.g. mAb, drug, peptides, DNA, radionuclides), to devise a multifunctional system which may take place in several applications in therapy.

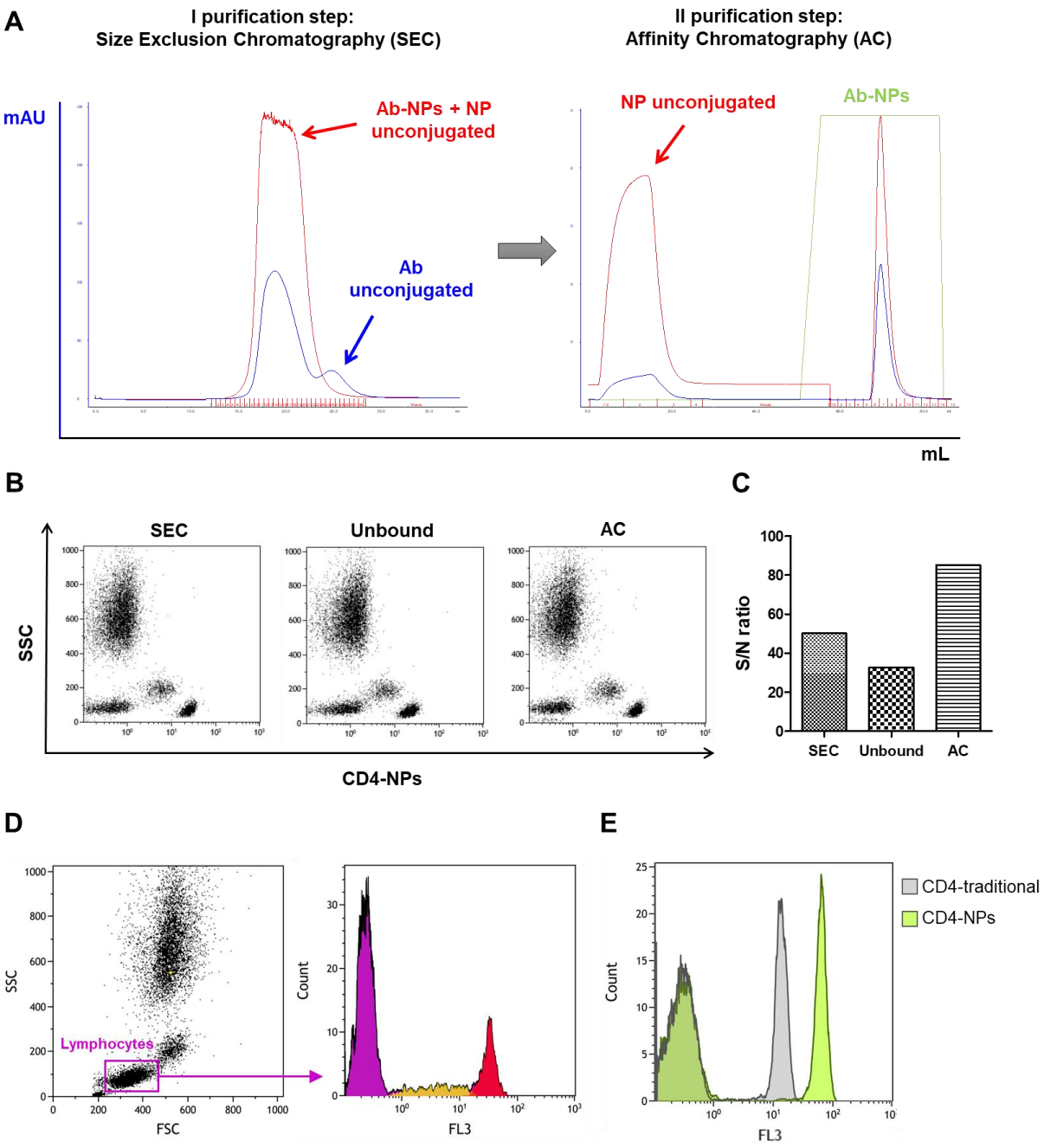

Fig. B2 Effects of the chromatography-based purification steps on SiNP conjugates and flow cytometric applications. (A) Size-exclusion chromatography (SEC) separates the unbound antibody from the bioconjugate, while affinity chromatography (AC) eliminates unbound nanoparticles thus reaching a high degree of purity for both antibodies and nanoparticles. HPLC chromatograms present a blue cure (280 nm) to monitor Ab and the red one (498 nm) for NPs, both free and conjugated. The green box highlights the final Ab-NP conjugate. (B) Flow cytometric dot plots of mouse anti-human anti -CD4 antibody (clone EDU-2, AcZon s.r.l.) conjugated to fluorescent SiNP, resulting from the different purification steps. (C) Signal-to-noise (S/N) ratios from CD4 staining on whole blood of the three products obtained during the purification steps. (D) Stained-and-lysed whole blood with Ms. anti-human anti-CD8 (clone 733, AcZon s.r.l.): FSC vs SSC dot plot for gating strategy of lymphocytes (violet) and resulting gated histogram with $CD8_{dim}$ (orange) and $CD8_{bright}$ (red) highlighted. (E) Flow cytometry histogram overlay of whole blood stained with Ms. anti-human anti-CD4 (clone EDU-2, AcZon s.r.l.) conjugated, respectively, with a traditional fluorochrome and fluorescent SiNPs, gated on lymphocytes.

Materials and Methods

All chemical reagents were purchased from Sigma-Aldrich Srl (St Louis, MO, USA).

Bioconjugation

NT_B700 NPs were firstly activated with the heterobifunctional cross-linker succinimidyl 4-(N-maleimidomethyl)cyclohexane-1-carboxylate (SMCC, Setareh Biotech, Eugene, OR, USA): 5 mL of NPs in 50 mM NaPi/1 mM EDTA pH=8 were made to react with 4.5 mg of SMCC (10 mM) for one hour at room temperature. The mixture was, then, purified by SEC using 50 mM MES/2 mM EDTA, to remove the SMCC that did not react. Afterwards, 2 mg of mouse anti-human CD4 (clone EDU-2, IgG2a) or CD8 (clone 733, IgG1) (AcZon s.r.l., Monte San Pietro, BO, Italy), previously reduced with 20 mM 1,4-dithiothreitol (DTT), were incubated with activated NPs for 1 h at room temperature (RT) under stirring, in the dark. Conjugation molar ratio depends on the biological molecules involved in the bioconjugations process (isotype and consequently sulfhydryl groups available on Ab hinge region)

Purification steps

Size Exclusion Chromatography (SEC)

The reaction mixture is first purified by size exclusion chromatography (SEC) on a XK16 column (GE Healthcare, Chicago, Il, USA), packed with Superdex^{TM} 200 resin (GE Healthcare, Chicago, Il, USA). The purification was carried out with ÄKTA purifier 10 HPLC system, (Amersham Pharmacia Biotech, Little Chalfont, UK), by applying the following instrument set-up:

Flow	2 mL/min
Pressure	< 3 MPa
UV1	280.0 nm
UV2	498.0 nm
UV3	ND
Column Volume	200 mL
Diameter	16 mm

Affinity chromatography (AC)

The bioconjugates were further purified by affinity chromatography where the stationary phase was Protein G Sepharose™ 4 fast Flow (GE Healthcare, Chicago, Il, USA), packed in XK16 column (GE Healthcare, Chicago, Il, USA). The samples were applied on protein G through HPLC system ÄKTA purifier 10 and we performed three different steps: (1) binding of conjugate on stationary phase, (2) washing of the unbound portion with PBS 1X (10 mM NaPi, 150 mM NaCl, pH 7.3-7.4) and (3) elution of the fraction which have bound the protein G with Fc region of mAb with 0.1 M Glycine pH 2.4. The purification process was performed by applying the following instrument set-up:

Flow	**Binding:** 0.5 mL/min
	Washing: 1 mL/min
	Elution: 2 mL/min
Pressure	< 3 MPa
UV1	280.0 nm
UV2	498.0 nm
UV3	ND
Column Volume	3 mL
Diameter	16 mm

The sample were dialyzed against PBS 1X using regenerated cellulose membrane tubing (*cut-off* 50 kDa) (VWR, Radnor, PA, USA) for at least 24 h, then, concentrated with Amicon stirred ultrafiltration cell (Merck Millipore Ltd., Tullagreen, Ireland) using PVDF membranes (*cut-off* 50 kDa) (VWR, Radnor, PA, USA) and, finally, centrifuged at 14000 rpm for 30 min at +4°C, discarding the pellet, if any.

Flow cytometric analysis

NP-conjugated monoclonal antibodies were added to 100 µL of whole peripheral blood, previously dispended into suitable tubes, vortexed at low speed and then incubated for 20 min at RT in the dark. After the incubation time, 2 mL of NH_4Cl lysing solution were added, mixed by vortexing and incubated for 10 min at RT (until the red blood cells were lysed). Finally, the

samples were acquired by flow cytometry. Cytometric experiments were carried out with a FACSCanto™ II flow cytometer (BD Biosciences, San Jose, CA, USA), equipped with an argon laser (Blue, Ex 488 nm), a helium-neon laser (Red, Ex 633 nm) and a solid-state diode laser (Violet, Ex 405 nm). For each sample, at least 10.000 events were acquired. Data analyses were performed with Kaluza Analysis 2.1 (Beckman Coulter, Brea, CA, USA).

References

Abbasi, E., Aval, S. F., Akbarzadeh, A., Milani, M., Nasrabadi, H. T., Joo, S. W., Pashaei-Asl, R. (2014). Dendrimers: Synthesis, applications, and properties. *Nanoscale Research Letters*, Vol. 9, pp. 1–10. Springer New York LLC. https://doi.org/10.1186/1556-276X-9-247

Auten, R. L., and Davis, J. M. (2009). Oxygen toxicity and reactive oxygen species: The devil is in the details. *Pediatric Research*, Vol. 66, pp. 121–127. Pediatr Res. https://doi.org/10.1203/PDR.0b013e3181a9eafb

Babu, A., Templeton, A. K., Munshi, A., and Ramesh, R. (2014). Nanodrug delivery systems: A promising technology for detection, diagnosis, and treatment of cancer. *AAPS PharmSciTech*, *15*(3), 709–721. https://doi.org/10.1208/s12249-014-0089-8

Bao, G., Mitragotri, S., and Tong, S. (2013). Multifunctional nanoparticles for drug delivery and molecular imaging. *Annual Review of Biomedical Engineering*, Vol. 15, pp. 253–282. Annu Rev Biomed Eng. https://doi.org/10.1146/annurev-bioeng-071812-152409

Barua, S., Yoo, J. W., Kolhar, P., Wakankar, A., Gokarn, Y. R., and Mitragotri, S. (2013). Particle shape enhances specificity of antibody-displaying nanoparticles. *Proceedings of the National Academy of Sciences of the United States of America*, *110*(9), 3270–3275. https://doi.org/10.1073/pnas.1216893110

Bayda, S., Adeel, M., Tuccinardi, T., Cordani, M., and Rizzolio, F. (2020). The history of nanoscience and nanotechnology: From chemical-physical applications to nanomedicine. *Molecules*, Vol. 25, p. 112. MDPI AG. https://doi.org/10.3390/molecules25010112

Bhatia, S. (2016). Nanotechnology and Its Drug Delivery Applications. In *Natural Polymer Drug Delivery Systems* (pp. 1–32). Springer International Publishing. https://doi.org/10.1007/978-3-319-41129-3_1

Blechinger, J., Bauer, A. T., Torrano, A. A., Gorzelanny, C., Bräuchle, C., and Schneider, S. W. (2013). Uptake kinetics and nanotoxicity of silica nanoparticles are cell type dependent. *Small*, *9*(23), 3970–3980. https://doi.org/10.1002/smll.201301004

Bonacchi, S., Genovese, D., Juris, R., Montalti, M., Prodi, L., Rampazzo, E., and Zaccheroni, N. (2011). Luminescent silica nanoparticles: Extending the frontiers of brightness. *Angewandte Chemie - International Edition*, *50*(18), 4056–4066. https://doi.org/10.1002/anie.201004996

Burke, B. P., Cawthorne, C., and Archibald, S. (2017). Multimodal nanoparticle imaging agents: design and applications. *Phil. Trans. R. Soc. A*, *375*(20170261). https://doi.org/10.1098/rsta.2017.0261

Çalış, S., Öztürk Atar, K., Arslan, F. B., Eroğlu, H., and Çapan, Y. (2019). Nanopharmaceuticals as Drug-Delivery Systems. *Nanocarriers for Drug Delivery*, 133–154. https://doi.org/10.1016/b978-0-12-814033-8.00004-7

Canonico, B., Cesarini, E., Montanari, M., Di Sario, G., Campana, R., Galluzzi, L., … Papa, S. (2020). Rapamycin re-directs lysosome network, stimulates er-remodeling, involving membrane CD317 and affecting exocytosis, in Campylobacter Jejuni-lysate-infected U937 cells. *International Journal of Molecular Sciences*, *21*(6). https://doi.org/10.3390/ijms21062207

Canonico, Barbara, Luchetti, F., Arcangeletti, M., Valentini, M., Papa, S., Natura, A., … Salvatore, S. (2009). Indagini citofluorimetriche nella vitalità e morte cellulare. II. Studio di altre funzioni cellulari. *Biochimica Clinica*, *33*(2), 93–103.

Cheng, Z., Al Zaki, A., Hui, J. Z., Muzykantov, V. R., and Tsourkas, A. (2012). Multifunctional nanoparticles: Cost versus benefit of adding targeting and imaging capabilities. *Science*, *338*(6109), 903–910. https://doi.org/10.1126/science.1226338

Choi, K. Y., Min, K. H., Yoon, H. Y., Kim, K., Park, J. H., Kwon, I. C., … Jeong, S. Y. (2011). PEGylation of hyaluronic acid nanoparticles improves tumor targetability in vivo. *Biomaterials*, *32*(7), 1880–1889. https://doi.org/10.1016/j.biomaterials.2010.11.010

Chu, Z., Huang, Y., Tao, Q., and Li, Q. (2011). Cellular uptake, evolution, and excretion of silica nanoparticles in human cells. *Nanoscale*, *3*(8), 3291–3299. https://doi.org/10.1039/c1nr10499c

De, G. G., Cruz, L., Rodríguez-Fragoso, P., Reyes-Esparza, J., Rodríguez-López, A., Gómez-Cansino, R., and Rodriguez-Fragoso, L. (2016). *Interaction of Nanoparticles with Blood Components and Associated Pathophysiological Effects Provisional chapter Interaction of Nanoparticles with Blood Components and*

Associated Pathophysiological Effects. https://doi.org/10.5772/intechopen.69386

Donahue, N. D., Acar, H., and Wilhelm, S. (2019). Concepts of nanoparticle cellular uptake, intracellular trafficking, and kinetics in nanomedicine. *Advanced Drug Delivery Reviews*, Vol. 143, pp. 68–96. Elsevier B.V. https://doi.org/10.1016/j.addr.2019.04.008

Duan, C., Kuang, L., Xiang, X., Zhang, J., Zhu, Y., Wu, Y., … Liu, L. (2020). Drp1 regulates mitochondrial dysfunction and dysregulated metabolism in ischemic injury via. *Cell Death and Disease*. https://doi.org/10.1038/s41419-020-2461-9

Eliasof, S., Lazarus, D., Peters, C. G., Case, R. I., Cole, R. O., Hwang, J., … Davis, M. E. (2013). Correlating preclinical animal studies and human clinical trials of a multifunctional, polymeric nanoparticle. *Proceedings of the National Academy of Sciences of the United States of America*, *110*(37), 15127–15132. https://doi.org/10.1073/pnas.1309566110

Fam, S. Y., Chee, C. F., Yong, C. Y., Ho, K. L., Mariatulqabtiah, A. R., and Tan, W. S. (2020). Stealth coating of Nanoparticles in drug-delivery systems. *Nanomaterials*, *10*(4), 1–18. https://doi.org/10.3390/nano10040787

Farokhzad, O. C., Cheng, J., Teply, B. A., Sherifi, I., Jon, S., Kantoff, P. W., … Langer, R. (2006). Targeted nanoparticle-aptamer bioconjugates for cancer chemotherapy in vivo. *Proceedings of the National Academy of Sciences of the United States of America*, *103*(16), 6315–6320. https://doi.org/10.1073/pnas.0601755103

Feynman, R. (1960). There's plenty of room at the bottom. In *Feynman and Computation*: *Vol. Institute* (pp. 63–76). https://doi.org/10.1201/9780429500459

Fiorani, M., Guidarelli, A., Blasa, M., Azzolini, C., Candiracci, M., Piatti, E., and Cantoni, O. (2010). Mitochondria accumulate large amounts of quercetin: Prevention of mitochondrial damage and release upon oxidation of the extramitochondrial fraction of the flavonoid. *Journal of Nutritional Biochemistry*, *21*(5), 397–404. https://doi.org/10.1016/j.jnutbio.2009.01.014

Fiorani, M., Guidarelli, A., Capellacci, V., Cerioni, L., Crinelli, R., and Cantoni, O. (2018). The dual role of mitochondrial superoxide in arsenite toxicity: Signaling at the boundary between apoptotic commitment and cytoprotection. *Toxicology and Applied Pharmacology*, *345*, 26–35. https://doi.org/10.1016/j.taap.2018.03.008

Grodzki, A. C., and Berenstein, E. (2010). Antibody purification: affinity chromatography - protein A and protein G Sepharose. *Methods in Molecular Biology (Clifton, N.J.)*, *588*, 33–41. https://doi.org/10.1007/978-1-59745-324-0_5

Gubala, V., Giovannini, G., Kunc, F., Monopoli, M. P., and Moore, C. J. (2020). Dye-doped silica nanoparticles: Synthesis, surface chemistry and bioapplications. *Cancer Nanotechnology*, Vol. 11, pp. 1–43. BioMed Central Ltd. https://doi.org/10.1186/s12645-019-0056-x

Guidarelli, A., Fiorani, M., Cerioni, L., and Cantoni, O. (2019). Calcium signals between the ryanodine receptor-and mitochondria critically regulate the effects of arsenite on mitochondrial superoxide formation and on the ensuing survival vs apoptotic signaling. *Redox Biology*, *20*, 285–295. https://doi.org/10.1016/j.redox.2018.10.015

Heinz, H., Pramanik, C., Heinz, O., Ding, Y., Mishra, R. K., Marchon, D., Ziolo, R. F. (2017). Nanoparticle decoration with surfactants: Molecular interactions, assembly, and applications. *Surface Science Reports*, Vol. 72, pp. 1–58. Elsevier B.V. https://doi.org/10.1016/j.surfrep.2017.02.001

Hermanson, G. (2008). Bioconjugate Techniques - 2nd Edition.

Hu, H., Ni, Y., Montana, V., Haddon, R. C., and Parpura, V. (2004). Chemically functionalized carbon nanotubes as substrates for neuronal growth. *Nano Letters*, *4*(3), 507–511. https://doi.org/10.1021/nl035193d

Huang, M., Ma, Z., Khor, E., and Lim, L. Y. (2002). Uptake of FITC-chitosan nanoparticles by A549 cells. *Pharmaceutical Research*, *19*(10), 1488–1494. https://doi.org/10.1023/A:1020404615898

Jeevanandam, J., Barhoum, A., Chan, Y. S., Dufresne, A., and Danquah, M. K. (2018). Review on nanoparticles and nanostructured materials: History, sources, toxicity and regulations. *Beilstein Journal of Nanotechnology*, Vol. 9, pp. 1050–1074. Beilstein-Institut Zur Forderung der Chemischen Wissenschaften. https://doi.org/10.3762/bjnano.9.98

Johnston, M. C., and Scott, C. J. (2018). Antibody conjugated nanoparticles as a novel form of antibody drug conjugate chemotherapy. *Drug Discovery Today: Technologies*, *30*, 63–69. https://doi.org/10.1016/j.ddtec.2018.10.003

Juan, A., Cimas, F. J., Bravo, I., Pandiella, A., Ocaña, A., and Alonso-Moreno, C. (2020). An Overview of Antibody Conjugated Polymeric Nanoparticles for Breast Cancer Therapy. *Pharmaceutics*, *12*(9), 802. https://doi.org/10.3390/pharmaceutics12090802

Khan, I., Saeed, K., and Khan, I. (2019). Nanoparticles: Properties, applications and toxicities. *Arabian Journal of Chemistry*, Vol. 12, pp. 908–931. Elsevier B.V. https://doi.org/10.1016/j.arabjc.2017.05.011

Kim, D., Shin, K., Kwon, S. G., and Hyeon, T. (2018). Synthesis and Biomedical Applications of Multifunctional Nanoparticles. *Advanced Materials*, *30*(49), 1–26. https://doi.org/10.1002/adma.201802309

Kou, L., Sun, J., Zhai, Y., and He, Z. (2013). The endocytosis and intracellular fate of nanomedicines: Implication for rational design. *Asian Journal of Pharmaceutical Sciences*, *8*(1), 1–10. https://doi.org/10.1016/j.ajps.2013.07.001

Kulkarni, S. A., and Feng, S. S. (2013). Effects of particle size and surface modification on cellular uptake and biodistribution of polymeric nanoparticles for drug delivery. *Pharmaceutical Research*, *30*(10), 2512–2522. https://doi.org/10.1007/s11095-012-0958-3

Lee, D. E., Koo, H., Sun, I. C., Ryu, J. H., Kim, K., and Kwon, I. C. (2012). Multifunctional nanoparticles for multimodal imaging and theragnosis. *Chemical Society Reviews*, *41*(7), 2656–2672. https://doi.org/10.1039/c2cs15261d

Li, X., Zhang, X.-N., Li, X.-D., and Chang, J. (2016). *Multimodality imaging in nanomedicine and nanotheranostics*. https://doi.org/10.20892/j.issn.2095-3941.2016.0055

Li, Y., Kröger, M., and Liu, W. K. (2015). Shape effect in cellular uptake of PEGylated nanoparticles: Comparison between sphere, rod, cube and disk. *Nanoscale*, *7*(40), 16631–16646. https://doi.org/10.1039/c5nr02970h

Ma, C., Xia, F., and Kelley, S. O. (2020). Mitochondrial Targeting of Probes and Therapeutics to the Powerhouse of the Cell. *Bioconjugate Chemistry*. https://doi.org/10.1021/acs.bioconjchem.0c00470

Mahapatro, A., and Singh, D. K. (2011). Biodegradable nanoparticles are excellent vehicle for site directed in-vivo delivery of drugs and vaccines. *Journal of Nanobiotechnology*, Vol. 9, p. 55. BioMed Central. https://doi.org/10.1186/1477-3155-9-55

McNeil, S. E. (2005). Nanotechnology for the biologist. *Journal of Leukocyte Biology*, *78*(3), 585–594. https://doi.org/10.1189/jlb.0205074

Mendes, P. M. (2013). Cellular nanotechnology: Making biological interfaces smarter. *Chemical Society Reviews*, Vol. 42, pp. 9207–9218. Royal Society of Chemistry. https://doi.org/10.1039/c3cs60198f

Miyazono, Y., Hirashima, S., Ishihara, N., Kusukawa, J., Nakamura, K. I., and Ohta, K. (2018). Uncoupled mitochondria quickly shorten along their long axis to form indented spheroids, instead of rings, in a fission-independent manner. *Scientific Reports*, *8*(1), 350. https://doi.org/10.1038/s41598-017-18582-6

Mohanraj, V. J., and Chen, Y. (2007). Nanoparticles - A review. *Tropical Journal of Pharmaceutical Research*, *5*(1), 561–573. https://doi.org/10.4314/tjpr.v5i1.14634

Moore, C. J., Montón, H., O'Kennedy, R., Williams, D. E., Nogués, C., Crean, C., and Gubala, V. (2015). Controlling colloidal stability of silica nanoparticles during bioconjugation reactions with proteins and improving their longer-term stability, handling and storage. *Journal of Materials Chemistry B*, *3*(10), 2043–2055. https://doi.org/10.1039/c4tb01915f

Nagamune, T. (2017). Biomolecular engineering for nanobio/bionanotechnology. *Nano Convergence*, Vol. 4, p. 9. Korea Nano Technology Research Society. https://doi.org/10.1186/s40580-017-0103-4

Nagy, K., and Vékey, K. (2008). Separation methods. In *Medical Applications of Mass Spectrometry* (pp. 61–92). Elsevier. https://doi.org/10.1016/B978-044451980-1.50007-0

Oh, N., and Park, J. H. (2014). Endocytosis and exocytosis of nanoparticles in mammalian cells. *International Journal of Nanomedicine*, Vol. 9, pp. 51–63. Dove Medical Press Ltd. https://doi.org/10.2147/IJN.S26592

Panariti, A., Miserocchi, G., and Rivolta, I. (2012). The effect of nanoparticle uptake on cellular behavior: Disrupting or enabling functions? *Nanotechnology, Science and Applications*, Vol. 5, pp. 87–100. Dove Press. https://doi.org/10.2147/NSA.S25515

Panowski, S., Bhakta, S., Raab, H., Polakis, P., and Junutula, J. R. (2014). Site-specific antibody drug conjugates for cancer therapy. *MAbs*, *6*(1), 34–45. https://doi.org/10.4161/mabs.27022

Pellegrino, C., Volpe, A., Juris, R., Menna, M., Calabrese, V., Sola, F., Ventola, A. (2018). Multiple Dye Doped Core-Shell Silica Nanoparticles: Outstanding Stability and Signal Intensity Exploiting FRET Phenomenon for Biomedical Applications. *Journal of Nanomaterials & Molecular Nanotechnology*, *s6*, 6–11. https://doi.org/10.4172/2324-8777.s6-003

Picraux, S. T. (2020). Nanotechnology. *Encyclopædia Britannica*. Retrieved from https://www.britannica.com/technology/nanotechnology

Presley, A. D., Fuller, K. M., and Arriaga, E. A. (2003). MitoTracker Green labeling of mitochondrial proteins and their subsequent analysis by capillary electrophoresis with laser-induced fluorescence detection. *Journal of Chromatography B: Analytical Technologies in the Biomedical and Life Sciences*, *793*(1), 141–150. https://doi.org/10.1016/S1570-0232(03)00371-4

Puri, A., Loomis, K., Smith, B., Lee, J. H., Yavlovich, A., Heldman, E., and Blumenthal, R. (2009). Lipid-based nanoparticles as pharmaceutical drug carriers: From concepts to clinic. *Critical Reviews in Therapeutic Drug Carrier Systems*, Vol. 26, pp. 523–580. Begell House Inc. https://doi.org/10.1615/CritRevTherDrugCarrierSyst.v26.i6.10

Rawat, R. S. (2015). Dense Plasma Focus - From Alternative Fusion Source to Versatile High Energy Density Plasma Source for Plasma Nanotechnology. *Journal of Physics: Conference Series*, *591*(1), 012021. Institute of Physics Publishing. https://doi.org/10.1088/1742-6596/591/1/012021

Rigogliuso, S., Sabatino, M. A., Adamo, G., Grimaldi, N., Dispenza, C., and Ghersi, G. (2012). Polymeric nanogels: Nanocarriers for drug delivery application. *Chemical Engineering Transactions*, *27*, 247–252. https://doi.org/10.3303/CET1227042

Sahoo, B., Devi, K. S. P., Banerjee, R., Maiti, T. K., Pramanik, P., and Dhara, D. (2013). Thermal and pH responsive polymer-tethered multifunctional magnetic nanoparticles for targeted delivery of anticancer drug. *ACS Applied Materials and Interfaces*, *5*(9), 3884–3893. https://doi.org/10.1021/am400572b

Sanvicens, N., and Marco, M. P. (2008). Multifunctional nanoparticles - properties and prospects for their use in human medicine. *Trends in Biotechnology*, *26*(8), 425–433. https://doi.org/10.1016/j.tibtech.2008.04.005

Senut, M. C., Zhang, Y., Liu, F., Sen, A., Ruden, D. M., and Mao, G. (2016). Size-Dependent Toxicity of Gold Nanoparticles on Human Embryonic Stem Cells and Their Neural Derivatives. *Small*, *12*(5), 631–646. https://doi.org/10.1002/smll.201502346

Sharma, V. K., Sayes, C. M., Guo, B., Pillai, S., Parsons, J. G., Wang, C., Ma, X. (2019). Interactions between silver nanoparticles and other metal nanoparticles under environmentally relevant conditions: A review. *Science of the Total Environment*, *653*, 1042–1051. https://doi.org/10.1016/j.scitotenv.2018.10.411

Shnoudeh, A. J., Hamad, I., Abdo, R. W., Qadumii, L., Jaber, A. Y., Surchi, H. S., and Alkelany, S. Z. (2019). Synthesis, Characterization, and Applications of Metal Nanoparticles. In *Biomaterials and Bionanotechnology*. Elsevier Inc. https://doi.org/10.1016/B978-0-12-814427-5.00015-9

Shrestha, D., Jenei, A., Nagy, P., Vereb, G., and Szöllősi, J. (2015). Understanding FRET as a research tool for cellular studies. *International Journal of Molecular Sciences*, Vol. 16, pp. 6718–6756. MDPI AG. https://doi.org/10.3390/ijms16046718

Silva, S., Almeida, A. J., and Vale, N. (2019). Combination of cell-penetrating peptides with nanoparticles for therapeutic application: A review. *Biomolecules*, *9*(1), 1–24. https://doi.org/10.3390/biom9010022

Soni, K. S., Desale, S. S., and Bronich, T. K. (2016). Nanogels: An overview of properties, biomedical applications and obstacles to clinical translation. *Journal of Controlled Release*, *240*, 109–126. https://doi.org/10.1016/j.jconrel.2015.11.009

Steckiewicz, K. P., Barcinska, E., Malankowska, A., Zauszkiewicz–Pawlak, A., Nowaczyk, G., Zaleska-Medynska, A., and Inkielewicz-Stepniak, I. (2019). Impact of gold nanoparticles shape on their cytotoxicity

against human osteoblast and osteosarcoma in in vitro model. Evaluation of the safety of use and anti-cancer potential. *Journal of Materials Science: Materials in Medicine*, *30*(2). https://doi.org/10.1007/s10856-019-6221-2

Suk, J. S., Xu, Q., Kim, N., Hanes, J., and Ensign, L. M. (2016). PEGylation as a strategy for improving nanoparticle-based drug and gene delivery. *Advanced Drug Delivery Reviews*, Vol. 99, pp. 28–51. Elsevier B.V. https://doi.org/10.1016/j.addr.2015.09.012

Taniguchi, N. (1974). *On the Basic Concept of Nanotechnology. Proceedings of the International Conference on Production Engineering*. 18–23. Retrieved from https://books.google.co.in/books?id=A-6uHAAACAAJ

Vácha, R., Martinez-Veracoechea, F. J., and Frenkel, D. (2011). Receptor-mediated endocytosis of nanoparticles of various shapes. *Nano Letters*, *11*(12), 5391–5395. https://doi.org/10.1021/nl2030213

Villanueva-Flores, F., Castro-Lugo, A., Ramírez, O. T., and Palomares, L. A. (2020). Understanding cellular interactions with nanomaterials: Towards a rational design of medical nanodevices. *Nanotechnology*, Vol. 31, p. 132002. Institute of Physics Publishing. https://doi.org/10.1088/1361-6528/ab5bc8

Wang, E. C., and Wang, A. Z. (2014). Nanoparticles and their applications in cell and molecular biology. *Integrative Biology (United Kingdom)*, Vol. 6, pp. 9–26. Integr Biol (Camb). https://doi.org/10.1039/c3ib40165k

Wang, L., Wang, K., Santra, S., Zhao, X., Hilliard, L. R., Smith, J. E. Tan, W. (2006). Watching silica nanoparticles glow in the biological world. *Analytical Chemistry*, Vol. 78, pp. 646–654. American Chemical Society . https://doi.org/10.1021/ac0693619

Yonezawa, T. (2018). Preparation of Metal Nanoparticles and Their Application for Materials. In *Nanoparticle Technology Handbook*. Elsevier B.V. https://doi.org/10.1016/B978-0-444-64110-6.00085-8

Chapter 1 and Chapter 2

Sola F, Canonico B, Montanari M, Volpe A, Barattini C, Pellegrino C, Cesarini E, Guescini M, Battistelli M, Ortolani C, Ventola A, Papa S. Uptake and Intracellular Trafficking Studies of Multiple Dye-Doped Core-Shell Silica Nanoparticles in Lymphoid and Myeloid Cells. *Nanotechnology, Science and Applications*. In Press 2021. Sub ID: 290867

Chapter 3

Sola F. et al. Fluorescent silica nanoparticles targeting mitochondria as delivery system for doxorubicin - *In preparation*